Anisotropy, Transport, and Spin-Phonon Interplay in Insulating Magnets

by

C. A. Pocs

B.A., Physics , UC Berkeley 2015

B.A., Applied Mathematics , UC Berkeley 2015

M.S., Physics, CU Boulder, 2017

A thesis submitted to the

Faculty of the Graduate School of the

University of Colorado in partial fulfillment

of the requirements for the degree of

Doctor of Philosophy

Department of Physics

2021

Committee Members:

Minhyea Lee, Chair

Leo Radzihovsky

Gang Cao

Margaret Murnane

Sandeep Sharma

Pocs, C. A. (Ph.D., Physics)

Anisotropy, Transport, and Spin-Phonon Interplay in Insulating Magnets

Thesis directed by Prof. Minhyea Lee

Insulating magnets are a diverse platform for uniquely quantum behavior and the realization of novel cooperative spin states with exotic magnetic and topological excitations. In addition to fundamental interest, such materials have many potential technological applications, from spintronic sensing devices to the next generation of solid-state memory storage and even crucial roles in quantum information processing. The bulk magnetic and thermal properties of these materials are a product of the complex interplay of many interacting spin, orbit, and lattice degrees of freedom on an atomic scale, thus experimental probes that can dissect these microscopic details and recognize new phenomena are highly desirable. This thesis provides an overview of magnetism, thermal transport theory and experimentation, and high-field resonant torsion magnetometry techniques for a wide range of unconventional quantum magnets. We focus on two particular insulating magnets, $CrCl_3$ and $CsYbSe_2$, each of which exemplifies distinct mechanisms of spin-phonon interaction that are manifest in the anisotropic, field-dependent behavior of their respective thermal conductivity tensors. Our work develops new tools to advance the understanding of spin-phonon interactions, and the identification of truly exotic spin states of matter in these, and many other insulating systems.

Dedication

To my parents.

Acknowledgements

To my advisor Minhyea, you always knew how to nudge me in the right direction, and how to turn nebulous ideas into real insights, thanks for your leadership, mentorship, and friendship. To my labmates and friends Ian and Peter, I am forever grateful for your company in enduring so many hours at the Maglab together. I could always rely on you, for your help, your skill, and your ears, whether I was bouncing ideas off you about science or any aspect of life. I want to thank the collaborators at CU that I have had the pleasure of working with on many projects, thank you, Gang Cao, Michael Hermele, Hengdi Zhao, Yu Zhang, Yifei Ni. Thanks also to the NHMFL and many wonderful collaborators and support staff that made almost all the data of this thesis possible. Thanks to the many other amazing people I met in graduate school itself, a handful of whom, James, Brendan, Zack, Kyle, Andrea, I really got to know, whether through the trials of Jackson, shredding the slopes, or sharing a home, y'all made Boulder an amazing place to be through it all. To my longtime friends Roman, Peter, and Michael, thanks for endless entertainment, valuable perspective, and for being there for me through it all. To my Babcia, no one is more selfless, caring, and intense, I am so thankful that you have been such a big part of my life from the beginning. To my Dziadek, although you did not make it to see me finish what I started, you would have been proud, thanks for your love and many happy memories. Lastly, to my parents, thank you for making my dreams possible and for your endless support along this journey. Dad, you instilled a love of science and the technical in me from the beginning and that spark no doubt got me to where I am today. Mom, your courage and strength have inspired me to reach higher and always given me the resolve to accomplish my goals.

Contents

Chapter

Tables

Table

Figures

Figure

Chapter 1

Introduction

1.1 Motivation

Insulating magnets lie at the forefront both of fundamental research into quantum matter and technological advances in the increasingly applied field of spintronics and quantum information processing [1, 2]. A primary goal of theoretical and experimental quantum magnetism is the investigation of exotic spin states that realize phenomena including quasi-particle fractionalization, long-ranged entanglement, and topological order [3, 4]. These properties, and unique spin states, are not only interesting from the perspective of fundamental science, but extremely desirable in far-reaching technological applications. Free from the strong decoherence affecting systems with mobile conduction electrons, insulating magnets can realize many novel ground states with exotic magnetic and topological excitations, providing an excellent testing ground for many theoretical models of charge-neutral, interacting spins [5, 6, 7]. Frustrated antiferromagnets, in particular, can take on many non-collinear magnetic phases and even exotic many-body states such as the much sought-after quantum spin liquid [8, 9]. In this context, thermal transport is a particularly sensitive probe that has long been used to identify elementary and possibly exotic spin excitations in unconventional magnetic insulators [10, 11, 12, 13, 14].

The study of thermal transport concerns how materials carry heat and what quasi-particle processes are involved. The condensed matter physics community understands a great deal about quasi-particles like phonons, the quantized lattice vibrations which are responsible for the lion's share of heat transport in insulators, and certain magnetic quasi-particles such as magnons, the

quantized spin waves that emerge in magnetically ordered phases of matter [15, 16, 17]. There are numerous spectroscopic tools, like calorimetry, inelastic neutron scattering, etc., that elucidate the dispersion and structure of these excitations in countless materials [18, 19, 20]. By contrast, the itinerant characteristics of these quasi-particles, are often difficult to infer directly, and the total thermal conductivity encodes a great deal of information not apparent from most equilibrium thermodynamic, or spectral properties alone. Despite intense theoretical interest, and enormous relevance to practical applications, much of the physics governing steady state transport characteristics of insulating magnets is not fully understood. This is partially a problem of enormous complexity: thermal transport properties are determined by many interacting spin, orbit, and lattice degrees of freedom. The complicated myriad of ways in which different quasi-particle excitations propagate and scatter with each other typically involves many multi-body processes that are not universally understood and nearly impossible to observe directly. Despite the enormous success of innovative transport measurements and precision thermometry that can clearly resolve minute thermal effects [21, 22, 23], the theory of thermal transport phenomena and typical modeling of the thermal conductivities of generic magnetic insulators, remains relatively rudimentary. The work of this thesis contributes two universal and widely-applicable non-system-specific models for analyzing thermal conductivity in systems where magnetic degrees of freedom are crucial to bulk transport properties.

As in many disciplines of science, the key to demystifying any complex system is to isolate specific mechanisms and the parameters they depend on. To this end, we commonly rely on the experimental control knobs of temperature, the strength of externally applied magnetic fields, and in the case of strongly anisotropic materials, the direction of an applied field relative to crystallographic axes. Cooling to cryogenic temperatures can be used to limit competing degrees of freedom and reduce much of the available complexity to a point of tractability. In this way temperature can be used to control thermal fluctuations, the strength of many-body interactions, and the occupation of excited energy states. External, controllable magnets are another invaluable tool, given that ion spins, both collectively and individually, respond strongly to magnetic fields, and fundamentally, the

magnetic field is one of the few experimental ways in which time-reversal symmetry can be broken in crystalline environments. In many materials, changes in the magnetization can even profoundly affect material properties with no immediately obvious connection to the ion spins themselves [24, 14]. In materials such as $CrCl_3$ and $CsYbSe_2$, phonon heat conduction and magnetism are inextricably linked, necessitating the development of new frameworks and models for dealing with spin-lattice interaction, a topic which this thesis explores in great detail.

In constructing a complete picture of any complex magnetic system complementary probes are essential to fully understand its thermodynamic properties and energy landscape. In addition to thermal transport, we use the cutting-edge technique of resonant torsion magnetometery [25], which measures frequency shifts in resonance of vibrating cantilever plus sample system to directly probe anisotropy in the curvature of the magnetic free energy, a fundamental thermodynamic quantity. In the context of crystalline environments, nature is rarely isotropic, thus the ability to explore anisotropy in the angular dependence of physical properties or perturbing effects like external fields is absolutely critical. Leveraging intense, rapidly-pulsed magnetic fields and inherent magnetic anisotropy, resonant torsion magnetometery can uniquely probe magnetic excitations, the thermal occupation of spin states, and the existence of nontrivial magnetic phases in a wide range of unconventional quantum magnets. These properties are not only critical for formulating robust models explicating the contribution of magnetism to heat conduction, but also necessary for exploring novel field-induced pathways to exotic spin states. Having only emerged in the last few years, this technique has been used to shed light on magnetic phase boundaries which vary as a function of applied-field-angle, quantum oscillations in semi-metals, and most recently by us, to unambiguously determine the energetics of exchange and crystal field effects in 4f rare-earth insulating magnets [25, 26]. Work such as ours in developing highly-universal models of spin-lattice-coupled thermal transport and novel analyses of complementary magnetometry probes is crucial for fundamental research into quantum materials and sharpening tools used in the identification of truly exotic spin states of matter.

1.2 Outline of this thesis

This thesis is organized as follows. Chapter 2 describes the essentials of magnetism crucial to understanding this work, including the basics of crystal field interactions and mean-field descriptions of magnetism necessary for much of our finite temperature modeling in later chapters. Chapter 3 explains the basics of quantum mechanical descriptions of lattice vibrations, laying out many important conventions, describing the general characteristics of phonon spectra, and explaining significant models for the heat capacity and thermal conductivity of insulators. Chapter 4 covers all the experimental methods of this thesis, providing a detailed description of thermal conductivity measurements, cantilever-based resonant torsion magnetometry, the underlying theory behind these methods, and many details essential to a their successful implementation. Chapter 5 presents a thermal transport study of $CrCl_3$ a conventional antiferromagnet which exhibits a enormous enhancement of its thermal conductivity under an applied field; in this chapter we introduce the first of our universal models, which empirically describes the effect of spin disorder on phonon scattering. Chapter 6 concerns anisotropic resonant torsion magnetometry measurements in the frustrated triangular lattice system $CsYbSe_2$ and explains how this technique is used to extract crucial microscopic information about crystal field and exchange interactions, providing a novel method for the determination of crystal electric field coefficients. Chapter 7 examines thermal transport in $CsYbSe_2$ and proposes a second highly-universal model of magnetoelastic interaction, a type of spin-phonon hybridization via strain modulation of the magnetic g-tensor, which is used to explain the unique, non-monotonic field-dependence of the thermal conductivity. Lastly, chapter 8 summarizes these ideas and the outlook of future works.

Chapter 2

Magnetism

Given that the fundamental particles of matter possess charge and spin, magnetism is ubiquitous in nature. Thanks to quantum mechanical exchange interactions, ions with net magnetic moments placed in a crystal lattice can interact quite strongly, their correlations giving rise to an incredible diversity of cooperative phenomenon. Ferromagnets, first discovered in the lodestone deposits of ferrous-ferric oxide, i.e. magnetite, are undoubtedly familiar to most of us, even common in daily life, often gracing our fridges. This is only one type of long-range-order however, and there are perhaps as many type of magnetism as there are crystal lattices, and ions to populate them with. In this chapter we shall discuss the essential basics of what makes a material magnetic and theoretical descriptions for the energetics of cooperative magnetic interactions. In addition, we will introduce a few topics that are more specifically tailored to the experimental content of this thesis, namely how crystal electric field interactions are manifest in 4f systems and how pseudospin 1/2 physics emerges in materials. Lastly, we discuss the temperature dependence of the magnetic susceptibility, and the general derivation thereof, in the context of a mean-field model XXZ model.

2.1 General principles & microscopic models

Fundamentally, an ion's magnetic properties are determined by its electronic state. An ion with unpaired valence electrons can have a net spin or orbital angular momentum as characterized by the angular momentum quantum numbers m_S, m_L, of its electronic ground state. An atom with

spin angular momentum $\mathbf{S}$ and orbital angular momentum $\mathbf{L}$ has a total magnetic dipole moment:

$$\boldsymbol{\mu} = -\frac{\mu_B}{\hbar}(g_S\mathbf{S} + g_L\mathbf{L}), \tag{2.1}$$

where g_S & g_L are the spin and orbital Landé g-factors respectively. In an external applied field $\mathbf{H}$, these moments tend to align with the direction of $\mathbf{H}$, thereby minimizing the Zeeman energy $-\boldsymbol{\mu} \cdot \mathbf{H}$. In materials composed of many individual magnetic ions, paramagnetism occurs because of this tendency toward microscopic alignment, resulting in a net macroscopic magnetization that increases with the strength of the applied field.

Microscopic, localized magnetic moments are also sensitive to the magnetic moments of their neighbors. While short-range dipole-dipole correlations between these moments certainly exist, their magnitude is typically dwarfed by a quantum mechanical effect, the exchange-interaction, which has no classical analog [27]. Electrons in adjacent orbitals are subject to a repulsive Coulomb interaction. Wavefunction overlap between these adjacent atomic orbitals and the Pauli exclusion condition that the overall wavefunction of identical fermionic particles be antisymmetric under particle-exchange, modifies the relative energy cost of aligning or anti-aligning individual electron spin moments. When this exchange interaction occurs between adjacent atoms with overlapping orbitals, it is termed direct exchange, but longer-range interactions through intermediary, and even possibly non-magnetic ions, are additionally possible, termed superexchange [17]. This type of effective exchange interaction is usually parameterized in the following way:

$$\mathcal{H}_{12} = \mathcal{J}\hat{\mathbf{S}}_2 \cdot \hat{\mathbf{S}}_2 \tag{2.2}$$

If $\mathcal{J} < 0$, the energy of these two spins is minimized by a parallel arrangement, thus this type of interaction favors a ferromagnetic alignment of spin moments. At temperatures low enough to suppress random thermal fluctuations, i.e. below a critical Curie temperature T_C a ferromagnetic material will spontaneously develop a nonzero magnetization even under zero applied field due to the simuletanous alignment of neighboring spin moments. By contrast if $\mathcal{J} > 0$, the energy of these two spins is minimized by an anti-parallel arrangement, favoring instead, an antiparallel arrangement

of adjacent spins. In bipartite lattices, below a critial Neel temperature T_N, antiferromagnetic materials can develop a Neel-order, in which adjacent spins alternate orientation, resulting in a state with net zero magnetization.

Combing exchange and Zeeman effects, we can write a highly generic spin Hamiltonian for a lattice of N total spins, coupling different components of the spins of nearest-neighbor moments $\hat{S}_{\alpha,i}$ under an applied field.

$$\hat{\mathcal{H}} = \sum_{\langle i,j \rangle} \mathcal{J}_{\alpha\beta} \hat{S}_{\alpha,i} \hat{S}_{\beta,j} - \mu_B \mu_0 \sum_i g_{\alpha\alpha} H_\alpha \hat{S}_{\alpha,i}, \tag{2.3}$$

where the Latin indices i, j denote lattice sites, greek indices α, β are spatial components x, y, z, repeated indices are implicitly summed-over, and $\langle \cdot, \cdot \rangle$ denotes a nearest-neighbor pair. To be completely generic, we have also included the possibility of an anisotropic g-tensor, $g_{\alpha\alpha}$ which may emerge in crystalline environments.

This work focuses mostly on anisotropic, antiferromagnetic materials, whose low temperature physics can produce an incredible diversity of magnetic states. In non-bipartite antiferromagnetic lattices, such as triangular or Kagome systems, it may be geometrically impossible to satisfy antiparallel alignment of every adjacent ion, without some energetic compromises, a condition which is referred to as magnetic frustration [28, 29, 30]. Frustration significantly reduces ordering temperatures and may produce non-collinear spin textures like 120-degree-order or even possibly exotic, highly-correlated states such as the much sought-after spin liquid [31, 32]. More complicated still, spin-orbit coupling effects can produce anti-symmetric exchange such as the Dzyaloshinskii–Moriya interaction [33], which favors perpendicular alignment of adjacent spins, contributing to the formation of canted, helical, or skyrmionic spin textures. With so many diverse microscopic interactions possible, the magnetic properties of any material is often determined by a complex interplay of many competing degrees of freedom and energy scales.

2.2 Weiss-mean-field theory

Solving the exact eigenstates of even the simplest examples of 3D spin Hamiltonians is a formidable N-body problem and analytically tackling such models is often impossible without a reasonable set of assumptions. Mean-field theory relies on the assumption that on average, each individual spin moment perceives its thermally-fluctuating neighbors as whatever their average spin moment is [34]. Such a model can be obtain by re-expressing our spin variables in terms of their fluctuations $\delta m_\alpha \equiv \hat{S}_\alpha - \langle \hat{S}_\alpha \rangle$ away from their thermal average values $m_\alpha \equiv \langle S_\alpha \rangle$ by the transformation $\hat{S}_\alpha \rightarrow m_\alpha + \delta m_\alpha$. In the case of Eqn. 2.3 this may be done explicitly:

$$\begin{aligned}\hat{\mathcal{H}} &= \sum_{\langle i,j \rangle} \mathcal{J}_{\alpha\beta}(m_\alpha + \delta m_{\alpha,i})(m_\beta + \delta m_{\beta,j}) - \mu_B \mu_0 \sum_i g_{\alpha\alpha} H_\alpha \hat{S}_{\alpha,i}, \\ &= \sum_{\langle ij \rangle} \mathcal{J}_{\alpha\beta} \left[m_\alpha m_\beta + m_\beta(\hat{S}_{\alpha,i} - m_\alpha) + m_\alpha(\hat{S}_{\beta,i} - m_\beta) \right] - \mu_B \mu_0 \sum_i g_{\alpha\alpha} H_\alpha \hat{S}_{\alpha,i} + \mathcal{O}(\delta m^2).\end{aligned}$$

Formally, the Weiss-mean-field approximation is made by assuming that the spin fluctuations are sufficiently small that we can drop all those terms that are 2nd order in the spin fluctuations. The remaining terms in the Hamiltonian are now decoupled, and we can then convert the sum over nearest neighbors to a sum over individual lattice sites $\sum_{\langle i,j \rangle} = (q/2) \sum_i$, where we have introduced the coordination number q, the number of nearest neighbors per lattice site, and the factor of $1/2$ accounts for double counting. This yields the mean-field (MF) Hamiltonian:

$$\hat{\mathcal{H}}_{MF} = \frac{Nq}{2} \mathcal{J}_{\alpha\beta} m_\alpha m_\beta - \sum_i \left[\mu_B \mu_0 g_{\alpha\alpha} H_\alpha - \frac{q}{2} \left(\mathcal{J}_{\alpha\beta} + \mathcal{J}_{\beta\alpha} \right) m_\beta \right] \hat{S}_{\alpha,i},$$

which is a sum of N decoupled 1-body problems. This is equivalent to replacing the magnetic field $\mathbf{H}$ at each lattice site with an effective field that is altered by a microscopic field generated by the thermal average moment of each adjacent magnetized ion:

$$H_{\alpha,\text{eff.}} = H_\alpha - \frac{q m_\beta}{2 \mu_B \mu_0 g_{\alpha\alpha}} \left(\mathcal{J}_{\alpha\beta} + \mathcal{J}_{\beta\alpha} \right), \tag{2.4}$$

From this form, we can mathematically justify the intuitive results that a ferromagnet $\mathcal{J}_{\alpha\alpha} < 0$ enhances the effects of an applied field, while an antiferromagnet $\mathcal{J}_{\alpha\alpha} > 0$, which favors zero net

magnetization, weakens the effects of an applied field. In such a model the spin expectations values can be found self-consistently:

$$m_\alpha = \langle \hat{S}_\alpha \rangle = \frac{1}{Z} \mathrm{Tr}\left[\hat{S}_\alpha e^{-\beta \hat{\mathcal{H}}_{MF}(m_\alpha)} \right], \tag{2.5}$$

Where $Z = \mathrm{Tr}[e^{\hat{\mathcal{H}}_{MF}}]$ is the mean-field partition function. The bulk magnetization in this model is indeed exactly proportional to the spin expectation value:

$$M_\alpha = \frac{\partial F}{\partial B_\alpha} = \mu_0 \mu_B g_{\alpha\alpha} m_\alpha. \tag{2.6}$$

This type of self-consistent MF model will fail to capture the behavior of the magnetization in the vicinity of a phase transition $T \sim T_c$, where spin fluctuations increase and higher order spin-spin correlations become relevant, but such a model should do well in paramagnetic or ferromagnetic state far away from T_c. In bipartite lattices, a mean field analysis may also be generalized to describe an antiferromagnetic Neel state, by considering 2 interspersed magnetic sublattices with differing partial magnetizations [35].

2.3 Crystal electric field interactions

A free ion's electronic ground state is determined by how its valence orbitals are filled. Hund's rules select an electron orbital filling that maximizes the number of unpaired electrons and thus the total spin moment S, and one that maximizes the total orbital angular momentum L [17]. According to the rules of addition for angular momenta, the total angular momentum J can take the following range of values $|L - S| \leq J \leq L + S$. Due to spin-orbit coupling $\mathcal{H}_{SO} \sim \lambda \mathbf{L} \cdot \mathbf{S}$ each corresponding $\{|J, m_J\rangle\}$-multiplet will have a different energy. According to Hund's 3rd rule, if an atom's outermost subshell is half-filled or less, then the multiplet with the lowest such energy corresponds to the lowest total angular momentum $J = |L - S|$ and in the case that the outermost subshell is more than half-filled the lowest energy multiplet instead corresponds to the maximal total angular momentum $J = L + S$.

In the absence of an external field, or any other perturbing effects, the ground state of the free ion electronic multiplet $\{|J, m_J\rangle\}$, $m_J = -J, \ldots J$, consists of $2J+1$ degenerate states. When placed

in a crystalline environment however, an ion is subject to electrostatic interactions with the charge distribution of its surrounding neighboring ions [36]. These electrostatic interactions introduce a perturbing interaction $\mathcal{H}_{\text{CEF}}$ that splits the degeneracy of the free ion multiplet, re-diagonalizing this multiplet into a set of crystal electric field eigenstates $\mathcal{H}_{\text{CEF}}$.

For example, placing a d-orbital transition metal ion in a tetragonal or octahedral arrangement of negative point charges, i.e. ligands, has the effect of splitting the otherwise degenerate d orbitals into 2 sets, the 3-fold degenerate t_{2g} orbitals: $\{d_{xy}, d_{yz}, d_{zx}\}$ and 2-fold degenerate e_g orbitals $\{d_{x^2-y^2}, d_{z^2}\}$ [37]. For d-orbital transition metals this CEF energy gap between t_{2g} and e_g orbitals is typically on the order of $.1 - 1$ eV, while for $4f$-orbital systems, which we focus on for the remainder of this chapter, typical crystal field energy gaps can be as small as ~ 10 meV. Thus, while the CEF gap for $3d$ ions is typically much larger than other significant energy scales, it is absolutely crucial to consider the CEF structure of high Z atoms (e.g. $4f$ systems) because this energy scale is quite similar to other important energy scales such as the exchange energy.

2.3.1 Parametrzing CEF effects

In complexes of $3d$, $4d$, $5d$ transition metal ions and $4f$ rare earth ions, the crystal electric field interaction $\mathcal{H}_{\text{CEF}}$ can be parameterized in terms of a set of Stevens Operators $\hat{O}_m^n$, which are linear combinations of J-total angular momentum operators that obey the the site symmetry of the local ionic environment. The site symmetry is the point-group symmetry describing the set of coordinate transformation operations under which the arrangement of nearest-neighbor ligands is invariant. As a concrete example, consider the RX_6 octahedral environment, X = O, S, Se, where R is a 3+ rare-earth lanthanide. In addition, the maximum order of terms in the CEF Hamiltonian must be less than $2J$ [38]. In the case of a trigonal D_{3d} environment, with a $J = 7/2$ or larger

moment, the appropriate symmetry-allowed set of Stevens operators is [39] :

$$\hat{O}_{20} = 3\hat{J}_z^2 - X,$$

$$\hat{O}_{40} = 35\hat{J}_z^4 - (30X - 25)\hat{J}_z^2 + 3X^2 - 6X,$$

$$\hat{O}_{43} = \frac{1}{4}\left[(\hat{J}_+^3 + \hat{J}_-^3)\hat{J}_z + \hat{J}_z(\hat{J}_+^3 + \hat{J}_-^3)\right],$$

$$\hat{O}_{60} = 231\hat{J}_z^6 - (315X - 735)\hat{J}_z^4 + (105X^2 - 525X + 294)\hat{J}_z^2 - 5X^3 + 40X^2 - 60X,$$

$$\hat{O}_{63} = \frac{1}{4}\left[(\hat{J}_+^3 + \hat{J}_-^3)\left(11\hat{J}_z^3 + (3X + 59)\,\hat{J}_z\right) + \left(11\hat{J}_z^3 + (3X + 59)\,\hat{J}_z\right)(\hat{J}_+^3 + \hat{J}_-^3)\right],$$

$$\hat{O}_{66} = \frac{1}{2}(\hat{J}_+^6 + \hat{J}_-^6), \tag{2.7}$$

where $X \equiv J(J+1)$. Therefore, for such a complex, the most generic crystal electric field interaction $\mathcal{H}_{\text{CEF}}$ is a linear combination $B_m^n \hat{O}_m^n$, where the specific sign and magnitude of the coefficients B_m^n depends on the particular ions R, X of the complex and distances between them. In writing these expressions of the Stevens operators. We have assumed that J is a "good" quantum number, however this analysis and formalism is still fully applicable if one chooses to work instead in the full L, S basis $\{|L, m_L\rangle \otimes |S, m_S\rangle\}$ basis where $\hat{J}$ is replaced by $\hat{L} + \hat{S}$.

2.3.2 Pseudospin 1/2 physics

Many theoretical models are based on an assumption of spin-1/2 physics, but there are relatively few known ions that offer true spin 1/2 systems, like Cu^{2+} for example. There are however, a variety of ways to approximate the physics of larger $J_{\text{eff.}}$ ions as effectively spin 1/2, provided that the ground state of spin-orbit and CEF interactions forms a 2-level system [40]. We consider the electronic spectrum of a magnetic ion whose lowest-lying CEF states form a doublet in zero field. Consider an ion with odd-half integer $\hat{\mathbf{J}}$, in such as system, the perturbing CEF interaction $\hat{H}_{CEF}$ will rediagonalize the $2J + 1$ states $\{|J, m_J\rangle\}$, into a set of doubly-degenerate eigenstates $\{|n_\pm\rangle\}$, where $n = 0, 1, \ldots J + 1/2$. This is a direct consequence of Kramer's theorem, which states that for every eigenstate of time-reversal symmetric Hamiltonian for a total half-integer

spin system, there is at least one state with the same energy. As fairly generic example, which is highly relevant to system of $CsYbSe_2$examined in chapters 7 & 8, we consider an XXZ model for the full spin-J system:

$$\hat{\mathcal{H}}_{\text{XXZ}} = \sum_{\langle ij \rangle} \left[\mathcal{J}_{\perp} \left(\hat{J}_{i,x} \hat{J}_{j,x} + \hat{J}_{i,y} \hat{J}_{j,y} \right) + \mathcal{J}_z \hat{J}_{i,z} \hat{J}_{j,z} \right]. \tag{2.8}$$

Provided that the energy gap Δ, between the ground-state doublet and next excited CEF level, is very small, compared to the thermal energy $k_B T$ it may suffice to treat this ion as an effective 2-level system, i.e. as a pseudospin 1/2 (PS-1/2). We can explicitly define PS-1/2 operators for the ground state doublet:

$$\hat{S}_x \equiv \frac{1}{2} \left(|0_+\rangle\langle 0_-| + |0_-\rangle\langle 0_+| \right), \tag{2.9}$$

$$\hat{S}_y \equiv \frac{i}{2} \left(|0_-\rangle\langle 0_+| - |0_+\rangle\langle 0_-| \right), \tag{2.10}$$

$$\hat{S}_z \equiv \frac{1}{2} \left(|0_+\rangle\langle 0_+| - |0_-\rangle\langle 0_-| \right), \tag{2.11}$$

In order to determine the correct reduced PS-1/2 Hamiltonian we must restrict the full Hamiltonian to the subspace of the lowest Kramer's doublet $\{|0_\pm\rangle\}$ using the projection operator $\hat{P}_0$:

$$\hat{P}_0 \equiv |0_+\rangle\langle 0_+| + |0_-\rangle\langle 0_-| \tag{2.12}$$

In the language of quantum information science, this is the action of projecting the full Hamiltonian system to a 2-level qubit subspace by the simple Hamiltonian transformation:

$$\hat{\mathcal{H}}_{\text{PS}\frac{1}{2}} = \hat{P}_0 \hat{\mathcal{H}} \hat{P}_0 \tag{2.13}$$

The overall projection operator for our $N \times (2J+1)$-dimensional vector space onto the ground state subspace of 2^N states is a tensor product of decoupled single-spin projection operators, so in the case of our XXZ Hamiltonian we can derive the effect from the action of this projection on a single spin operator, e.g.

$$\hat{P}_0 \hat{J}_z \hat{P}_0 = \langle 0_+|\hat{J}_z|0_+\rangle |0_+\rangle\langle 0_+| + \langle 0_-|\hat{J}_z|0_-\rangle |0_-\rangle\langle 0_-|, \tag{2.14}$$

$$= 2\langle 0_+|\hat{J}_z|0_+\rangle \hat{S}_z, \tag{2.15}$$

The computation plays out similarly for $\hat{J}_x$, allowing us to re-write the full reduced PS-1/2 Hamiltonian in terms of the PS-1/2 operators $\hat{S}_\alpha$:

$$\hat{\mathcal{H}}_{\text{XXZ, PS}\frac{1}{2}} = \hat{P}_0 \hat{\mathcal{H}}_{\text{XXZ}} \hat{P}_0 = \sum_{\langle i,j \rangle} \left[\mathcal{J}'_\perp \left(\hat{S}_{i,x}\hat{S}_{j,x} + \hat{S}_{i,y}\hat{S}_{j,y} \right) + \mathcal{J}'_z \hat{S}_{i,z}\hat{S}_{j,z} \right], \tag{2.16}$$

with new, effective PS-1/2 exchange constants:

$$\mathcal{J}'_\perp = 4|\langle 0_\pm|\hat{J}_x|0_\mp\rangle|^2 \mathcal{J}_\perp, \qquad \mathcal{J}'_z = 4|\langle 0_\pm|\hat{J}_z|0_\pm\rangle|^2 \mathcal{J}_z. \tag{2.17}$$

Now consider the Zeeman interaction with an external applied field:

$$\hat{\mathcal{H}}_Z = -\mu_0 \mu_B g_J \mathbf{H} \cdot \sum_i \hat{\mathbf{J}}_i, \tag{2.18}$$

$$\hat{\mathcal{H}}_{Z,\text{PS}\frac{1}{2}} = \hat{P}_0 \hat{\mathcal{H}}_Z \hat{P}_0 = -\mu_0 \mu_B g_{\alpha\alpha} H_\alpha \sum_i \hat{S}_{i,\alpha}, \tag{2.19}$$

where we introduce the PS-1/2 g-tensor:

$$g_{xx} = g_{yy} = 2g_J|\langle 0_\pm|\hat{J}_x|0_\mp\rangle|, \qquad g_{zz} = 2g_J|\langle 0_\pm|\hat{J}_z|0_\pm\rangle|. \tag{2.20}$$

Thus even if the external field couples isotropically to the full $\hat{J}$ moments, the crystal field renders the effective Zeeman interaction anisotropic.

2.4 Magnetic susceptibility of the half integer J, XXZ model

We examine the magnetic susceptibility of the type of XXZ model considered in section 2.3.2, with total half-integer J and CEF eigenstates $\{|n_\pm\rangle\}$. This result is crucial to our analysis of the triangular lattice aniferromagnet $CsYbSe_2$ in chapter 6, and readily generalizes to many multi-level magnetic systems. To see how the spectrum and partition function is modified by an external field we consider the perturbative effects of an external field introduced by a Zeeman term 2.18. We can define a generalized g-tensor for the H-linear perturbation of each level:

$$g^n_{\perp(z)} = 2g_J\langle n_\pm|\hat{J}_{x(z)}|n_\mp\rangle, \tag{2.21}$$

And a van-Vleck coefficient which describes the second order H-quadratic perturbation of the external field:

$$\alpha_{\perp(z),n} = \mu_B^2 g_J^2 \sum_{k\neq n} \frac{|\langle k_\pm|\hat{J}_{x(z)}|0_+\rangle|^2}{\omega_n(0)-\omega_k(0)}, \tag{2.22}$$

The result of which is an energy spectrum at finite field:

$$\omega_{n,\pm} = \omega_n(0) + \alpha_\perp^n H_{\perp,\text{eff.}}^2 + \alpha_z^n H_{z,\text{eff.}}^2 + \pm\frac{\mu_0\mu_B}{2}\sqrt{(g_\perp^n H_{\perp,\text{eff.}})^2 + (g_z^n H_{z,\text{eff.}})^2} + \mathcal{O}(H^3), \tag{2.23}$$

where in terms of $m_{\perp(z)} = \langle \hat{J}_{x(z)}\rangle = \text{Tr}[\hat{J}_{x(z)}e^{-\beta\hat{\mathcal{H}}}]$, the effective fields in the MF approximation take the form:

$$H_{\perp(z),\text{eff.}} = H_{\perp(z)} - \frac{q\mathcal{J}_{\perp(z)}}{\mu_B g_J} m_{\perp(z)} \tag{2.24}$$

Defining the energy gaps of excited CEF levels as $\Delta_{n0} = \omega_n - \omega_0$. we may write the full MF single-particle partition function up to quadratic order in H as:

$$\begin{aligned} Z_1 &= \text{Tr}\left[e^{-\beta\hat{\mathcal{H}}_{MF}}\right], \\ &= 2e^{\beta\frac{z}{2}(\mathcal{J}_x m_x^2 + \mathcal{J}_z m_z^2)} e^{-\beta\omega_0(0)} \\ &\quad\times\left[e^{-\beta(\alpha_\perp^0 H_{\perp,\text{eff.}}^2 + \alpha_z^0 H_{z,\text{eff.}}^2)}\cosh\left(\frac{\beta\mu_0\mu_B}{2}((g_\perp^0 H_{\perp,\text{eff.}})^2 + (g_z^0 H_{z,\text{eff.}})^2)^{1/2}\right)\right. \\ &\quad\left. + e^{-\beta\Delta_{10}-\beta(\alpha_\perp^1 H_{\perp,\text{eff.}}^2 + \alpha_z^1 H_{z,\text{eff.}}^2)}\cosh\left(\frac{\beta\mu_0\mu_B}{2}((g_\perp^1 H_{\perp,\text{eff.}})^2 + (g_z^1 H_{z,\text{eff.}})^2)^{1/2}\right) + \dots\right]. \end{aligned} \tag{2.25}$$

The low-field susceptibility can be computed exactly, expanding $\partial^2 F/\partial H^2$ in H/T, keeping only those terms which are non-vanishing as $H \to 0$:

$$\begin{aligned} \chi_{\perp(z)} &= -\frac{\partial}{\partial H_x}\left(\frac{\partial F}{\partial H_x}\right)_{\beta H_x\to 0} = \frac{N}{\beta}\frac{\partial^2 \log(Z_1)}{\partial H_x^2}\bigg|_{\beta H_x\to 0}, \\ \chi_{\perp(z)} &= \frac{N\mu_0\mu_B^2 g_J^2}{k_B}\left[T\frac{\sum_n e^{-\beta\Delta_{n0}}}{\sum_n\left(|\langle n_+|\hat{J}_{x(z)}|n_{-(+)}\rangle|_n^2 - \frac{2\alpha_{\perp(z)}^n}{\beta\mu_B^2 g_J^2}\right)e^{-\beta\Delta_{n0}}} + \frac{q\mathcal{J}_{\perp(z)}}{k_B}\right]^{-1}, \end{aligned} \tag{2.26}$$

At low-T, this reduces to the familiar $C/(T+\Theta_C W)$, Curie-Weiss form, of the magnetic susceptibility which approximates the system as pseudo-spin 1/2. At high temperatures the system also

resembles a $1/T$ Curie-Weiss-like form, but for entirely different reasons, the slope and intercept of $\chi^{-1}(T)$ depending mainly on the magnitude of $J(J+1)$ and the lowest order crystal field interaction strength respectively. The generic form 2.26 seamlessly bridges the non-trivial temperature dependence between both limits.

Chapter 3

Phonons and thermal properties of insulators

3.1 Quantum mechanical formulation of phonon lattice models

A large portion of our work is concerned with heat transport and thermodynamics in insulators, thus it is vital to discuss the fundamental aspects of lattice vibrations and their normal modes. The phonon is the quantum of the field of ionic displacement, the emergent bosonic quasiparticle of a sound wave. This chapter aims to establish the necessary formalism and conventions for describing phonon spectra, their heat capacity, and their contribution to thermal conductivity.

3.1.1 1D chains and general characteristics of real spectra

The most accessible starting point for analyzing general characteristics of phonon spectra is the 1D harmonic chain of atoms [15, 16, 41]. The model consists of N atoms at lattice sites r_i labeled by an index $i = 1, \ldots, N$ each spatially separated from its nearest neighbors by lattice constant a. Each atom can move back and forth in one spatial dimension, but is subject to a harmonic Hooke's law restoring force that depends on how far it is displaced from its equilibrium position relative to its nearest neighbors. This can be visualized as a series of springs connecting adjacent atoms in the chain. We can write the harmonic Hamiltonian for this system in terms of the ionic displacements $\mathbf{u}(r)$ from equilbrium positon at each lattice site r_i, and the conjugate momentum density $\pi(r)$ with canonical commutation relation $[u(r), \pi(r')] = i\hbar\delta_{\alpha\beta}\delta_{rr'}$

$$\mathcal{H} = \sum_{i=1}^{N} \frac{\pi(r_i)^2}{2m} + \frac{K}{2} \sum_{i=1}^{N-1} (u(r_i) - u(r_{i+1}))^2, \tag{3.1}$$

where m is an atomic mass, and K is an effective spring constant for the restoring force in a harmonic approximation,. The problem is most easily treated by transforming to momentum space, using the Fourier conventions

$$u(r) = \frac{1}{\sqrt{N}} \sum_k e^{ikr} u(k), \tag{3.2}$$

$$\pi(r) = \frac{1}{\sqrt{N}} \sum_k e^{ikr} \pi(k) \tag{3.3}$$

Allowing us to express the Hamiltonian in k-space as:

$$\mathcal{H} = \frac{1}{2m} \sum_k [\pi_k \pi_{-k} + K(1 - \cos ka) u_k u_{-k}] \tag{3.4}$$

If periodic boundary conditions are imposed, the discrete set of N nonzero k is quantized as $k = k_m = 2\pi m/Na$, where $m = 0, \pm 1, \pm 2, \cdots \pm N/2$. The quantized eigenvalues of this Hamiltonian are vibrational normal modes, referred to as phonons. Each normal modes has an energy:

$$\omega_k = \sqrt{\frac{4K}{m}} \left| \sin\left(\frac{ka}{2}\right) \right| = \frac{2 v_s k_c}{\pi} \left| \sin\left(\frac{\pi k}{2k_c}\right) \right|, \tag{3.5}$$

This dispersion relation serves as a very generic example of the spectra of acoustic phonons, i.e. phonons whose energy goes to zero as $k \to 0$. Near zone center, i.e. $k = 0$, the dispersion relation is approximately linear in k and the group velocity $v_g = d\omega/dk$ equals the phase velocity $v_p = \omega/k$. The second expression parameterizes $\omega(k)$ in terms of the linear slope near zone center ($k \sim 0$), which is referred to as the speed of sound $v_s = \sqrt{Ka^2/m}$, and the wavevector at the edge of the Brillouin zone, denoted $k_c = \pi/a$. As we will see in subsequent sections these parameters are quite important in analyses of the heat capacity and bulk thermal conductivity. We can also define a set of ladder operators

$$a_k = \sqrt{\frac{m\omega_k}{2\hbar}} (u_k + \frac{i}{m\omega_k} \pi_{-k}), \tag{3.6}$$

$$a_k^\dagger = \sqrt{\frac{m\omega_k}{2\hbar}} (u_{-k} - \frac{i}{m\omega_k} \pi_k), \tag{3.7}$$

Allowing us to re-express the Hamiltonian in a second quantized notation:

$$\mathcal{H} = \sum_k \hbar\omega_k (a_k^\dagger a_k + \tfrac{1}{2}), \tag{3.8}$$

Because phonons are bosonic, n of them can occupy the same eigenstate $\mathbf{k}$ simultaneously, thus full set of energy eigenvalues of this Hamiltonian is an evenly spaced ladder of discrete $E_n = (n + 1/2)\hbar\omega_k$, at each value of k. From the form of 3.8 it is apparent that we have a fock space describing N indept. harmonic oscillators, allowing us to express the total state vector in terms of the number of phonons in each linearly-independent mode: $|n_{k_{-N/2}}, \ldots, n_{k_N/2}\rangle$. From this point on, we can redefine the energy of the vacuum state $|0, \ldots 0\rangle$ such that we can drop the zero point energy $\sum_k \hbar\omega_k/2$, without any physical consequences.

This problem can be generalized to a 3-dimensional crystal with N atoms, however each mode at wavevector $\mathbf{k}$ will have 3 possible polarizations: 1 longitudinal mode with displacement eigenvectors parallel to $\mathbf{k}$, and 2 transverse modes with displacement eigenvectors perpendicular to $\mathbf{k}$ [41]. This results in $3N$ total possible phonon modes.

3.1.2 Diatomic 1D chain and optical modes

We also consider a chain of alternating species of atoms, with masses m_1, m_2 on sublattices A and B respectively, that are interspersed. Each atom of sublattice A (B) is connected to 2 adjacent atoms of sublattice B (A) with an effective spring characterized by K, the hamiltonian for which, may be written:

$$\sum_{r_i \in A} \frac{\pi(r_i)^2}{2m_1} + \sum_{r_i \in B} \frac{\pi(r_i)^2}{2m_2} + \frac{K}{2} \sum_{\langle ij \rangle} (u(r_i) - u(r_j))^2 \tag{3.9}$$

As before, we can transform into momentum space using the same set of Fourier conventions, and solve the equations of motion to obtain a dispersion relation for the allowed set of eigenfrequencies. In this case however, the eigenvalue problem has 2 solutions, or phonon branches, for each value of k:

$$\omega_{k,\pm}^2 = K \left[\frac{1}{m_1} + \frac{1}{m_2} \pm \sqrt{\left(\frac{1}{m_1} + \frac{1}{m_2} \right)^2 - \frac{4}{m_1 m_2} \sin^2 \left(\frac{ka}{2} \right)} \right], \tag{3.10}$$

Alternatively, we can write an express m_2/m_1 as a ratio r and write $\omega_{k,\pm}$ in terms of the zone center speed of sound v_s, zone cuttoff frequency $k_c = \pi/a$.

$$\omega_{k,\pm} = \frac{v_s k_c}{\pi} \cdot \frac{1+r}{\sqrt{2r}} \sqrt{1 \pm \sqrt{1 - \frac{4r}{(1+r)^2} \sin^2\left(\frac{\pi k}{2k_c}\right)}}. \tag{3.11}$$

This model is also functionally equivalent to another type of monatomic model for one species of atom with mass m, where instead adjacent atoms of the chain are connected by springs with varying spring constants $K_2 = rK_1$. The lower energy branch, which corresponds to the in-phase motion of nearest neighbor atoms, is a set of acoustic phonons, with a vanishing, linear dispersion at zone center. The higher frequency phonon branch on the other hand, which corresponds to out-of-phase motion of nearest neighbor atoms, retains a finite energy as $k \to 0$. Because alternating atoms of an ionic lattice have opposing charges, their out-of phase motion corresponds to microscopic oscillating electrical dipole moments. The motion of these dipoles may be readily driven by electromagnetic radiation, hence excitations of the upper branch are termed optical phonon.

This result generalizes as follows: in a 3-dimensional crystal with p-atoms per primitive cell, there will always be 3 acoustic phonon branches, one for each independent polarization, and $3(p-1)$ optical phonon branches, for a total of $3Np$ independent phonon modes in a crystal contain N total formula units, i.e. N copies of its primitive cell.

3.1.3 Elastic stress-strain tensor and sound velocities

A pure deformation of a 3D crystal lattice, without translation or rotations can be described in terms of the symmetric stress-strain tensor [41]:

$$\varepsilon_{\alpha\beta}(\mathbf{r}) = \frac{1}{2}\left[\partial_\alpha u_\beta(\mathbf{r}) + \partial_\beta u_\alpha(\mathbf{r})\right], \tag{3.12}$$

Because the stress-strain tensor is symmetric, there are only 6 independent components, thus this rank-2 tensor can alternatively be expressed as a 6-element collumn vector in Voigt notation, using an index $1, \ldots, 6$ corresponding to xx, yy, zz, yz, zx, xy respectively [42]. In a harmonic approximation, which effectively captures long-wavelength excitation, we can write the elastic energy of the

atom at site $\mathbf{r}$ in terms of elastic moduli $C_{\alpha\beta\gamma\delta}$ that couple different components of the stress-strain tensor. Working in this approximation (and using an implicit Einstein summation convention for repeated indices) we can write a general Hamiltonian for the 3D monatomic crystal:

$$\mathcal{H} = \sum_{\mathbf{r}} \left[\frac{\pi_\alpha(\mathbf{r})\pi_\alpha(\mathbf{r})}{2m} + \frac{C_{\alpha\beta\gamma\delta}}{2} \varepsilon_{\alpha\beta}(\mathbf{r})\ \varepsilon_{\gamma\delta}(\mathbf{r}) \right] \tag{3.13}$$

$C_{\alpha\beta\gamma\delta}$ is a rank-4 tensor; in Voigt notation this can be expressed as 6×6 matrix with 36 constants, only 21 of which are independent, given that the parabolicity of the harmonic lattice potential forces this tensor to be symmetric. The elastic moduli must additionally be invariant under the symmetry operations of the crystal lattice, further reducing the number of constants. An isotropic solid for instance only has 2 independent constants, $C_{11} = C_{22} = C_{33}$ and $C_{12} = C_{23} = C_{31}$, while a triclininc crystal has the full set of 21 indept. constants [41].

We explicitly examine the isotropic case to illustrate the effect that this has on the speeds of sounds of different modes. This has the explicit Hamiltonian:

$$\mathcal{H} = \sum_{\mathbf{r}} \left[\frac{\pi_\alpha \pi_\alpha}{2m} + \frac{C_{11}}{4} \left(\partial_\alpha u_\beta \partial_\alpha u_\beta + \partial_\alpha u_\beta \partial_\beta u_\alpha \right) + \frac{C_{12}}{4} \left(2\partial_\alpha u_\alpha \partial_\beta u_\beta - \partial_\alpha u_\beta \partial_\alpha u_\beta - \partial_\alpha u_\beta \partial_\beta u_\alpha \right) \right] \tag{3.14}$$

As a technical note, this is a truly isotropic continuum model if one replaces the sum over lattice sites with an integral over all space $\sum \mathbf{r} \to \int d^3r$, and treats m as a mass density. The displacement and momentum operators obey the canonical commutation relation $[u_\alpha(\mathbf{r}), \pi_\beta(\mathbf{r}')] = i\hbar\delta_{\alpha\beta}\delta_{\mathbf{r}\mathbf{r}'}$, with Fourier conventions:

$$u_\alpha(\mathbf{r}) = \frac{1}{\sqrt{N}} \sum_{\mathbf{k}} e^{i\mathbf{k}\cdot\mathbf{r}} u_\alpha(\mathbf{k}), \tag{3.15}$$

$$\pi_\alpha(\mathbf{r}) = \frac{1}{\sqrt{N}} \sum_{\mathbf{k}} e^{i\mathbf{k}\cdot\mathbf{r}} \pi_\alpha(\mathbf{k}). \tag{3.16}$$

Additionally, we know that each displacement eigenvector will have 3 polarizations $\hat{\epsilon}_\lambda(\mathbf{k})$, where $\lambda = \{\mathrm{LA}, \mathrm{TA}_1, \mathrm{TA}_2\}$ corresponds to the 1 longitudinal and 2 transverse acoustic modes respectively. Thus we may write express each displacement operator in this basis:

$$u_\alpha(\mathbf{k}) = \sum_\lambda [\hat{\epsilon}_\lambda(\mathbf{k})]_\alpha u_\lambda(\mathbf{k}), \tag{3.17}$$

Thus we may write the full Hamiltonian in momentum space as:

$$\mathcal{H} = \sum_{\mathbf{k},\lambda} \left[\frac{1}{2m} \pi_\lambda(\mathbf{k}) \pi_\lambda(-\mathbf{k}) + \frac{m\omega_\lambda(\mathbf{k})^2}{2} u_\lambda(\mathbf{k}) u_\lambda(-\mathbf{k}) \right] \tag{3.18}$$

Where we have identified 2 eigenvalues for the different phonon polarizations.

$$\omega_{\mathrm{LA}} = \sqrt{\frac{C_{11}}{2m}}\ k, \tag{3.19}$$

$$\omega_{\mathrm{TA}_1} = \omega_{\mathrm{TA}_2} = \sqrt{\frac{C_{11} - C_{12}}{4m}}\ k. \tag{3.20}$$

The specific values of C_{11} and C_{12} are determined by microscopic interatomic forces. Note that positive definiteness of the energy eigenvalues produces an additional constraint $C_{11} > C_{12}$. This model demonstrates that even in the isotropic case, the longitudinal speed of sound does not generically equal the transverse speed of sound. Furthermore in other crystalline systems, v_{TA1} need not equal v_{TA2}.

Once more, we can express the Hamiltonian in a second quantized notation using ladder operators:

$$\hat{a}_{\mathbf{k},\lambda} = \sqrt{\frac{m\omega_{\mathbf{k},\lambda}}{2\hbar}} \left(u_{\mathbf{k},\lambda} + \frac{i}{m\omega_{\mathbf{k},\lambda}} \pi_{-\mathbf{k},\lambda} \right), \tag{3.21}$$

$$\hat{a}^\dagger_{\mathbf{k},\lambda} = \sqrt{\frac{m\omega_{\mathbf{k},\lambda}}{2\hbar}} \left(u_{-\mathbf{k},\lambda} - \frac{i}{m\omega_{\mathbf{k},\lambda}} \pi_{\mathbf{k},\lambda} \right), \tag{3.22}$$

subject to the commutation relation $[\hat{a}_{\mathbf{k},\lambda}, a_{\mathbf{k}',\lambda'}] = i\hbar\delta_{\lambda\lambda'}\delta(\mathbf{k} - \mathbf{k}')$. Dropping the zero-point energy we have:

$$\mathcal{H} = \sum_{\mathbf{k},\lambda} \hbar\omega_{\mathbf{k},\lambda} \hat{a}^\dagger_{\mathbf{k},\lambda} \hat{a}_{\mathbf{k},\lambda}, \tag{3.23}$$

In the harmonic approximation, this is indeed the most generic form of the Hamiltonian for a realistic 3D material. For materials with p atoms per primitive cell, we can extend the index λ to have $L = 3p$ values, thereby including all additional $3p-3$ optical branches. In an arbitrary material however, the exact spectrum of $\omega_\lambda(\mathbf{k})$ can only be modeled with a significant ab-intio understanding of the ionic orbitals and inter-atomic forces. Usually an ab-initio treatment uses DFT in a Born-approximation where electronic wavefunctions are assumed to remain in instantaneous eigenstates

of the full set of lattice positions $\mathbf{r}_i$ to electrostatic force constants for various normal modes of the crystal [43].

Despite the difficulty of analyzing a material's phonon spectrum exactly without significant simulation and inelastic neutron scattering data to support it, this phonon description is useful for explaining general equilibrium and steady-state thermal characteristics of insulators, especially those governed by those long wavelength excitations near zone center which are unambiguously linearly-dispered. As we shall see in chapter 7, a phonon model of the type of 3.23 can even be leveraged to explain features of spin-phonon coupling in a real material.

3.2 Heat capacity and equilibrium thermal properties

The partion function for the elastic harmonic Hamiltionian is computed rather straightforwardly. Because each phonon mode is decoupled, the full partition function becomes product of $L \times N$ single mode partition functions $Z = \prod_{\mathbf{k},\lambda} Z_{\mathbf{k},\lambda}$, where $Z_{\mathbf{k},\lambda} = \mathrm{Tr}[e^{-\beta\hbar\omega_{\mathbf{k},\lambda}\hat{a}^\dagger_{\mathbf{k},\lambda}\hat{a}_{\mathbf{k},\lambda}}]$, each of which accounts for the fact that phonon modes, being bosonic, can be occupied $n = 0, 1, 2, \ldots$ times over:

$$Z = \mathrm{Tr}\left[e^{-\beta\mathcal{H}}\right] = \prod_{\mathbf{k},\lambda}\left(\sum_{n=0}^{\infty} e^{-n\beta\hbar\omega_\lambda(\mathbf{k})}\right), \tag{3.24}$$

$$= \prod_{\mathbf{k},\lambda}\left(\frac{1}{1-e^{\beta\hbar\omega_\lambda(\mathbf{k})}}\right), \tag{3.25}$$

It is then a straightforward task to compute any other thermodynamic quantities like the heat capacity:

$$C_v = k_B\beta^2\frac{\partial^2\ln(Z)}{\partial\beta^2} = k_B\sum_{\mathbf{k},\lambda}\frac{\beta^2}{Z_{\mathbf{k},\lambda}}\left[\frac{\partial^2 Z_{\mathbf{k},\lambda}}{\partial\beta^2} - \frac{1}{Z_{\mathbf{k},\lambda}}\left(\frac{\partial Z_{\mathbf{k},\lambda}}{\partial\beta}\right)^2\right], \tag{3.26}$$

$$= k_B\sum_{\mathbf{k},\lambda}(\beta\hbar\omega_{\mathbf{k},\lambda})^2\left[\langle(\hat{a}^\dagger_{\mathbf{k},\lambda}\hat{a}_{\mathbf{k},\lambda})^2\rangle - \langle\hat{a}^\dagger_{\mathbf{k},\lambda}\hat{a}_{\mathbf{k},\lambda}\rangle^2\right]. \tag{3.27}$$

It is common practice to refer to each summand as the spectral heat capacity $c_{\mathbf{k},\lambda}$ associated with the mode $\mathbf{k}, \lambda$. For 3.25, the spectral heat capacity is explicitly:

$$c_{\mathbf{k},\lambda} = \frac{k_B}{4}(\beta\hbar\omega_{\mathbf{k},\lambda})^2\mathrm{csch}^2\left(\frac{\beta\hbar\omega_{\mathbf{k},\lambda}}{2}\right). \tag{3.28}$$

The sum over k can be converted to an integral $\sum_{\mathbf{k}} \rightarrow \int_0^{k_c} g(k)dk$ where the density of states is normalized such that $\int_0^{k_c} g(k)dk = N$ [15, 16]. The cutoff frequency corresponds to the minimum allowed wavelength for a normal mode in real space, for the cubic crystal this is twice the lattice spacing, thus, $k_c = \pi/a$, which corresponds to the edge of the first Brillouin zone. For an isotropic dispersion, this implies $g(k) = 3Nk^2/k_c^3$. We can alternatively express this heat capacity as an integral over ω, using $g(\omega) = g(k)(d\omega/dk)^{-1} = 3N\omega^2/(v_g v_p^2)$

$$C_v = 3Nk_B \left(\frac{k_B T}{\hbar}\right)^2 \sum_{\lambda} \int_0^{\omega_c} \frac{d\omega}{v_{g,\lambda}(\omega) v_{p,\lambda}(\omega)^2} \left(\frac{\hbar\omega}{k_B T}\right)^4 \frac{e^{\hbar\omega/k_B T}}{(e^{\hbar\omega/k_B T} - 1)^2}, \tag{3.29}$$

The Debye approximation for the heat capacity of the acoustic phonon modes consists of approximating the actual dispersion relation of the transverse and longitudinal modes by a single effective, and isotropic, speed of sound v_s such that $\omega_\lambda(\mathbf{k}) = v_s k$; under this simplifying assumption the sum over lambda in the monatomic case reduces to simple a factor of 3 and we have:

$$C_v = 9Nk_B \left(\frac{T}{T_D}\right)^3 \int_0^{T_D/T} \frac{x^4 e^x}{(e^x - 1)^2}\, dx, \tag{3.30}$$

Where the customary substitution of variables $x = \beta\hbar\omega$ has been made, and the result has been expressed in terms of the so-called Debye temperature, defined as $T_D = \hbar\omega_c/k_B = \pi\hbar v_s k_B^{-1}(6N/\pi V)^{1/3}$. At temperatures $T \ll T_D$ the integral becomes independent of temperature and a T^3 heat capacity is obtained. At temperatures $T \gg T_D$ this result asymptotes to a constant $C_v = 3NkB$. For monatomic crystals this is the expected Dulong-Petit limit, given that there are no optical modes. For a crystal with $p > 1$ atoms per units cell, the heat capacity of the other $3p - 3$ optical modes, which only become thermodynamically relevant at intermediate and high temperatures, can be accounted for using an additional Einstein-like heat capacity, describing modes with non-vanishing frequency at zone center.

3.3 Thermal Conductivity

The process of heat conduction in generic insulating crystals is usually, predominately phonon-mediated. Only occasionally, and at very low temperatures, can any other type of itinerant

quasi-particle, like the spin-wave excitations of a long-range-ordered magnetic state, overtake the phonon-contribution to heat conduction. Thus, any realistic model in magnetic insulators at finite temperature is going to have to account for their contribution to the bulk thermal conductivity tensor.

3.3.1 Debye-Callaway/relaxation time approximation

One of the most rudimentary models for the thermal conductivity of 3D crystal is the Debye-Callaway model [44]. This model assumes that the acoustic phonon spectrum is Debye-like, i.e. the acoustic phonon energy levels can be approximated by $\omega(k) = v_s k$, and thus the spectral heat capacity of these modes is identical to that of i.e. 3.30, i.e.

$$c(x)g(x) = 9k_B \left(\frac{T}{T_D}\right)^3 \frac{x^4 e^x}{(e^x - 1)^2}, \tag{3.31}$$

This also implies a constant group and phase velocity $v_g = d\omega/dk = v_p = v_s$. The model also assumes that phonons have a mean lifetime $\tau(x)$. The total thermal conductivity, or rate of heat transfer [W] per unit temperature [K] and per unit length is given as a product of the group velocity squared, mean lifetime, and spectral heat capacity, summed over all phonon modes:

$$\kappa_{xx} = \int_0^{\omega_c} \tau(\omega)\ v_g^2\ c(\omega), \tag{3.32}$$

$$= \frac{k_B}{2\pi^2 v_s} \left(\frac{k_B T}{\hbar}\right)^3 \int_0^{T/T_D} \frac{x^4 e^x}{(e^x - 1)^2}\ \tau(x)\ dx. \tag{3.33}$$

In all real materials, a finite phonon lifetime is a consequence of Normal & Umklapp 3-phonon scattering processes, impurity/defect scattering, scattering off the boundaries of the crystal etc. The relaxation time approximation one typically uses to account for all these different types of scattering assumes that the total relaxation rate is a sum of several different independent relaxation rates:

$$\tau^{-1} = \tau_b^{-1} + \tau_{pd}^{-1} + \tau_N^{-1} + \tau_U^{-1}. \tag{3.34}$$

τ_b^{-1} is a boundary scattering term characterized by a length scale ℓ_0, which is the effective low-temperature mean free path of phonons.

$$\tau_b^{-1} = v_s/\ell_0 \tag{3.35}$$

ℓ_0 can represent an effective disorder length scale, mean distance between crystal grain boundaries, or in the case of a relatively pristine crystal, it can be approximately the size of the minimum sample dimension, which limits ballistic transport at very low temperatures. The so-called point defect term τ_{pd}^{-1} accounts for isotopic differences in ionic mass as well as possible lattice impurities and randomly-distributed defects.

$$\tau_{pd}^{-1} = \frac{V\Gamma}{12\pi N^2} g(\omega)\omega^2 = \frac{V\Gamma}{4\pi N v_p^2 v_g}\omega^4 = A\omega^4. \tag{3.36}$$

As shown, this is typically formulated in terms of a fitting parameter A, which is in principle proportional to the mean squared deviation Γ of atomic masses, and depends inversely on the speed of sound. This scattering term is analagous to Rayleigh scattering of photons, hence the quartic dependence on photon frequency. τ_N^{-1} and τ_U^{-1} represent Normal and Umklapp 3-phonon scattering processes respectively. N processes conserve total phonon momentum, whereas U processes do not. Although there is not universal agreement on the exact forms of these relaxation rates, which depend on several simplifying assumptions, the most commonly encountered forms are:

$$\tau_U = B_1 T\omega^2 e^{-T_D/3T}, \tag{3.37}$$

$$\tau_N = B_2 T\omega^2. \tag{3.38}$$

B_1, B_2 are fitting parameters that depend quadratically on the mean Gruneisen parameter, and inversely on the speed of sound:

$$B_1, B_2 \sim \frac{\hbar\gamma^2}{v_p^2 T_D}. \tag{3.39}$$

A brief survey of the literature reveals many potential variations of these expressions [45, 46, 47, 68]. In some cases a better fit is achieved by modifying the exponential of the U term with an additional

fitting parameter: cT_D/T, or the exponential is omitted entirely, whereby a distinction between N and U processes can no longer be drawn.

In principle, the microscopic parameters determining A, B_1, B_2 are often difficult to independently verify by independent measurements or estimate without extremely detailed ab-initio modelling, so in practice, generating a convincing description of $\kappa_{xx}(T)$ according to 3.33 relies heavily on multi-parameter fitting, subject to all the usual pitfalls of trying to identify a unique solution in a potentially highly-degenerate parameter space. In particular, it is typically possible to partially compensate a reduction in one scattering amplitude coefficient, by an adjustment of some combination of the others, thus guaranteeing uniqueness in a Debye-Callaway fit is a near impossibility. Because of a lack of firm consensus on how to model and derive such scattering terms, especially for N, U processes, and the extreme difficulty of guaranteeing uniqueness, these expressions should be viewed as mostly empirical tools and one should be wary of drawing specific conclusions about microscopic details from the face value of any single isolated fit. Nonetheless, such a formulation is incredibly valuable for conceptualizing the complicated interplay and macroscopic effects of such a diverse array of potential scattering mechanisms.

3.3.2 Kubo-Green relation

The Kubo-Green formula, is a fluctuation-dissipation relation [48, 49], that relates the thermal conductivity tensor to equilibrium fluctuations in the microscopic heat current density at temperature T:

$$\kappa_{\alpha\beta} = \frac{V}{k_B T^2} \int_0^\infty dt \ \langle q_\alpha(0) q_\beta(t) \rangle. \tag{3.40}$$

This form provides us with some additional crucial insight into how the relaxation time approximation that produces the Debye-Callaway result 3.33 is justified and furthermore how such a result can be generalized. Working in k-space, we can write quantum mechanical thermal heat current operator for each mode with polarization λ and wavevector $\mathbf{k}$ on the harmonic phonon lattice

associated with a Hamiltonian $\sum_{\mathbf{k},\lambda} \hbar\omega_{\mathbf{k},\lambda}\hat{a}^\dagger_{\mathbf{k},\lambda}\hat{a}_{\mathbf{k},\lambda}$:

$$\mathbf{q}_{\mathbf{k},\lambda}(0) = \frac{\hbar\omega_{\mathbf{k},\lambda}\mathbf{v}_{\mathbf{k},\lambda}}{V}\left(\hat{a}^\dagger_{\mathbf{k},\lambda}\hat{a}_{\mathbf{k},\lambda} - \langle\hat{a}^\dagger_{\mathbf{k},\lambda}\hat{a}_{\mathbf{k},\lambda}\rangle\right) \tag{3.41}$$

Where $\mathbf{v}_{\mathbf{k},\lambda} = d\omega_{\mathbf{k},\lambda}/d\mathbf{k}$ is the group velocity of each mode. Intuitively speaking, the heat current is the net energy flow per unit time, per unit area, and this form clearly illustrates that the heat current per mode $(\mathbf{k},\lambda)$ is the product of the group velocity (or propogation speed) of that given mode times the deviation of that mode's energy from its equilibrium expectation value per unit volume. Here, $\langle\hat{O}\rangle$ denotes a thermal average: $Z^{-1}\mathrm{Tr}[\hat{O}e^{-\beta\mathcal{H}}]$. To account for decoherence in the time-dependence, due to scattering and anharmonicty, we introduce the mean phonon lifetime $\tau_{\mathbf{k},\lambda}$ for the decoherence/damping of each mode $(\mathbf{k},\lambda)$. Naturally, we expect that any density matrix initialized in some pure state $\hat{\rho}(0) = |n_{\mathbf{k},\lambda}\rangle\langle n_{\mathbf{k},\lambda}|$ in a real material will decohere over a timescale. $\tau_{\mathbf{k},\lambda}$, i.e. the probability associated with finding the system in this mode should decay over t as $e^{-t/\tau}$. This fact can be formally accounted for by the addition of a complex non-hermitian part to the harmonic Hamiltonian [50], $\mathcal{H}_{\mathbf{k},\lambda} \to \mathcal{H}_{\mathbf{k},\lambda} - i(\tau_{\mathbf{k},\lambda})^{-1}/2$, so that the time evolution operator acting on a state at $\mathbf{k},\lambda$ becomes $\hat{U}(t)|n_{\mathbf{k},\lambda}\rangle = e^{-i\omega_{\mathbf{k},\lambda}t}e^{-t/2\tau_{\mathbf{k},\lambda}}|n_{\mathbf{k},\lambda}\rangle$. In this way, we may write the time-dependent RTA heat current operator according to the non-unitary evolution: $\hat{U}^\dagger(t)\mathbf{q}_{\mathbf{k},\lambda}(0)\hat{U}(t)$ so that it becomes:

$$\mathbf{q}_{\mathbf{k},\lambda}(t) = \frac{\hbar\omega_{\mathbf{k},\lambda}\mathbf{v}_{\mathbf{k},\lambda}}{V}\left(\hat{a}^\dagger_{\mathbf{k},\lambda}\hat{a}_{\mathbf{k},\lambda} - \langle\hat{a}^\dagger_{\mathbf{k},\lambda}\hat{a}_{\mathbf{k},\lambda}\rangle\right)e^{-t/2\tau_{\mathbf{k},\lambda}} \tag{3.42}$$

From this, we may apply the Kubo-Green formula to compute the longitudinal thermal conductivity:

$$\kappa = \sum_{\mathbf{k},\lambda}\frac{k_B}{V}\beta^2\int_0^\infty dt\ (\hbar\omega_{\mathbf{k},\lambda})^2 e^{-t/\tau_{\mathbf{k},\lambda}}\left\langle v^2_{\mathbf{k},\lambda}\left(\hat{a}^\dagger_{\mathbf{k},\lambda}\hat{a}_{\mathbf{k},\lambda} - \langle\hat{a}^\dagger_{\mathbf{k},\lambda}\hat{a}_{\mathbf{k},\lambda}\rangle\right)^2\right\rangle, \tag{3.43}$$

$$= \frac{k_B}{V}\sum_{\mathbf{k},\lambda}\tau_{\mathbf{k},\lambda}\ v^2_{\mathbf{k},\lambda}\ (\beta\hbar\omega_{\mathbf{k},\lambda})^2\left[\langle(\hat{a}^\dagger_{\mathbf{k},\lambda}\hat{a}_{\mathbf{k},\lambda})^2\rangle - \langle\hat{a}^\dagger_{\mathbf{k},\lambda}\hat{a}_{\mathbf{k},\lambda}\rangle^2\right]. \tag{3.44}$$

We have exactly recovered the relaxation time approximation which expresses the total thermal conductivity as the product of group velocity squared, the mean phonon lifetime, and spectral heat capacity $c_{\mathbf{k},\lambda}$, as identified in eqn 3.27, summed over all phonon modes:

$$\kappa = \frac{1}{V}\sum_{\mathbf{k},\lambda}\tau_{\mathbf{k},\lambda}\ v^2_{\mathbf{k},\lambda}\ c_{\mathbf{k},\lambda} \tag{3.45}$$

In describing a typical insulator, $\tau_{\mathbf{k},\lambda}$ will usually have a functional dependence on T and $\mathbf{k}$ as outlined in equations 3.34 - 3.39. More generically, for a Hamiltonian that separates into a Kronecker sum over indept. modes $\mathcal{H} = \bigoplus_{\mathbf{k}} \mathcal{H}_{\mathbf{k}}$ we could alternatively write the Kubo-Green formula for the RTA thermal conductivity in the following form:

$$\kappa = \frac{\beta^2 k_B}{V} \sum_{\mathbf{k}} \int_0^\infty dt \ \left[\langle (v_{\mathbf{k}} \mathcal{H}_{\mathbf{k}} e^{-t/2\tau_{\mathbf{k}}})^2 \rangle - \langle v_{\mathbf{k}} \mathcal{H}_{\mathbf{k}} e^{-t/2\tau_{\mathbf{k}}} \rangle^2 \right], \tag{3.46}$$

In chapter 8 this formula is applied in the computation of a spin-phonon hybridized spectrum to model the field-dependence in the thermal conductivity tensor of $CsYbSe_2$.

Chapter 4

Experimental Techniques

4.1 Thermal Transport

As discussed in the introductory chapters, the thermal conductivity is a richly complicated parameter that accounts for many potential itinerant quasi-particles and sources of scattering and anharmonicity affecting the propagation of said quasi-particles. While the theoretical underpinnings of heat transport in insulators, particularly those that feature prominent interaction between spin and lattice degrees of freedom, is complicated and often entirely intractable without significant simplifying assumptions, toy-models, or empirically-motivated descriptions, thermal conductivity measurements themselves are rather straight-forward. This section aims to cover all the essentials of measuring thermal conductivity in single crystal samples and identify the important experimental considerations that go into designing and conducting such measurements.

4.1.1 κ_{xx}, Longitudinal thermal conductivity

Fourier's law of heat conduction provides a straight-forward linear relationship between the heat current density $\mathbf{q}$ [W/m^2] flowing at a point $\mathbf{x}$ and the gradient of the local steady-state temperature arising in this region in terms of the thermal conductivity tensor $\boldsymbol{\kappa}$,

$$\mathbf{q}(\mathbf{x}) = -\boldsymbol{\kappa} \cdot \boldsymbol{\nabla} T(\mathbf{x}). \tag{4.1}$$

The most ideal geometry for measuring the longitudinal thermal conductivity is a rectangular bar geometry, pictured below in Fig. 4.1, with a uniformly-flowing heat current. Typically an as-grown

single-crystal sample is cut and polished so that it has a uniform cross sectional area along its length, so that a condition of parallel isotherms along the length of the sample can be assumed, and the problem of heat transport can be effectively one-dimensionalized. A more complicated geometry may necessitate a finite element treatment or some degree of simulation. The bar has a

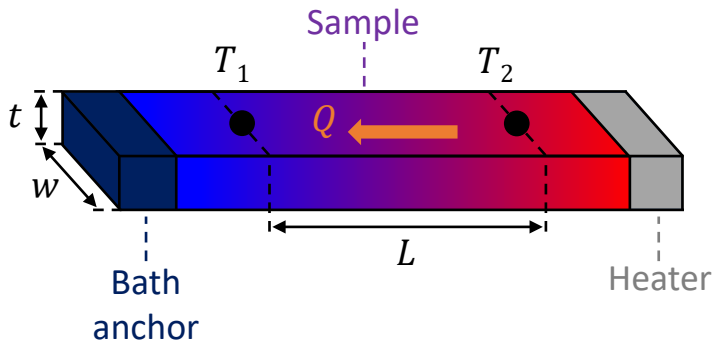

Figure 4.1: A rectangular sample thermally-anchored at one end, with a uniform heat current Q driven by the heater fixed to its other end. This arrangement results in parallel isotherms which are perpendicular to the direction of heat flow. 2 such isotherms at temperatures T_1, T_2 are experimentally measured.

uniform area $A = w \times t$. The pictured geometry can be used to measured thermal conductivity in a one-heater, two-thermometer configuration. Using a resistive heater, we drive a heat current Q [W] through the sample, which is anchored to the probe at one of its ends so that it thermalizes with the bath (cold finger), and we measure temperatures T_1, T_2 which can be easily done with either thermocouples or resistive thermometers. For this arrangement, the differential form of Fourier's law can be solved:

$$q = \frac{Q}{A} = -\kappa_{xx}\frac{dT}{dx}, \tag{4.2}$$

$$\frac{Q}{wt}\int_0^L dx = \int_{T_1}^{T_2} \kappa_{xx} dT. \tag{4.3}$$

If we assume κ_{xx} is a constant (or varies little as a function of temperature) this arrangement results in a steady state thermal gradient:

$$\frac{Q}{wt} = \kappa_{xx}\frac{T_2 - T_1}{L}, \tag{4.4}$$

where we have denoted the lengthwise dimension of the sample by $\hat{x}$. We purposefully anchor the sample at only one end, in a "diving-board" configuration, so that the majority of the heat generated by the heater flows to the thermal bath through this anchor point. Parasitic heat loss, i.e. the transfer of heat through pathways other than the sample and bath anchor point, is purposefully minimized by placing the sample assembly in a vaccuum, and by using extremely thin current leads, so that the total heat current through the sample is approximately equal to the entirety of the Ohmic joule heating $Q \approx I^2 R_H$ induced in the sample heater. The topic of parasitic heat loss is covered in a succeeding section. Thus in a real experiment we can invert the above equation to determine κ_{xx} by measuring the linear response of $\Delta T = T_2 - T_1$ to a given applied heater current I:

$$\kappa_{xx} = \frac{L}{A} \cdot \frac{I^2 R_H}{\Delta T}, \tag{4.5}$$

In these experiments, the heat current is provided by a ~ 1 kΩ sample heater, with typical dimensions ~ 1 mm $\times$ .2 mm$\times$ .1 mm, which is directly affixed to the sample using epoxy and connected to a DC current source. The precise resistance of this heater $R_H(T)$ must additionally be calibrated as a function of temperature.

In general however, $\kappa_{xx}(T)$ itself is a function of temperature, so a more careful treatment of 4.3 is worth considering. To analyze this, we consider a change of variables $T \to T'$, where T' is a deviation from the mean temperature $T_m = (T_1 + T_2)/2$.

$$T' = T - T_m, \qquad T_1' = -\frac{\Delta T}{2}, \qquad T_2' = \frac{\Delta T}{2}. \tag{4.6}$$

Expressing the thermal conductivity using a Taylor expansion about its mean T_m value:

$$\kappa_{xx}(T) = \kappa(T_m + T') = \kappa_{xx}(T_m) + T' \frac{\partial \kappa_{xx}}{\partial T}\bigg|_{T_m} + \dots, \tag{4.7}$$

allows us to write the differential form of Fourier's law 4.3 as a systematic expansion:

$$Q\frac{L}{A} = \int_{-\Delta T/2}^{\Delta T/2} \left[\kappa_{xx}(T_m) + T' \frac{\partial \kappa_{xx}}{\partial T}\bigg|_{T_m} + \frac{(T')^2}{2} \frac{\partial^2 \kappa_{xx}}{\partial T^2}\bigg|_{T_m} + \dots \right] dT', \tag{4.8}$$

$$= \Delta T \ \kappa_{xx}(T_m) + \frac{(\Delta T)^3}{24} \frac{\partial^2 \kappa_{xx}}{\partial T^2}\bigg|_{T_m} + \mathcal{O}(\Delta T^5). \tag{4.9}$$

This result 4.9 shows that the form of eqns. 4.4,4.5 is completely valid in terms of the thermal conductivty $\kappa_{xx}(T_m)$ at the value of the sample mean temperature, provided that we can experimentally ensure the total thermal gradient ΔT across the sample is small. For this reason a measurement of κ_{xx} requires actively selecting appropriate heater currents I such that the resulting gradients do not exceed a few percent of the mean sample temperature, this is even more crucial when measuring thermal conductivity in the vicinity of a region where the slope of κ_{xx} versus T is changing most rapidly. To verify the linearity of the thermal gradients, the DC current source of the heater is typically programmed to ramp the heater current up in several discrete steps whereby a linear fit of ΔT versus $I^2 R_H$ may be obtained to deduce κ_{xx} as illustrated in the data below, Fig. 4.2.

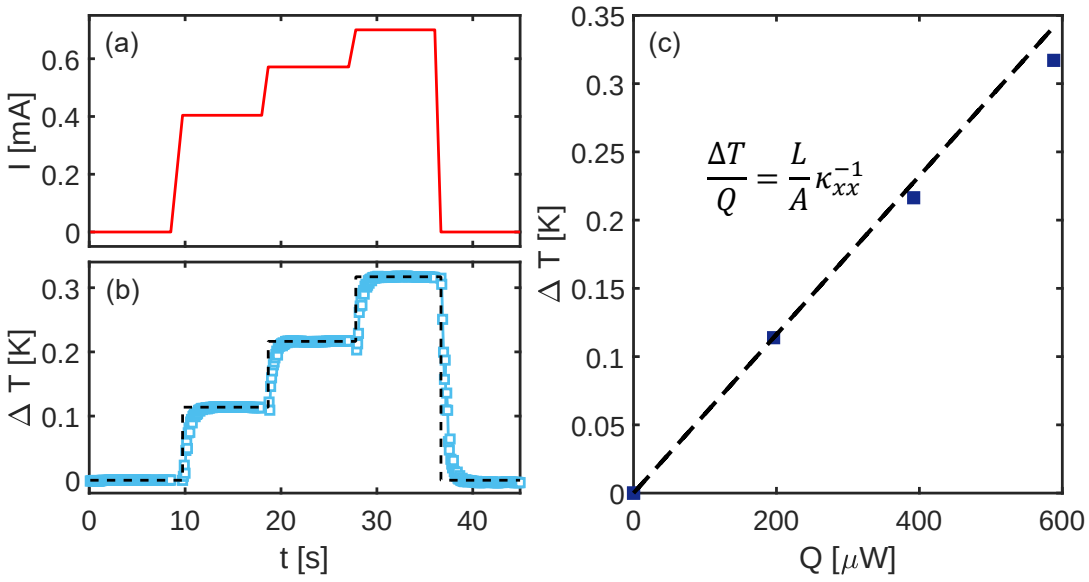

Figure 4.2: (a) The ramp profile of the applied heater current $I(t)$. Each step is chosen so that I^2R is incremented uniformly. (b) The resulting, measured profile of $\Delta T(t)$ takes a finite amount of time to reach a steady state equilibrium, thus the time duration of each step must be appropriately long to capture the equilibration process. The dotted line represents an averaged ΔT in a steady state condition. (c) We plot ΔT versus Q, the slope of this linear relation is the thermal resistance, $L\kappa_{xx}^{-1}/A$. For the chosen heater currents, some small degree of nonlinearity is clearly observed.

4.1.2 κ_{xy}, Thermal Hall effect

While phonons and magnons alike are net-zero-charge excitations, and therefore not subject to a Lorenz force in a magnetic field, there exist several analogs of the anomalous electron Hall effect for phonons and magnetic quasiparticles. There are in fact several physical mechanisms by which the thermal conductivity tensor can acquire non-zero off-diagonal terms (κ_{xy}) in the presence of a finite magnetic field, including, but not limited to: spatially asymmetric spin-phonon scattering, non-trivial Berry curvature of itinerant magnon bands, and non-collinear antiferromagnetic spin textures [51, 52, 53]. The topic of microscopic mechanisms of the so called thermal Hall effect (THE) is not a central topic of this thesis, but for completeness we will summarize the essential aspects of measuring and characterizing a THE.

We again consider a rectangular ($L \times w \times t$) slab geometry with a single heater that drives a heat current Q in the transverse ($\hat{x}$) direction, but in this case we attach an additional thermometer, and position the others as to measure both a transverse ($\Delta_y = T_3 - T_2$) and longitudinal temperature gradient ($\Delta_x = T_2 - T_1$) as below: In this case, Fourier's law can be written as a 2-dimensional

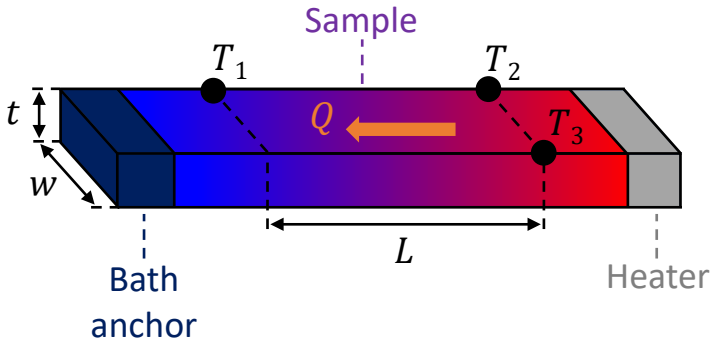

Figure 4.3: In this case, the off-diagonal component of the thermal conductivity tensor results in a transverse temperature gradient. As a consequence, the isotherms are not longer purely perpendicular to the direction of heat flow and the temperature must be measured at 3 points in the xy plane of the sample to determine both longitudinal (ΔT_x) and transverse (ΔT_y) temperature gradients.

matrix equation:

$$\begin{pmatrix} Q/wt \\ 0 \end{pmatrix} = \begin{pmatrix} \kappa_{xx} & \kappa_{xy} \\ -\kappa_{xy} & \kappa_{xx} \end{pmatrix} \begin{pmatrix} \Delta T_x/L \\ \Delta T_y/w \end{pmatrix}, \tag{4.10}$$

This results in 2 equations, from which one can obtain expressions for the longitudinal and thermal Hall conductivities

$$\kappa_{xx} = \frac{Q}{Lwt} \cdot \frac{\Delta T_x}{(\Delta T_y/w)^2 + (\Delta T_x/L)^2},$$
$$\kappa_{xy} = \frac{Q}{w^2 t} \cdot \frac{\Delta T_y}{(\Delta T_y/w)^2 + (\Delta T_x/L)^2},$$

Or alternatively for the experimentally dependent variables $\Delta T_x, \Delta T_y$:

$$\Delta T_y = \frac{Q}{t} \cdot \frac{\kappa_{xy}}{\kappa_{xx}^2 + \kappa_{xy}^2}, \tag{4.11}$$

$$\Delta T_x = Q \frac{L}{wt} \frac{\kappa_{xx}}{\kappa_{xx}^2 + \kappa_{xy}^2}. \tag{4.12}$$

In most materials that do exhibit a measurable THE, there will be at least a 4-order-of-magnitude discrepancy, $\kappa_{xy}/\kappa_{xx} < 10^{-4}$, in these coefficients, meaning that it is usual justifiable to use the approximate expressions:

$$\Delta T_y \approx \frac{\kappa_{xy}}{\kappa_{xx}^2} \cdot \frac{Q}{t}, \tag{4.13}$$

$$\Delta T_x \approx \kappa_{xx}^{-1} \frac{QL}{wt}. \tag{4.14}$$

The later expression of course is the usual longitudinal thermal conductivity in the absence of any THE. The equation for ΔT_y illustrates some of the challenges inherent in reliably measuring a THE. Given the small typically size of κ_{xy} compared to κ_{xx}, it can be very hard to obtain a measurable ΔT_y while also simultaneously measuring a linearly-responding ΔT_x. The thickness of the sample also works against the signal size, meaning that any samples measured must be made very thin, in some cases entirely precluding the possibility of a one-end-fixed setup if the sample is too delicate. It is also an absolute necessity to anti-symmetrize the ΔT_y signal, which is generically an odd function of H and therefore changes sign with applied field:

$$\Delta T_{y,\text{actual}}(H) = (\Delta T_y(H) - \Delta T_y(-H))/2. \tag{4.15}$$

This anti-systematization helps to avoid deceiving oneself with a measured gradient that arises purely from geometrical misalignment of the thermometers or inhomogeneity of heat flow.

4.1.3 High-Field investigations, in-situ rotation

All high-field investigations of the thermal conductivity were performed at using the 18/20 Tesla General Purpose Superconducting Magnet SCM2 at the National High-Magnetic Field Lab in Tallahassee Florida. This cryostat has two insert options, a He^3 charcoal-sorption pump insert for operating down to temperatures as low as 300 mK, and a variable temperature insert (VTI) which is best suited for operation at intermediate temperatures in the range of 2-150 K. Each probe is equipped with a cylindrical socket rotator that can provide a $\pm 180^\circ$ rotation of a sample/device.

Due to potential parasitic heat loss through any residual exchange gas, the concerns of which are elaborated on in the succeeding section, it is crucial that thermal conductivity measurements are performed in a high-quality vacuum. For this reason, we employ the custom-machined Copper-Beryllium vacuum cells pictured in Fig. 4.4, which are adapted from the original designs of Eun Sang Choi at the NHMFL.

These handmade cells included a modular sample stage with an electrical feedthrough for up to 32 wires. At room temperature, they are evacuated down to $\sim 10^{-6}$ torr and indium sealed. As the cell and sample cools to cryogenic temperatures, this vacuum improves further. The cells are specifically designed for compatibility with the SCM2 rotator probes as shown in fig 4.4, allowing a full in-situ exploration of applied -field anisotropy in the thermal conductivity of measured samples, a striking example of which is explored in chapter 7.

4.1.4 Parasitic heat loss

If there are other pathways for heat to travel from the sample heater to the bath other than the intended anchor point, then the measured thermal conductivity, estimated as $\kappa_{xx} = LQ/A\Delta T$ can be distorted from its true value. While the thermal conductivity we measure for single crystals is an intrinsic quantity, this problem is most conveniently analyzed in terms of the extrinsic quantities

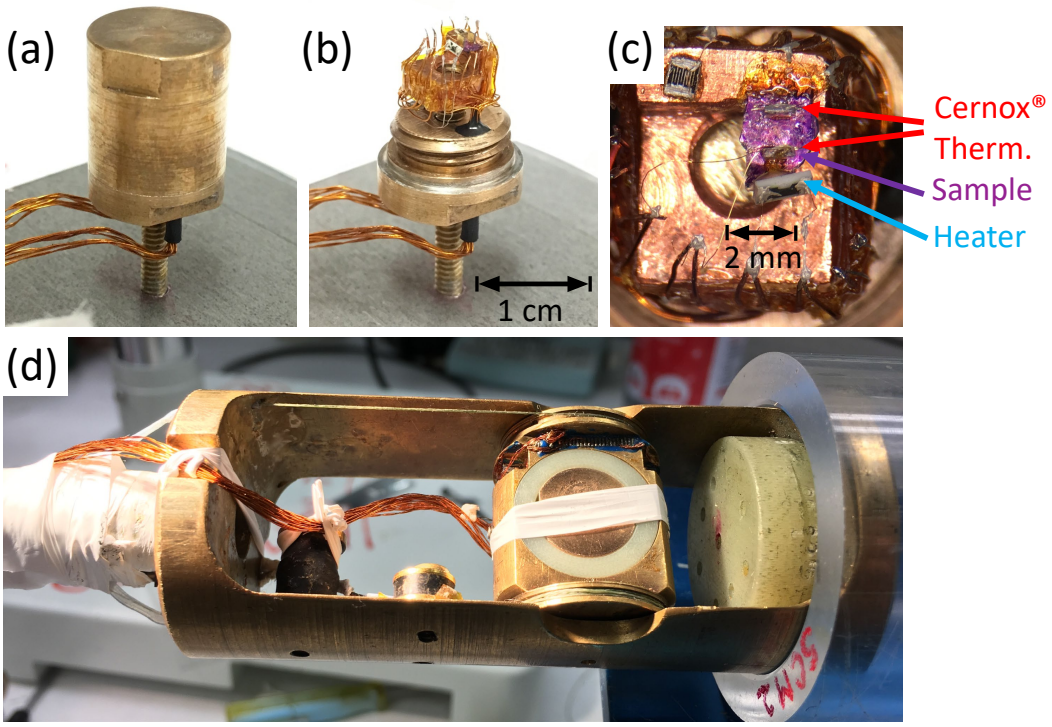

Figure 4.4: Panel (a) shows the capped cylindrical copper-beryllium vacuum cell. Twisted-pair electrical connections feedthrough the bottom of the cell. These feedthroughs are sealed with a stycast epoxy. (b) shows the vaccum cell with the cap off. The sample stage consists of a piece of copper on which a sample assembly is anchored. The stage is surrounded by wires and all electrical contacts are affixed with gold wire and silver paint. A remnant of the indium seal between the base and cap is visible as a ring around the circumference of the base. (c) Top down view of the diving board sample assembly with thermometry, heater, and all contacts visible. The single crystal $CrCl_3$ sample is the bright purple rectangle. (d) The bottom of the SCM2 rotator probe with the vacuum cell secured in the cylindrical rotator.

for the thermal conductance K, and its inverse, the thermal resistance, denoted here by $R = K^{-1}$. The thermal conductance is the absolute total rate of energy flow per unit temperature difference [W/K], between two points at a temperature ΔT. Thus for the ideal rectangular sample considered in the previous sections, the thermal conductance is $K = A\kappa_{xx}/L = Q/\Delta T$.

Fourier's law of heat conduction, Eqn. 4.1, is mathematically equivalent to Ohm's law with the heat current density and thermal conductivity tensor naturally assuming the roles of electrical current density and conductivity tensor respectively, and temperature replacing the electrical voltage. This means that we can write down a completely analogous thermal Ohm's law relation

$T = QR$ ($V = IR$) and analyze heat flow in terms of circuit diagrams subject to thermal analogs of Kirchoff's rules and all the same intutions of electrical circuit theory. We consider the diving board sample geometry of the previous sections, with an additional parasitic heat pathway to the bath, pictured in Fig. 4.5, as a pathway through the heater electrical contacts, but the parastic thermal resistance R_p can be generically account for heat loss through other avenues, such as residual exchange gas inside the vacuum cell.

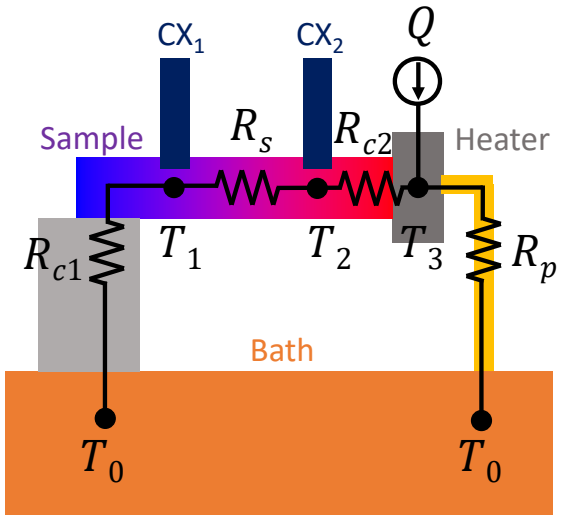

Figure 4.5: A sample with thermal resistance R_2 in a realistic diving board configuration, with 2 Cernox thermometers (CX_1,CX_2) measuring the temperatures T_1 and T_2. There is a parasitic heat pathway with thermal resistance R_p to the bath through the heater wires on the right hand side. The thermal circuit diagram appropriate for analyzing this situation is overlaid. R_{c1} & R_{c2} characterize the thermal linkages between the sample and bath or heater respectively. Functionally, the heater at temperature T_3 is a source of current Q and the bath at temperature T_0 is a sink for this current.

We denote the heat current through the sample and left hand side as Q_s, and the parasitic heat current through the right hand side as Q_p. By conservation of energy flux, we must have that $Q = Q_s + Q_p$. The thermal Ohm's law equations determining the thermal gradients are:

$$T_2 - T_1 = R_s Q_s, \tag{4.16}$$

$$T_3 - T_0 = (R_{c1} + R_{c2} + R_s)Q_s = R_p Q_p. \tag{4.17}$$

The latter equation can be rewritten in terms of $Q_p = Q - Q_s$, rearranged for Q_s and divided by the

experimental gradient $T_2 - T_1$ to find an expression for the naively measured thermal conductivity $K_{\text{meas.}} = Q/\Delta T$ in terms of the actual thermal conductance $K_s = A\kappa_{xx}/L$:

$$K_{\text{meas.}} = K_s \frac{R_{c1} + R_{c2} + R_s + R_p}{R_p}, \tag{4.18}$$

$$= K_s + K_p + K_s \frac{K_{c1}^{-1} + K_{c2}^{-1}}{K_p^{-1}}. \tag{4.19}$$

This form highlights the importance of eliminating parasitic heat pathways and thus minimizing K_p. In the limit that $K_p \ll K_s$, Eqn. 4.19 reduces to:

$$\lim_{K_p \to 0 \ (R_p \to \infty)} K_{\text{meas.}} = K_s, \tag{4.20}$$

Thus, the naively measured result equals the actual sample thermal conductance if we can satisfy the condition that the entire heat current Q produced by the heating element flows through the sample alone. It is reassuring that the result in this case does not depend on R_{c1} and R_{c2}, given the difficulty of estimating these thermal resistances, which account for heat transfer through amalgams of various materials, interfaces, and highly variable epoxy contacts.

4.1.5 Thermometry Calibration

In the experiments described in this thesis we employ calibrated negative-temperature-coefficient (NTC) cernox thermometers, whose resistances $R(T)$ are measured in a 4-probe (I^+, I^-, V^+, V^-) configuration using an AC resistance bridge. These thermometers are chosen because of their enormous sensitivity to minute temperature changes, $|dR/dT|$, at low temperatures, necessary to resolve small temperature gradients that do not perturb a sample beyond its linear thermal conductivity response regime. As a general rule of thumb, for longitudinal measurements, we need to resolve thermal gradients that are on the order of 0.1-1% of the average sample temperature at any given point, and in the case of thermal Hall measurements it may be necessary to resolve gradients that are $10^4 - 10^5$ times smaller. In general, a well-calibrated cernox pair at temperatures on the order of 1 K has no problem resolving a gradient ΔT that is 100s or even 10s of μK with only a few 100s of points to average. Greater temperature resolution requires a cryostat with extreme bath

stability and very consistent sample cooling power, and long averaging times to combat random temperature fluctuations. A representative Cernox resistance curve $R(T)$ is plotted below.

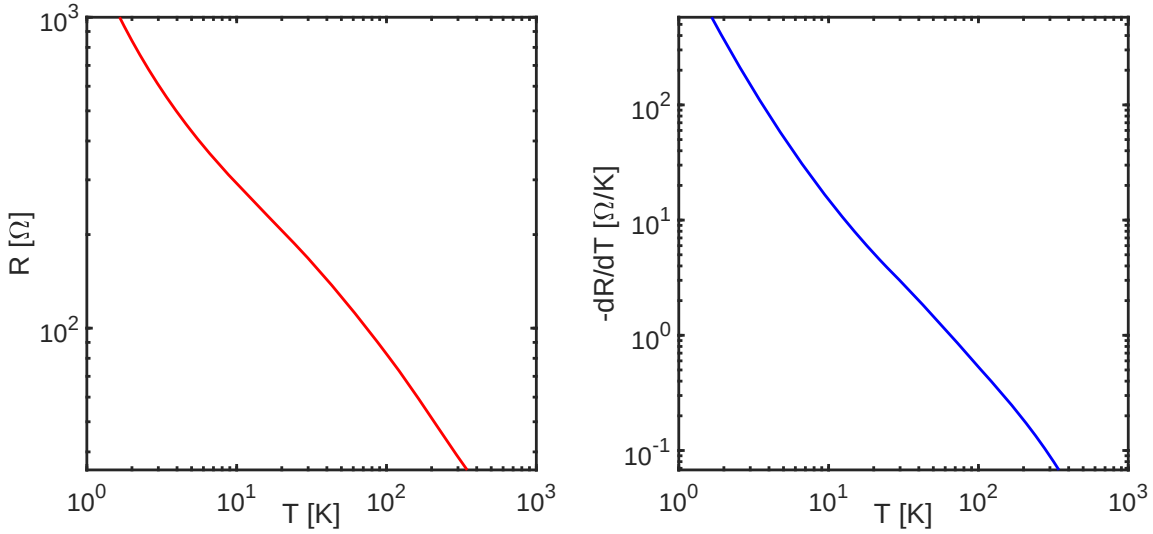

Figure 4.6: The left hand side shows a typical Cernox resistivity $R(T)$ from 1.6 K to 300 K. And the right hand side shows the sensitivity $-dR/dT$ over the same temperature range.

While offering an exceptional sensitivity to small temperature changes, Cernoxes have their fair share of drawbacks. The Cernox itself is a metal-film resistor deposited on a sapphire substrate. The fabrication process is somewhat variable and acutely sensitive to imperfections of the substrate and deposition process. This means that no two Cernoxes are exactly alike in their $R(T)$ profile, and each must be calibrated carefully. Given the typically small size of the single-crystal samples we measure, the only from-factor-appropriate Cernox is the bare-chip variety, the surface of which is largely unprotected and liable to change its $R(T)$ profile subtlety during mounting, thermal cycling, or reuse. This means that the thermometers need to be re-calibrated often and this is usually most reliably done in-situ on the sample setup against another more robust bath reference thermometer. Usually this bath thermometer is another Cernox, albeit one that is highly protected in a sealed metal housing, and one that has been thermally cycled many times, demonstrating a robust temperature reference.

Like many generic resistors, Cernoxes also exhibit siginificant magnetoresistance at tempera-

tures $T < 10$K. Near $T = 2$ K the fractional magneotresistance $\Delta R/R_0 = [R(H) - R(0)]/R(0)$ can be as large as $\sim 20\%$ at $\mu_0 H = 20$ T. This means that low-temperature field-dependent studies also require accurate field calibration $R(H, T)$ for each Cernox. This is usually performed in-situ against a robust, field-calibrated thermometer, or by using a capacitive thermometer which exhibits no instrinsic magnetoresistance.

4.2 High-field Resonant Torsion Magnetometry

In real materials, there is usually some degree of magnetic anisotropy, typically emerging as a consequence of either differences between the magnitudes of interactions that couple distinct spatial components of the spin moments of magnetic ions, i.e. exchange anisotropy, or differences in how the magnetic field itself couples to individual moments along distinct crystallographic directions, i.e. g-tensor anisotropy. When an anisotropic magnetic sample is placed in an external magnetic field $\mathbf{H}$, its corresponding Helmholtz free energy gains a magnetic component $F(T, \mathbf{H})$ that depends on the angle of the applied field relative to the crystallographic axes of the material. This directional-dependence can profoundly affect any of the sample's thermodynamic properties in a finite field.

By experimentally probing the magnetic anisotropy of materials, there is generally a great deal that we can learn about their fundamental mechanisms of magnetism, microscopic interactions, competing energy scales, and magnetic structures. This section explains one such experimental method, resonant torsion magnetometry, which exploits anisotropy in the vibrational dynamics of a cantilever-mounted sample under finite field to directly probe the curvature of the magnetic Helmholtz free energy and shed light on the microscopic details governing its magnetic properties.

4.2.1 τ, k, General principles

As a result of anisotropic interactions, a crystal may magnetize more easily along one direction than another, i.e. a given magnetic field $\mathbf{H}$ applied to a material will produce a different total magnetization $\mathbf{M}$ depending on its direction relative to the material's crystallographic axes. This is typically characterized in terms of differences in principle spatial components of the material's

susceptibility tensor $\boldsymbol{\chi}$. Directions that correspond to maxima or minima of $\boldsymbol{\chi}$ are often called easy or hard axes respectively [17]. Because of precisely these differences in components of the susceptibility tensor, the magnetization $\mathbf{M}$ produced by some external field $\mathbf{H}$ applied in an arbitrary direction between either an easy or hard axis is not guaranteed to be collinear to the applied field. Thus, such a sample will generically experience a magnetic torque $\boldsymbol{\tau} = \mathbf{M} \times \mathbf{H}$ [54]. As an initial explicit toy example, consider a sample with unequal orthogonal principle components of its magnetic susceptibility tensor χ_1, χ_3 in a particular plane. For a field applied within this plane of the sample, parametrized as: $\mathbf{H} = H \sin\theta \hat{\mathbf{x}} + H \cos\theta \hat{\mathbf{z}}$, (where H is small enough that linearity of the induced magnetization can be assumed) the free energy is equal to the magnetostatic energy of the resulting magnetization $\mathbf{M} = \chi_1 H \sin\theta \hat{\mathbf{x}} + \chi_3 H \cos\theta \hat{\mathbf{z}}$:

$$F(T, H, \theta) = -\frac{1}{2}\mathbf{M} \cdot \mathbf{H} = -\frac{H^2}{2}(\chi_1 \sin^2\theta + \chi_3 \cos^2\theta), \tag{4.21}$$

$$= \frac{H^2}{4}(\chi_1 + \chi_3) + \frac{H^2}{4}(\chi_3 - \chi_1)\cos(2\theta), \tag{4.22}$$

As we rotate the field in the xz-plane, we can compute the torque experienced by the sample along the $\hat{y}$ axis in the usual manner:

$$\tau(\theta) = [\mathbf{M} \times \mathbf{H}]_2 = \frac{H^2}{2}(\chi_3 - \chi_1)\sin(2\theta), \tag{4.23}$$

There is another general way to express the torque. The magnetic torque is actually a first-order thermodynamic variable [25], and much in the same way that one might express the magnetization $M = -\partial F/\partial B$ or entropy $S = -\partial F/\partial T$ at fixed temperature and volume respectively, one can define the component of the magnetic torque along a direction $\hat{\mathbf{n}}$, as a first derivative of the magnetic Helmholtz free energy w.r.t. the angle $\vartheta(\hat{\mathbf{n}})$ by a counterclockwise rotation of the field $\mathbf{H}$ in a plane perpendicular to the axis $\hat{\mathbf{n}}$, while H, T, V are fixed:

$$\tau_{\hat{\mathbf{n}}}(\vartheta) = -\left(\frac{\partial F}{\partial \vartheta(\hat{\mathbf{n}})}\right)\Bigg|_{H,T,V} \tag{4.24}$$

For the simple example of 4.23, where $\vartheta(\hat{\mathbf{y}}) = \theta$, this derivative relation is quite obvious to verify. In terms of the variables T, V, B, θ we can write the full thermodynamic relation:

$$dF = -SdT - PdV - MdB + \tau d\theta, \tag{4.25}$$

In general experiments where one probes the magnetic torque of a cantilever-mounted sample, either by directly measuring the cantilever deflection via a differential capacitance measurement or by the piezeoresitive response of the cantilever, the torque exhibits the characteristic H^2 and $\sin(2\theta)$ dependence of 4.23 when applied fields are small enough that the assumed linearity of $M_i = \chi_i H_i$ holds.

Similarly, we may define a 2nd order thermodynamic variable k, the magnetotropic coefficient, as the curvature of the free energy with respect to angular displacements of the applied field angle:

$$k(H,\vartheta) = \left(\frac{\partial^2 F(T,H,\vartheta)}{\partial \vartheta^2}\right)\Bigg|_{H,T,V} = -\left(\frac{\partial \tau_{\hat{\mathbf{n}}}(H,\vartheta)}{\partial \vartheta}\right)\Bigg|_{H,T,V}. \tag{4.26}$$

Intuitively, the magnetotropic coefficient represents the magnetic *rigidity* of the material with respect to small angular displacements, due to the associated energy cost of rotating a sample with an anisotropic free energy in a finite field. Although helpful in certain contexts, such a magnetic free energy does not need to be conceptualized in terms of macroscopic magnetizations and could instead be modeled via the explicit field dependence of a microscopic spin Hamiltonian $\hat{\mathcal{H}}(H,\vartheta)$

$$F(\beta,H,\vartheta) = -\frac{1}{\beta}\log \mathrm{Tr}\left[e^{-\beta\hat{\mathcal{H}}(H,\vartheta)}\right], \tag{4.27}$$

In the low field limit ($M_i = \chi_i H_i$) k is quadratic in H and exhibits a $\cos(2\theta)$ dependence with minima that are out of phase with those of the torque signal. If a material undergoes a magnetic phase transition at some critical field H_c or angle θ_c, the thermodynamic free energy $F(H,\theta)$ can be non-analytic. In particular, if the phase transiton is second order, according to an Ehrenfest classication, as in the case of a PM $\rightarrow$ FM transition, then k can be discontinuous, exhibiting a lambda-like anomally as a function of either H or θ.

Consider now, the case of uniaxial sample with c-axis perpendicular to its ab plane, which will be relevant to the discussion of $CsYbSe_2$ in chap. 6. we can define the total vector magnetization at a finite field, with $H_\perp = H\sin\theta$, $H_z = H\cos\theta$, in terms of component magnetizations M_{ab}, M_c:

$$\mathbf{M}(\mathbf{H}) = M_{ab}(H_\perp, H_z)\hat{\mathbf{x}} + M_c(H_\perp, H_z)\hat{\mathbf{z}} \tag{4.28}$$

The torque as function of angle explicitly becomes:

$$\tau(\theta) = \mathbf{M} \times \mathbf{H} = M_{ab} H \cos\theta - M_c H \sin\theta \tag{4.29}$$

Using this notation for $\mathbf{M}$, in addition to the usual susceptibilities,

$$\begin{aligned} \chi_{ab} &= \lim_{h\to 0} \frac{M_{ab}(H_\perp = h, H_z = 0)}{h}, \\ \chi_c &= \lim_{h\to 0} \frac{M_c(0,h)}{h}, \end{aligned}$$

we can additionally define the *transverse* susceptibilities at finite field, for the magnetization induced by a small field h applied perpendicular to an arbitrarily large finite field H:

$$\chi^T_{ab}(H) = \lim_{h\to 0} \frac{M_{ab}(H_\perp = h, H_z = H) - M_{ab}(0,H)}{h}, \tag{4.30}$$

$$\chi^T_c(H) = \lim_{h\to 0} \frac{M_c(H,h) - M_c(H,0)}{h}. \tag{4.31}$$

Using these definitions, we can write the magnetotropic coefficient $k(\theta) = -\partial\tau/\partial\theta$ at high-symmetry angles $\theta = 0$ and $\pi/2$, denoted $k_{ab}(H) = k(\theta = \pi/2, H)$ and $k_c(H) = k(\theta = 0, H)$, as:

$$k_{ab}(H) = H M_{ab}(H_\perp = H, H_z = 0) - H^2 \chi^T_c(H), \tag{4.32}$$

$$k_c(H) = H M_c(0,H) - H^2 \chi^T_{ab}(H), \tag{4.33}$$

In the low field limit, the transverse susceptibilities are in fact identical to their ZF values so that $k_{ab} = -k_c = (\chi_{ab} - \chi_c)H^2$. Given these expressions at high and low field, we can interpret the magnetotropic coefficient at a given applied field-angle θ as the energy difference of the real magnetostatic potential energy at that given angle minus the naively expected energy cost of magnetizing the sample in a completely perpendicular direction based linearly on the present value of its transverse susceptibility.

4.2.2 The vibrating cantilever

In order to measure the magneotropic coefficient k of a real magnetic sample, we employ a piezooresistive silicon cantilever mounted on the end of a quartz tuning fork. Such a device

must be able to use an oscillatory driving voltage to excite cantilever vibrations, and it must also be self-sensing in the sense that driven vibrations produce a measurable output signal. The commercially-available Akiyama probe is a self-actuating oscillatory atomic force microscopy sensor that satisfies these criteria, is relatively inexpensive, and it requires only minimal preparation to be mounted on a cryostat probe. To do so, the cantilever must be carefully detached from the piece of ceramic plate it is fabricated on, electrical leads must be attached, and a sample must be mounted using the smallest possible application of a suitably chosen vacuum grease.

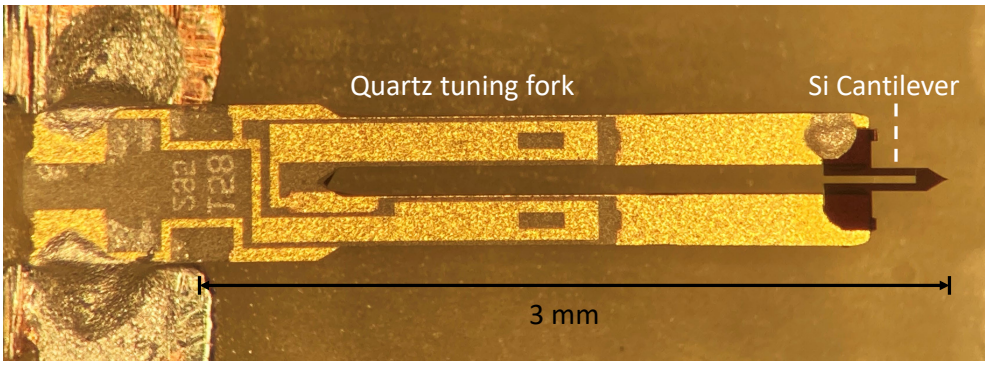

Figure 4.7: The Akiyama probe cantilver and tuning fork assembly.

The entire assembly has a very small form factor that can fit inside virtually any external magnet bore, and the measurement is best suited to samples that are only 10s of nanograms. The quartz tuning fork itself is approximately 2.5 mm in length and 100 μm thick, while the silicon cantilever is exactly 310 μm long and 3.7 μm thick. The coupled system of the tuning fork plus cantilever has a lowest vibrational mode at a frequency of 45-50 kHz which corresponds to motion of the cantilever tip out of the plane of the cantilever [25]. The precise location of this resonance frequency is extremely sensitive to any changes to the cantilever, in particular, the anisotropic energy cost associated with displacing a tip-mounted sample in a finite magnetic field. This sensitivity provides the basis for its use in measuring the magneotropic coefficient and probing the curvature of the free energy.

In order to understand the energetics of the vibrating cantilever plus sample system, we adopt

a harmonic approximation for its Lagrangian. At zero field we may write such a Lagrangian in terms of an effective bending stiffness K and moment of inertia I:

$$\mathcal{L}(\Delta\theta, \dot{\Delta\theta}) = \frac{I}{2}(\dot{\Delta\theta})^2 - \frac{K}{2}(\Delta\theta)^2, \tag{4.34}$$

Where the positional variable $\Delta\theta$ is the angular displacement of the cantilever tip from its equilibrium position. A more careful treatment, which approximates the cantilever as a one-end-fixed Bernoulli-beam with appropriate boundary conditions and derives the effective stiffness in terms of the elastic moduli of silicon appears in the supplemental information of ref. [26], but those details are not essential to our analysis, and indeed we can typically ensure a harmonic limit of operation $\Delta\theta \ll 1$ via our control of the driving voltage amplitude, and by appropriately limiting the size of sample itself, thereby constraining the magnetic torque-driven displacement of the cantilever tip.

When an external field is applied, there will be an additional energetic contribution corresponding to the magnetic free energy cost of displacing the sample from $\theta \to \theta + \Delta\theta$, which can be appropriately Taylor-expanded in terms of the thermodynamic variables of the preceding section:

$$F(\theta + \Delta\theta) - F(\theta) = \Delta\theta \left.\frac{\partial F}{\partial \theta}\right|_{\theta} + \frac{(\Delta\theta)^2}{2} \left.\frac{\partial^2 F}{\partial \theta^2}\right|_{\theta} + \ldots, \tag{4.35}$$

$$= -\tau\Delta\theta + \frac{k}{2}(\Delta\theta)^2 + \ldots. \tag{4.36}$$

Thus, in the harmonic approximation up to quadratic order in $\Delta\theta$, the zero-field Lagrangrian 4.34 is modified:

$$\mathcal{L}(\Delta\theta, \dot{\Delta\theta}) = \frac{I}{2}(\dot{\Delta\theta})^2 + \tau\Delta\theta - \frac{K+k}{2}(\Delta\theta)^2. \tag{4.37}$$

The Euler Lagrange equation: $\partial_t(\partial\mathcal{L}/\partial\dot{\Delta\theta}) = \partial_{\Delta\theta}\mathcal{L}$, may be used to derive an equation of motion for the vibrating cantilever:

$$I\ddot{\Delta\theta} = \tau - (K+k)\Delta\theta, \tag{4.38}$$

Due to the finite torque on the cantilever, its tip is shifted from the zero-field equilibrium position by a fixed amount as illustrated below:

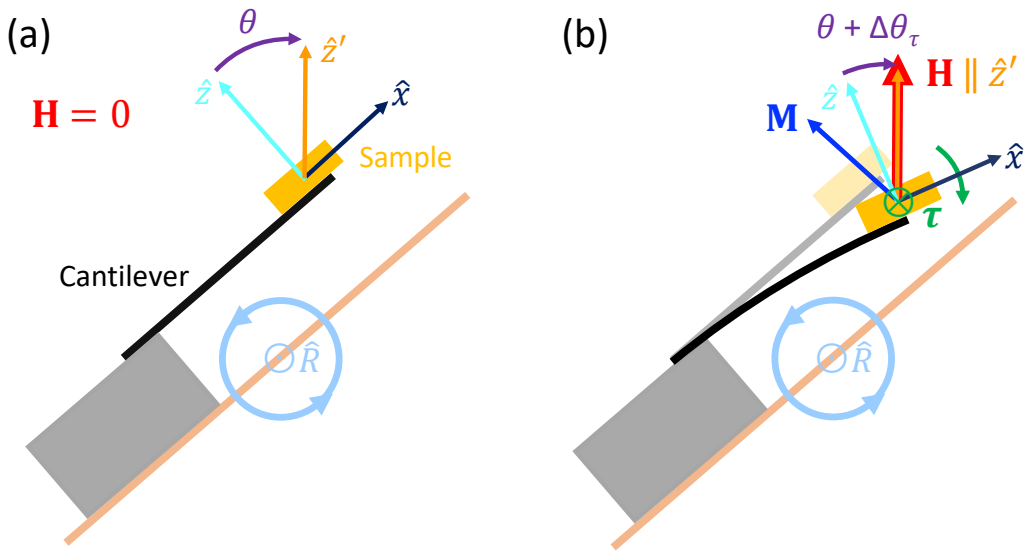

Figure 4.8: $\hat{z}'$ is the axis of the cryostat solenoid in fixed, lab-centric coordinates, defining the direction of any experimentally applied fields. $\hat{x}, \hat{z}$ are axes for sample-centric coordinates that rotate with the sample. (a) shows the experimental cantilever arrangement in zero applied field. $\hat{R}$ is a vector defining the axis of rotation for the entire cantilever apparatus, which provides the experimental adjustment of θ as measured between $\hat{z}$ and $\hat{z}'$. In (b), a uniform field $\mathbf{H}$ is applied, generating a finite sample magnetization $\mathbf{M}$, and therefore a magnetic torque τ, which shifts the sample orientation $\theta \to \theta + \Delta\theta_\tau$ as determined by 4.40. The cantilever oscillates approximately harmonically about this new equilibrium position.

To solve the equation of motion, we make the assumption that the angular shift can be decomposed into the sum of a constant time-indept. part ($d\Delta\theta_\tau/dt = 0$), due to the torque, and a time varying, sinusoidally-oscillating part:

$$\Delta\theta = \Delta\theta_\tau + \widetilde{\Delta\theta} e^{i\omega t}, \tag{4.39}$$

whereby we can solve the equation of motion 4.38 to obtain equations for the time-indept. torque shift and the frequency of oscillation:

$$\Delta\theta_\tau = -\frac{\tau}{K+k}, \tag{4.40}$$

$$\omega^2 = (\omega_0 + \Delta\omega)^2 = \frac{K+k}{I}, \tag{4.41}$$

in terms of $\omega_0 = K/I$. From the above expression, we can deduce that up to linear order in k/K, the ZF frequency, $f_0 = \omega_0/2\pi$, of the cantilever is shifted by an amount Δf that is directly

proportional to the magnetotropic coefficient k:

$$\frac{\Delta f}{f_0} = \frac{k}{2K}, \tag{4.42}$$

while the effect of the magnetic torque on such a measurement is merely a static and proportional deflection of the cantilever. Thus, by adiabatically tracking the resonance frequency of the sample-mounted cantilever as a function of applied field magnitude and angle, we can obtain a directly proportional measure of the magnetotropic coefficient and thus the curvature of the sample's magnetic free energy.

4.2.3 Pulsed field versus DC field operation

The measurement technique is amenable to either DC or pulsed magnetic fields, although the precise means of obtaining $\Delta f(T, H, \theta)$ differs in either case. While the former is well suited to measurements where any of H, T, θ are continuously varied, the nature of pulsed-field data acquisition, while extremely fast, precludes anything other than H sweeps at fixed θ, T, meaning that evolution of k as function of these other parameters must be inferred by interpolating a sufficiently dense set of $k(H)$.

4.2.3.1 DC fields

DC-field magnetotropic measurements were performed using the 18/20 Tesla General Purpose Superconducting Magnet SCM2 at the National High-Magnetic Field Lab in Tallahassee Florida. For a more detailed description, refer to Section 4.1.3. Because we cannot rotate the field itself in this arrangement, we rely on the rotator probe to provide continuous angular dependence.

Tracking the resonance frequency relies on a custom software-implemented phase-locked-loop developed by K. A. Modic et. al [25], provided to us by collaborators Arakdy Shekter and R. D. McDonald. This software functions by performing a frequency scan through the normal mode resonance. We can model the piezo-voltage response $V(t)$ of the cantilever at a driving frequency ω, using the classical equation of motion for the damped harmonic oscillator at resonant frequency

ω_0 with a sinusoidal driving force $\omega^2 V_0 \sin(\omega t)$:

$$\frac{d^2V}{dt^2} + \Gamma\frac{dV}{dt} + \omega_0^2 V = \omega^2 V_0 \cos(\omega t), \tag{4.43}$$

where Γ is a damping parameter, representing the characteristic ring-down time of the oscillator, defined in terms of the Q factor as $Q = \omega_0/\Gamma$. This equation has a steady state solution:

$$V(t) = \frac{V_0\omega^2}{\left[(\omega-\omega_0)^2 + (\Gamma\omega)^2\right]^{1/2}} \cos(\omega t + \varphi), \tag{4.44}$$

where the phase of oscillation is $\varphi = \tan^{-1}[\Gamma\omega/(\omega^2 - \omega_0^2)]$. Denoting the amplitude of this oscillation by $|\tilde{V}|$, such that $V_0(t) = |\tilde{V}|\cos(\omega t + \varphi)$ we can also write this equation in terms of the in- and out-of-phase components of the oscillation, i.e. $V = V_x \cos(\omega t) + V_y \sin(\omega t)$ where:

$$V_x = |\tilde{V}|\cos\varphi, \tag{4.45}$$

$$V_y = -|\tilde{V}|\sin\varphi. \tag{4.46}$$

The measurement software ramps the drive frequency continuously and uses a high-frequency lock-in amplifier to measure both the in-phase (V_x) and out-of-phase (V_y) amplitudes of the piezo response to fit the response of the cantilever to the Lorentzian line-shape of 4.44 and thereby extract the resonant frequency ω_0 (f_0), as a function of the experimental parameters (T, H, θ). For additional details, refer to [25] .

4.2.3.2 Pulsed fields

Pulsed-Field measurements were performed using the 65 Tesla magnet at the National High-Magnetic Field, Pulsed-Field-Facility (PFF) at Los Alamos National Laboratory. The PFF cryostats are equipped with a closed-cycle He^3 charcoal sorption pump system to access temperatures as low as 300 mK. We rely on a rotator probe to obtain angle dependence at a discrete set of angles.

A pulsed field resonant torsion measurement relies on 2 principles, namely (1) that even when active driving of the cantilever motion ceases, the cantilever has a sufficiently high Q-factor that it will continue to ring-down without losing a majority of its oscillation amplitude over the duration

of a magnetic field pulse $H(t)$, and (2) the period of oscillation is sufficiently small compared to the duration of the pulse, such that changes in the cantilever resonance frequency can be considered adiabatic, and it may be assumed that the cantilever continues to resonate at the instantaneous resonance frequency $f(H)$ as the field is swept. The 65 T magnet at the PFF produces pulses with a total duration of approximately 80 ms, reaching peak field in $<$ 10 ms, see Fig. 4.9. At cryogenic temperatures, a pristine cantilever will oscillate at approximately 45-50 kHz, with a Q factor of 1.0-1.5$\times 10^4$, thus it will generally oscillate for at least 200 ms, an entire order of magnitude larger than the time it takes for peak field to be reached. Additionally, the period of cantilever oscillation, $\sim$ 20 μs is a full three orders of magnitude less than the rise time of the pulse, justifying the assumption (2) of adiabaticity.

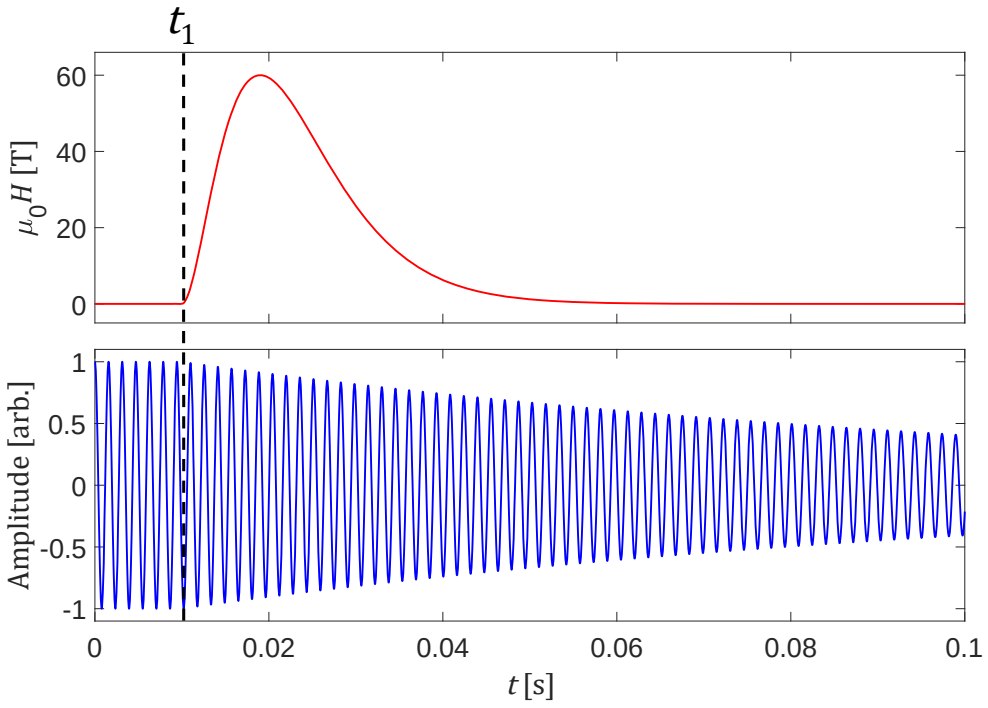

Figure 4.9: The upper panel shows a typical 60 T field pulse over 80 ms beginning at time t_1, indicated via a dotted line. The lower panel illustrates a synchronous cantilever ring-down, where the driving stops at time t_1. Note that the period of oscillation has been exaggerated for conceptual clarity of the figure, and the actual frequency of oscillation is $\sim$10 times higher than pictured.

As illustrated in 4.9, an actual pulsed field measurement proceeds as follows: (1) for times $t < t_1$ a sinusoidal AC voltage source is used to resonantly drive the cantilever at its zero-field resonance frequency $f_0 = f(H = 0)$; (2) at time t_1, the field pulse starts, and driving of the cantilever simultaneously stops; (3) for times $t > t_1$ the cantilever rings-down, continuing to resonate at its instantaneous resonance frequency $f(H)$, tracking the field evolution of f; (4) A time-resolved, moving-window FFT is used to determine $\Delta f(H) = f(H) - f_0$; (5) by repeating the measurement at a full set of angles, and at other temperatures, we can interpolate to find $\Delta f(\theta)$ at a particular fixed H, or determine the evolution as a function of T.

4.2.4 Complications, details, minutia

There are a few sizeable systematic effects which can distort the measured $\Delta f(\theta)$ from its expected behavior. Gravity and field inhomogeneity, perhaps the most obvious culprits for non-ideal behavior, certainly have an effect on the cantilever, as discussed in detail in the supplemental information of [26], but their effect on the cantilever deflection and frequency shift is typically dwarfed by the magnetotropic response of the sample itself even at moderate fields. The systematics we do consider are experimental misalignment of the cantilever, which is heavily effected by human error, and cantilever anharmonicity, which can become relevant if the applied field strength, and therefore field-induced deflections, become large enough. First and foremost, we discuss the various types of misalignment of the experimental apparatus, and what does and does not contribute to spurious effects.

4.2.4.1 Cantilever misalignment

Experimentally, we control θ by rotating the cantilever stage. In the lab frame coordinates the generator corresponding to these rotations is ∂_θ or $\partial_{\vartheta(\hat{R})}$, where $\hat{R}$ is the unit vector defining the rotational axis of the cantilever stage, and the angular derivative with respect to an arbitrary

vector direction $\hat{n}'$ is given by:

$$\partial_{\vartheta(\hat{n}')} = \hat{n}' \cdot (\hat{\mathbf{r}} \times \boldsymbol{\nabla}), \tag{4.47}$$

$$= [n_2' \cos\phi - n_1' \sin\phi]\partial_\theta + [n_3' - (n_1' \cos\phi + n_2' \sin\phi)\cot\theta]\partial_\phi. \tag{4.48}$$

In writing down the harmonic cantilever Lagrangian, the magnetotropic term k is precisely the curvature of the free energy as the sample is displaced in the plane of vibration of the cantilever, as defined by the unit normal vector $\hat{n}$. Hence, the partial derivative relevant to the magnetotropic response is $\partial^2_{\vartheta(\hat{n})} F(\mathbf{H})$, given that the generator corresponding to displacements of the sample in the cantilever vibrational plane is $\partial_{\vartheta(\hat{n})}$.

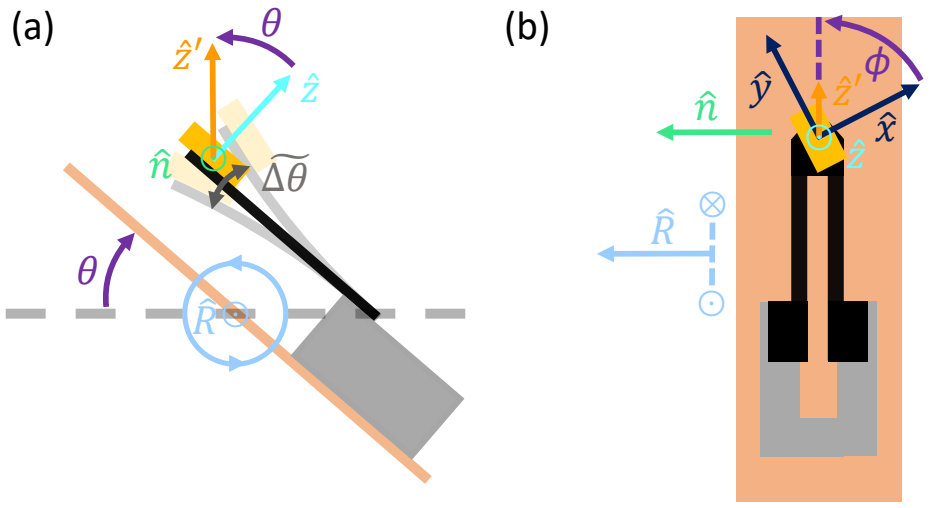

Figure 4.10: We illustrate the side (a) and top (b) views of the cantilever stage with ideal alignment. $\hat{n}$ is a unit normal vector defining the plane of vibration of the cantilever and $\hat{R}$ is a unit normal vector defining the stage rotational axis. For generality, we place the sample on the cantilever such that crystallographic sample-centric coordinates $\hat{x}, \hat{y}$ are rotated by an angle of ϕ with respect to the vibrational/rotational planes.

In the situation of perfect alignment, illustrated in 4.8 and 4.10, $\hat{n}$ and $\hat{R}$ are exactly identical. In sample-centric coordinates we may write:

$$\hat{R} = \hat{n} = (-\sin\phi,\ \cos\phi,\ 0), \tag{4.49}$$

$$\mathbf{H} = (\sin\theta\cos\phi,\ H\sin\theta\sin\phi,\ H\cos\theta)\,. \tag{4.50}$$

Crucially, the equivalence of $\hat{n}, \hat{R}$ implies that $\partial_{\vartheta(\hat{n})} = \partial_{\vartheta(\hat{R})} = \partial_\theta$, which means that our measurement is sensitive to the curvature of F in precisely the same angular direction $\hat{\theta}$ we are varying by rotating the stage.

As a first case for potential misalignment, consider the situation in which the ZF equilibrium orientation of the is not parallel to the base of the rotation stage, but instead shifted by some amount θ_0, as illustrated in Fig. 4.11 (a). Keeping the rotator coordinate labeled as θ, and considering sample-centric coordinates, this misalignment leaves $\hat{R}$ unchanged, but modifies the field direction, so that we have:

$$\hat{R} = \hat{n} = (-\sin\phi,\ \cos\phi,\ 0), \tag{4.51}$$

$$\mathbf{H} = (\sin(\theta+\theta_0)\cos\phi,\ H\sin(\theta+\theta_0)\sin\phi,\ H\cos(\theta+\theta_0))\,. \tag{4.52}$$

The vectors $\hat{n}$ and $\hat{R}$ remain completely identical, thus we are still measuring curvature in the same angular direction: $\partial^2_\theta F(H, \theta+\theta_0, \phi)$, the only difference being that our experimental quantities reflect a trivial redefinition of θ by the addition of θ_0.

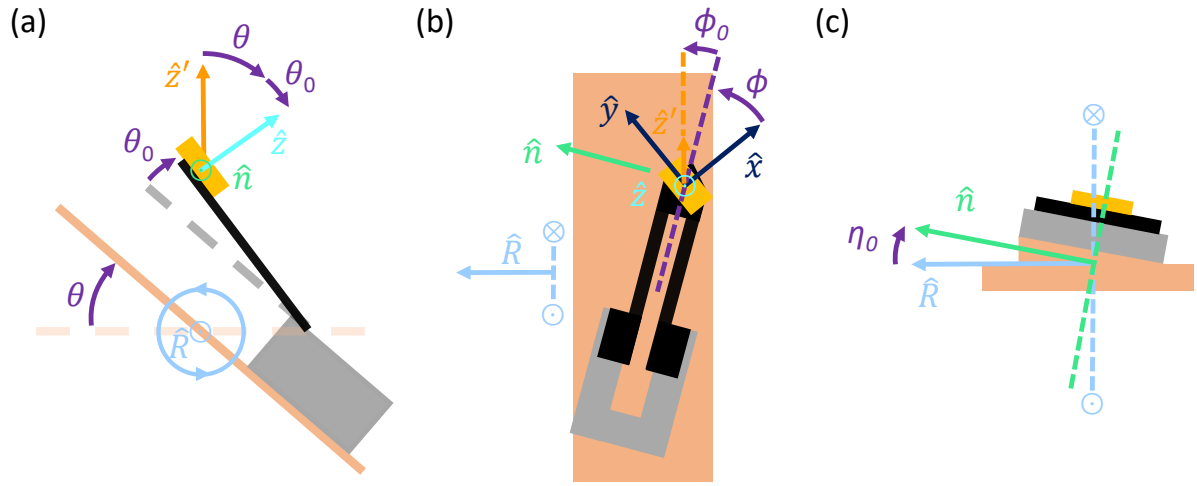

Figure 4.11: Panels (a), (b), & (c) illustrate the cases of θ, ϕ, and η misalignment, respectively, as discussed in this section.

Suppose instead, the cantilever is misaligned in the ϕ direction by some angle ϕ_0, i.e. we had mounted the cantilever such that its length is no longer running parallel to the base of the rotation

stage as pictured in Fig. 4.11 (b). For this case of misalignment, both $\hat{R}$ and the field are modified in sample-centric coordinates:

$$\hat{R} = (-\sin(\phi+\phi_0), \cos(\phi+\phi_0), 0), \tag{4.53}$$

$$\mathbf{H} = (\sin\theta\cos(\phi+\phi_0),\ H\sin\theta\sin(\phi+\phi_0),\ H\cos\theta)\,. \tag{4.54}$$

Although $\hat{R}$ and $\hat{n}$ are no longer parallel, angular variations along these axes still correspond to rotations by the same polar angle θ, and $\partial_{\vartheta(\hat{n})} = \partial_{\vartheta(\hat{R})} = \partial_\theta$. Even with this ϕ misalignment, we are still measuring curvature in the same angular direction: $k = \partial_\theta^2 F(H, \theta, \phi+\phi_0)$, this time with a trivial redefinition of ϕ.

The last case of potential mislaignment to consider is that in which the cantilever assembly is not sitting flush with the stage, but tilted at an angle η as pictured in Fig. 4.11 (c). In sample-centric coordinates we have:

$$\hat{R} = (-\cos\eta\sin\phi, \cos\eta\cos\phi, \sin\eta), \tag{4.55}$$

$$\mathbf{H} = (\sin\theta\cos\phi + \cos\theta\sin\phi\sin\eta,\ H\sin\theta\sin\phi - \cos\theta\cos\phi\sin\eta,\ H\cos\theta\cos\eta)\,. \tag{4.56}$$

Thus in computing the magneotropic response, there are two caveats to worry about: (1) the free energy is modified:

$$F(H,\theta,\phi) = F(H_x(\theta,\phi,\eta), H_y(\theta,\phi,\eta), H_z(\theta,\phi,\eta)), \tag{4.57}$$

and (2) the angular derivative corresponding to vibrational displacements of the cantilever is non-trivially modified: $\partial_{\vartheta(\hat{n})} = \cos\eta\partial_\theta + \sin\eta\partial_\phi$, resulting in a measured magnetotropic response:

$$k(\theta,\phi) = \frac{\partial^2 F(\theta,\phi)}{\partial\vartheta(\hat{n})^2} = \cos\eta\frac{\partial}{\partial\theta}\left(\cos\eta\frac{\partial F}{\partial\theta} + \sin\eta\frac{\partial F}{\partial\phi}\right) + \sin\eta\frac{\partial}{\partial\phi}\left(\cos\eta\frac{\partial F}{\partial\theta} + \sin\eta\frac{\partial F}{\partial\phi}\right), \tag{4.58}$$

Such a magneto-tropic coefficient is no longer sampled along a particular slice of the free energy corresponding to a fixed plane, but rather a conical section intersecting F.

4.2.4.2 Extensions to cantilever Lagrangian

We now consider eqn. 4.37 with the addition of a leading order anharmonicity term $(\Delta\theta)^3 W/6$ and include the third-order contribution of the Taylor-expanded free energy:

$$\mathcal{L}(\Delta\theta, \dot{\Delta\theta}) = \frac{I}{2}\left(\dot{\Delta\theta}\right)^2 + \tau\Delta\theta - \frac{K+k}{2}(\Delta\theta)^2 - \frac{W + \frac{\partial^3 F}{\partial\theta^3}}{6}(\Delta\theta)^3, \tag{4.59}$$

To derive a corrected equation of motion for the vibrating cantilever:

$$I\ddot{\Delta\theta} = \tau(\theta) - (K + k(\theta))\Delta\theta - \frac{(\Delta\theta)^2}{2}\left(W + \frac{\partial k}{\partial\theta}\right), \tag{4.60}$$

As before, we make the assumption: $\Delta\theta \approx \Delta\theta_\tau + \widetilde{\Delta\theta} e^{i\omega t}$, ignoring higher harmonics of ω in the oscillatory motion, obtaining:

$$I\ddot{\Delta\theta} = -\tau - (K-k)\Delta\theta - \frac{1}{2}\frac{\partial k}{\partial\theta}(\Delta\theta)^2, \tag{4.61}$$

$$-I\omega^2\widetilde{\Delta\theta}e^{i\omega t} = -\tau - (K-k)\left[\Delta\theta_\tau + \widetilde{\Delta\theta}e^{i\omega t}\right] - \frac{1}{2}\left(W + \frac{\partial k}{\partial\theta}\right)\left[(\Delta\theta_\tau)^2 + 2\Delta\theta_\tau\widetilde{\Delta\theta}e^{i\omega t} + (\widetilde{\Delta\theta})^2 e^{2i\omega t}\right], \tag{4.62}$$

We drop the most quickly oscillating terms which are associated with higher harmonic components of the motion, and drop those terms which are higher than second order in $\Delta\theta$, obtaining the 2 more correct equations:

$$\tau = -(K+k)\Delta\theta_\tau - \frac{1}{2}\left(W + \frac{\partial k}{\partial\theta}\right)(\Delta\theta_\tau)^2, \tag{4.63}$$

$$I(\omega_0 + \Delta\omega)^2 = (K+k) + \left(W + \frac{\partial k}{\partial\theta}\right)\Delta\theta_\tau \tag{4.64}$$

Examining the first equation, we obtain the valid solution:

$$\Delta\theta_\tau = -\frac{K+k}{(W + \partial k/\partial\theta)}\left(1 - \sqrt{1 - 2\tau\frac{W + \partial k/\partial\theta}{(K+k)^2}}\right), \tag{4.65}$$

We treat the derivative correction as a perturbation via the small parameter: $x = (W + \partial k/\partial\theta)/(K + k)$, to derive corrections to the naive result $-\Delta\theta_\tau = a_0 = \tau/(K+k)$:

$$\Delta\theta_\tau = -\frac{1 - \sqrt{1 - 2a_0 x}}{x} = -\left(a_0 + \frac{a_0^2}{2}x + \frac{a_0^3}{2}x^2 + \frac{5a_0^4}{8}x^3 + \dots\right) \tag{4.66}$$

The second corrected equation of motion gives the frequency shift to linear order:

$$\begin{aligned} I\omega_0^2\left(1+2\frac{\Delta\omega}{\omega_0}\right) &= K+k+\left(W+\frac{\partial k}{\partial\theta}\right)\Delta\theta_\tau, \\ \frac{\Delta\omega}{\omega_0} &= \frac{1}{2K}\left[k+\left(W+\frac{\partial k}{\partial\theta}\right)\Delta\theta_\tau\right], \\ &= \frac{k}{2K}-\frac{K+k}{2K}x\left(a_0+\frac{a_0^2}{2}x+\frac{a_0^3}{2}x^2+\dots\right), \end{aligned} \tag{4.67}$$

Plugging in for the leading order torque shift and small parameter we obtain:

$$\frac{\Delta\omega}{\omega_0} = \frac{k}{2K}-\frac{\tau}{K(K+k)}\left(W+\frac{\partial k}{\partial\theta}\right). \tag{4.68}$$

Thus if τ/K becomes large enough, i.e. the cantilever deflection is large enough that the magnetic torque and elastic energy of the cantilever become comparable in magnitude, cantilever anharmonicity and higher angular derivatives of k can distort the measured frequency shift, and eventually the harmonic approximation breaks down entirely. As a consequence, the condition $\tau(H)/K \ll 1$ places an upper limit on the size of samples such a measurement can accommodate at very high fields.

4.2.5 Finite mean curvature

The magnetization is antisymmetric with respect to the applied field, i.e. $\mathbf{M}(-\mathbf{H}) = -\mathbf{M}(\mathbf{H})$ thus the magnetic torque $\tau = \hat{n}\cdot[\mathbf{M}\times\mathbf{H}]$, magnetotropic coefficient $k = -\partial\tau/\partial\theta$, and indeed all higher order θ-derivatives of F must be even functions of the field. This implies a π-periodicity of τ and k, i.e. invariance of such measurements for every 180 degrees of rotation. Furthermore if we integrate $k(\theta)$ over one π-period, we should obtain:

$$k_0 = \frac{1}{\pi}\int_{\theta_0}^{\theta_0+\pi} k(\theta)\ d\theta = \frac{1}{\pi}\tau(\theta)\Big|_{\theta=\theta_0}^{\theta_0+\pi} = 0. \tag{4.69}$$

The mean curvature k_0 equals 0 as a direct consequence of the π-periodicity of $\tau(\theta)$. This seemingly generic fact does not appear to be true in all scenarios however, and as pictured in Fig. 8.1, certain magnetotropic measurements have exhibited a nonzero negative mean curvature k_0 that grows monotonically with the applied field.

At least for cantilever motion that is still approximately sinusoidal, the leading order effect of anharmonicity, as described by Eqn. 4.68 cannot accounted for a nonzero k_0, given that its constituents are still even functions of $\mathbf{H}$. Alternatively, one could integrate the expressions, 4.32, 4.33, finding that a nonzero k_0 implies a magnetization that is not field odd, i.e. $M(\mathbf{H})+M(-\mathbf{H}) \neq 0$. Field inhomogeneity can perhaps explain some of this deviation, given that the rotator does not perfectly rotate the sample about a single point in space, thus a variation in the field δH between the configuration for some angles θ_0 and $\theta_0 + \pi$ could account for a portion of the magnetotropic response that is order $\sim (\delta H/H)^2 k(H)$.

η misalignment of the cantilever, as described in Eqns. 4.55−4.57, can additionally account for some amount of mean curvature, i.e., the distorted magneotropic coefficient of 4.58, can in fact produce a finite positive or negative integral over one π-period. However, while the mean curvature due to misalignment does grow monotonically with applied field, it produces a mean curvature that is order $\sim \eta^2 k$, thus the misalignment angle η would have to be particularly egregious to produce a sizeable k_0.

The observed size of $k_0(H)$ in magnetotropic measurements using Na_2IrO_3 and $CsErSe_2$ far exceeds what can be accounted for by either field inhomegenity, or η misalignment, even while the fractional frequency shift $\Delta\omega/\omega_0$ and associated fractional torque τ/K remain valid small parameters. The discrepancy poses an intriguing puzzle. Thus far however, we have only considered a free energy which is analytical over the whole domain of θ.

The free energy is necessarily a continuous function of $F(\mathbf{H})$, but in the case of a magnetic phase transition, it need not be analytic as a function of (H, θ). Although there is still much theoretical, experimental, and simulation work before this outstanding problem can resolved in any satisfyingly rigorous manner, we can explain why a negative mean curvature may be present in the vicinity of a phase transition. Consider the generic example of a material with 2 magnetic phases, denoted I & II, with boundaries at two critical angles $0 < \theta_{c1} < \theta_{c2} < \pi$, with phase II existing for angles that fall between θ_{c1}, θ_{c2}. There are clearly at least 2 critical angles, because we must return to the same phase in a single π-rotation. We can write the integral of $k(\theta)$ again:

$$k_0 = \frac{1}{\pi}\int_0^{\pi} k(\theta)\ d\theta = \frac{1}{\pi}\left[\int_{\theta_{c2}-\pi}^{\theta_{c1}} k_{\mathrm{I}}(\theta)\ d\theta + \int_{\theta_{c1}}^{\theta_{c2}} k_{\mathrm{II}}(\theta)\ d\theta\right], \tag{4.70}$$

$$= \frac{1}{\pi}\left[\tau_{\mathrm{I}}(\theta_{c1}) + \tau_{\mathrm{II}}(\theta_{c2}) - \tau_{\mathrm{I}}(\theta_{c2}) - \tau_{\mathrm{II}}(\theta_{c1})\right], \tag{4.71}$$

If $\tau(\theta)$ is discontinuous at either critical angle, i.e. $\lim_{\Delta\theta\to 0}\tau_I(\theta_{c1}-\Delta\theta) \neq \lim_{\Delta\theta\to 0}\tau_{II}(\theta_{c1}+\Delta\theta)$, then this integral will be nonzero, resulting in a finite mean curvature. Thus a free energy whose slope dFd/θ is discontinuous at a phase transition can produce a finite mean curvature. In this scenario, it is likely that the delta-function-like anomaly produced in $k(\theta)$ would be too sharp for a magneotropic measurement to resolve clearly.

Chapter 5

Giant Thermal Magneto-conductivity in $CrCl_3$, quantifying spin-phonon scattering

5.1 Introduction

Transport measurements are a pillar of experimental condensed matter physics. In insulating crystalline systems the thermal conductivity, $\kappa(T)$, ranks as one of the most valuable probes for investigating the low-energy excitations [55]. Unlike thermal equilibrium quantities such as the specific heat, $c(T)$, $\kappa(T)$ is a steady-state transport property and thus contains fundamental information about the itinerant characteristics of a system, most notably the relaxation times and scattering strengths of the low-energy excitations. In the field of insulating quantum magnets, low-dimensional spin systems may host a wide range of exotic ground states and $\kappa(T)$ has long been one of the most important probes of their unconventional spin excitations [10, 11, 12, 13, 24, 56, 57, 58, 14]. Because the lattice phonons invariably constitute a strong and relatively well-characterized contribution to thermal transport, $\kappa(T)$ measurements offer particular insight into the dominant spin-phonon scattering mechanisms. Even in materials whose thermal conductivity is phonon-dominated, meaning that there is no significant heat transport due to coherent magnetic modes, a strong field-dependence of $\kappa(T)$ may still be present due to destructive effects of the spin sector on the phonon transport.

$CrCl_3$ is an insulating, layered, honeycomb-lattice compound and has attracted considerable recent attention from two independent lines of research. One concerns the "candidate Kitaev" material α-$RuCl_3$ [59, 60, 61, 62, 63], whose proximity to Kitaev physics may be gauged from the nature of its magnetic excitations [31, 64, 65, 66, 67]. While $\kappa(T)$ measurements have not

been able to provide conclusive evidence of fractionalized fermionic spin modes in α-$RuCl_3$, one of the primary reasons why the issue remains open concerns the role and indeed the nature of spin-phonon scattering, which is manifestly strong over a wide range of temperatures [14, 68]. $CrCl_3$ is the 3d transition-metal structural analog of α-$RuCl_3$, and as such represents the latter material in the absence of significant spin-orbit coupling. Although one may fear that this removal of Kitaev character removes any connection between the two systems, we will show here that $CrCl_3$ presents a test case for spin-phonon scattering effects that are at least as strong as any comparable phenomena in α-$RuCl_3$.

The second avenue leading to $CrCl_3$ as a key material to understand is its position in the structural series CrX_3, where X = Cl, Br, I is a halide. Structurally, the chromium trihalides are van der Waals materials, allowing them to be cleaved easily and prepared in mono- or few-layer forms that show strong differences in their physical properties. Magnetically, the honeycomb layers have ferromagnetic (FM) in-plane interactions and indeed both CrI_3 and $CrBr_3$ are bulk ferromagnets. This magnetic character has therefore promoted a keen interest in spin and lattice control in the context of topological magnonics [7], spintronics, and magnetoelectronics [69, 70]. $CrCl_3$ is a historical "mixed FM/AF" system, with antiferromagnetic (AF) interlayer interactions ensuring an AF ground state of anti-aligned FM layers [71, 72, 73, 74, 75], and because of the rather low field scale ($\mu_0 H_s \simeq 2$ T, independent of direction) for complete spin polarization is an excellent candidate for studying magnetic-field effects on spin and lattice transport.

In Fig. 5.1 we show our key experimental result, that the in-plane thermal conductivity of $CrCl_3$ is greatly enhanced by a magnetic field. We comment for clarity that by "in-plane" we refer to measurements of $\kappa(T)$ performed with the temperature gradient, ∇T, oriented in the ab-plane and with the field also applied in the plane ($H \parallel \nabla T$). Qualitatively, this field-dependence of $\kappa_{xx}(T)$ resembles the behavior typical of magnetoresistance in magnetic conductors, where the electrical conductivity often increases as the field is increased [76]; this effect is caused by the field-induced reduction of the spin-dependent scattering and is often most prominent in the vicinity of the magnetic ordering transition. In $CrCl_3$, the origin of this giant thermal magnetoresistance

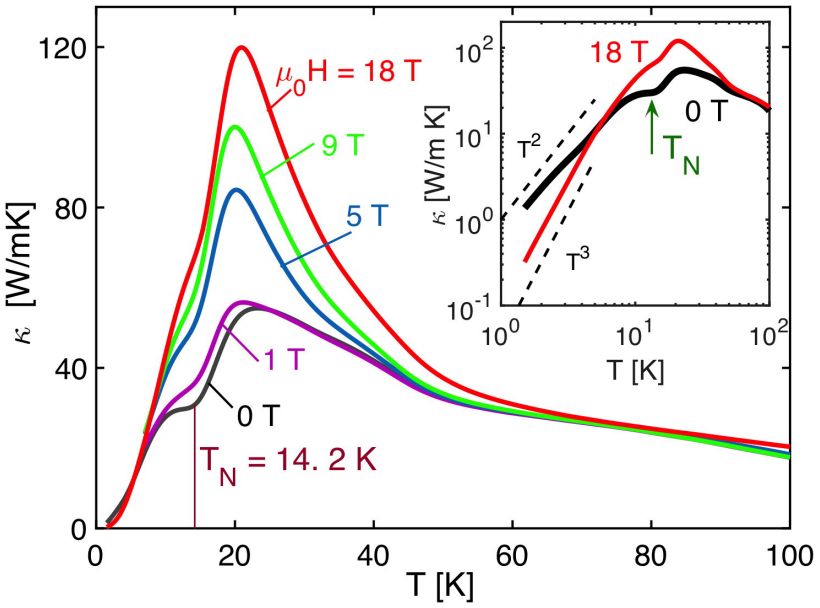

Figure 5.1: κ_{xx} shown as a function of T for different values of the magnetic field applied parallel to the temperature gradient in the ab plane. Inset: $\kappa_{xx}(T)$ shown on a logarithmic scale for comparison of the low-T data with the power-law forms $\kappa(T) \propto T^2$ and T^3.

lies in the very strong field-induced suppression of the spin-phonon scattering, and one may also observe in Fig. 5.1 that it is particularly prominent at the ordering transition (T_N). Quantitatively, the phenomenon is anomalously large and is particularly unusual in that it extends over essentially the entire range of temperatures shown in Fig. 5.1. Here we will show that it can be modelled accurately with a minimal number of assumptions and empirical parameters.

In many cases, the phonon thermal conductivity is well captured by the highly refined Debye-Callaway (DC) model [44, 77], in which all of the most important mechanisms for phonon scattering are considered over a wide range of temperatures. One obtains the form

$$\kappa_{\rm ph} = \frac{k_B^4}{2\pi^2 v_s \hbar^3} T^3 \int_0^{\Theta_D/T} \frac{x^4\, e^x}{(e^x-1)^2}\, \tau(\omega, T)\, dx, \tag{5.1}$$

where ω is the phonon frequency, Θ_D is the Debye temperature, v_s is a characteristic average phonon velocity, and the integration variable is $x = \hbar\omega/k_B T$. In the relaxation-time approximation, it is assumed that all possible scattering mechanisms contribute independently to the phonon scattering

time, $\tau(\omega, T)$, and hence

$$\tau^{-1} = \tau_b^{-1} + \tau_{pd}^{-1} + \tau_U^{-1} + \tau_{\rm res}^{-1}, \tag{5.2}$$

where the four relaxation times account respectively for boundary scattering, point-defect scattering, Umklapp scattering, and resonant scattering due to impurities, magnetic excitations, or other collective modes. A similar formalism can be adopted for the direct contributions to $\kappa(T)$ of well-defined magnon modes. This type of model has been used to obtain a quantitative account of the thermal conductivity in a number of low-dimensional spin systems where both the spin excitations and their phonon-scattering effects, appearing in the $\tau_{\rm res}^{-1}$ term, can be characterized accurately [11, 78, 24, 13].

Despite the experimentally verified success of the DC model for certain cases, in practical applications the model of Eq. (5.2) requires at minimum seven to ten fitting parameters to reproduce even rather smoothly varying $\kappa(H, T)$ curves. The microscopic implications of each term are often very difficult to verify independently, unless the respective fitting parameters can be compared among closely related materials (for example by doping or elemental substitution). Most importantly for the $CrCl_3$ problem, there are no well-defined spin excitations over most of the (H, T) phase diagram, and hence no possibility of describing the giant spin-phonon scattering within a $\tau_{\rm res}^{-1}$ term. Clearly the form of this term in Eq. (5.2) is too restrictive to capture the rich spectrum of possible interactions between the phonons and magnetic excitations of a quantum magnet, particularly if the latter are fractionalized. Thus we will introduce a more general approach to modelling the thermal conductivity of a magnetic insulator, a task in which we will be phenomenological but quantitative.

The focus of our contribution is to describe the heat conduction of magnetic insulators in the common situation where this is governed mostly by phonons, but subject to a spin-phonon scattering to which multiple mechanisms may contribute. In such a case, it would be highly desirable to have a method of understanding the magnetic scattering of phonons without invoking either the microscopic details of the scattering mechanism or system-specific characteristics such

as the phonon and magnon (or spinon) dispersion relations. Here we present a phenomenological model to quantify the T- and H-dependence of κ_{xx}, for the worked example of $CrCl_3$, by considering the phonon heat conduction in the presence of scattering by magnetic degrees of freedom. The parameters determined empirically in our model enable us to quantify the dominant scattering mechanisms regardless of the energy scales of the phonons and of the magnetic excitations.

The structure of this article is as follows. In Sec. 6.2 we summarize briefly our samples and experimental methods. In Sec. 5.3 we show the results of our $\kappa(H,T)$ observations at all measured fields and compare these with measurements of the magnetization and specific heat. In Sec. 5.4 we present the details of our empirical modelling procedures for the physically different regimes and extract the quantities required to describe spin-phonon scattering in $CrCl_3$. Section 5.5 provides a discussion and conclusion.

5.2 Material and Methods

Thin, purple, plate-like single crystals of $CrCl_3$ were grown by chemical vapor tranport [79, 18]. $CrCl_3$ is known [80] to have a rhombohedral low-temperature crystal structure composed of hexagonal lattices of Cr^{3+} ions in the ab plane, whose ABC $\hat{c}$-axis stacking is ensured by only rather weak (van der Waals) structural interactions. Magnetically, as noted in Sec. 5.1, the $S = 3/2$ (high-spin) Cr^{3+} ions in the honeycomb layers have FM interactions, of strength $J = -5.25$ K [74], which is a consequence of the near-90° Cr-Cl-Cr geometry (edge-sharing $CrCl_6$ octahedra), while the inter-layer interactions (J') are AF.

The magnetization, $m(T)$, and heat capacity, $c(T)$, were measured over a range of temperatures from 2 to 100 K and of applied magnetic fields up to 18 T using, respectively, Quantum Design MPMS and PPMS systems. The in-plane longitudinal thermal conductivity, $\kappa_{xx} \equiv \kappa$, was measured on an as-grown sample of dimensions 2×4×0.5 mm using a single-heater, two-thermometer configuration in steady-state operation with the field applied in the ab plane and in the direction of the thermal gradient ($\nabla T \parallel \mathbf{H} \in ab$); limited κ measurements were also performed with the field normal to the plane. The difference in absolute temperatures across the sample was set never

to exceed 5% of the bath temperature throughout the entire T range of the measurements. All thermometry was performed using Cernox resistors, which were pre-calibrated individually and *in situ* under the maximum applied fields of each instrument.

5.3 Experimental Measurements

5.3.1 Thermal conductivity, $\kappa(T)$

Figure 5.1 shows the complete picture of κ as a function of temperature for all values of the applied in-plane field, H, that we measured. At zero field (ZF), $\kappa(T)$ exhibits a somewhat flat maximum at 20–25 K with a gentle decline to higher temperatures; at lower T it has a marked plateau-type region at and below the magnetic ordering temperature, $T_N = 14.2$ K. As H is increased, it is clear that fields on the order of $\mu_0 H = 1$ T have only a minor effect on $\kappa(T)$. However, beyond 1 T the applied field causes a dramatic increase of $\kappa(T)$ at all temperatures and the development of a strong and sharp peak at $T_p \simeq 20$ K; at 18 T the maximum exceeds its ZF value by a factor of 2.2. As we will show below, in fact $\kappa(T)$ is almost completely independent of the direction of the applied field, indictating a minimal magnetic anisotropy.

At high fields, the peak at T_p and the line shape on both sides of it, which retains only a minor remnant of the plateau at T_N, are characteristic of phonon-dominated thermal conductivity. The value of T_p varies little as H is increased. Its physical origin lies in a crossover between the dominant phonon scattering mechanisms. At $T > T_p$, Umklapp processes dominate and τ_U^{-1} is the largest term in Eq. (5.2); for $T < T_p$, defect- (τ_{pd}) and boundary-scattering processes (τ_b) take over. It is reasonable to assume that $\kappa(T)$ at $\mu_0 H = 18$ T is closest to reproducing the purely phononic response, $\kappa_{\rm ph}(T)$, of $CrCl_3$, and we return to this topic in detail in Sec. 5.4C. As the inset of Fig. 5.1 makes clear, at this field the low-T $\kappa_{xx}(T)$ exhibits a T^3 dependence, suggesting that the thermal conduction is due to ballistic transport of acoustic (linearly dispersive) phonons.

At all lower fields, including zero, $\kappa(T)$ reflects a systematic suppression due to additional spin-dependent phonon-scattering processes over essentially the entire T range. Only at very low

temperatures ($T < 5$ K) does the ZF κ exceed that at all other fields, because this is where the contributions of coherent magnon excitations in the magnetically ordered phase become important. From the inset of Fig. 5.1, the thermal conductivity in this regime has no simply characterized form, and may be a consequence of comparable magnon and phonon contributions, at least one of which does not show ballistic transport [19]. By contrast, at all temperatures above 5 K the dominant effect of the spins is not an additive contribution, from three-dimensionally coherent excitations, but a destructive effect that we assume is due to scattering of the phonons by incoherent spin fluctuations. It is the field-induced suppression of these fluctuations that brings about the striking enhancement we observe in κ.

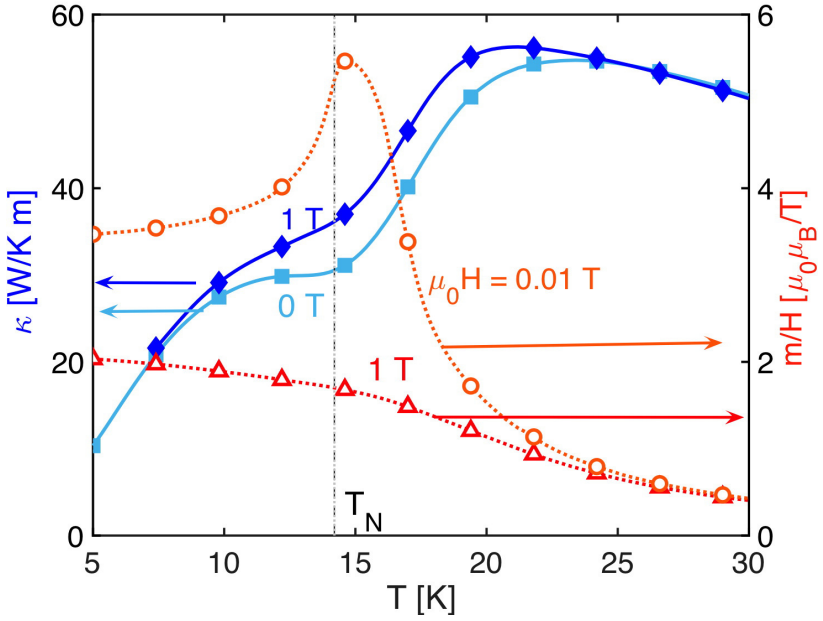

Figure 5.2: Data for $\kappa_{xx}(T)$ at 0 and 1 T reproduced for comparison with the field-normalized magnetization, $\chi(T) = m/H$. The very strong peak in the low-field $\chi(T)$, indicative of strong fluctuations towards magnetic order around $T = T_N$, matches the plateau in $\kappa(T)$ where its growth is arrested.

5.3.2 Magnetization

To understand this interplay of lattice and magnetic excitations, we first consider the magnetic properties of $CrCl_3$. The magnetization, $m(H)$, is shown in the inset of Fig. 5.6 for several different

temperatures. As noted in Sec. 5.1, a moderate field $\mu_0 H \approx 2$ T, applied in the plane, is sufficient at $T < 5$ K to rotate the FM planes against the AF interplane interaction and drive the system to saturation. We comment that the field scale for this process suggests, in contradiction to the conclusion of Ref. [74], that the interplane J' is of order 1 K. We deduce a saturation moment, $m_s = m(T \to 0)$, of $2.88\mu_B$ per Cr^{3+} ion. The same value of m_s is obtained by applying the same field in the out-of-plane direction, demonstrating that in $CrCl_3$, unlike $RuCl_3$, the magnetic anisotropy is extremely weak [18]. This m_s value is fully consistent with the spin contribution expected for a single Cr^{3+} ion of $S = 3/2$ when the g-factor appropriate for a magnetically isotropic system, $g = 2$, is assumed.

For perspective on the relation between $\kappa(T)$ and $m(T)$, in Fig. 5.2 we show $\kappa(T)$ on the same temperature axis as the field-normalized magnetization, $m(T)/H \equiv \chi(T)$, for fields of 0 and 1 T in κ and 0.01 and 1 T in χ. This low-field regime is where the plateau in $\kappa(T)$ around T_N is most pronounced, and the field is not sufficient to suppress the spin-induced scattering of the phonons conducting the heat. For very small fields, it is clear that $\chi(T)$ becomes very large in the region of the ordering transition, indicating strong magnetic fluctuations and hence the origin of the κ plateau. This behavior is suppressed considerably at 1 T, where the plateau begins to lose its form. Above 25 K, the residual m scales precisely with H.

5.3.3 Magnetic specific heat

To obtain further insight into both the phonons and their spin-mediated scattering, next we consider the specific heat as a function of T and H. Figure 5.3(a) shows our measurements of the total specific heat, $c(T)$, which are fully consistent for all H with previously reported results [18]. To estimate the phonon contribution, $C_{\rm ph}(T)$, we employ a three-dimensional (3D) Debye-model fit of heat-capacity data for the non-magnetic analog $ScCl_3$ [81]. The resulting $C_{\rm ph}(T)$, shown by the green line in Fig. 5.3(a), agrees well with our data for $CrCl_3$ in the high-temperature regime, which as the inset illustrates is $T \gtrsim 100$ K.

We attribute the remaining, strongly field-dependent portion of the specific heat to the mag-

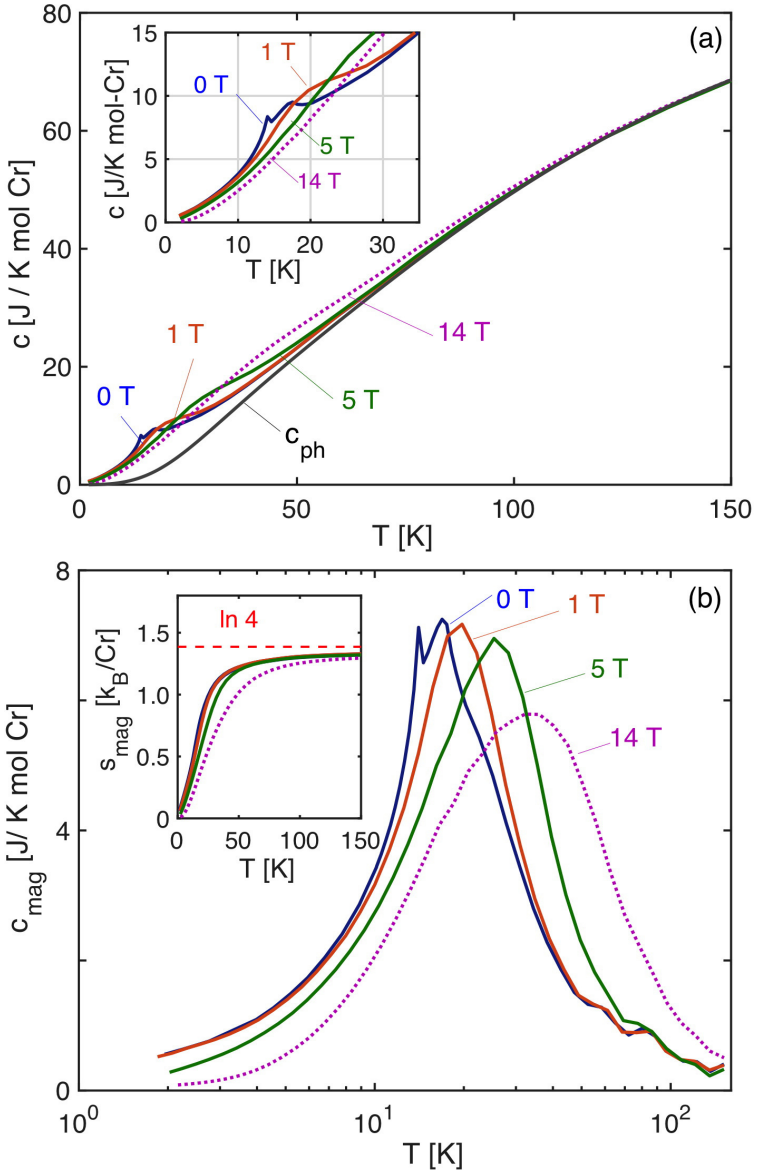

Figure 5.3: (a) Specific heat, $c(T)$, for a selection of different applied magnetic fields. The green line shows our estimate of the phonon contribution, $C_{\rm ph}(T)$, obtained from a Debye-model fit to $c(T)$ data for the non-magnetic analog $ScCl_3$ [81]. (b) Estimated magnetic specific heat, $C_{\rm mag}(T)$, obtained by subtracting $C_{\rm ph}(T)$ from $c(T)$ at each field. The inset shows the magnetic entropy, $s_{\rm mag}(T)$, which in the high-temperature limit approaches the value $k_B \ln 4$.

netic degrees of freedom, meaning we define $C_{\rm mag}(T) = c(T) - C_{\rm ph}(T)$. Figure 5.3(b) shows $C_{\rm mag}(T)$ on a logarithmic temperature axis. At ZF there are clearly two peaks, a sharp, λ-type anomaly at the Néel transition, $T_N = 14.2$ K, and a rounder maximum at 17-18 K. When the applied magnetic field is increased to 1 T, the λ anomaly is completely lost, and in fact a detailed study of the low-

field evolution of this feature [18] found that a field of 0.2 T is sufficient to suppress this indicator of the ordering transition. As the applied field is increased, the location, $T_{\max}(H)$, of the broad maximum shows an abrupt initial shift towards higher temperatures, before increasing more slowly with $\mu_0 H$ to a value of 36 K at 14 T.

Quite generally, the broad maximum in $C_{\rm mag}(T)$ fingerprints the energy scale of the dominant local spin-flipping processes in the system. In $CrCl_3$, this is the energy cost for reversing a single spin in the FM honeycomb layers (in the rhombohedral structure one would anticipate an energy of $3|J| + J'$). The initial increase in $T_{\max}(H)$ can be understood as a straightforward reinforcement of this magnetic stiffness while the applied field competes with J' to reorient the FM layers. The slower increase at $\mu_0 H > 2$ T corresponds to a competition of the field with $3|J|$, which in Ref. [18] was formulated as a progressive development of ferromagnetic correlations in the plane. Because of the low spin-coercivity in an applied field, FM alignment of very large domains becomes thermodynamically favorable at higher T. It is important to note that T_N, the temperature for 3D magnetic order, almost coincides with the broad maximum at ZF. Thus despite the quasi-2D nature of the structure of $CrCl_3$, the AF state at ZF is magnetically 3D, with T_N of the same order as the Curie-Weiss temperature ($\theta_{\rm CW} \simeq 30$ K both from our data below the structural transition at 240 K and from that of Ref. [18]).

While one may fear that our estimated $C_{\rm mag}(T)$, as a small difference between two larger numbers, is subject to significant errors, a complete validation of its accuracy may be obtained by integration. The magnetic entropy, $s_{\rm mag}(T) = \int_0^T dT'\, c(T')/T'$, is shown in the inset of Fig. 5.3(b). Clearly at temperatures beyond 50 K, $s_{\rm mag}(T)$ for all fields displays a smooth and accurate approach to the limit $k_B \ln 4$ expected for the four-level system corresponding to free $S = 3/2$ spins. This result, which contrasts strongly with the entropies shown in Ref. [18], indicates that our approach of deducing the lattice contribution from the material $ScCl_3$ provides a quantitatively accurate estimate of $C_{\rm ph}(T)$.

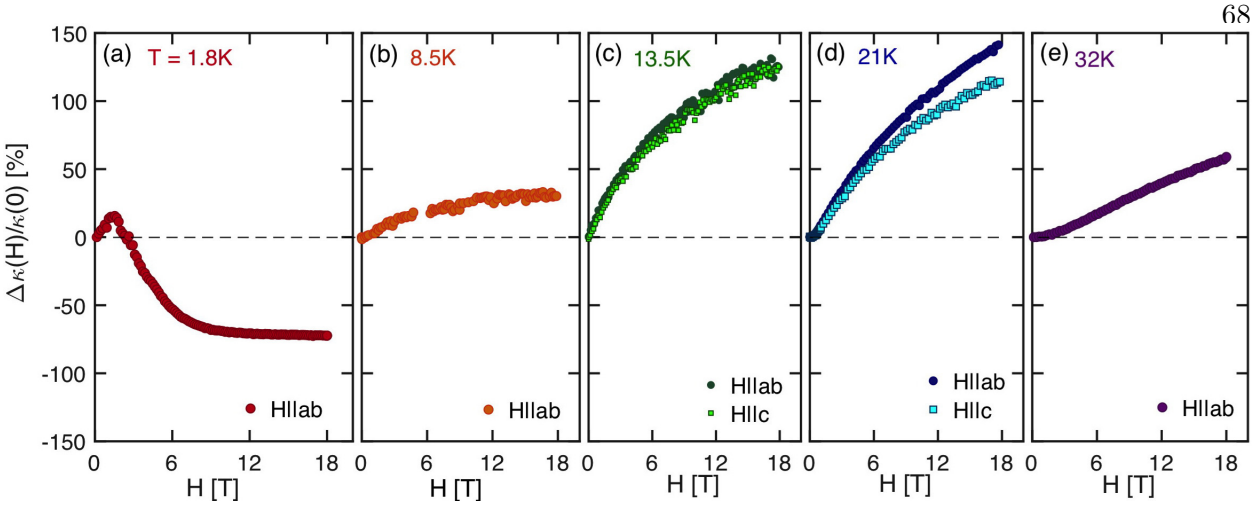

Figure 5.4: Fractional change in $\kappa_{xx}(H)$. For each selected temperature value we define $\Delta\kappa_{xx}/\kappa_0 = [\kappa_{xx}(H) - \kappa_{xx}(0)]/\kappa_{xx}(0)$. H is applied in the ab plane in every panel, and also along the c-axis at $T = 13.5$ and 21 K, which highlights the very low magnetic anisotropy. For all temperatures $T > 4$ K, the applied field causes a monotonic enhancement of κ. Only at $T < 4$ K is a different behavior observed as a consequence of the coherent magnonic contribution: κ_{xx} is enhanced by a small applied field (which causes magnon stiffening) but suppressed by all higher fields (where the energy cost of magnon excitation becomes prohibitive).

5.3.4 Thermal conductivity, $\kappa(H)$

The clearest way to gauge the effects of the magnetic state on the thermal conductivity is to consider the isothermal H-dependence of κ_{xx}. In Fig. 5.4 we show for a range of temperatures the fractional change $\Delta\kappa_{xx}/\kappa_0 = [\kappa_{xx}(H) - \kappa_{xx}(0)]/\kappa_{xx}(0)$ caused by an applied magnetic field. It is apparent immediately that the generic field response is a monotonic increase in $\Delta\kappa_{xx}/\kappa_0$, except at the lowest temperatures.

Although our $T = 1.6$ K data are something of an outlier for our present purpose, which is to discuss the generic behavior beyond the ordered regime, we focus first on the low-T case. Here $\kappa_{xx}(H)$ increases initially, peaking around 2 T before decreasing to negative values of $\Delta\kappa_{xx}/\kappa_0$ and becoming H-independent at fields $\mu_0 H > 8$ T. This behavior, which is observed for $T < 4$ K, indicates a coherent magnonic contribution to heat conduction that is comparable to the phononic one. The coherent spin-sector contribution to thermal conductivity has been the focus of numerous studies [10, 11, 24, 56, 57, 14] and can in general be described as an independent additive term

beyond the phonon contribution, i.e. $\kappa_{\rm tot} = \kappa_{\rm ph} + \kappa_{\rm mag}$. At low fields, the initial rise of $\kappa_{xx}(H)$ can be explained by the magnon stiffening that occurs when $\mu_0 H$ overcomes J' to orient all of the layers ferromagnetically, which results in an increase of the magnon propagation speed and hence of $\kappa_{\rm mag}$ [30]. However, this contribution decreases as soon as the field-induced magnon gap exceeds the measurement temperature, at which point the magnon population is suppressed exponentially, leaving a smaller and largely H-independent thermal conductivity, $\kappa_{\rm tot} \to \kappa_{\rm ph}$. The coherent magnon contribution also diminishes quickly as T increases, and in fact $\Delta\kappa_{xx}/\kappa_0$ changes character well below T_N (e.g. $T = 8.5$ K in Fig. 5.4).

At all temperatures $T > 4$ K, it is clear that the leading role of magnetic fluctuations is as scattering centers, rather than as participants in any kind of coherent heat conduction. While this type of behavior has been observed in certain quantum magnetic materials at specific temperatures, where it can be described by a $\tau_{\rm res}^{-1}$ term in Eq. (5.2) [13, 24, 58], systems in which it appears across the full range of temperatures are not widely known. Nonetheless, κ increases monotonically with field in all the relevant panels of Fig. 5.4; we remark again that this behavior is largely independent of the field direction. While it remains the case that increasing H suppresses the spin fluctuations, its effect is a uniform suppression of the spin-phonon scattering by an effective reduction in the density of scattering centers, thus bringing the system closer to purely phononic heat conduction.

5.4 Empirical Model for $\kappa(H, T)$

To model the thermal conductivity in the presence of such a large and obviously destructive spin-phonon interference effect, we base our analysis on the thermal conductivity, $\kappa_{\rm ph}(T)$, due to phonons. We first reexpress Eq. (5.2) in the form

$$\tau^{-1} = \tau_0^{-1} + \tau_{\rm mag}^{-1}, \tag{5.3}$$

i.e. we assume that the effective phonon scattering rate can be separated into a part $\tau_0^{-1} \equiv \tau_0^{-1}(T)$ containing all the field-independent terms in Eq. (5.2) and a part $\tau_{\rm mag}^{-1} \equiv \tau_{\rm mag}^{-1}(H, T)$ containing all phonon scattering processes involving magnetic degrees of freedom.

To capture the behavior of $\kappa_{xx}(H,T)$ phenomenologically, we assume that the relative scattering rate, $\tau_{\rm mag}^{-1}/\tau_0^{-1}$, will depend on the population of magnetic fluctuations, which we denote $n_{\rm mag}$, and on a dimensionless coupling constant describing the strength, or effectiveness, of the phonon scattering processes, $\lambda(H,T)$. Thus the key equation underpinning our empirical treatment is that the thermal resistivity will be given by

$$\kappa_{xx}^{-1}(H,T) = \kappa_{\rm ph}^{-1}(T)[1 + \lambda(H,T)\, n_{\rm mag}(H,T)], \tag{5.4}$$

where $\kappa_{\rm ph}$, the phonon thermal conductivity in the absence of spin-phonon interactions, is H-independent and would be recovered at high applied fields. By some straightforward algebra, one may verify that $\lambda n_{\rm mag} = \tau_{\rm mag}^{-1}/\tau_0^{-1} = \tau_0/\tau_{\rm mag}$. We normalize $n_{\rm mag}$ to the total number of Cr^{3+} spins so that it represents a fractional density, and thus the field-dependence of κ_{xx} is encoded in two unitless parameters, $0 < n_{\rm mag} < 1$ and $0 < \lambda$.

Focusing now on the spin fluctuations responsible for phonon scattering, because these change character across the (H,T) phase diagram, we begin by subdividing this into the two regimes shown schematically in Fig. 5.5. Qualitatively, at high fields and low temperatures one expects the fluctuations to be well-defined but 2D spin-wave excitations within the FM layers, whereas for temperatures high relative to the field one expects random fluctuations of weakly coupled spins. Specifically, for $CrCl_3$ we define region (**I**) as covering low temperatures ($T < T_N$) for fields $H \geq 2$ T and $T < 30$ K at our highest measurement field; here we will find that $n_{\rm mag}$ corresponds closely to the density of magnon excitations originating within the honeycomb layers, which are highly spin-polarized and strongly ferromagnetically correlated, and hence remain coherent 2D entities outside the AF phase. Region (**II**) covers temperatures $T > T_N$ for low fields, and at our higher fields temperatures $T > 40$ K; here $n_{\rm mag}$ corresponds to the average density of free spins that are not aligned with the field direction, and as such is well described by a Weiss-field picture, within which the net magnetization is determined by conventional paramagnetic behavior. As Fig. 5.5 makes clear, the AF ordered state occupies a very small region of the (H,T) phase diagram, and because the contributions of coherent 3D magnon excitations to κ are also small (Fig. 5.1), the

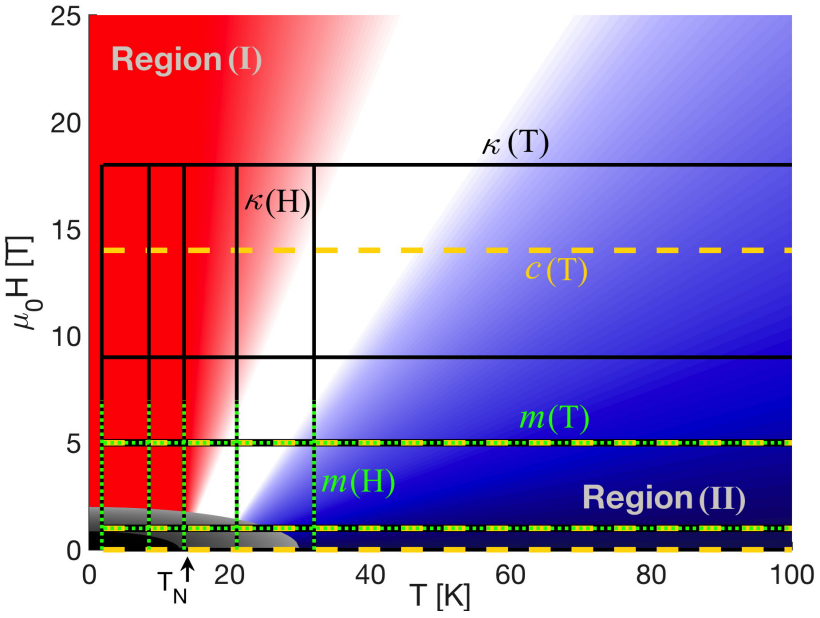

Figure 5.5: Schematic representation of the (H, T) phase diagram of $CrCl_3$. Graded red colors denote the extent to which the system is in the regime of high H/T [region (**I**)] and blue colors the regime of low H/T [region (**II**)]. The black color denotes the regime of long-ranged 3D AF order and the gray colors the extent to which the approximations we apply in regions (**I**) and (**II**) are invalidated by the residual presence of short-ranged magnetic correlations. Solid black lines denote the fields and temperatures over which we have measured the $\kappa(T)$ data shown in Fig. 5.1 and the $\kappa(H)$ data shown in Fig. 5.4, dashed orange lines the specific-heat data shown in Fig. 5.3, and dashed green lines the $m(H)$ and $m(T)$ data shown respectively in Figs. 5.6 and 5.8.

ordered regime is not the focus of our study. However, we comment that short-ranged magnetic correlations in the vicinity of the ordered state (gray colors) will act to limit the applicability of the approximations we apply below.

By considering the magnetic scattering in the high-H/T (**I**) and low-H/T regions (**II**) of Fig. 5.5, we will minimize the ambiguity at intermediate H/T ratios. In both regions, the fractional density of magnetic fluctuations, either of 2D spin-wave excitations or of freely fluctuating spins, can be fixed accurately to known limits. In region (**I**) this limit is the fractional deviation, $1 - m(H, T)/m_s$, of the net magnetization from its high-H/T saturation value, which is $m_s \equiv m(H \rightarrow \infty)$. In region (**II**) it is the fractional polarization, $m(H, T)/m_s$, which vanishes in the low-H/T limit.

It is apparent from Eq. (5.4) that the type of phenomenological approach we adopt requires a

reliable estimate of the pure (field-independent) phonon thermal conductivity, $\kappa_{\rm ph}(T)$, to be useful or even viable. If the dependence of κ on the applied field is sufficiently weak at strong fields, many authors [56, 82] use the $\kappa_{xx}(T)$ data at their highest available magnetic field as a measure of $\kappa_{\rm ph}$. In Sec. 5.4C we will use our modelling procedure to obtain a field-independent $\kappa_{\rm ph}(T)$ by extrapolating from our $\kappa(H,T)$ measurements (shown in Fig. 5.1), and hence will determine how close our $\kappa(\mu_0 H = 18$ T) data are to saturation.

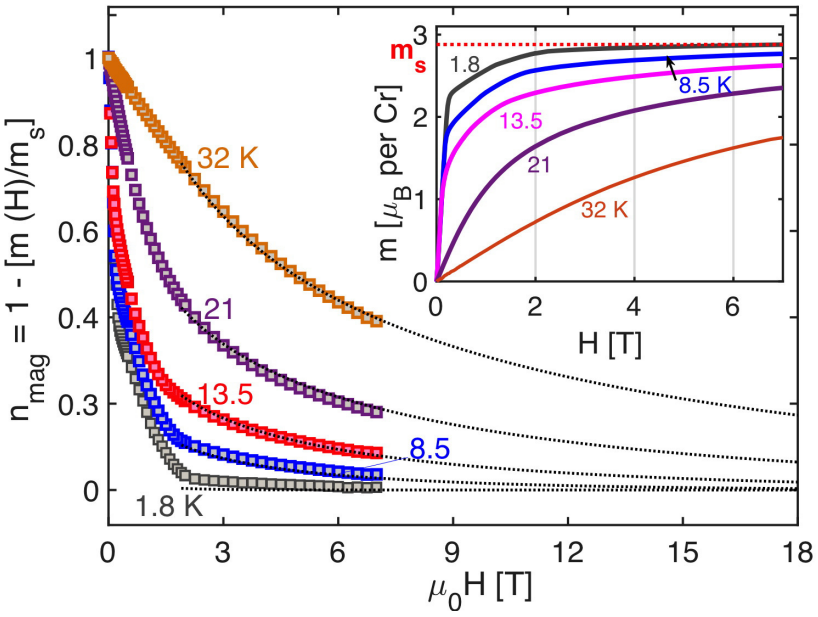

Figure 5.6: Estimate of the population of magnetic scattering centers, $n_{\rm mag}(H) = 1 - m(H)/m_s$, taken from the fractional deviation of the magnetization, $m(H)$, measured in the MPMS at several fixed low temperatures from its high-H saturation value. The black dotted lines show the same quantity computed for 2D magnetic excitations on a FM honeycomb lattice, using Eq. (5.5) with $d = 2$; this approach can be extended far beyond the range of the available data. Inset: isothermal magnetization, $m(H)$, for fields up to 7 T, shown for the same temperatures.

5.4.1 Region (I): dominant magnon scattering

Our magnetization data (inset Fig. 5.6) show that, for temperatures $T < 30$ K, fields $\mu_0 H \geq 5$ T are strong enough to polarize more than 50% of the Cr^{3+} spins. This temperature and field range lie well within the "spin-flop" regime [74, 18], where the spins are forced into a quasi-FM-ordered state of the honeycomb layers. To model this regime, we assume 2D FM spin-wave excitations with

the field-gapped dispersion relation $\hbar\omega(\mathbf{k}, H) = \frac{1}{2}\tilde{J}(ka)^2 + g\mu_B H$, valid at small k, where a is the lattice constant and $\tilde{J}$ is an effective magnetic interaction strength. The population of magnetic excitations per unit volume in d dimensions may then be estimated using the expression [17]

$$n_{\mathrm{mag}}(H,T) = \int \frac{d^d k}{(2\pi)^d} \frac{1}{e^{\hbar\omega(\mathbf{k},H)/k_B T} - 1}, \tag{5.5}$$
$$= \alpha \left(\frac{k_B T}{\tilde{J}}\right)^{d/2} \mathrm{Li}_{d/2}\left(e^{-g\mu H/k_B T}\right).$$

From the structure of this expression, only wave vectors $\mathbf{k}$ near the zone center contribute significantly to n_{mag}, and thus we take the upper limit of the integral to infinity; it is also not necessary to specify the departure of $\omega(\mathbf{k}, H)$ from a simple quadratic at higher k values. α is a unitless constant set by the dimension, d, and the normalization. $\mathrm{Li}_s(x)$ is the polylogarthmic function of order s, which has an infinite series expression that is easy to evaluate numerically. As Fig. 5.6 makes clear, this approach provides an excellent account of the H- and T-dependence of m, effective even at temperatures (21 and 32 K) outside region (**I**) as it is represented in Fig. 5.5. In Fig. 5.6 the only fitted parameter is the effective interaction, $\tilde{J} = 13.1$ K; clearly $\tilde{J} \approx 3J$ is again close to the characteristic energy scale of the 2D FM layers at ZF. Here we have treated $\tilde{J}$ as a constant, anticipating that fields up to 7 T cause only weak changes in the effective in-plane stiffness, certainly when compared with their gapping effects (this is to be contrasted with the "magnon stiffening" discussion in Secs. 5.3C and 5.3D, where the field dominates J').

At high H/T, when the total magnetization remains a significant fraction of m_s, we equate the measured deviation directly with n_{mag}, the population of 2D magnons obtained using Eq. (5.5) with $d = 2$. The agreement remains good for all temperatures $T < 2T_N$ when $\mu_0 H \geq 2$ T. Given the discrepancy between the in-plane FM interactions and the out-of-plane AF ones, whose 3D coupling effects are suppressed beyond 2 T (inset Fig. 5.6), it is not surprising that quasi-2D excitations dominate the spectrum. We comment here that the CrX_3 materials have been considered as candidates for hosting topological magnons with Dirac cones in their (graphene-type) dispersion relations [7], but at finite applied fields a full gap is opened and the magnon dispersion has the quadratic form assumed in our model.

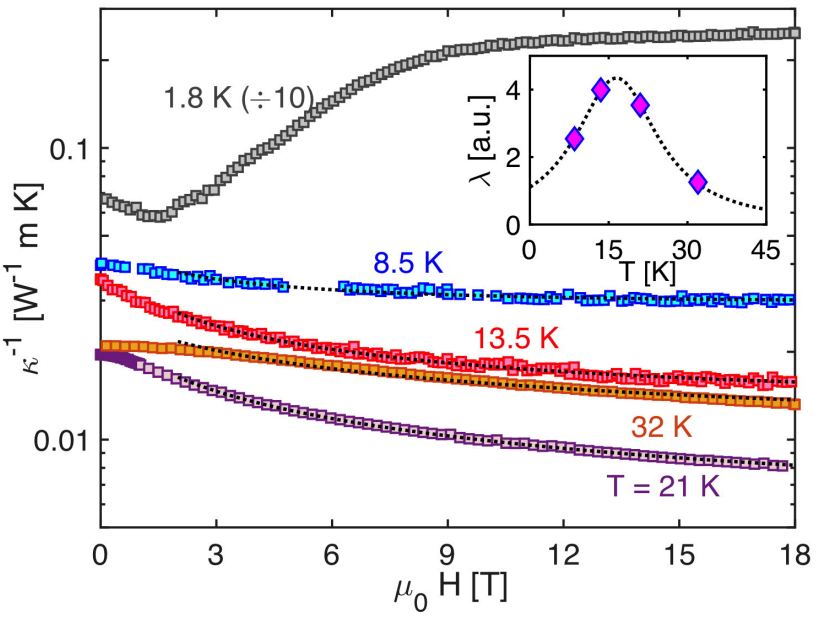

Figure 5.7: Isothermal thermal resistivity, $\kappa^{-1}(H)$, obtained from Fig. 5.4. The dotted black lines are fits of the data at $\mu_0 H > 2$ T to the form of Eq. (5.4), from which we deduce values for the high-field limit [the phonon thermal resistivity, $\kappa_{\rm ph}^{-1}(T)$], and the dimensionless and field-independent coupling strength, $\lambda(T)$. The inset shows the values of $\lambda(T)$ deduced at each temperature.

We stress again that, as shown in Fig. 5.1, these magnonic fluctuations are a significant source not of heat conduction but of phonon scattering. This situation is not generic, and indeed many of the systems reviewed in Sec. 5.1 provide examples of significant contributions to thermal conductivity from essentially 1D or 2D excitations in a 3D material [10, 11, 12, 13, 24, 56, 57, 58]. In general one expects that, when such low-dimensional excitations are not mutually coherent between planes or chains with characteristic transverse coupling constant $J_\perp$, they will act to destroy each others' coherence on a timescale governed by $J_\perp/J_\parallel$, where $J_\parallel$ is a characteristic energy scale (a gap or a stiffness) within the planes or chains. Thus for a large system and non-negligible transverse coupling, the low-dimensional excitations would not contribute to thermal transport, as we observe for the 2D-coherent magnons of $CrCl_3$, where $J_\perp/J_\parallel \equiv J'/3J \simeq 1/15$, in region (**I**). However, cases in which J' is extremely small, the gap is very large, or other characteristics conspire to allow significant transport, have attracted attention precisely because they contradict this tendency towards incoherence.

The destructive effects of the 2D magnons on thermal conductivity are parameterized by the phonon scattering strength, $\lambda(H,T)$, in Eq. (5.4). To analyze $\lambda(H,T)$, in Fig. 5.7 we fit the thermal resistivity data, $\kappa_{xx}^{-1}(H)$, for four of the five temperatures shown in Fig. (5.4). We find that an excellent description is obtained with a function $\lambda(H,T) \equiv \lambda(T)$ completely independent of the field. Thus in region (**I**) the field-dependence of $\kappa(H,T)$ is contained entirely within our straightforward assumptions about $n_{\rm mag}(H,T)$. Further, we observe that $\lambda(T)$ peaks in temperature close to T_N, and thus we deduce that scattering by coherent but "only" 2D magnetic excitations has its strongest effect on the phonon thermal conductivity in the regime around T_N itself; from the form of the magnetic specific heat [Fig. 5.3(b)], it is no surprise that phonon scattering should be most efficient around this characteristic temperature. This leads to a suppression effect that includes the peak region (around $T_p \approx 20$ K) and becomes unusually large as the applied field is reduced below 2 T, where $n_{\rm mag}$ rises strongly (Fig. 5.6). We note that, even in a van der Waals material, the phonons are in general much more 3D in nature than are the magnons once their interlayer correlations have been destroyed by the applied field, as a result of which good 2D magnons with no interlayer coherence are only damaging to phonons, and hence to thermal conduction.

5.4.2 Region (II): dominant paramagnetic fluctuations

At higher temperatures, the magnetic fluctuations may no longer be regarded as well-defined 2D spin-wave excitations. As the energy scale of thermal fluctuations becomes large compared to that of the field, planar FM order is destroyed and the behavior of the spin system becomes paramagnetic. Despite this loss of coherent 2D magnons, magnetic scattering continues to play a significant role in controlling the thermal conductivity in region (**II**), as Fig. 5.1 shows clearly. This effect must be a consequence of phonon scattering off randomly fluctuating free paramagnetic spins, whose relative density is also given by the fractional deviation of the magnetization from m_s.

Although the dominant physics in region (**II**) is thermal fluctuations that flip individual spins against the magnetic field, the underlying spin interactions may by no means be neglected. We model the magnetization profile, $m(T)$, of $CrCl_3$ by a Weiss-field approach [17] in which the

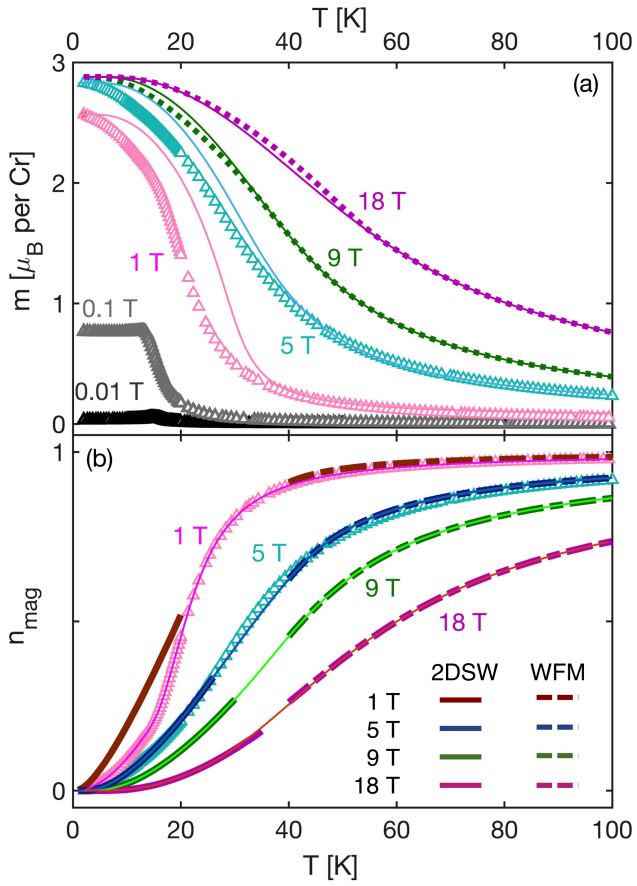

Figure 5.8: (a) Magnetization, $m(T)$, measured at fixed field values of 0.01, 0.1, 1, and 5 T. Thin solid lines are fits made by applying the Weiss-field model [Eq. (5.6)] at $T > 40$ K. This model can be extrapolated to $T = 0$, although of course it does not include the AF magnetic order, and this accounts for the deviations at $T < 40$ K for low fields. In addition we show calculations made with the same model parameters for $m(T)$ at 9 and 18 T, beyond the range of the data, where deviations due to AF order would be very small. (b) $n_{\rm mag}(T)$ deduced from $m(T)$; here we show the quantity $n_{\rm mag}(H,T) = 1 - m(H,T)/m_s(H,T=0)$ at each constant value of H. Solid lines marked 2DSW are estimates of $n_{\rm mag}(T)$ obtained from the 2D spin-wave model of Sec. 5.4A. Dashed lines marked WFM are estimates of $n_{\rm mag}(T)$ obtained from the Weiss-field model of Sec. 5.4B. Solid lines for 5, 9, and 18 T mark spline fits connecting the two regimes; at 1 T the 2DSW approach is not effective because it does not contain the magnetic order, and here the solid line is a fit to the data.

molecular-field term takes into account the FM correlations within the honeycomb planes. In this framework

$$m(H,T) = m_s B_S\left[\frac{g\mu_{\rm B}S}{k_BT}\left(\mu_0 H + B_{\rm mol}\frac{m(T)}{m_s}\right)\right], \tag{5.6}$$

where $B_S(y)$ is a Brillouin function of order S, $S = 3/2$, and $g = 2$. The solution for $m(T)$ is found by fixed-point iteration and, as shown in Fig. 5.8(a), an exceptionally good fit to the measured

magnetization is obtained over the entire paramagnetic temperature range, $T \geq 40$ K, for all fields below 7 T. The fitted constant $B_{\rm mol} = 22.4$ T $\simeq 15$ K is given once again by the FM in-plane coupling scale. In addition to providing smooth and easily computed curves at all measured field strengths, this model allows us to predict $m(T)$ with high confidence over the same temperature range at fields of $\mu_0 H = 9$ and 18 T that are prohibitively high for SQUID magnetometer measurements (Fig. 5.8). The clear deviations between model and measurement at low fields and temperatures are consequences of the AF order, and are suppressed by fields in excess of 1 T (inset Fig. 5.6), to the point where deviations at the fields we can only model ($\mu_0 H = 9$ and 18 T) are expected to be negligible.

To estimate the scattering strength, $\lambda(H,T)$ in Eq. (5.4), in region (**II**), we observe first that when $T \to \infty$ the magnetic degrees of freedom become entirely disordered, meaning that $n_{\rm mag} \to 1$. Thus to preserve the empirical observation that the field-dependence of $\kappa_{xx}(T)$ disappears at high T (Fig. 5.1), it is necessary that $\lambda(H,T) \to 0$ as $T \to \infty$. On physical grounds, this must be the case because different phonon scattering mechanisms will overwhelm the magnetic contribution in Eq. (5.3), rendering $\tau_{\rm mag}^{-1} \ll \tau_0^{-1}$. However, from the Weiss-field estimate of $m(H,T)$ shown in Fig. 5.8, it is clear that this regime is reached only at our lowest measurement fields, and that $n_{\rm mag}(H,T)$ remains significantly less than unity over the available temperature range for all fields above 1 T.

From experiment we have been able to obtain four highly accurate estimates of $\lambda(T)$ at temperatures up to $T = 32$ K, as shown in the inset of Fig. 5.7. Because the function $\lambda(T)$ is already well past its peak value, we use the logic of the previous paragraph to adopt test functions for the form of the vanishing of $\lambda(T)$ in region (**II**), taking for specificity Gaussian, exponential, and power-law (Lorentzian) forms. Stated briefly, all forms of this functional tail give equally valid fits to the data throughout region (**II**), and we pursue the quantitative aspects of this assertion in conjunction with the extraction of the phonon thermal conductivity, $\kappa_{\rm ph}(T)$, in the next subsection. The key qualitative point to be made here is that any H-dependence of the functional tail is so weak that, once again, a completely adequate fit to all data is obtained by taking $\lambda(H,T) \equiv \lambda(T)$, exactly

as in region (**I**). Thus we have obtained the profound result that, to a very good approximation, the effect of a magnetic field on the thermal conductivity may be encoded entirely within the number of magnetic fluctuations, $n_{\rm mag}(H,T)$, acting to scatter the phonons transporting the heat, while their scattering efficiency is effectively H-independent.

5.4.3 Phonon Thermal Conductivity

In the preceding subsections we have shown that is it possible to obtain excellent descriptions of $m(T)$, and hence $n_{\rm mag}(T)$, in both regions (**I**) and (**II**), as shown respectively in Figs. 5.6 and 5.8, by using minimal physical assumptions. Even without a quantitative matching of our two treatments, it is possible on this basis to obtain accurate fits of $\kappa^{-1}(H,T)$ at all fields and temperatures (Fig. 5.7) by using Eq. (5.4) with a field-independent scattering strength, $\lambda(T)$. The exercise of matching the models of Secs. 5.4A and 5.4B across the intermediate temperature regime would involve the extrapolation of either into a parameter range where it is explicitly no longer valid. However, the 2D spin-wave model applied in region (**I**) does account correctly for the temperature regime around the peak in $\kappa(T)$ for all fields in our measurement range, and thus this matching takes place only on the high side of the peak.

It is clear from Eq. (5.4) that $\kappa(T)$ is governed largely by the "continuous parameter" $\kappa_{\rm ph}(T)$, and as such that the most systematic matching of the two regimes would be ensured by obtaining an optimal estimate of this quantity. $\kappa_{\rm ph}(T)$, as the thermal conductivity due only to phonon contributions, is in principle obtained in region (**I**) as the $H \to \infty$ limit, where the spin excitations have an infinite gap and $n_{\rm mag} \to 0$, whence $\kappa(T) \to \kappa_{\rm ph}(T)$. In Sec. 5.1 we summarized the difficulties in obtaining $\kappa(T)$ from a DC formalism [44, 77], and in fact these are manifest even in obtaining $\kappa_{\rm ph}(T)$. Despite the many parameters, the form of the available relaxation-time terms remains highly constraining; in the present case, in the absence of a non-resonant spin-phonon suppression term, it is not possible to satisfy the low- and high-T limits simultaneously with an accurate estimate of the peak position, T_p. An approach simpler than the full DC treatment is to

proceed from the expression [55]

$$\kappa_{\rm ph}(T) = \tfrac{1}{3} c_{\rm ph}(T) v_s \ell_{\rm eff}(T) = \tfrac{1}{3} c_{\rm ph}(T) v_s^2 \tau_{\rm eff}(T), \tag{5.7}$$

where $c_{\rm ph}(T)$, the specific heat in the lattice sector, is known, v_s is again an average phonon velocity, and a simple model can be constructed for the effective mean free path, $\ell_{\rm eff}$, whose corresponding effective scattering time, $\tau_{\rm eff}(T)$, may be connected to Eq. (5.3). However, once again it is not possible within such a simplified framework to obtain an accurate value of T_p, and hence $\kappa(H,T)$ cannot be reproduced with any quantitative accuracy.

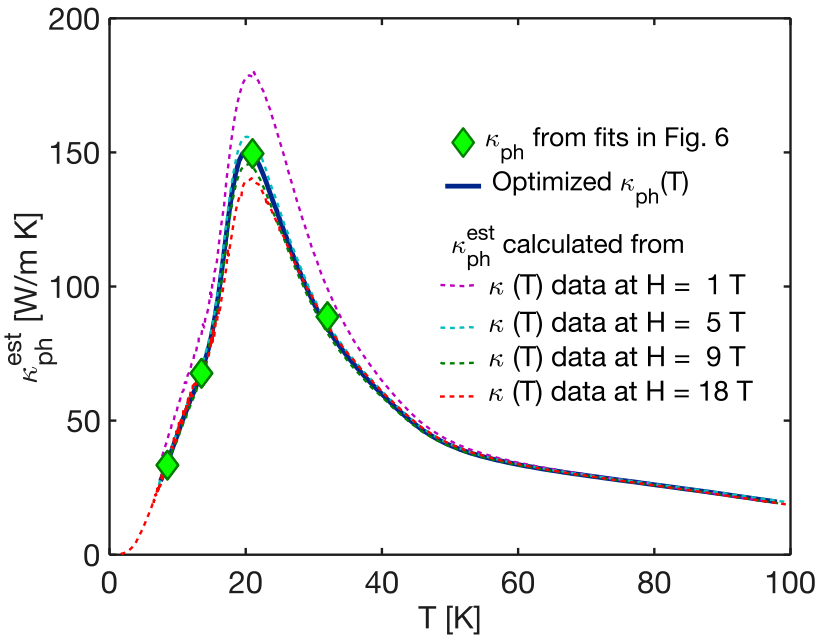

Figure 5.9: Estimates of the field-independent lattice contribution, $\kappa^{\rm est}_{\rm ph}(T)$ (dashed lines), obtained by using Eq. (5.4) with our measured thermal conductivity data (Fig. 5.1) at constant fields of 1, 5, 9, and 18 T. Green diamonds show values of $\kappa_{\rm ph}$ obtained from fits of the isothermal $\kappa(H)$, shown in Fig. 5.7, at temperatures of 8.5, 13, 21, and 32 K. The thick solid line shows the optimal $\kappa_{\rm ph}(T)$ deduced from the $\kappa^{\rm est}_{\rm ph}(T)$ curves (see text).

To ensure full generality of our treatment and to avoid the pitfalls inherent in adopting any approximate forms, we proceed instead directly from our data to compute the estimates $\kappa^{\rm est}_{\rm ph} = \kappa(H,T)[1 + \lambda(T) n_{\rm mag}(H,T)]$ for each available field value. Our fits of $\kappa^{-1}_{xx}(H)$ in region (**I**), shown in Fig. 5.7, provide reliable estimates of $\kappa_{\rm ph}$ at four discrete temperatures, which are shown as the green diamonds in Fig. 5.9. Inverting our $\kappa(H,T)$ data requires quantitative estimates of $\lambda(T)$ and

a single function $n_{\rm mag}(H,T)$. For the latter we proceed, as shown in Fig. 5.8(b), by comparing our 2D spin-wave estimates at all low temperatures (solid lines) and our Weiss-field estimates at all high temperatures (dashed lines) with our $m(T)$ data at 1 T and 5 T. As in Fig. 5.8(a), we also use our Weiss-field estimates at 9 and 18 T. By inspection, the upper temperature, $T_u(H)$, beyond which the Weiss-field approach is quantitatively accurate, may be taken as $T_u(H) = 40$ K for all fields; in fact a constant $T_u(H)$ would not be anticipated simply from the extent of region (**II**) in Fig. 5.5, and this result is actually a consequence of the additional effects of magnetic correlations above T_N at low fields. The lower temperature, $T_l(H)$, below which the 2D spin-wave result is quantitatively accurate, appears to be approximately 25, 30, and 35 K at 5, 9, and 18 T, values which track the edge of region (**I**) as represented in Fig. 5.5. At 1 T, the spin-wave approach is clearly no longer appropriate, because the tendency to AF order created by J' is not fully suppressed (Fig. 5.5; while we may use the $m(T)$ data here for quantitative purposes, we observe that the spin-wave result for a monolayer appears to be reliable to approximately 20 K. We note that these values of $T_l(H)$ are not dissimilar to the values $T_{\rm max}(H)$ obtained from the peak in the magnetic specific heat (Sec. 5.3C), and comment that this latter scale might indeed be anticipated as the upper limit to an ordered magnetic configuration on which to base a 2D spin-wave treatment. To bridge the shrinking gap between $T_l(H)$ and $T_u(H)$, we adopt the spline fits shown in Fig. 5.8(b).

For $\lambda(T)$, as noted in Sec. 5.4B, we have tested three functions that reproduce the four data points spanning the peak in this quantity shown in the inset of Fig. 5.7; one has a Gaussian form, $\lambda_1(T) = a_1 \exp[-(T-T_1)^2/2\sigma^2]$, one an exponential form, $\lambda_2(T) = a_2 T^b \exp(-T/T_2)$, and one a Lorentzian form, $\lambda_3(T) = a_3\gamma/\pi[(T-T_3)^2+\gamma^2]$. The three functions differ only in the rate at which λ vanishes in the high-T regime and all three may be used to obtain consistent descriptions of the data with only minor differences in the value of the estimated $\kappa_{\rm ph}(T)$ at $T > 40$ K and in the temperature at which all datasets converge. Because of a mild but unexpected bulge around 40 K in our measured $\kappa(T)$ data (Fig. 5.1), which is most pronounced at 18 T and which we believe is not intrinsic to the phonon thermal conductivity, a rapid vanishing of $\lambda(T)$ cannot accommodate this feature. To avoid an ill-defined subtraction of this poorly understood contribution, it is most

convenient to use the Lorentzian continuation of $\lambda(T)$, but we make no claim to have proven a physical underpinning for this form.

Inverting our $\kappa(H,T)$ data using these estimates of $n_{\rm mag}(H,T)$ and $\lambda(T)$ provides four different curves for $\kappa_{\rm ph}^{\rm est}(T)$ based on our measurements at 1, 5, 9, and 18 T. From Fig. 5.9 it is clear that all four estimates of $\kappa_{\rm ph}(T)$ are very similar across the full range of temperatures and that they converge completely in both the low- and high-T limits. In detail, the estimate based on our 1 T data, which are affected by the AF ordering tendencies, are something of an outlier. Otherwise, the three estimates based on 5, 9, and 18 T converge to high accuracy at all temperatures, with a maximum deviation of order 10% at T_p. Because the minor bulge in our $\kappa(T)$ data around 40 K (Fig. 5.1) is strongest at 18 T, we judge the near-identical $\kappa_{\rm ph}(T)$ curves deduced from $\mu_0 H = 5$ and 9 T to be the most representative and adopt these as our definitive result for the phonon thermal conductivity.

Fixing $\kappa_{\rm ph}(T)$ allows us unprecedented physical insight into the effects of phonon scattering by the spin fluctuations, and into the way in which these effects are suppressed by the magnetic field. In Fig. 5.10(a) we show the quantity $\lambda n_{\rm mag}$, which is equivalent to the relative scattering rate $\tau_0/\tau_{\rm mag}$. At 5, 9, and 18 T (dotted lines), $\lambda n_{\rm mag}$ displays a clear peak around 20 K that is suppressed from a value of nearly 1 by a factor of approximately 2 at each field step. For comparison, we show as solid lines the equivalent quantities for 0 and 1 T, which we have taken directly from our data because our methods for estimating $n_{\rm mag}$ are not suitable at these low fields. We observe the same general form, but with the peak twice as strong again.

In Fig. 5.10(b) we show the suppression factor, $f = (1+\lambda n_{\rm mag})^{-1}$, corresponding to Fig. 5.10(a), which is an inverted function reaching a minimum of 1/3 at T_p for a field of 0 T, where $\lambda n_{\rm mag} \simeq 2$. Thus the quantitative conclusion concerning spin-fluctuation scattering of the phonon modes in $CrCl_3$ is that this mechanism is so effective around the Néel temperature of the AF ordered phase that 2/3 of the phonon contributions to the thermal conductivity are removed. The spin-scattering effect is not at all resonant, retaining a significant value over the entire range of temperatures from 0 to 100 K. Finally, in Fig. 5.10(c) we use our deduced values of $\kappa_{\rm ph}(T)$, $n_{\rm mag}(H,T)$, and

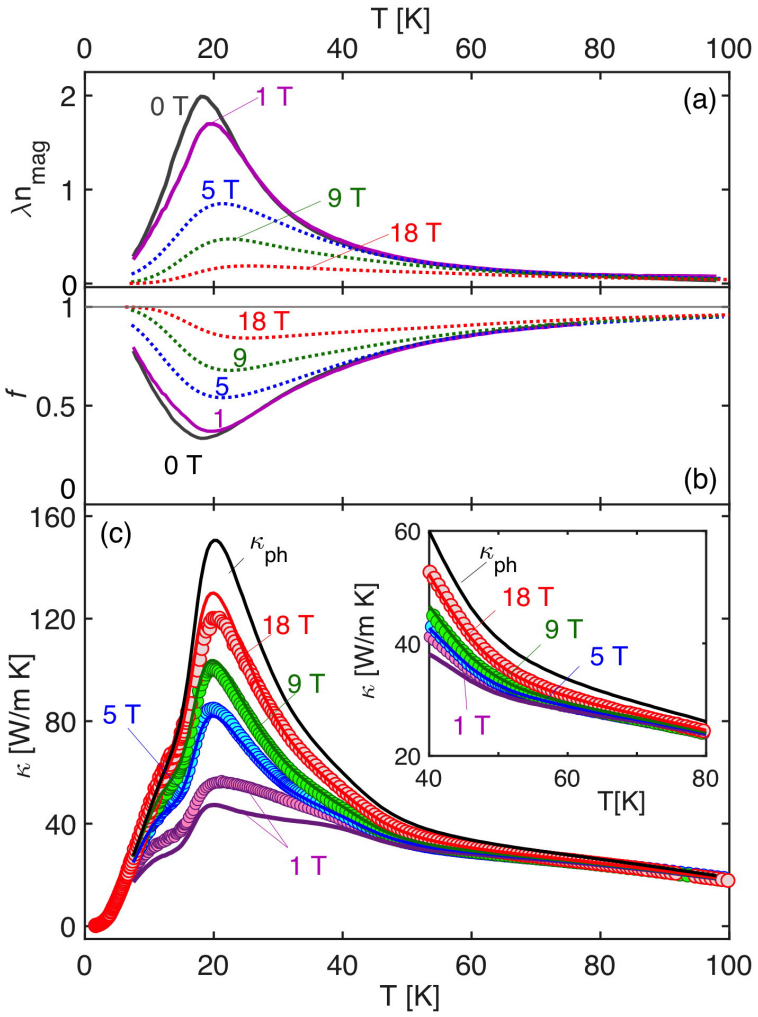

Figure 5.10: (a) The quantity $\lambda n_{\rm mag}$ shown as a function of temperature for fields of 0, 1, 5, 9, and 18 T. Dotted lines for 5, 9, and 18 T are obtained from our estimated $n_{\rm mag}(H,T)$ (Secs. 5.4A and 5.4B) multiplied by the Lorentzian continuation of $\lambda(T)$ (see text); solid lines for 0 and 1 T, shown for comparison, were obtained directly from the data. (b) Suppression factor, $f = 1/(1+\lambda n_{\rm mag})$, corresponding to $\lambda n_{\rm mag}$ in panel (a). (c) Reconstruction of our measured $\kappa(H,T)$ data, shown as discrete points, based on the empirical model of Eq. (5.4). Calculated $\kappa(H,T)$ values (solid lines) are based on a single curve for $\kappa_{\rm ph}(T)$ (solid black line) and use the Lorentzian continuation of $\lambda(T)$. Inset: magnification of the high-T regime ($T > 40$ K) to illustrate convergence of the data and calculations to $\kappa_{\rm ph}(T)$.

$\lambda(T)$ to reconstruct our measured $\kappa(H,T)$ data for all fields and temperatures. Quantitatively excellent agreement is achieved in all cases, with deviations from 1% at 5 and 9 T to 15% around the peak at 1 T, where in any case our approximations are of limited validity. We stress that this is not a circular exercise, because all of the field-dependence of $\kappa(H,T)$ is reproduced using only

$n_{\mathrm{mag}}(H,T)$. We comment also that $\kappa_{\mathrm{ph}}(T)$ does lie significantly above our 18 T data; while this separation may be slightly exaggerated in the high-T regime [inset Fig. 5.10(c)] by our use of the Lorentzian continuation, the 20% difference around the peak position is a robust result that serves as a warning against assuming that high-field data must lie beyond the range of spin fluctuations.

It is clear that our models provide a quantitatively accurate fit to the thermal conductivity at all fields and temperatures with only one exception. This is the low-field plateau in the measured $\kappa(T)$ that arises due to the ordering transition, a feature that lies explicitly beyond our modelling. Thus we have shown that $CrCl_3$ provides an ideal system for modelling the magnetic fluctuations at finite fields and temperatures, and that the dramatic suppression of its thermal conductivity caused by these fluctuations can further be modelled by multiplying their density by a field-independent phonon scattering strength.

5.5 Discussion and Conclusion

We first reiterate what we have achieved in describing the thermal conductivity of a correlated magnetic insulator with significant spin-lattice coupling. We have shown that, beyond a very narrow regime of field and temperature hosting 3D magnetic order, the thermal conductivity is due entirely to phonons, but that the contributions of these phonons is subject to a suppression factor. This suppression is due entirely to scattering from spin fluctuations that are not coherent in 3D, and can be extremely strong (up to 65%), but can itself be suppressed to zero by a sufficiently strong magnetic field. This phenomenon can be captured quantitatively by expressing the suppression in terms of only two parameters, an independently determined number of active magnetic fluctuations and a dimensionless parameter for their scattering efficiency. This latter turns out to be entirely independent of the field, meaning that the scattering strength is dictated only by the temperature, while the full suppressive effects of the applied field are contained within the number of fluctuations.

Applying this very general framework, for $CrCl_3$ we model the fluctuation number, $n_{\mathrm{mag}}(H,T)$, by considering the two regimes of high and low H/T. In the former, magnetic fluctuations take the form of field-gapped 2D spin waves in the FM honeycomb planes and n_{mag} is given by a conventional

spin-wave theory, but the complete lack of interlayer coherence means that these modes are not only incapable of transporting heat themselves but are destructive to the more 3D phonons that do so. In the latter, the system is paramagnetic and dominated by thermal fluctuations, but it is still field-polarized and thus the intrinsic intralayer FM interaction continues to play a role. The energy scale of this interaction, of order 15 K, is in fact fundamental to the thermodynamic and transport response of the system at all fields and temperatures, and its fingerprints are found in quantities ranging from the magnetic specific heat to the empirically determined phonon scattering-strength parameter, $\lambda(T)$, which peaks in temperature around this value before falling to zero. With these ingredients, our formalism can reproduce, and indeed predict the form of, $\kappa(T)$ at different applied fields over the entire temperature range. Discrepancies between the data and the model appear only at low fields in the vicinity of T_N, where n_{mag} cannot describe adequately the population of fluctuating spins in the critical regime.

A key strength of our modelling procedure is its basis in the simple phonon-scattering form expressed in Eq. (5.4). Despite its phenomenological nature, our approach is both completely general and fully quantitative. It is not dependent on specific properties of the magnetic state of the system and, crucially, it is independent of the nature of the magnetic excitations, which in the quantum limit may not necessarily be conventional magnons, but topological ones or even only fractions of a single spin-flip [11, 78]. Our treatment is also insensitive to specific phonon scattering mechanisms, which as Sec. 5.1 makes clear can take many possible forms; in this context we note again that the spin-fluctuation scattering we consider is non-resonant and that these fluctuations are paramagnons (quasi-FM spin fluctuations in the paramagnetic regime) over the entire range of T and H. While we have kept our treatment independent of assumptions about the phonon thermal transport in order to make it fully quantitative (Sec. 5.4C), one may also ask whether the analysis could be improved, or otherwise brought into contact with conventional treatments based on the specific heat or the DC framework. While this is certainly possible in parts of the parameter space, we have not been able to find a global description for $CrCl_3$ within either approach, and on this basis would not expect this type of traditional formalism to be suitable for general magnetic

materials. We stress again that, if the $\kappa_{\rm ph}(T)$ curve we extract from our data is regarded as a given, the number of "free" parameters in our modelling procedure can be argued to be zero, should one allow that $\tilde{J}$ in region (**I**) and $B_{\rm mol}$ in region (**II**) are given by the in-plane FM energy scale, $3J \approx T_N$, and that the form of the high-T vanishing of $\lambda(T)$ is immaterial.

An essential aspect of our study is the issue of system dimensionality. While all magnetic insulators are 3D, in low-dimensional quantum magnets the regime of 3D behavior may be a very small part of the (H,T) parameter space. In $CrCl_3$, the stronger coupling in the honeycomb layers mandates a 2D treatment in the regime of large H/T, where the field destroys 3D correlations but does not damage the 2D FM correlations; by contrast, thermal fluctuations act to damage all correlations. The FM nature of the layers also has another unexpected consequence in that, although the CrX_3 systems are regarded structurally as van der Waals materials, featuring a very low cohesive energy for exfoliation [18], $CrCl_3$ does not show the conventional features of a 2D magnet. In the specific heat, the 3D ordering peak effectively coincides with the broad maximum characterizing the majority of the spin-fluctuation processes, while the minimal anisotropy is also consistent with 3D magnetism. In more detail, the interlayer superexchange interaction, $J' \approx 1$ K, while not an insignificant fraction of the intralayer $J = -5.25$ K, is indeed rather smaller, and it is the FM nature of the in-plane order that allows J' to "leverage" a T_N scale of order $3|J|$. We comment that layered magnetic materials are ubiquitous both in condensed matter and in the heterostructures being fabricated for spintronic functionalities, and hence our considerations can be expected to have far-reaching applicability.

While it is intuitively clear that the origin of the giant magnetoconductivity we observe lies in "strong spin-lattice coupling" [18], we stress that this is not merely another spin-phonon story. The qualitative difference in the present study is that we are measuring a transport property, meaning a property exclusively of the excitations in the spin and lattice sectors of the system. In this sense our focus is a specific and sensitive probe of a much less commonly studied aspect of magnetoelastic coupling, namely the nature and scattering of these two sets of excitations over the complete (H,T) parameter space.

One may nonetheless ask why, quantitatively, the scattering effect is so strong in $CrCl_3$. Here we point to the possibility that the spin-phonon coupling can be relatively normal but J is in fact anomalously small. As noted in Sec. 6.2, the FM J is a consequence of the near-90° Cr-Cl-Cr bond angle enforced by edge-sharing $CrCl_6$ octahedra, and this type of interaction is far smaller in magnitude than comparable AF bonds at higher angles. In general, the interaction strength is very sensitive to the bond angle in this regime, implying that small phononic displacements may have strong relative effects; when normalized by the small J values, these magnetoelastic effects then appear in the conventional range. While first-principles calculations have been performed recently to accompany the experimental observation that the interlayer magnetic interaction strength, J', changes over a wide range in few-layer $CrCl_3$ samples [83], we are not aware of calculations investigating the lattice-sensitivity of the in-plane interaction, J, which could in principle be modulated by pressure in bulk samples or by substrate choice in few-layer heterostructured samples.

Returning to α-$RuCl_3$, small Heisenberg interactions, J, are also a sought-after feature of candidate Kitaev materials. When these dominant magnetic effects are suppressed, the remaining terms in the anisotropic spin Hamiltonian are thought to give rise to fractional spin excitations (of Majorana [8, 31, 66] or generalized Majorana character [84]) and to spin-liquid ground states in the presence of an applied magnetic field [14, 64, 85]. It is clear [14] that the thermal conductivity measured in α-$RuCl_3$ shows strong spin-phonon scattering effects over the entire range of temperatures, but a detailed interpretation lies beyond the scope of a DC approach [68] and a theoretical analysis of phonon scattering by fractionalized spins is still awaited. We comment in passing that phonon coupling to chiral Majorana edge states has recently been invoked [86, 87] as an ingredient essential for the interpretation of controversial thermal Hall conductivity data reported [88] for α-$RuCl_3$ at finite fields; however, we stress that the strong spin-phonon scattering observed in both α-$RuCl_3$ and $CrCl_3$, and which we model here, involves the bulk spin excitations. We suggest that the more general, data-oriented approach we adopt for $CrCl_3$ may help to clarify the situation even in the absence of a microscopic discussion of phonon scattering by fractional spin excitations.

Returning to the higher chromium trihalides, $CrBr_3$ has been proposed [7] as a candidate for

hosting topological magnons. CrI_3 is known [70] to present a situation where the bulk material has FM interlayer interactions, but the few-layer form takes on a different interlayer structure and these interactions become AF. In a similar vein, it has been found very recently in $CrCl_3$ that the interlayer interaction remains AF [89] as the system thickness is reduced to two layers, while showing the dramatic increase noted above [83]. Efforts to include $CrBr_3$ in a systematic comparison are ongoing [90]. These results have drawn a great deal of attention with a view to fabricating highly controllable spintronic materials, possibly functioning with topologically protected information. While thermal conductivity measurements on few- or many-layer samples are not yet available, our results offer both a general framework for analyzing the different possible contributions to spin and thermal transport and a general warning concerning the need to take full account of spin-phonon scattering effects.

In summary, we have investigated the thermal conductivity of the layered ferromagnet $CrCl_3$ over a wide range of temperature and magnetic field. We find a giant field-induced enhancement of the phononic contribution at all temperatures below 70 K, pointing towards a strong spin-fluctuation scattering effect. We construct an empirical model for the thermal conductivity by introducing a general framework based on two quantities that can be determined separately, the number of active spin-flip processes and their efficiency in scattering phonons. This formalism provides a quantitative description of our measured data at all fields and temperatures, has predictive power in unmeasured regions, and allows an accurate extraction of the purely phononic response. We anticipate that this approach will find wide application in interpreting the spin and thermal transport properties of many insulating magnetic materials, where spin-phonon scattering is a strong and unavoidable feature of the physics.

CAP and IAL acknowledge the support of the Colorado Energy Research Collaboration. A portion of this work was performed at the National High Magnetic Field Laboratory, which is supported by National Science Foundation Cooperative Agreement No. DMR-1644779 and by the State of Florida. Work at CAU was supported through National Research Foundation Grant No. 2019R1A2C3006189 by the Ministry of Science and ICT of South Korea.

Chapter 6

Anisotropy and Exchange in the 4f triangular magnet $CsYbSe_2$

6.1 Introduction

The quantum spin liquid (QSL) is a nonmagnetic many-body ground state in which the spin correlations have long-ranged quantum entanglement [9]. Despite many theoretical studies of these enigmatic phases, which have served to drive detailed investigations of a wide range of magnetic compounds, neither a universally agreed QSL phase in a real material nor an unambiguous set of experimental QSL criteria has yet emerged. The strong quantum fluctuations responsible for producing exotic spin states are a consequence of generalized magnetic frustration, which leads to a highly degenerate manifold of competing states. Early examples of material realizations of candidate models for hosting QSL states were based on geometrical frustration in structures with triangular motifs, including kagome [91], pyrochlore [92, 29], and triangular lattices [93, 94, 95, 96], mostly of real $S = 1/2$ spins.

Magnetic insulators with strong spin-orbit coupling are now widely recognized as a platform for extending very significantly the nature of frustration and the variety of quantum many-body phases (including QSLs) and phenomena that can be realized. When compared to spin-1/2 magnetic insulators based on $3d$ ions, these systems tend to exhibit complex microscopic physics even at the single-ion level. Magnetic materials containing $5d$ and $4d$ transition-metal ions possess interactions that are anisotropic in both spin space and real space, leading to complex phenomenology in pyrochlore systems [92, 97, 5] and in proximate Kitaev materials [98, 99, 100, 101, 102]. Compounds based on $4f$ rare-earth ions that combine the geometric frustration of pyrochlore and triangular

lattices with strong spin-orbit coupling have also provided fertile ground for quantum magnetism research [38, 103, 104, 105]. However, in these materials a detailed understanding of the microscopic physics is a prerequisite for developing effective spin models that serve as a basis for theories of many-body phenomena.

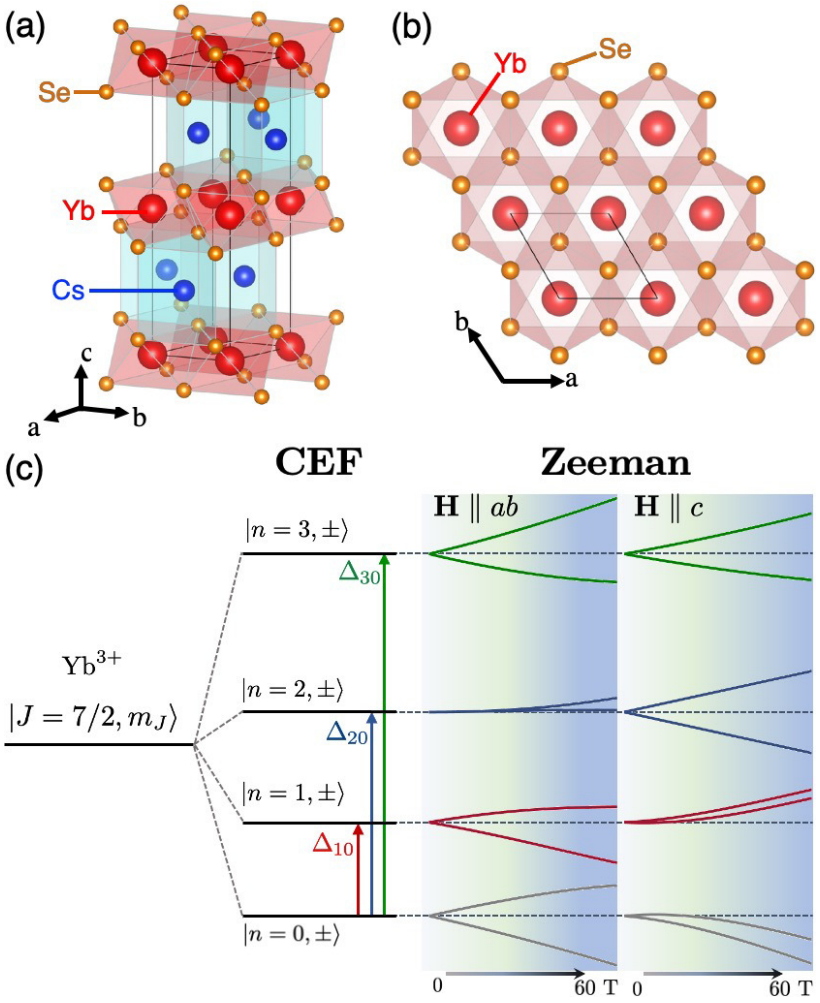

Figure 6.1: **Crystal structure and CEF spectrum.** (a) $CsYbSe_2$ adopts the $P6_3/mmc$ space group. (b) Yb^{3+} (red) triangular layers formed by edge-sharing $YbSe_6$ octahedra are separated by layers of Cs^+ ions. (c) Schematic origin of the CEF energy spectrum of Yb^{3+}. The CEF interactions allowed by the D_{3d} site symmetry split the Yb^{3+} ground-state manifold into four Kramers doublets. The application of a magnetic field lifts the doublet degeneracy in a spatially anisotropic manner whose leading nonlinear contributions are captured by the van Vleck coefficients defined in Eq. (6.7).

In insulating $4f$ materials, the key to a microscopic description of the magnetic interactions is a reliable determination of the single-ion crystal electric-field (CEF) Hamiltonian ($\mathcal{H}_{\text{CEF}}$) [92, 29].

In many rare-earth compounds, CEF effects split the degeneracy of the ground multiplet of the total angular momentum, J. For half-odd-integer J, the result is a set of Kramers doublets. At sufficiently low temperatures, a restriction of the dynamics to the lowest such doublet may be invoked to justify using an effective pseudospin-1/2 model [106, 38, 107, 108]. From an experimental standpoint this allows a significant diversification of both materials and magnetic phenomena, while on the theoretical side a minimal model may be relatively simple, or even a realization of one of the paradigm models in frustrated magnetism.

The leading system-specific parameters in are commonly determined by inelastic neutron scattering (INS), which provides direct information about the spectrum of CEF multiplets. However, there are in general more symmetry-allowed parameters in than there are gaps between CEF multiplets, resulting in an underdetermined fit of the CEF parameters and hence to uncertainties in the appropriate pseudospin-1/2 model that can be qualitative rather than merely quantitative corrections. Methods allowing the unambiguous determination of with higher reliability are thus very desirable. In this article, we present a high-fidelity determination of the CEF parameters of a selected $4f$ system, obtained by using a combination of low-field magnetic susceptibility and high-field (up to 60 T) resonant torsion magnetometry (RTM) measurements.

Yb-based triangular-lattice compounds offer an excellent combination of geometric frustration, quasi-two-dimensional nature, half-odd-integer J, and a strongly split CEF spectrum that suggests the validity of pseudospin-1/2 models of quantum magnetism. In particular, the family of $A\mathrm{Yb}X_2$ delafossites (with A = Na, Cs and X = O, S, Se) has attracted intensive interest [109, 110, 111, 112, 107, 113, 47, 108]. Unlike the material $\mathrm{YbMgGaO_4}$ [114, 115, 116, 117], they are free from potential site disorder [39, 118] and no members of the family have been found to exhibit magnetic ordering at temperatures down to tens of mK, while several have been reported to exhibit continua of low-energy magnetic excitations [107, 108, 119]. Their magnetic response is highly anisotropic between the in- and out-of-plane directions, providing a valuable opportunity to use the magnetic field to vary the free-energy landscape. Thus the trianguar-lattice delafossites present an ideal test case for unambiguous fitting of the field-induced CEF spectra and subsequent

establishment of the effective spin-1/2 states in rare-earth compounds.

As an example material we focus on $CsYbSe_2$ [Figs. 6.1(a-b)]. The complete CEF spectrum is specified by the coefficients of six Stevens operators, and thus the challenge is to measure enough independent physical quantities beyond the low-energy limit. From the susceptibility we extract not only the linear Zeeman coefficients for both of the primary, high-symmetry field directions but also the van Vleck (VV) coefficients for the ground doublet, which are the second-order corrections (i.e. quadratic in the applied field). While these VV coefficients are often used to describe the magnetic response of rare-earth compounds in terms of an additive contribution to the susceptibility [120, 111], in fact they are embedded in a nontrivial way in the full expression for this quantity. We will show how the multiple roles of the ground-state VV coefficients and their significance as stand-alone physical quantities, with direct implications for the high-field magnetic anisotropy, have yet to be appreciated in connection with CEF fitting. They facilitate the bridge to the field range covered by our RTM measurements, from which we extract the full field- and temperature-dependence of the magnetotropic coefficients for the same two high-symmetry field directions. These round out a complete set of eight observables, allowing us to determine a unique set of microscopic CEF parameters and thus the full CEF spectrum. As Fig. 6.1(c) makes clear, our results reveal an intricate energy landscape and level-repulsion behavior in the CEF spectrum of $CsYbSe_2$ up to high magnetic field values and for both field directions.

The physical content of our analysis is to interpret the essential role of the VV coefficients in determining magnetic properties, even at low fields and temperatures, where they are often neglected in pseudospin-1/2 models. Quantifying the VV corrections allows us to demarcate the field-temperature range over which a pseudospin-1/2 approximation is appropriate in $CsYbSe_2$, and to describe the high-field limit accurately. The resulting full characterization of the CEF spectra is essential for investigating their experimental consequences, for example when the application of intense magnetic fields causes multiple real or avoided level-crossings in narrowly spaced CEF spectra. It is also a prerequisite to study further mechanisms leading to different forms of magnetic frustration, in which additional degrees of freedom, such as phonons, hybridize with the electronic

spectrum to cause profound effects to appear in low-temperature thermodynamics and transport properties [121, 122]. Finally, while we have focused on one example material, our analysis can be applied widely to localized $4f$-electron systems.

The structure of this paper is as follows. In Sec. 6.2 we introduce $CsYbSe_2$, our experimental methods, the complete Stevens operator formalism for CEF levels and some approximate treatments. In Sec. 6.3 we show all the results of our susceptibility measurements and their analysis for the two primary field directions. Section 6.4 presents our RTM measurements and extraction of the magnetotropic coefficients, allowing us to determine the full set of Stevens operators. In Sec. 6.5 we discuss the physical interpretation of the results and their consequences for experimental analysis, effective pseudospin-1/2 models in frustrated quantum magnetism, and materials selection for candidate QSL systems. Section 6.6 contains a brief summary of our contribution and four Appendices provide additional information concerning details of the analysis.

6.2 Materials and Methods

While most of the $A\mathrm{Yb}X_2$ family crystallizes in the $R\bar{3}bm$ space group, the layer stacking sequence of $CsYbSe_2$ gives a $P6_3/mmc$ structure [123, 124], in which the triangular-lattice planes are constructed from edge-sharing $YbSe_6$ octahedra, as illustrated in Figs. 6.1(a-b). The ratio of inter- and intra-layer distances separating the Yb^{3+} ions results in a quasi-2D magnetic system [123]. Within each plane, the Se atoms mediate identical AFM superexchange interactions between all nearest-neighbor Yb^{3+} ion pairs, resulting in highly frustrated triangular magnetism. In fact the system does not order at zero field for temperatures down to 0.4 K, although an applied in-plane field induces an up-up-down ordering, as demonstrated by the observation of a 1/3 plateau in the magnetization, $M(H)$, at this temperature [123].

Magnetization and susceptibility measurements were performed on single-crystalline samples using a Quantum Design MPMS. All susceptibilities we report are obtained from $\chi_{ab,c} = \frac{dM_{ab,c}}{dH}$, where the indices denote measurements performed with the field oriented in the triangular-lattice plane ($H \parallel ab$) or perpendicular to it ($H \parallel c$).

Beyond the 7 T upper limit of our magnetization measurements, we employ resonant torsion magnetometry (RTM) to probe the nature of the magnetic anisotropy. The sample is mounted on the tip of a vibrating cantilever and the measured shifts in the resonant frequency ($f_0 \approx 40$ kHz) reflect changes in the magnetic rigidity caused by changes in the direction of the applied magnetic field, which are quantified by a tensor of magnetotropic coefficients, $k(\vec{H})$. We focus on $k(H,T)$ at the high-symmetry angles $\theta = \pi/2$ (to measure k_{ab}) and 0 (k_c), where θ is the polar angle of the applied field measured from the crystalline c-axis. The measurement configuration is summarized in Sec. 6.4 and described in detail elsewhere [25, 26]. All RTM data were taken using the capacitive magnet of the NHMFL pulsed-field facility at Los Alamos National Laboratory.

6.2.1 CEF Analysis and Model Hamiltonian

Yb^{3+} ions subject to the CEF interactions of their surrounding anion charge distribution have a total $J = 7/2$ ground-state multiplet of allowed electronic states. Unlike the triangular-lattice material $YbMgGaO_4$, the Yb^{3+} ions in $CsYbSe_2$ are largely free from any site disorder associated with the non-magnetic ions. To describe $CsYbSe_2$, we parametrize the single-ion CEF interaction as a linear combination of the six symmetry-allowed Stevens operators, $\hat{O}_n^m$, for the D_{3d} site symmetry of the $YbSe_6$ octahedral environment [109, 110, 111, 112, 107, 113, 47, 108] to obtain

$$\hat{\mathcal{H}}_{\text{CEF}} = B_2^0\hat{O}_2^0 + B_4^0\hat{O}_4^0 + B_4^3\hat{O}_4^3 + B_6^0\hat{O}_6^0 + B_6^3\hat{O}_6^3 + B_6^6\hat{O}_6^6 \tag{6.1}$$

This Hamiltonian splits the $J = 7/2$ multiplet into four Kramers doublets, $|n_\pm\rangle$ with $n = 0$, 1, 2, 3, whose energies we use to define the separations from the ground-state doublet ($n = 0$) as Δ_{10}, Δ_{20}, and Δ_{30} [Fig. 6.1(c)]. The corresponding wave functions are obtained by diagonalizing Eq. (6.1). A CEF spectrum for the zero-field limit can be identified using spectroscopic probes, particularly INS and Raman spectroscopy, but to date little information is available with which to investigate the high-field reorganization of the energy spectrum.

The symmetries of the triangular lattice of Yb^{3+} ions permit a nearest-neighbor superexchange interaction with XXZ spin symmetry [125]. Additional symmetry-allowed and bond-dependent

anisotropic pseudo-dipolar exchange terms [126] are found to give vanishing contributions in a standard Weiss mean-field approximation. Thus we restrict our analysis to the minimal XXZ spin model, $\hat{H}_{\mathrm{XXZ}}$, describing nearest-neighbor interactions between adjacent in-plane $J = 7/2$ moments in terms of two interactions, $\mathcal{J}_\perp$ and $\mathcal{J}_z$, which are the respective couplings of spin components transverse and parallel to $\hat{z}$, i.e.

$$\hat{\mathcal{H}}_{\mathrm{XXZ}} = \sum_{\langle ij \rangle} \Big[\mathcal{J}_\perp \Big(\hat{J}_{i,x} \hat{J}_{j,x} + \hat{J}_{i,y} \hat{J}_{j,y} \Big) + \mathcal{J}_z \hat{J}_{i,z} \hat{J}_{j,z} \Big], \tag{6.2}$$

in which the indices $\langle i, j \rangle$ refer to nearest-neighbor lattice sites and $\hat{J}_{i,\gamma}$, with $\gamma = x, y, z$, labels the components of spin $J = 7/2$ moments on site i.

To account for Zeeman coupling to the external field we add the term

$$\hat{\mathcal{H}}_{\mathrm{Z}} = -\mu_0 \mu_B g_J \mathbf{H} \cdot \sum_i \hat{\mathbf{J}}_i, \tag{6.3}$$

where the Landé g-factor, $g_J = 8/7$, is used for Yb^{3+} moments. We note that the quantization axis defining the $\hat{z}$ direction of the chosen basis of spin operators in $\hat{H}_{\mathrm{CEF}}$ and $\hat{H}_{\mathrm{XXZ}}$ is identically the crystallographic c-axis, whence the component H_z refers to a field ($\mathbf{H} \parallel c$) applied along the c-axis in experiment. Similarly, $H_\perp = \mathbf{H} \parallel ab$ refers to a field component perpendicular to the c axis, which lies precisely in the hexagonally symmetric ab-plane. In none of our experiments did we find a discernible difference in the response for different in-plane field directions, and hence we do not distinguish between these. The two separate contributions to the spin response under an external magnetic field, arising from the single-ion anisotropy and the superexchange anisotropy (both of which have their origin in the CEF spectrum), are then captured by the Hamiltonian

$$\hat{\mathcal{H}}_{\mathrm{tot}} = \hat{\mathcal{H}}_{\mathrm{CEF}} + \hat{\mathcal{H}}_{\mathrm{XXZ}} + \hat{\mathcal{H}}_{\mathrm{Z}}. \tag{6.4}$$

6.2.2 Weiss Mean-Field Approximation

We treat the physics of the system at finite temperature within a self-consistent Weiss mean-field approximation for the Yb^{3+} spins, which we will find captures the bulk magnetic behavior of

$CsYbSe_2$ exceptionally well at all measurement temperatures ($T \geq 2$ K). In the Weiss mean-field treatment, Eq. (6.4) reduces to a system of N decoupled Yb^{3+} ions each subject to the Hamiltonian

$$\begin{aligned}\hat{\mathcal{H}}^{\mathrm{sg}}_{\mathrm{MF}} = \hat{\mathcal{H}}_{\mathrm{CEF}} - \tfrac{1}{2}q\left[\mathcal{J}_{\perp}\langle\hat{J}_x\rangle^2 + \mathcal{J}_z\langle\hat{J}_z\rangle^2\right] \\ - \left[\mu_0\mu_B g_J \mathbf{H} - q\left(\mathcal{J}_{\perp}\langle\hat{J}_x\rangle\hat{\mathbf{x}} + \mathcal{J}_z\langle\hat{J}_z\rangle\hat{\mathbf{z}}\right)\right]\cdot\hat{\mathbf{J}},\end{aligned} \tag{6.5}$$

where $q = 6$ is the nearest-neighbor coordination number on the triangular lattice and the mean-field expectation values of the spin operators are determined self-consistently as $\langle\hat{J}_\alpha\rangle = \mathrm{Tr}[\hat{J}_\alpha e^{-\beta\hat{\mathcal{H}}^{\mathrm{sg}}_{\mathrm{MF}}}]/Z$, with $Z = \mathrm{Tr}[e^{-\beta\hat{\mathcal{H}}^{\mathrm{sg}}_{\mathrm{MF}}}]$, with $\beta = 1/k_BT$. Because we find that the bulk magnetic susceptibility of $CsYbSe_2$ is almost entirely uniaxial, we make the additional simplifying assumption that the external magnetic field lies in the xz-plane, such that $\mathbf{H} = H_{\perp}\hat{\mathbf{x}} + H_z\hat{\mathbf{z}}$.

The precise determination of the mean-field Hamiltonian given in Eq. (6.5) poses a major challenge because it contains eight unknown parameters, six coefficients $\{B^n_m\}$ of the Stevens operators in Eq. (6.1) and two energy scales, $\mathcal{J}_{\perp}$ and $\mathcal{J}_z$, specifying the interactions of the $J = 7/2$ spins. INS spectra are used widely to extract the coefficients B^n_m [104, 105], but as noted above measuring the three CEF level-splittings, Δ_{10}, Δ_{20}, and Δ_{30} [Fig. 6.1(c)], is not sufficient to determine six unknowns. Thus the parameter space for fitting the measured CEF spectra usually remains highly degenerate, even with accurate spectral measurements in an applied field and well-constrained g-tensors, and hence the uniqueness of a fitted set of Stevens-operator coefficients cannot be guaranteed [39, 113, 47]. The method we apply to solve this problem has two key components. First we apply a detailed consideration of the second-order corrections in the field-dependence of the CEF spectrum, encoded as the VV coefficients we extract from the low-field susceptibility. Then we leverage extensive RTM data providing systematic temperature- and field-dependent information about the magnetotropic coefficients for the two high-symmetry field directions to fix a unique set $\{B^n_m\}$.

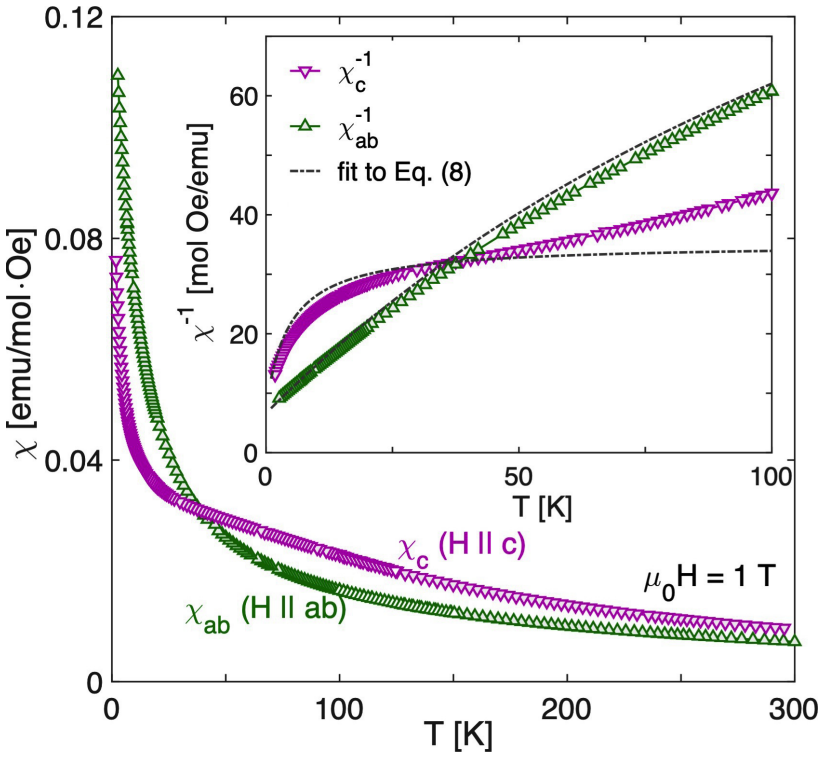

Figure 6.2: Temperature-dependence of the magnetic susceptibilities, χ_{ab} and χ_c, measured for $CsYbSe_2$ in a field of $\mu_0 H = 1$ T applied respectively in the ab and c directions. The inset shows the inverse susceptibilities, χ_{ab}^{-1} and χ_c^{-1}, compared with fits obtained by applying Eq. (6.8) in the regime $T \leq 45$ K ($\ll \Delta_{10}/k_B$) in order to determine the interaction parameters, $\mathcal{J}_\perp$ and $\mathcal{J}_z$, and the VV coefficients, $\alpha_\perp^0$ and α_z^0, for the ground-state doublet.

6.3 Anisotropic magnetic susceptibilities

6.3.1 Experiment: deviations from Curie-Weiss

In Fig. 6.2 we show the temperature-dependences of the two magnetic susceptibilities, $\chi_{ab}(T)$ and $\chi_c(T)$, measured for $CsYbSe_2$ in the presence of an external magnetic field $\mu_0 H = 1$ T applied respectively within the ab plane and along the c axis. There is no indication of long-range ordering down to $T = 2$ K. The crossing of the two curves around $T = 35$ K reflects a crossover from easy-plane behavior ($\Delta\chi = \chi_{ab} - \chi_c > 0$) at low temperatures to easy-axis anisotropy ($\Delta\chi < 0$) at high T.

Both susceptibilities increase rapidly as the temperature is lowered below 50 K, and the corresponding inverse quantities shown in the inset of Fig. 6.2 make clear the susceptibility anisotropy,

with $\chi_c^{-1}(T)$ exhibiting a significantly sharper downward trend as T decreases. While a qualitative inspection suggests that a Curie-Weiss form might capture $\chi_{ab}^{-1}(T)$ for $T < 50K$, this is clearly impossible for $\chi_c^{-1}(T)$. This type of low-T downturn in $\chi^{-1}(T)$ is observed quite commonly in similar rare-earth magnetic materials [120, 109, 111, 106, 127, 38], but to date lacks a detailed analysis. Next we show that this behavior can be explained entirely by analyzing the field-induced evolution of the CEF energy levels, where the leading deviations from a linear (effective Zeeman) form are contained in two strongly anisotropic ground-state VV coefficients.

Table 6.1: Comparison of the lowest zero-field CEF level-splitting, Δ_{10}, g-tensor components, and the VV coefficients for $n = 0$ in a number of Yb-based triangular-lattice compounds. For $CsYbSe_2$ we show two sets of g-factors and VV coefficients, one obtained by a full calculation [Eq. (6.7)] using the B_m^n coefficients and wave functions, i.e. assisted by fitting to the RTM data as shown in Sec. 6.4, and the other from fitting $\chi_{ab,c}(T)$ using Eq. (6.8). For the other compounds, Δ_{10} and the g-factors are quoted from the respective references and we calculated the VV coefficients using the reported B_m^n coefficients. The compound nominally most similar to $CsYbSe_2$, $NaYbSe_2$, displays slightly less anisotropy in its VV coefficients and this is consistent with the differing forms of $\chi_{ab}(T)$ and $\chi_c(T)$ reported in Ref. [111]. For $NaYbO_2$ we note that the two sets of Stevens coefficients (Fit 1 and Fit 2) deduced in Ref. [113] yield dramatically different values of $\alpha_\perp^0$ and α_z^0, which underlines the crucial role of the VV coefficients in a complete and consistent characterization of . $YbMgGaO_4$ is found to be least anisotropic among these materials, and its small VV coefficients are consistent with the reported Curie-Weiss form of the susceptibility.

	Δ_{10} [meV]	$g_\perp$	g_z	$\alpha_\perp^0$ $[10^{-4}\frac{\text{meV}}{\text{T}^2}]$	α_z^0 $[10^{-4}\frac{\text{meV}}{\text{T}^2}]$	Reference
$CsYbSe_2$	13.6	3.52	1.33	-3.31	-18.8	calculated from Eq. (6.5)
$CsYbSe_2$	–	3.77	1.76	-2.93	-17.9	$\chi_{ab,c}(T)$ fit to Eq. (6.8) [Fig. 6.2]
$NaYbSe_2$	17.5/17.7	2.87/2.87	1.18/1.33	-5.51/-5.44	-12.5/-18.8	Fit 1/Fit 2 in Ref. [47]
$NaYbSe_2$	13.8	3.13	1.01	–	–	electron-spin resonance [111]
$NaYbO_2$	34.0/34.7	3.39/3.54	1.71/1.75	$-1.10/-2.85$	$-7.39/-3.62$	Fit 1/Fit 2 in Ref. [113]
$NaYbS_2$	16.7	3.19	0.57	-	-	electron-spin resonance Ref. [109]
$YbMgGaO_4$	39.3/39.4	3.22/3.21	3.70/3.73	$-2.25/-2.29$	$-2.60/-2.58$	Fit 1/Fit 2 in Ref. [39]

6.3.2 Van Vleck coefficients and low-field limit

The splitting of the CEF levels in a finite applied magnetic field can be understood systematically by perturbation theory. We express the H-linear and -quadratic corrections to the energy

eigenvalues of $\hat{\mathcal{H}}_{\rm CEF}$ due to $\hat{H}_{\rm Z}$ in the form

$$E_{n,\pm}(H) = E_n^0 \pm \tfrac{1}{2}\mu_0\mu_B\sqrt{(g_\perp^n H_\perp)^2 + (g_z^n H_z)^2} + \alpha_\perp^n H_\perp^2 + \alpha_z^n H_z^2 + \mathcal{O}(H^3), \tag{6.6}$$

where E_n^0 refers to the four CEF energy levels at zero field (and setting the ground-state energy, E_0^0, to zero gives $E_n^0 = \Delta_{n0}$ for n = 1, 2, and 3). The second term describes the H-linear Zeeman splitting with a generalized g-tensor for all levels (n = 0, 1, 2, 3) defined as $g_{\perp(z)}^n = 2g_J\langle n_\pm|\hat{J}_{x(z)}|n_{\mp(\pm)}\rangle$, where the subscripts $\perp, z$ denote a field applied respectively within the ab-plane or along the c-axis. The conventional effective spin-1/2 g-tensor components are $g_\perp^0$ and g_z^0, to which we refer henceforth, without the superscript 0, as the g-factors of the system.

We define all of the phenomena obtained at second order in the perturbative effect of $\hat{H}_{\rm Z}$ on the zero-field eigenstates of $\hat{H}_{\rm CEF}$ as the VV contribution. To describe the full field- and temperature-dependence of the susceptibility we define the VV coefficients, $\alpha_\perp^n$ and α_z^n, for the nth CEF level by

$$\alpha_{\perp(z)}^n = (\mu_0\mu_B g_J)^2 \sum_{n'\neq n} \frac{|\langle n'_\pm|\hat{J}_{x(z)}|n_+\rangle|^2}{\Delta_{nn'}}, \tag{6.7}$$

where $\Delta_{nn'} = E_n^0 - E_{n'}^0$. Although it is often stated that one may define a "VV susceptibility," $\chi_{\rm VV}$, that is a small, additive, temperature-independent, and paramagnetic contribution to the total susceptibility, this is rarely an accurate approximation. By inspecting the form of the VV coefficients, one observes that the $n = 0$ terms should be negative, giving the expected type of 2nd-order correction to the ground state. The physics content of the anisotropic VV coefficients can be read from Fig. 6.1(c), where the field-dependence of the CEF levels is quite strongly nonlinear due to level-repulsion effects between adjacent doublets. In $CsYbSe_2$ this repulsion, which is equivalent to a negative curvature of the lower (and positive of the upper) branch in each case, is strongest between the $n = 0$ and 1 doublets for $H \parallel c$.

We obtain analytical formulas for the low-field magnetic susceptibilities of the system by using the N-particle partition function calculated with Eq. (6.5). The full expression for $\chi_{ab(c)}(T)$, which includes the contributions of all four CEF levels, is presented in Eq. (2.26) of sec. 2.4.

Here we focus on the regime of temperatures sufficiently small that only the lowest-lying Kramers doublet need be considered, i.e. $k_BT \ll \Delta_{10}$, and write the inverse susceptibility as

$$\begin{aligned}\chi^{-1}_{ab(c)} &= \frac{1}{\mathcal{C}}\left[\frac{T}{|\langle 0_+|\hat{J}_{x(z)}|0_{-(+)}\rangle|^2 - \frac{2k_B\alpha^0_{\perp(z)}}{\mu_0^2\mu_B^2 g_J^2}T} + \Theta^{\rm CW}_{\perp(z)}\right] \\ &= \frac{\mu_0 k_B}{N}\left[\frac{T}{\frac{1}{4}g^2_{\perp(z)}\mu_0^2\mu_B^2 - 2\alpha^0_{\perp(z)}k_BT} + \Theta^{\rm CW}_{\perp(z)}\right], \end{aligned} \tag{6.8}$$

where $\mathcal{C} = N\mu_0\mu_B^2 g_J^2/k_B$ is a constant. We have defined the quantities $\Theta^{\rm CW}_{\perp(z)} = q\mathcal{J}_{\perp(z)}/k_B$ in order to obtain an adapted Curie-Weiss (CW) form for the two applied-field directions and in the second line we have used the definition of the g-factors (above) to make this form more transparent. We note that the regime of validity of Eq. (6.8) is also that in which the system can be approximated by an effective pseudospin-1/2 description.

It is clear from Eq. (6.8) that the contrast to a conventional CW form, $\chi^{-1} \propto T + \widetilde{\Theta}$, is the additional T-linear term in the denominator, whose prefactor is the corresponding VV coefficient. The key advantage of our formulation is to observe that the same (VV) coefficients describing the H^2 correction that gives the leading nonlinear contribution to the CEF levels at low temperatures and finite fields [Eq. (6.6)] are those describing the nonlinear, "beyond-CW" form of the susceptibility at zero field and finite temperatures [Eq. (6.8)]. Thus one may conclude that the latter effect is also related to level-repulsion between doublets, the fact that the susceptibility is a second field derivative of the free energy meaning that second-order perturbative effects do not vanish in the limit $H \to 0$.

Returning to Fig. 6.2, the gray dashed lines in the inset show fits to Eq. (6.8), made in the regime $T < 45$ K, for each field direction. From these fits we obtain two exchange energies, $\mathcal{J}_\perp$ and $\mathcal{J}_z$ in Eqs. (6.2) and (6.5), and two VV coefficients for the ground-state doublet. A complete fit is deferred to Sec. 6.5. Starting with the VV coefficients, we find the values $\alpha^0_\perp = -(2.9 \pm 0.1) \times 10^{-4}$ meV/T^2 from χ^{-1}_{ab} and $\alpha^0_z = -(17.9 \pm 0.1) \times 10^{-4}$ meV/T^2 from χ^{-1}_c. We stress that α^0_z is six times larger than $\alpha^0_\perp$, which for all fields beyond 5 T becomes clearly manifest as a much larger downward level-repulsion of the lowest Kramers doublet [Fig. 6.1(c) and the quantitative analysis of Sec. 6.5].

Turning to the magnetic interactions, we find $\mathcal{J}_\perp = 0.54 \pm 0.01$ K from χ_{ab} and $\mathcal{J}_z = 0.61 \pm 0.01$ K from χ_c, both encapsulated in $\Theta^{\rm CW}_{\perp(z)}$. If one reduces the system to an effective pseudospin-1/2 model, the corresponding interaction terms are $\mathcal{J}'_\perp = 5.12$ K ($\simeq 0.44$ meV) and $\mathcal{J}'_z = 0.84$ K ($\simeq 0.07$ meV), as detailed in Eqn 2.17 of Sec. 2.3.2. We discuss the physical implications of these interaction parameters in Sec. 6.5B.

As noted above, downward curvature of the low-temperature χ^{-1} has been observed in other rare-earth compounds and our fitting results demonstrate that this feature should be characterized by using the VV coefficients as a part of a full description of the anisotropic magnetism. The validity of Eq. (6.8) as a replacement for the CW form of the susceptibility is confirmed by capturing the different T-dependences correctly for the two field directions with two VV coefficients that are consistent with Eq. (6.6). Although the VV coefficients are not parameters appearing directly in the system Hamiltonian, they impose constraints that are essential for a unique determination of the full parameter set, a topic we discuss further in the next section.

In Table 1 we compare the VV coefficients and other physical characteristics for a variety of Yb delafossites. For all compounds listed other than $CsYbSe_2$, the Δ_{10} and g-tensor parameters are taken from experimental data. All $\alpha^0_\perp$ and α^0_z values were calculated from Eq. (6.7) using the Stevens coefficients (B^n_m) provided by each reference, where they were obtained from fits to the CEF spectrum obtained by INS. We stress again the fact that, in several of the studies cited, different sets of Stevens coefficients can provide equally good descriptions ("Fit 1" and "Fit 2") of the same INS data due to the underconstrained nature of the problem. The anisotropy of $CsYbSe_2$, $\alpha^0_z/\alpha^0_\perp \approx 6$, is strikingly higher than the values reported for other compounds in the same family. Although all of the $NaYbX_2$ materials seem to show considerable directional anisotropy, this may not apply to $NaYbO_2$, except that the two sets of proposed B^n_m parameters yield wildly different VV coefficients, indicative of an underlying ambiguity of the type we demonstrate how to resolve. In this regard the sole non-delafossite in Table 1, $YbMgGaO_4$, is a nearly isotropic outlier.

Before proceeding, we reiterate two important attributes of the VV coefficients as a mean of characterizing the magnetic anisotropy of a CEF system. First, nonzero VV coefficients are imme-

diately evident in $\chi(T)$, as strong deviations from a CW form, and thus failure to account for them means that the interaction parameters, $\mathcal{J}_{\perp,z}$, cannot be determined correctly. Second, it is evident from Eq. (6.8) that caution is required in applying an effective pseudospin-1/2 description, because even at low T, where only the lowest Kramers doublet is thermally populated, the repulsion from the higher CEF levels cannot be ignored. Hence the twin roles of the anisotropic VV coefficients in dictating H- and T-dependent physical properties generic to many $4f$ electronic systems (Table 1) must be taken into account to obtain a meaningful description of the spin physics.

6.4 Resonant Torsion Magnetometry

6.4.1 Dependence on Field and Temperature

Having characterized the magnetic response at low fields using $\chi(T)$, and thereby obtained four independent physical quantities to include in the fitting procedure, we turn for more information to the magnetropic coefficients. The RTM method allows these to be measured over wide ranges of both field and temperature, which we will show provides enough input for an unambiguous determination of all the remaining free parameters in Eq. (6.5). The magnetotropic coefficient is defined as $k(H,\vartheta) = \partial^2 F(H,\vartheta)/\partial\vartheta^2$, where $F(H,\vartheta)$ is the portion of the Helmholtz free energy depending on the magnitude and orientation of the magnetic field (ϑ is the angular direction of $\hat{H}$ measured in the plane of vibration of the sample [25, 26]). k quantifies the magnetic rigidity of a material, whose origin lies in the energy cost of rotating a sample with an anisotropic magnetic free energy in a finite field, and RTM measurements constitute a highly sensitive probe of this magnetoanisotropy.

The variation of the magnetotropic coefficients at finite field produces a shift in the resonant frequency of a system composed of a cantilever and an attached sample given by

$$\frac{\Delta f}{f_0} = \frac{k}{2K}, \tag{6.9}$$

with K the intrinsic bending stiffness of the cantilever at zero field [25, 26]. In the low-field limit, where χ is constant at constant temperature, both the torque and the magnetotropic coefficient

are not only straightforward functions of the polar angle, θ, but are also quadratic in H. Thus the magnetotropic coefficient can be expressed in terms of the difference, $\Delta\chi = \chi_{ab} - \chi_c$, between the principal components of the susceptibility tensor in the plane of vibration, as $k = \Delta\chi H^2 \cos 2\theta$. More detailed derivations of field-dependent expressions for the high-symmetry angles (k_{ab} for $\theta = 0$ and k_c for $\theta = \pi/2$) can be deduced by introducing the transverse susceptibility, as shown in Eqn. 4.31 of Sec. 4.2.1.

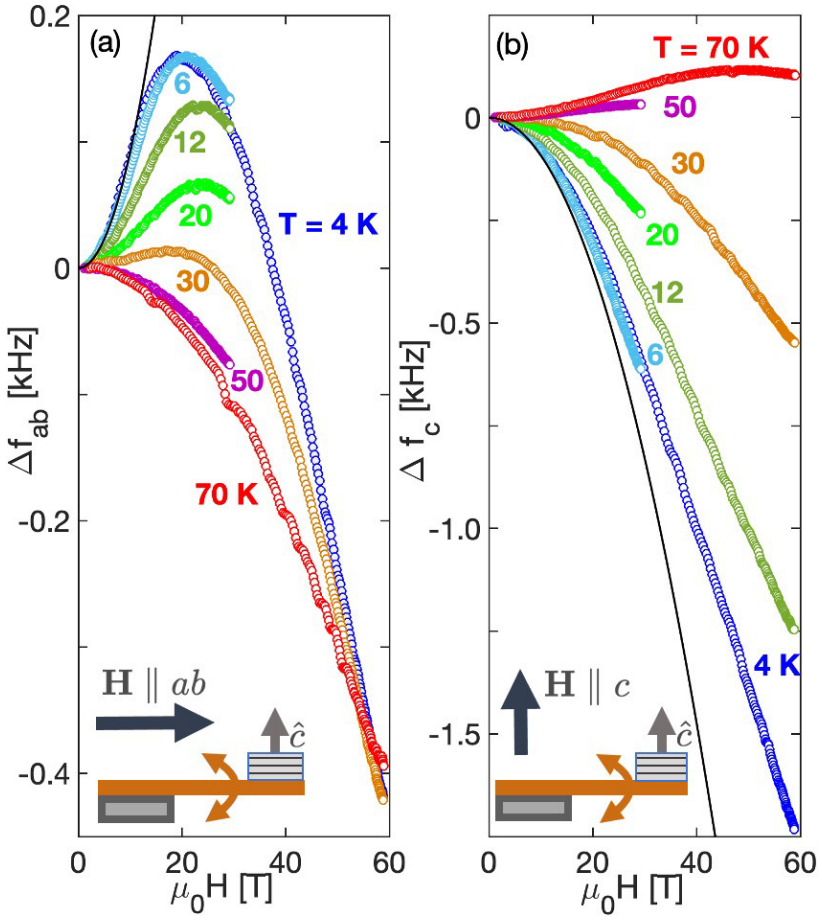

Figure 6.3: Dependence on the applied field magnitude of the resonant frequency shifts (a) Δf_{ab} for $H \parallel ab$ ($\theta = \pi/2$) and (b) Δf_c for $H \parallel c$ ($\theta = 0$). Thin solid lines show the low-field H^2 dependences, with coefficients of $\Delta\chi$ and $-\Delta\chi$, taken at $T = 4$ K from Fig. 6.2. The nonmonotonic H-dependence leading to a local maximum in the $H \parallel ab$ configuration is attributed to the saturation of the magnetization and is explained in Sec. 6.5 by considering the effective susceptibility in the transverse direction. The insets illustrate the applied-field configurations of the RTM measurements on the layered triangular lattice of $CsYbSe_2$ in each case.

Figures 6.3(a) and 6.3(b) show the frequency shifts, Δf_{ab} and Δf_c, which are directly pro-

portional to the magnetotropic coefficients, k_{ab} and k_c [Eq. (6.9)], as functions of field in the $H \parallel ab$ and $H \parallel c$ geometries. We note that the vibration plane of the cantilever and the rotation plane of H are the same, meaning that in this experimental configuration the angle ϑ of Eq. (4.26) is identically the polar angle, θ, relative to the crystallographic c-axis.

At low fields, where χ_{ab} and χ_c are H-independent constants (i.e. the magnetizations m_{ab} and m_c are linear in H), both k_{ab} and k_c are indeed proportional both to H^2 and to $\Delta\chi$ with opposing signs. As the temperature is increased, $\Delta\chi(T)$ in Fig. 6.2 changes its sign above 50 K, and this is reflected in the sign-changes of Δf_{ab} and Δf_c between $T = 30$ and 50 K.

As the field is increased, $\Delta f_{ab}(H)$ deviates from an H^2 dependence and becomes nonmonotonic, with a local maximum at low temperatures [$T \leq 30$ K in Fig. 6.3(a)]. The origin of this behavior lies primarily in $m_{ab}(H)$ saturating in this field range, which we confirm from our calculations in Sec. 6.5. By contrast, the behavior of $\Delta f_c(H)$ remains monotonic in the same T range, where $m_c(H)$ continues to increase with H. We comment that $\Delta f_c(H)$ does exhibit a weak maximum in H at $T = 70$ K, whereas no such behavior is found in Δf_{ab} at this temperature. This feature is also captured qualitatively by calculating the eigenstates of the full mean-field Hamiltonian [Eq. (6.5)], as we show next.

6.4.2 Fitting k_{ab} and k_c

Taking the magnetic interaction parameters $\mathcal{J}_\perp$ and $\mathcal{J}_z$ determined from $\chi_{ab,c}(T)$ [Fig. 6.2], we fit the measured data for $k_{ab}(H)$ and $k_c(H)$ using the full mean-field Hamiltonian based on Eq. (6.5), in which the six coefficients of the Stevens operators are free parameters to be determined. However, obtaining the ground-state VV coefficients, $\alpha_\perp^0$ and α_z^0, from the fit to Eq. (6.8) reduces the number of fitting parameters to four. Given the wide ranges of T and H covered by the RTM data, the remaining unknowns can be determined with an unprecedentedly high level of confidence by using k_{ab} and k_c.

Figure 6.4 displays the magnetotropic coefficients converted from the measured Δf data in both geometries. It is clear that the fits capture the full field-dependence of $k_{ab}(H)$ and $k_c(H)$

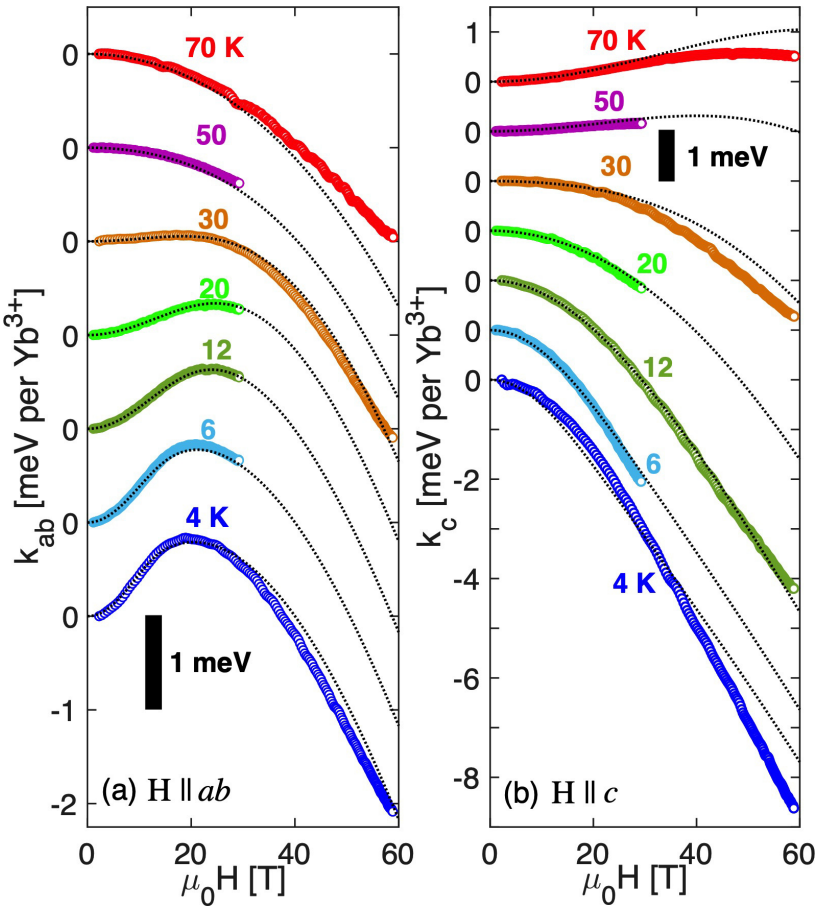

Figure 6.4: Magnetotropic coefficients, k_{ab} and k_c, shown per Yb^{3+} ion as a function of field in the respective geometries $H \parallel ab$ (a) and $H \parallel c$ (b). Open symbols mark measured data and dotted lines show the best fits achieved by self-consistent diagonalization of the full mean-field Hamiltonian [Eq. (6.5)]. The values of $\mathcal{J}_\perp$ and $\mathcal{J}_z$ are taken from the susceptibility fits [Fig. 6.5], leaving the six coefficients of the Stevens operators as free parameters constrained by the extracted VV coefficients, $\alpha^0_\perp$, and α^0_z. Curves are shown for clarity with a constant offset.

Table 6.2: Values of the Stevens-operator coefficients [Eq. (6.1)] obtained from the fits shown in Fig. 6.4.

unit	B_2^0	B_4^0	B_4^3	B_6^0	B_6^3	B_6^6
10^{-2} meV	-42.33	1.17	54.94	0.03	0.52	-0.04

in an excellent manner, despite the minimal spin model and the mean-field approximation. In particular, the low-field H^2 curvature is fully consistent with $|\Delta\chi|$ (Sec. 6.4A). At $\mu_0 H > 30$ T, beyond the range of some of the data, the agreement is no longer quantitative for all temperatures simultaneously, but the model continues to capture the majority of the field-dependent behavior for

both field directions. One possible source of these deviations would be high-field magnetostrictive effects, which can distort the lattice structure and thus modify both the magnetic interactions and possibly even the sizes of the CEF coefficients at sufficiently large applied fields [128]. We use the optimal fits to obtain the six Stevens-operator coefficients [Eq. (6.1)] shown in Table 2 and we discuss the physical implications of having this fully determined spin Hamiltonian [Eq. (6.5)] in the next section.

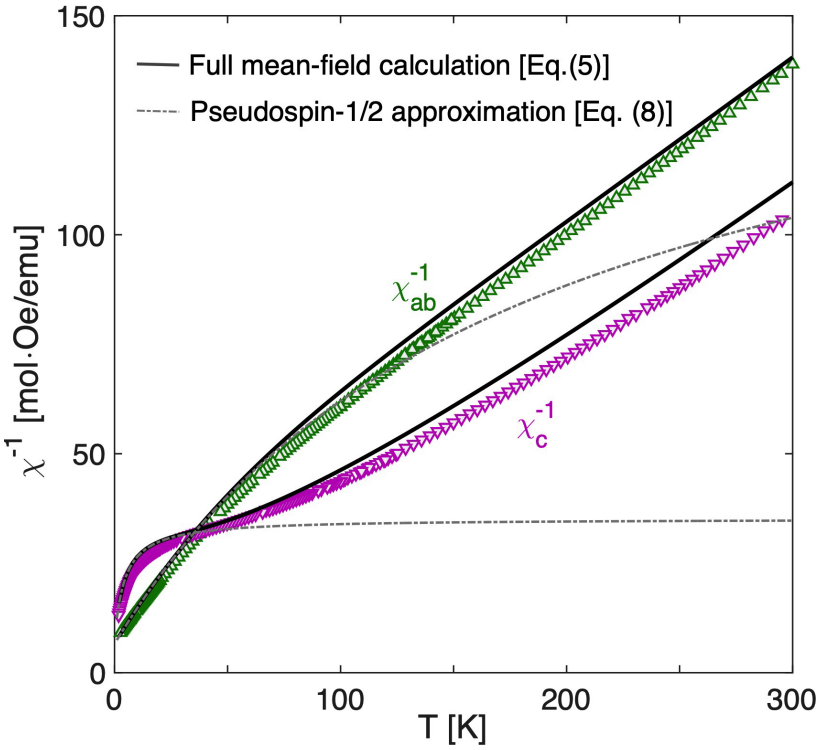

Figure 6.5: Data for the measured inverse susceptibilities (symbols, inset Fig. 6.2) shown over the full range of temperature together with fits (solid lines) computed using the Stevens-operator coefficients of Table 2. Thin dot-dashed lines show fits obtained from a pseudospin-1/2 description [Eq. (6.8)] applied at low temperatures, which align well with the full matrix calculation for $T < 60$ K.

6.5 Discussion

6.5.1 CEF spectrum and VV coefficients

Having determined a full set of eight fitting parameters from the RTM data, we first verify the self-consistency of this fit against the measured magnetic susceptibilities, which are shown as $\chi_{ab}^{-1}(T)$ and $\chi_{c}^{-1}(T)$ over the full temperature range in Fig. 6.5. The solid lines show the same quantities calculated from the mean-field Hamiltonian of Eq. (6.5). The agreement of the fit with the data is quantitatively excellent over the entire measured T range, including temperatures allowing significant population of the higher CEF levels. The dot-dashed lines were calculated using the pseudospin-1/2 approximation, i.e. the contributions from the ground-state doublet [Eq. (6.8)], which as expected captures the T-dependence below a specific energetic cut-off; by inspection we find this cut-off at $T \approx 60$ K in $CsYbSe_2$ for both directions of $\hat{H}$.

As discussed in Sec. 6.3, the difference in T-dependence for the two primary field directions is accounted for in the modelling procedure by the large discrepancy in the VV coefficients. While this anisotropy is also reflected in the very different prefactors of the H-quadratic part of the energy spectrum for the two different field geometries, we stress again the fact that it affects the susceptibility strongly even at zero field. As a consequence, the susceptibility fits in Fig. 6.2 provide an independent determination of $\alpha_{\perp}^{0}$ and α_{z}^{0}, as well as of the squared matrix elements $|\langle|0_{\pm}|\hat{J}_{x(z)}|0_{\mp(\pm)}\rangle|^2$. These constitute additional constraints on the allowed Stevens-operator coefficients that are crucial for reducing the enormous degeneracy of the six-variable parameter space describing the CEF levels. It is well known that suitable sets of coefficients are often highly degenerate, in the sense of yielding many indistinguishable fits of INS data for the CEF spectrum and g-tensor values [39, 113, 104]. In Table 1, we compare the ground-state g-tensor values and VV coefficients obtained by fitting $k_{ab,c}(H)$ (top line, Fig. 6.4) and χ^{-1} (second line, Fig. 6.5), where we find agreement at the 10% level.

Next we use our fit coefficients to calculate the CEF energy levels, which are shown in Fig. 6.6 as a function of field at zero temperature. The black solid lines show the spectra calculated, for $\hat{H}$

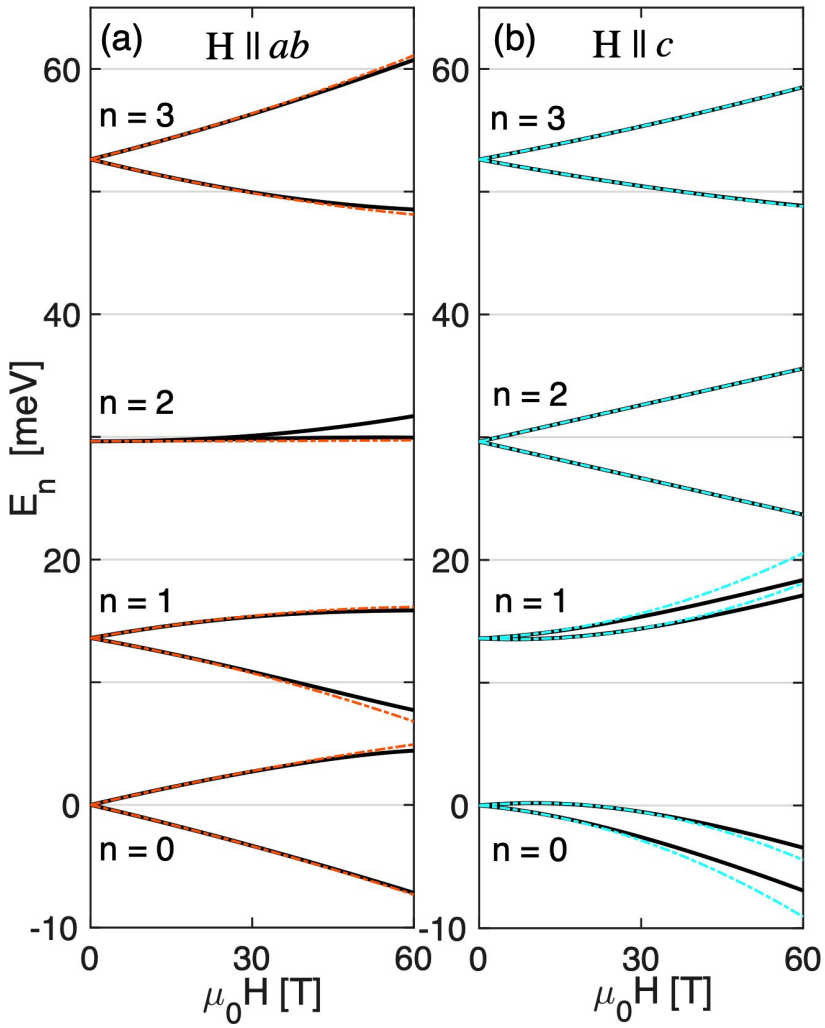

Figure 6.6: CEF spectrum calculated using the fitting result from Fig. 6.4] (solid lines). Quadratic and higher-order dependences on the applied field are clearly visible for all four Zeeman-split Kramers doublets. We comment that the $n = 2$ level remains mostly degenerate in fields $\mathbf{H} \parallel ab$ because of their dipolar-octupolar nature. Dot-dashed lines show the perturbative expression of each energy level at second order, as in Eq. (6.6).

oriented in the ab-plane [panel (a)] and along the c-axis [panel (b)], by the direct diagonalization of $\hat{\mathcal{H}}_{\rm CEF} + \hat{\mathcal{H}}_{\rm Z}$. Focusing first on zero field, we obtain the level-splittings $\Delta_{10} = 13.6$ meV, $\Delta_{20} = 29.6$ meV, and $\Delta_{30} = 52.6$ meV. Thus Δ_{10} in $CsYbSe_2$ is similar to that of $NaYbSe_2$ (≈ 17.7 meV [47]), but is significantly lower than the values reported for delafossites in which the Yb^{3+} ion has an oxygen environment [113, 39]. The g-factor values we obtain for the ground state, $g_{ab} = 3.52$ and $g_c = 1.33$, are comparable to those measured in all of the Yb-based delafossites, as summarized in

Table 1.

Turning to finite fields, a comparison of the ground-state doublet ($n = 0$) in Figs. 6.6(a) and 6.6(b) shows the expected strong anisotropy, which lies predominantly in the fact that the H-quadratic component is much larger for $H \parallel c$ (the aforementioned factor-6 difference between α_z^0 and $\alpha_\perp^0$). Because the quadratic curvatures are a consequence of repulsion between adjacent CEF levels, the $n = 1$ doublet exhibits a clear opposing curvature for $H \parallel c$ (dominating the behavior of both doublet components), whereas in the $H \parallel ab$ configuration this effect is weaker than the higher-order corrections. The dot-dashed lines in Fig. 6.6 illustrate the fidelity of a fit made only at the level of second-order energy corrections for each n [Eq. (6.6)], i.e. by using all the VV coefficients, which agrees well until $\mu_0 H > 50$ T in both $\hat{H}$ directions.

Moving up in the CEF spectrum, our results also capture the unique properties of the $n = 2$ state. This dipolar-octupolar doublet, $|J, m_J = \pm 3/2\rangle$ [6, 106, 127, 4], does not transform as a magnetic dipole because the threefold rotational symmetry excludes any mixing between states with $m_J = \pm 3/2$ and those with other values of m_J [129]. Instead this doublet combines the features of dipolar and octupolar moments [106, 127]. In particular, only one component of the dipole moment (in this case oriented along the c-axis) appears in the vector of pseudospin-1/2 operators, which makes the Zeeman splitting of the $n = 2$ level appear very different between $H \parallel ab$ and $H \parallel c$. In the latter case, the $m_J = 3/2$ state remains an exact eigenstate up to arbitrarily large field, so the Zeeman splitting is exactly H-linear with no higher-order perturbative corrections [Fig. 6.6(b)], i.e. $\alpha_z^2 = 0$. By contrast, for $H \parallel ab$ the matrix elements $\langle 2_\pm | J_x | 2_\mp \rangle$ are zero and the H-linear Zeeman splitting vanishes ($g_\perp^2 = 0$). Thus these doublet components remain nearly degenerate [Fig. 6.6(a)] until the field is sufficiently strong that higher-order perturbative corrections become visible.

A further key experimental quantity we consider is the magnetization. The solid lines in Fig. 6.7 show the magnetization of the system at several different temperatures calculated for fields in the two primary directions using the full Hamiltonian matrix [Eq. (6.5)]. In the low-field range, m_{ab} and m_c reproduce exactly our experimental data measured up to $\mu_0 H = 7$ T. At higher

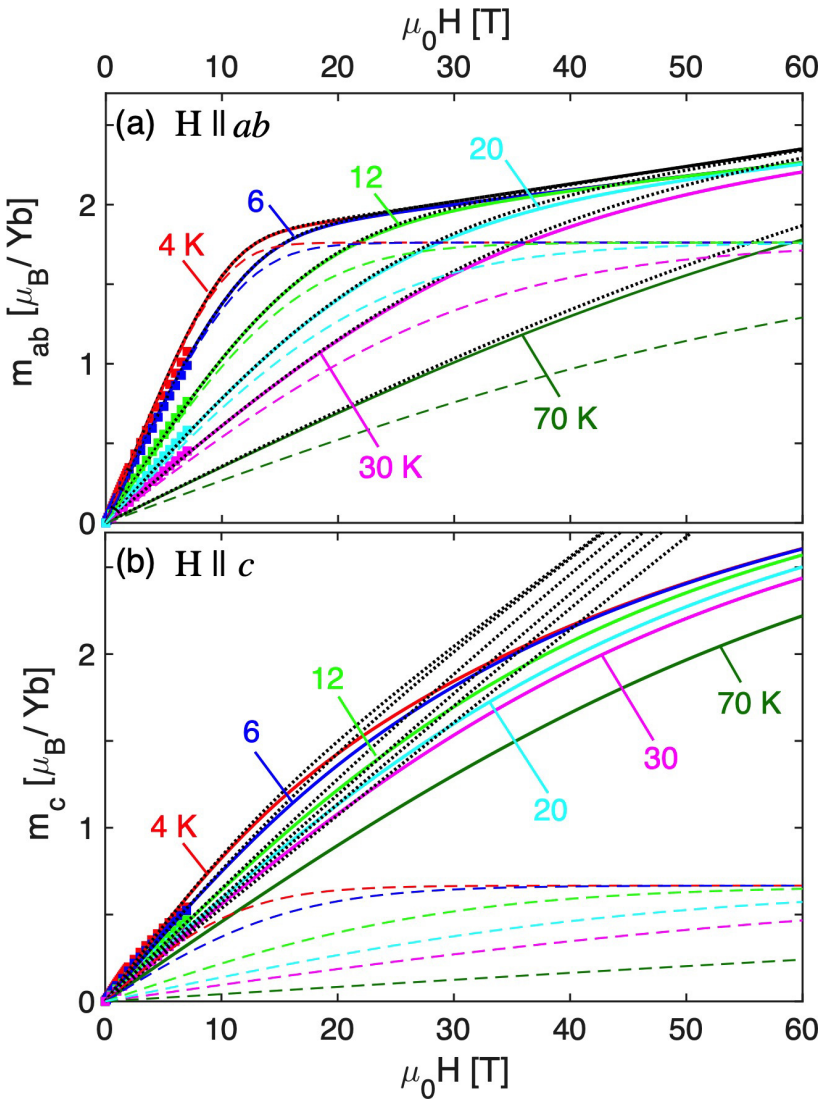

Figure 6.7: Magnetizations, m_{ab} (a) and m_c (b), calculated for selected values of the temperature from Eq. (6.5) (solid lines), in a pseudospin-1/2 approximation with VV corrections (dotted lines), and in a pseudospin-1/2 approximation without VV corrections (dashed lines). Solid symbols show magnetization data measured up to 7 T.

fields, m_{ab} calculated from the full spectrum begins to saturate at $\mu_0 H \approx 12$ T (at $T = 4$ K), beyond which it continues to increase more slowly with increasing field. This behavior is consistent with the broad maximum in the RTM frequency shift, $\Delta f_{ab}(H)$, at low temperatures (Fig. 6.3). Such a saturation is absent in m_c, although the overall slope does decrease as H is raised beyond approximately 25 T. This behavior is not immediately evident in the RTM measurements, but can be found within the detailed H-dependence of the free energy, which we parameterize using the

transverse susceptibilities, $\chi^T_{ab}(T)$ and $\chi^T_c(T)$, in 4.31.

Finally, the magnetization presents an excellent test case for the validity of a pseudospin-1/2 description of $CsYbSe_2$, meaning the extent to which any physical property is explained by the contributions from the ground-state doublet ($n = 0$) alone. In Figs. 6.7(a) and 6.7(b) we show in addition the magnetizations obtained using a pseudospin-1/2 approximation with (dotted lines) and without (dashed lines) the VV correction. For reference, the efficacy of the VV corrections in reproducing the full field-induced evolution of the ground doublet can be gauged in Fig. 6.6. For $m_{ab}(H)$, a pseudospin-1/2 model with no VV correction captures the field-dependence up to $\mu_0 H \approx 10$ T before flattening to the generic tanh function of a Zeeman doublet. By contrast, a model with VV correction follows the full solution very closely over the entire field range to 60 T. This contrasts with the situation for $m_c(H)$, where even the VV-corrected model shows a clear departure from the full solution that sets in around 15 T, beyond which the approximate treatment separates systematically, and it is clear that higher-order corrections to the doublet spectrum are required. For the model with no VV correction, $m_c(H)$ does not even reproduce the low-field regime. Recalling the very significant magnetic anisotropy ($\alpha^0_z/\alpha^0_\perp \approx 6$), the effectiveness of the VV corrections for the two directions is no surprise. As a function of temperature, we observe that the VV-corrected magnetizations in both geometries show increasing discrepancies at the same field as T is increased to 70 K (Fig. 6.7), even though the nominal thermal cutoff imposed by the next CEF level is $\Delta_{10}/k_B \approx 160$ K.

Thus our experiments and analysis demonstrate two key results. The first is that all of the nontrivial magnetic properties of a material are captured by a single concept, the VV coefficients. The second is that the contrast between conventional and nontrivial magnetic properties can be found in a single material due to anisotropic VV coefficients that differ strongly between the field geometries $H \parallel ab$ and $H \parallel c$. We have shown that the origin of the VV coefficients lies in the large matrix elements governing the mixing and consequent repulsion of adjacent CEF levels. Although the ground-state VV coefficients, $\alpha^0_\perp$ and α^0_z, are zero-field quantities whose effects can be found in non-CW behavior of the susceptibility, their strongest impact emerges as H increases

(Fig. 6.6). Our analysis also demonstrates that the success or failure of the popular pseudospin-1/2 approximation to the magnetic properties of a Kramers-doublet system depends directly on the magnitude of the VV coefficients.

Our conclusions rely completely on determining all of the CEF parameters with high accuracy, which allows a detailed characterization of all the magnetic properties throughout the (H, θ, T) parameter space within a single and self-consistent model. The simplest indication for a significant contribution from the VV coefficients is a deviation of the susceptibility from a CW form, which is visible most clearly as a downward curvature in $\chi^{-1}(T)$ as $T \to 0$; this type of behavior is obvious in $\chi_c^{-1}(T)$ in Fig. 6.5, but not in $\chi_{ab}^{-1}(T)$. As noted above, a more detailed characterization of the VV coefficients requires experiments under significant applied fields. Quantitatively, the origin of the VV coefficients in second-order perturbation theory [Eq. (6.7)] gives them a systematic dependence on Δ_{n0}^{-1}, as well as on the expectation values of $\hat{J}_{x(z)}$. Although the latter terms are primarily responsible for the strong directional anisotropy in the Yb-based delafossites whose reported Δ_{10} values and extracted VV coefficients are collected in Table 1, the related material $YbMgGaO_4$ presents an example where the large value of Δ_{10} suppresses the VV coefficients, leading to a predominantly CW-type behavior of $\chi^{-1}(T)$ [116].

We stress again that our full microscopic model is directly applicable to the computation of all aspects of the magnetic response of a material. Here we have illustrated the situation for our own magnetic susceptibility, magnetization, and RTM data, and we await its extension to describe magnetic specific-heat, torque and magnetocalorimetric measurements. We have also distilled the properties of the full model to the physically relevant VV coefficients, which can be understood as governing the nonlinear field-dependence of the CEF energy levels (Fig. 6.6) and thus affect all of the magnetic properties. This linking function allows the use of our analysis to resolve a number of contradictions that have emerged in recent studies of delafossites by different techniques. One example is the report from single-crystal INS measurements on $CsYbSe_2$ of no CEF levels below 20 meV [123], in direct contradiction to the present conclusions (Fig. 6.6). By using the diagonalized CEF matrix to calculate the scattering cross-section in the crystalline geometry of the measurement,

we find that the INS cross-section for the $0 \rightarrow 1$ transition is four orders of magnitude weaker than that expected for a polycrystalline sample. We note also that the two sets of Stevens-operator coefficients proposed [107] for $NaYbO_2$ based on INS measurements of the CEF spectrum have widely divergent VV coefficients, whereas similar fits to the INS spectra of $NaYbSe_2$ show much more agreement when refined with complementary Raman scattering data [111].

6.5.2 Magnetic interaction parameters and triangular-lattice spin models

We turn our discussion from the Stevens operators determining the CEF levels to the magnetic interaction parameters that govern the low-energy physics, and hence the extent to which the Kramers-doublet system can be used as an effective realization of any of the paradigm $S = 1/2$ models in quantum magnetism. As Sec. 6.5A made clear, an adequate understanding of the CEF energies and their evolution in an applied field is a prerequisite in the search for phenomena including field-induced phase transitions and candidate QSL phases [9]. In particular, narrowly spaced CEF levels that undergo significant mutual repulsion at a specific field scale offer a complex and correlated energy landscape that could accommodate unconventional spin states.

Focusing on the triangular geometry, the nearest-neighbor triangular-lattice Heisenberg model is the original [130] and still one of the deepest problems in frustrated quantum magnetism [32, 131]. Although the ground state of this model has a modest amount of magnetic order, triangular lattices have attracted extensive interest from a number of angles over the decades. Not only does this geometry have multiple materials realizations, but each generation of materials has opened a new dimension in research [32]. Triangular organic compounds drove a discussion of proximity to the Mott transition [93, 95, 96, 94], Cs_2CuCl_4 and Cs_2CuBr_4 [3, 132, 133, 134, 135] drove studies of the spatially anisotropic (J-J') triangular-lattice models [136, 131], and the cobaltates $Ba_3CoNb_2O_9$ [137, 138], $Ba_3CoSb_2O_9$ [139, 140, 141], and $Ba_8CoNb_6O_{24}$ [142] spurred the consideration of spin-anisotropic triangular lattices with XXZ symmetry. In recent years, Yb-based triangular-lattice materials have sparked very strong interest in further spin anisotropies, in the form of J^{++} and J^{+z} terms [118, 143, 126], all of which widen considerably the scope for finding QSL states. On the

theoretical side, it has been shown that second-neighbor Heisenberg interactions also drive a QSL state, whose gapped or gapless nature remains undetermined at present [144, 145, 146, 147, 148]. In the nearest-neighbor model, the systematic treatment of parton-based formulations has led to qualitative advances in calculating the dynamical excitation spectrum by both Schwinger-boson [149] and pseudofermion methods [146, 150]. Long-standing questions about the thermodynamic properties may soon be answered by DMRG methods [151], despite the constraints of working on a rather narrow cylinder, and by tensor-network methods [152] despite the challenge posed by the high connectivity of the triangular lattice.

In Sec. 6.2 we restricted our considerations to a triangular-lattice model of XXZ form [Eq. (6.2)], meaning that we allowed only a minimal spin anisotropy of Ising or XY form. Working at the mean-field level [Eq. (6.5)], in Sec. 6.3B we obtained the results $\mathcal{J}_\perp = 0.54 \pm 0.01$ K and $\mathcal{J}_z = 0.61 \pm 0.01$ K for the magnetic interactions in the system of $J = 7/2$ Yb^{3+} ions. As shown in Sec. 2.3.2, the interaction terms of the corresponding effective pseudospin-1/2 model are $\mathcal{J}'_\perp = 5.12$ K ($\simeq 0.44$ meV) and $\mathcal{J}'_z = 0.84$ K ($\simeq 0.07$ meV), meaning that, in contrast to present assumptions, $CsYbSe_2$ is very strongly in the XY limit ($\mathcal{J}'_z/\mathcal{J}'_\perp \simeq 0.16$). We expect further investigations of $CsYbSe_2$ to confirm this result. As the most straightforward indicator of XY or Ising physics, we suggest that the width in field of the regime over which the 1/3 plateau (i.e. the state of up-up-down spin order) in the magnetization is stabilized constitutes a quantity rather sensitive to the ratio $\mathcal{J}'_z/\mathcal{J}'_\perp$ [125, 28]. This plateau is evident in the data of Ref. [123], although a lower temperature would assist a quantitative analysis. However, the relevant regime of parameter space is yet to be investigated theoretically for a field applied in the *ab* plane of the system. Finally, while we cannot exclude terms of J^{++} and J^{+z} type from the spin Hamiltonian, the accuracy of our fit indicates that the effect of any missing terms is extremely small in $CsYbSe_2$; either they are genuinely small or they are relevant only at the lowest temperatures where a treatment beyond the present mean-field level would be required.

On the materials side, it is also fair to say that the continuing lack of experimental signatures for QSL ground states can be blamed on two primary issues, namely the scarcity of candidate materials and the paucity of measurable physical quantities offering unambiguous signatures or

predictors for QSL properties (such as fractional quantum numbers and nonlocal entanglement). To address the first of these, our analysis provides a definitive guide to the field-induced physics of highly spin-anisotropic systems such as the Yb-delafossites, and hence to the regions of parameter space where competing energy scales establish an environment conducive to the occurrence of exotic spin states. Although we cannot solve the second issue, we can provide a comprehensive understanding of the single-ion energy spectrum that identifies the extent to which a given material replicates a target pseudospin-1/2 model, thereby streamlining the experimental search for QSL fingerprints by available experimental methods.

6.6 Summary

We have investigated the anisotropic magnetic response of an insulating $4f$ electronic system by measuring two key thermodynamic quantities, the magnetic susceptibility in the low-field limit and the magnetotropic coefficients over very wide field and temperature ranges (up to $\mu_0 H = 60$ T and $T = 70$ K). We have shown that the anisotropies in both quantities can be formulated within a set of anisotropic van Vleck (VV) coefficients, which arise as the second-order perturbative corrections of the Zeeman interaction to the zero-field crystal electric field (CEF) spectrum. This leads to the essential finding that the VV coefficients constitute independent physical quantities that describe the crucial magnetic properties of $4f$ spin systems across the full range of applied fields and extant anisotropies. A proper account of the ground-state VV coefficients is indispensable for an accurate and unambiguous determination of the microscopic parameters governing the CEF Hamiltonian, a process for which otherwise few routes are known to date. The VV coefficients fulfill the vital function of unifying the low-field, low-temperature magnetic susceptibility with the high-field magnetotropic coefficients and CEF levels, and in this sense their role as stand-alone physical quantities allowing a full interpretation of magnetic anisotropies has not been appreciated before.

Our experimental results highlight the value of the resonant torsion magnetometry (RTM) method, which is accurate and profoundly powerful in terms of the parameter ranges it accesses.

The magnetotropic coefficients we extract over these broad field and temperature ranges play the key role in obtaining a unique set of Stevens operators describing the microscopic CEF Hamiltonian with unprecedent fidelity. We reiterate that a fitting analysis must provide complete consistency from zero to high field and at all relevant temperatures, and our fits meet this challenge. With the full CEF spectrum in hand, we can examine the validity of different and popular approximations that have been applied to many materials. Specifically, we identify the limits of a CW fit to the temperature-dependence of the magnetic susceptibility and the boundaries of the effective pseudospin-1/2 description for systems with a ground-state Kramers doublet.

We have developed and applied our analysis for the material $CsYbSe_2$, which is a member of a family of Yb-delafossites displaying triangular-lattice geometry. Because the CEF levels of the Yb^{3+} ion are four Kramers doublets, these compounds are leading candidates in the search for quantum spin-liquid (QSL) behavior, and indeed the full CEF spectrum we obtain up to high fields [Fig. 6.6] reveals an intricate and anisotropic energy landscape amenable to unconventional magnetism. This spectrum allows one to construct a maximally informed pseudospin-1/2 model for the low-energy physics of the system, and within a minimal XXZ spin Hamiltonian we conclude that $CsYbSe_2$ is a strongly XY triangular antiferromagnet. While we await further experimental confirmation of this result, we note again that our analysis is applicable to a wide range of $4f$ materials with complex CEF spectra and especially with ground-state doublets allowing an effective spin-1/2 description, which should expand significantly the scope of the search for QSL phases.

We thank M. Mourigal and K. Ross for helpful discussions. We are grateful to M. Chan and A. Shekhter for technical assistance with our pulsed-field measurements. Experimental work at the University of Colorado Boulder was supported by Award No. DE-SC0021377 of the U.S. Department of Energy (DOE), Basic Energy Sciences (BES), Materials Sciences and Engineering Division (MSE). Theoretical work at the University of Colorado Boulder was supported by Award No. DE-SC0014415 of the U.S. DOE, BES, MSE. Work at Oak Ridge National Laboratory (ORNL) was supported by the U.S. DOE, BES, MSE. A portion of this work was performed at the National High Magnetic Field Laboratory, in the Pulsed Field Facility at Los Alamos National Laboratory

(LANL), which is supported by National Science Foundation Cooperative Agreement No. DMR-1644779, the State of Florida, and the U.S. DOE.

Chapter 7

The hybridization of phonons and spin excitations via strain modulation of the g-tensor, and its direct effect on thermal transport in $CsYbSe_2$.

7.1 Introduction

The thermal conductivity of $CsYbSe_2$, and in fact many other frustrated magnets [24, 68, 14], often exhibits strong, non-monotonic field-dependence, even when the state of magnetic lattice is disordered. In such an arrangement a strong itinerant contribution from dispersive magnetic quasi particles is highly unlikely in typical scenarios, and heat transport is almost certainly phonon-dominated. This generally leaves 2 possibilities either phonons are strongly scattered by magnetic ions, and directly sensitive to short-range-order correlations and disorder, as explored in the case of $CrCl_3$ in chapter 5, or phonons may be hybridizing with spin excitations [154, 122, 50, 52], thereby modifying their spectra. In this chapter we explore the later, and present a Jaynes Cummings type Hamiltonian that captures a fairly generic mechanism of phonon interaction with an ionic 2-level spin system via a strain-modulation of the magnetic g-tensor. The basic mechanism relies on the fact that an external magnetic field splits the lowest Kramers doublet of Yb^{3+} ions, producing a small spin-flip gap $\omega_c(H)$. At fields $H < 20$ T the size of this gap is comparable to acoustic phonon energies, allowing for potential hybridization. The hybridized spectra of this model under applied fields is enormously successful in reproducing the rich qualitative features of anisotropic field-dependent transport data in $CsYbSe_2$, and is potentially widely applicable to other time-reversal-symmetry-broken magnets. Building upon our knowledge of the anisotropic crystal-electric field spectrum of $CsYbSe_2$ we present a novel and highly generic way in which phonon heat conduction

can acquire unique field-dependence through the hybridization of phonons and spin flip excitations of ground-state crystal-electric field doublet, or indeed any suitable 2-level magnetic system.

7.2 Anisotropic field-dept. thermal conductivity

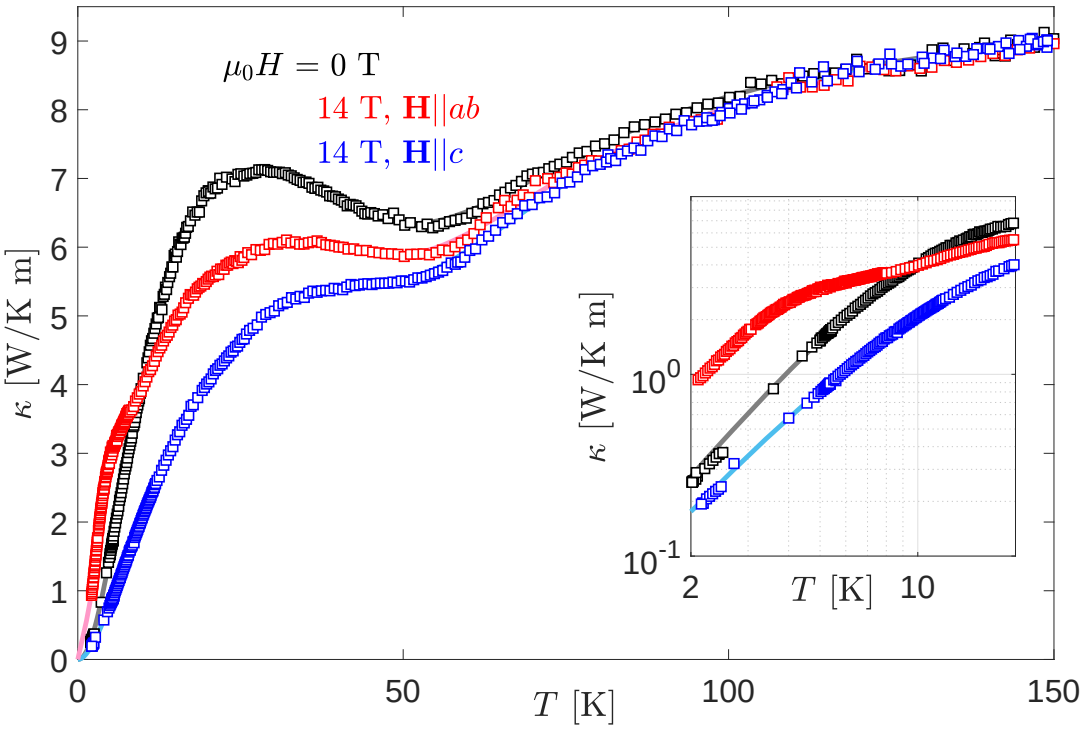

Figure 7.1: Longitudinal thermal conductivity measured at ZF, and at 14 T in the **H**||c and **H**||ab orientations. Squared are data and the solid lines are included as a guide to the eyes. The inset shows the low-T nearly ballistic regime in a log-log scale.

We measure the in-plane longitudinal thermal conductivity κ in a ^{4}He refrigerator with applied external magnetic fields up to 18 T. In-plane κ was measured in an as-grown single-crystal sample of approximate dimensions 1 mm $\times$ 3 mm $\times$ 10 , using a single-heater, dual-thermometer configuration in steady state operation with fields applied both in-plane in the direction of the thermal current **H** $\parallel$ ab $\parallel$ ∇T and out-of-plane **H** $\parallel$ c. For all thermometry, we use Cernox resistors, calibrated individually and in-situ under maximum applied fields.

We first measured the thermal conductivity at zero field and at a fixed applied field of $\mu_0 H =$

14 T in both orientations as pictured in Fig. 7.1 in the temperature range $2 < T < 150$ K. The data show that in both orientations, and at all temperatures ¿ 20 K the application of a large field (14 T) has the effect of suppressing the thermal conductivity, an effect which is more pronounced for fields $\mathbf{H}||c$. At very low temperatures, by contrast, the effect of an external field is very direction-dependent. A field $\mathbf{H}||c$ monotonically suppresses the total thermal conductivity, while a field $\mathbf{H}||ab$ has the opposite effect, monotonically enhancing the field. Strikingly, this field in-plane enhancement is unexpectedly large, increasing the total thermal conductivity at $T = 1.5$ K by an entire order of magnitude when an 18 T field is applied in-plane. A closer examination of the H-dependence of the thermal conductivity, reveals that $\kappa(\mathbf{H}||c)$ is almost entirely monotonically decreasing with applied field at all measured temperatures, while $\kappa(\mathbf{H}||ab)$ is incredibly non-monotonic as pictured in figure fig 7.2 .

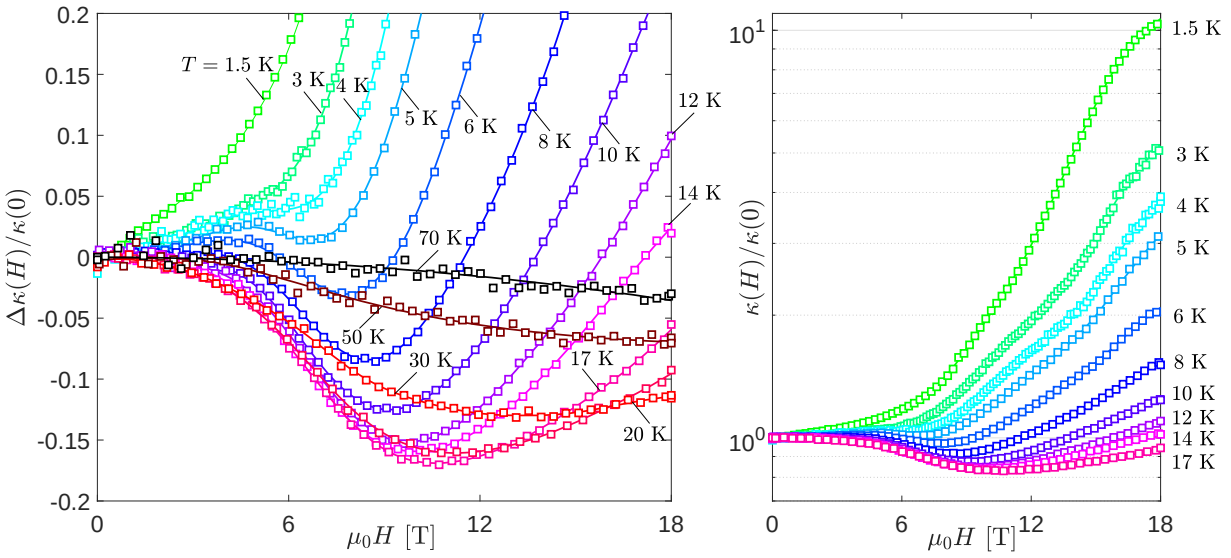

Figure 7.2: The left hand side shows isothermal traces of $\Delta\kappa(H)/\kappa_0$ up to $T = 70$K with fields applied in-plane ($\mathbf{H}||ab$). The right hand side shows $\kappa(H)/\kappa_0$ for the same dataset up to 17 K in a log scale to emphasize the large enhancement at low-T.

At temperatures $T > 5$ K the shape of the fractional change in $\kappa(\mathbf{H}||ab)$, denoted $\Delta\kappa(H)/\kappa_0 \equiv [\kappa(H) - \kappa(0)]/\kappa(0)$, is characterized by an initial suppression of the thermal conductivity and an eventual enhancement at higher fields, resulting in a pronounced minimum at a field H_c which

is unique at each temperature. Although a high-field increase is never observed for the traces at $T = 50, 70$ K, our modeling suggests that an enhancement of $\kappa(H)$ eventually wins out at all $T > 5$ K, and the expected minima are simply beyond the experimentally accessible field range

7.3 Theoretical model of spin-phonon hybridization

In this section we outline a potential model for spin-phonon interaction, describe the most generic symmetry allowed spin-lattice interaction Hamiltonian relevant to a description of $CsYbSe_2$, and derive the wave vector dependence of interaction term. This model is equivalent to a particular generalization of the Jaynes Cummings Hamiltonian on a lattice that places a N two-level system at each lattice site and quantifies their interaction with $3N$ acoustic phonon modes.

7.3.1 Unperturbed Elastic & Magnetic Hamiltonian

To describe the unperturbed lattice, we assume an elastic Hamiltonian of the form:

$$\mathcal{H}_E = \sum_{\mathbf{k},\lambda} \hbar\omega_{\mathbf{k},\lambda} \hat{a}^\dagger_{\mathbf{k},\lambda} \hat{a}_{\mathbf{k},\lambda} \tag{7.1}$$

for N atoms at lattice sites $\mathbf{r}_i$, as outlined in section 3.1.3, subject to the same Fourier conventions 3.15,3.16, 3.17, with second-quantized operators defined according to 3.21, 3.22.

If we are sufficiently low temperatures that only the ground state Kramers doublet of $CsYbSe_2$ is thermally occupied, we can describe the physics of each magnetic ion using a pseudospin 1/2 approximation in terms of the effective PS-1/2 operators 2.9,2.10,2.11. Thus in the presence of an external field the magnetic part of the Hamiltonian takes the form:

$$\mathcal{H}_M = \mu_0 \mu_B g_{\alpha\alpha} \sum_i H_\alpha S_\alpha(\mathbf{r}_i), \tag{7.2}$$

We can write the spin operator at lattice site $\mathbf{r}$ in terms of the pauli matrices, subject to the

following canonical commutation relations $[\hat{\sigma}^-_{\mathbf{r}}, \hat{\sigma}^+_{\mathbf{r}'}] = \delta_{\mathbf{r},\mathbf{r}'}$:

$$S_x(\mathbf{r}) = \frac{\hbar}{2}(\hat{\sigma}^+_{\mathbf{r}} + \hat{\sigma}^-_{\mathbf{r}}), \tag{7.3}$$

$$S_y(\mathbf{r}) = \frac{\hbar}{2i}(\hat{\sigma}^+_{\mathbf{r}} - \hat{\sigma}^-_{\mathbf{r}}), \tag{7.4}$$

$$S_z(\mathbf{r}) = \hbar\left(\hat{\sigma}^+_{\mathbf{r}}\hat{\sigma}^-_{\mathbf{r}} - \frac{1}{2}\right). \tag{7.5}$$

We can transform into Fourier space using the following convention:

$$\hat{\sigma}^-_{\mathbf{r}} = \frac{1}{\sqrt{N}}\sum_{\mathbf{q}} e^{i\mathbf{q}\cdot\mathbf{r}}\hat{\sigma}^-_{\mathbf{q}} \tag{7.6}$$

So that in Fourier space, the spin operators may be represented:

$$S_x(\mathbf{q}) = \frac{\hbar}{2}(\hat{\sigma}^+_{-\mathbf{q}} + \hat{\sigma}^-_{\mathbf{q}}), \tag{7.7}$$

$$S_y(\mathbf{q}) = \frac{\hbar}{2i}(\hat{\sigma}^+_{-\mathbf{q}} - \hat{\sigma}^-_{\mathbf{q}}), \tag{7.8}$$

$$S_z(\mathbf{q}) = \frac{\hbar}{2}\hat{\sigma}^z_{\mathbf{q}} \equiv \hbar\left(\hat{\sigma}^+_{\mathbf{q}}\hat{\sigma}^-_{\mathbf{q}} - \frac{1}{2}\right). \tag{7.9}$$

If we choose the quantization axis $\hat{z}'$ such that the field points along this axis, we can write the magnetic portion of the Hamiltonian as

$$\mathcal{H}_M = \frac{\hbar\omega_c}{2}\sum_{\mathbf{q}} \hat{\sigma}^{z'}_{\mathbf{q}} \tag{7.10}$$

Where we have defined $\omega_c = \mu_0\mu_B g_{zz} H$.

7.3.2 Magneto-Elastic interaction terms

The g-tensor in the magnetic Hamitonian $\mathcal{H}_M$ can certainly change if the local Yb^{3+} environment is distorted, i.e. the g-tensor will depend on the strain of the lattice, resulting in a coupling between phonons and the single-ion spin-flip excitations under applied magnetic field. As long as time reversal is maintained, there is no way to split the ground state Kramers doublet, therefore there is no interesting zero-field magnetoelastic coupling, as long as we're only focusing on the ground state doublet. We can write this magnetoelastic Hamiltonian as:

$$\mathcal{H}_{ME} = \mu_0\mu_B\delta g_{\alpha\beta}H_\alpha S_\beta, \tag{7.11}$$

where we take the distortion of the g-tensor δg to be linear in $\partial_\alpha u_\beta$, appropriate for small distortions of the crystal. Note that δg cannot depend on u_α (without a derivative), because then it would change under a uniform translation of the entire crystal $\mathbf{u} \to \mathbf{u} + \mathbf{a}$. In fact δg can only depend on the symmetric strain tensor $\varepsilon_{\alpha\beta} = \frac{1}{2}(\partial_\alpha u_\beta + \partial_\beta u_\alpha)$. To understand why, consider a rotated configuration $u_\alpha = \epsilon_{\alpha\beta\gamma}\Omega_\beta r_\gamma$. This corresponds to a uniform rotation of the crystal about the $\hat{\Omega}$ axis. Clearly the magnetoelastic coupling terms should not change if we rotate the whole crystal. The term $\partial_\alpha u_\beta = \epsilon_{\alpha\beta\gamma}\Omega_\gamma$ however is completely antisymmetric, so we see that the ME coupling terms cannot depend on $\partial_\alpha u_\beta - \partial_\beta u_\alpha$, but can only depend on the symmetric tensor strain tensor.

To find the allowed terms in $\mathcal{H}_{ME}$, we decompose $\varepsilon_{\alpha\beta}$ into irreps. of the Yb^{3+} site symmetry group D_{3d}. Similarly, we decompose $H_\alpha S_\beta$, with no symmetrization of indices required. To enumerate the terms in $\mathcal{H}_{ME}$, we consider pairs of irreps., where one member of the pair is an irrep. appearing in the decomposition of $\partial_\alpha u_\beta$, and the other member appears in the decomposition of $H_\alpha S_\beta$. This results in the following symmetry-allowed total magnetoelastic Hamiltonian:

$$\begin{aligned}
\mathcal{H}_{ME} = &\left[\zeta_{c1}(\partial_x u_x + \partial_y u_y) + \zeta_{c2}\partial_z u_z\right] H_z S_z + \left[\zeta_{a1}(\partial_x u_x + \partial_y u_y) + \zeta_{a2}\partial_z u_z\right](H_x S_x + H_y S_y) \\
&+ \eta_{c1} H_z \left[(\partial_x u_x - \partial_y u_y)S_y + (\partial_x u_y + \partial_y u_y)S_y + (\partial_x u_y + \partial_y u_x)S_x\right] \\
&+ \eta_{c2} H_z \left[\partial_y u_z + \partial_z u_y)S_y + (\partial_x u_z + \partial_z u_x)S_x\right] \\
&+ \eta_{a1} \left[(\partial_x u_x - \partial_y u_y)(H_x S_x - H_y S_y) + (\partial_x u_y + \partial_y u_x)(H_x S_y + H_y S_x)\right] \\
&+ \eta_{a2} \left[(\partial_x u_x - \partial_y u_y)H_y + (\partial_x u_y + \partial_y u_x)H_x\right] S_z, \\
&+ \eta_{a3} \left[(\partial_y u_z + \partial_z u_y)(H_x S_x - H_y S_y) + (\partial_x u_z + \partial_z u_x)(H_x S_y + H_y S_x)\right] \\
&+ \eta_{a4} \left[(\partial_y u_z + \partial_z u_y)H_y + (\partial_x u_z + \partial_z u_x)H_x\right] S_z.
\end{aligned}$$

Here we have separated terms depending on H_z (with a c subscript) from those depending on H_x and H_y (with an a subscript). Note that not all of these terms will lead to an anti-crossing in the spin-phonon hybridized spectrum, but only those terms that induce transitions between the ground and excited states of $\mathcal{H}_Z$. First suppose the magnetic field is applied along the z-direction. Then the ζ_c terms cannot induce transitions between ground and excited states, while the η_c terms can.

The same holds when the magnetic field is applied within the ab-plane for the ζ_a and η_a terms respectively. If the magnetic field is applied at some angle between the ab-plane and the c-axis, then presumably any of the terms can induce spin-flip transitions.

7.3.3 A Janyes Cummings type model for spin-lattice interaction

An an explicit example, we first consider the case in which the field is applied along the $\hat{z}$ direction.

$$\mathcal{H}_{ME} = H_z \sum_{\mathbf{r}} \Big\{ \eta_{c1} \left[(\partial_x u_x - \partial_y u_y) S_y + (\partial_x u_y + \partial_y u_x) S_x \right] + \eta_{c2} \left[(\partial_y u_z + \partial_z u_y) S_y + (\partial_x u_z + \partial_z u_x) S_x \right] \Big\}, \tag{7.12}$$

Here, we define a gyromagnetic ratio $\gamma_c = \omega_c / H_z$, allowing us to express H_Z in terms of the field-induced splitting ω_c. In Fourier space, this Magnetoelastic Hamiltonian takes the form:

$$\begin{aligned} \mathcal{H}_{ME} = \frac{\hbar\omega_c}{2\gamma_c} \sqrt{\frac{\hbar}{2m}} \sum_{\mathbf{k},\lambda} \frac{1}{\sqrt{\omega_\lambda(\mathbf{k})}} \left[\hat{a}^\dagger_\lambda(-\mathbf{k}) + \hat{a}_\lambda(\mathbf{k}) \right] \\ \times \Big\{ \eta_{c1} \left[(ik_x \hat{\epsilon}_{\lambda x}(\mathbf{k}) - ik_y \hat{\epsilon}_{\lambda y}(\mathbf{k})) S_y(-\mathbf{k}) + (ik_x \hat{\epsilon}_{\lambda y}(\mathbf{k}) + ik_y \hat{\epsilon}_{\lambda x}(\mathbf{k})) S_x(-\mathbf{k}) \right] \\ + \eta_{c2} \left[(ik_y \hat{\epsilon}_{\lambda z}(\mathbf{k}) + ik_z \hat{\epsilon}_{\lambda y}(\mathbf{k})) S_y(-\mathbf{k}) + (ik_x \hat{\epsilon}_{\lambda z}(\mathbf{k}) + ik_z \hat{\epsilon}_{\lambda x}(\mathbf{k})) S_x(-\mathbf{k}) \right] \Big\}, \end{aligned} \tag{7.13}$$

Keeping only those terms $\hat{a}^\dagger \hat{\sigma}^-, \hat{a}\hat{\sigma}^+$ which do not change the total number of excitations, the magnetoelastic interaction Hamiltonian may be written:

$$\mathcal{H}_{ME} = \hbar \sum_{\mathbf{k},\lambda} \left[f_\lambda(\mathbf{k}) \hat{a}_{\mathbf{k},\lambda} \hat{\sigma}^+_{\mathbf{k}} + f^*_\lambda(\mathbf{k}) \hat{a}^\dagger_{\mathbf{k},\lambda} \hat{\sigma}^-_{\mathbf{k}} \right] \tag{7.14}$$

Where the function $f_\lambda(k)$, with units of frequency is defined:

$$\begin{aligned} f_\lambda(\mathbf{k}) = \frac{\omega_c}{2\gamma_c} \sqrt{\frac{\hbar}{2m\omega_\lambda(\mathbf{k})}} \Big\{ \eta_{c1} \left[(k_x \hat{\epsilon}_{\lambda x}(\mathbf{k}) - k_y \hat{\epsilon}_{\lambda y}(\mathbf{k})) + i(k_y \hat{\epsilon}_{\lambda x}(\mathbf{k}) + k_x \hat{\epsilon}_{\lambda y}(\mathbf{k})) \right] \\ + \eta_{c2} \left[(k_y \hat{\epsilon}_{\lambda z}(\mathbf{k}) - k_z \hat{\epsilon}_{\lambda y}(\mathbf{k})) + i(k_x \hat{\epsilon}_{\lambda z}(\mathbf{k}) + k_z \hat{\epsilon}_{\lambda x}(\mathbf{k})) \right] \Big\}, \end{aligned} \tag{7.15}$$

Given an explicit wavevector, for example $\mathbf{k} = k(\cos\phi_{\mathbf{k}}, \sin\phi_{\mathbf{k}}, 0)$, we can work out these expressions for each polarization: $\hat{\epsilon}_1 = \hat{z},\ \hat{\epsilon}_2 = (-\sin\phi_{\mathbf{k}}, \cos\phi_{\mathbf{k}}, 0)$, and $\hat{\epsilon}_3 = (\cos\phi_{\mathbf{k}} \sin\phi_{\mathbf{k}}, 0)$:

$$\begin{aligned} f_1(\mathbf{k}) &= \frac{\eta_{c2}\omega_c}{\gamma_c}\sqrt{\frac{\hbar}{2m\omega_1(\mathbf{k})}}\left[k_y + ik_x\right], \\ &= ie^{-i\phi_{\mathbf{k}}}\tilde{\eta}_{c2}\frac{\omega_c k}{\sqrt{2m\omega_1(\mathbf{k})/\hbar}}, \end{aligned} \tag{7.16}$$

$$\begin{aligned} f_2(\mathbf{k}) &= \frac{\eta_{c1}\omega_c}{\gamma_c}\sqrt{\frac{\hbar}{2m\omega_1(\mathbf{k})}}k\left[(-\sin\phi_{\mathbf{k}}\cos\phi_{\mathbf{k}} - \cos\phi_{\mathbf{k}}\sin\phi_{\mathbf{k}}) + i\left(\cos^2\phi_{\mathbf{k}} - \sin^2\phi_{\mathbf{k}}\right)\right], \\ &= ie^{-2i\phi_{\mathbf{k}}}\tilde{\eta}_{c1}\frac{\omega_c k}{\sqrt{2m\omega_2(\mathbf{k})/\hbar}}, \end{aligned} \tag{7.17}$$

$$f_3(\mathbf{k}) = ie^{-2i\phi_{\mathbf{k}}}\tilde{\eta}_{c1}\frac{\omega_c k}{\sqrt{2m\omega_3(\mathbf{k})/\hbar}}. \tag{7.18}$$

For each polarization, a dimensionless parameter $\tilde{\eta} \equiv (\eta/\gamma_c)$ controls the size of this interaction. This exercise can likewise be computed for the other terms of the magnetoelastic Hamiltonian, in the case that the field is applied in the xy plane, this results in $f_\lambda(k)$ with the same functional dependence on k, depending instead on a distinct combination of the other η_{ai}. Thus for the cases considered, a field either purely along c or in the ab plane, we can choose appropriate quantization axis $\hat{z}'||\mathbf{H}$ such that the total Magnetoelastic Hamiltonian can be written:

$$\mathcal{H}_{JC} = \hbar\sum_{\mathbf{k}}\left\{\frac{\omega_c}{2}\hat{\sigma}^{z'}_{\mathbf{k}} + \sum_{\lambda}\left[\omega_{\mathbf{k},\lambda}\hat{a}^\dagger_{\mathbf{k},\lambda}\hat{a}_{\mathbf{k},\lambda} + f_\lambda(\mathbf{k})\hat{a}_{\mathbf{k},\lambda}\hat{\sigma}^+_{\mathbf{k}} + f^*_\lambda(\mathbf{k})\hat{a}^\dagger_{\mathbf{k},\lambda}\hat{\sigma}^-_{\mathbf{k}}\right]\right\}. \tag{7.19}$$

Which is a Jaynes-Cummings type model (JCM) [153] for a periodic set of 2-level systems, that to my knowledge has not been explored in the context of either condensed matter or quantum optics systems to date. In describing a realistic crystal system such as $CsYbSe_2$, anisotropy enters into the directional dependence of $\omega_c(H)$ or the particular coefficients $\tilde{\eta}$ determining the strength of the spin-phonon mixing. Our analysis of resonant torsion magnetometry described in chapter 6 quantitatively describes the anisotropy of $CsYbSe_2$ which results in an unequal spin excitation energy gap $\omega_c(H)$ between pseudospin up/down states of the ground state doublet of the Yb^{3+}

ion, depending on whether an external field is applied in-plane ($\mathbf{H}||ab$) or out of plane ($\mathbf{H}||c$). This characterized in terms of the anisotropic g-tensor, which predicts a 0.203 meV/T and 0.0735 meV/T spin excitation gap for $\mathbf{H}||ab$ and $\mathbf{H}||c$ respectively.

7.4 Analytical toy model for spin-phonon hybridization

In the field range studied $\mu_0 H < 20$ T, the size of ω_c does not exceed ~ 4 meV, thus it is only necessary to consider hybridization between spin flip excitations and the three branches of acoustic phonons. While the full JCM does not have a closed-form expression for an arbitrary phonon spectrum $\{\omega_\lambda(\mathbf{k})\}$, it can be exactly diagonalized if we make the Debye-like assumption that the acoustic phonons can be described by a single effective branch, i.e. $\omega_{LA} = \omega_{TA_1} = \omega_{TA_2} = \omega(\mathbf{k})$.

The Hamiltonian 7.19 is completely separable for distinct wavevectors, i.e. it may be written as $\mathcal{H}_{JC} = \bigoplus_{\mathbf{k}} \mathcal{H}_{\mathbf{k}}$, where $\oplus$ denotes a Kronecker sum. Thus, we may consider the eigenvalues of $\mathcal{H}_{JC}$ for each $\mathbf{k}$ separately. We denote the phonon states at a given $\mathbf{k}$ using a Fock State $|n_1, n_2, n_3\rangle$ where $1, 2, 3$ index the 3 acoustic polarizations, and the spin flip excitation $|s\rangle = |0\rangle$ or $|1\rangle$. Note that in k-space, the $|0\rangle/|1\rangle$ state can no longer be thought of as a single, localized pseudospin up/down on a single lattice site, but rather a representative of a dispersion-less, completely de-localized band of spin flip excitations. The interaction Hamiltonian couples each combined phonon-spin flip state $|n_1, n_2, n_3\rangle \otimes |1\rangle$ to 3 distinct states:

$$|(n_1 - 1), n_2, n_3\rangle \otimes |0\rangle, \qquad |n_1, (n_2 - 1), n_3\rangle \otimes |0\rangle, \qquad |n_1, n_2, (n_3 - 1)\rangle \otimes |0\rangle, \tag{7.20}$$

each of which preserves the total number of excitations. This results in a Hamiltonian that is block-diagonal, with each successively larger block $\mathcal{H}_{\mathbf{k}}^{(n)}$ corresponding to each total integer amount of excitations $n = n_1 + n_2 + n_3 + s$: The trivial vacuum block $\{|0, 0, 0\rangle \otimes |0\rangle\}$, with eigenvalue 0, couples to no other states. The hamiltonian may written thusly:

$$\mathcal{H}_{\mathbf{k}} = \begin{pmatrix} 0 & 0 & 0 & 0 & \dots \\ 0 & \mathcal{H}_{\mathbf{k}}^{(1)} & 0 & 0 & \\ 0 & 0 & \mathcal{H}_{\mathbf{k}}^{(2)} & 0 & \\ 0 & 0 & 0 & \mathcal{H}_{\mathbf{k}}^{(3)} & \\ \vdots & & & & \ddots \end{pmatrix} \tag{7.21}$$

The first non-trivial block, corresponding to 1 total excitation, may be written in the basis $\{|0,0,0,1\rangle$, $|1,0,0,0\rangle, |0,1,0,0\rangle, |0,0,1,0\rangle\}$ explicitly:

$$\mathcal{H}_{\mathbf{k}}^{(1)} = \begin{pmatrix} \omega_c & f_1 & f_2 & f_3 \\ f_1^* & \omega & 0 & 0 \\ f_2^* & 0 & \omega & 0 \\ f_3^* & 0 & 0 & \omega \end{pmatrix} \tag{7.22}$$

where, we have suppressed the notation $\omega = \omega(\mathbf{k})$ for readability. The 2-excitation block, includes 9 total states. In a basis $\{|1,0,0,1\rangle, |0,1,0,1\rangle, |0,0,1,1\rangle, |2,0,0,0\rangle, |0,2,0,0\rangle, |0,0,2,0\rangle, |1,1,0,0\rangle$, $|0,1,1,0\rangle, |1,0,1,0\rangle\}$, this takes the explicit form:

$$\mathcal{H}_{\mathbf{k}}^{(2)} = \begin{pmatrix} \omega+\omega_c & 0 & 0 & \sqrt{2}f_1 & 0 & 0 & f_2 & 0 & f_3 \\ 0 & \omega+\omega_c & 0 & 0 & \sqrt{2}f_2 & 0 & f_1 & f_3 & 0 \\ 0 & 0 & \omega+\omega_c & 0 & 0 & \sqrt{2}f_3 & 0 & f_2 & f_1 \\ \sqrt{2}f_1^* & 0 & 0 & 2\omega & 0 & 0 & 0 & 0 & 0 \\ 0 & \sqrt{2}f_2^* & 0 & 0 & 2\omega & 0 & 0 & 0 & 0 \\ 0 & 0 & \sqrt{2}f_3^* & 0 & 0 & 2\omega & 0 & 0 & 0 \\ f_2^* & f_1^* & 0 & 0 & 0 & 0 & 2\omega & 0 & 0 \\ 0 & f_3^* & f_2^* & 0 & 0 & 0 & 0 & 2\omega & 0 \\ f_3^* & 0 & f_1^* & 0 & 0 & 0 & 0 & 0 & 2\omega \end{pmatrix} \tag{7.23}$$

The 3-excitation block has 16 states and so on. Explict computer-assisted diagonalization of the first several blocks reveals that each n-total-excitation block will have a degenerate eigenvalue $n\omega$, and another set of eigenvalues defined below, each labeled by $q = 1, 2, \ldots n$, whose degeneracies grow with q,

$$\omega_{q,\pm}^{(n)} \equiv (n-1)\omega + \frac{\omega+\omega_c}{2} \pm \sqrt{\left(\frac{\omega_c-\omega}{2}\right)^2 + q\,(|f_1|^2 + |f_2|^2 + |f_3|^2)}, \tag{7.24}$$

Which are generalizations of the dressed states of the usual Jaynes Cummings model for a single 2-level system. Examining the eigenvalues 7.24 it appears that the combination $\sum_i |f_i|^2$ always occurs in its entirely, so we may replace the sum of all coupling constants by a single effective $\tilde{f}$, which in fact generalizes to other physical examples with a number of polarizations other than the $L = 3$ case under consideration:

$$\tilde{f}^2 \equiv \frac{1}{L}(|f_1|^2 + \cdots + |f_L|^2). \tag{7.25}$$

While there are possibly several independent $\tilde{\eta}$ for each polarization in the generic model, see Eqns. 7.16-7.18, this we only need to worry about the quadrature sum of all $\tilde{\eta}$ involved, given that all

f_λ share the same functional dependence on k and ω in the Debye-like model. Thus from the perspective of our all our fits, for a single field orientation, there is only one effective independent $\tilde{\eta}$ parameter controlling the size of the spin-phonon interaction. The multiplicities of the eigenvalues determined above are explicitly enumerated in the tables below for n-total excitation blocks up to $n = 3$, for the cases of $L = 1$ polarization, applicable to a longitudinally confined 1d chain, 2 polarizations, applicable to an analagous photon cavity model, the 3 acoustic polarization spin-phonon hybridization model of course, and a fictitious 4 polarization model. The degeneracies of

$1:$

L \ ω_i	$\omega^{(1)}_{1,\pm}$	ω
1	1	0
2	1	1
3	1	2
4	1	3

$2:$

L \ ω_i	$\omega^{(2)}_{2,\pm}$	$\omega^{(2)}_{1,\pm}$	2ω
1	1	0	0
2	1	1	1
3	1	2	3
4	1	3	6

$3:$

L \ ω_i	$\omega^{(3)}_{3,\pm}$	$\omega^{(3)}_{2,\pm}$	$\omega^{(3)}_{1,\pm}$	3ω
1	1	0	0	0
2	1	1	1	1
3	1	2	3	4
4	1	3	6	10

Figure 7.3: Degeneracies of the eigenvalues of $\mathcal{H}_{JC}$ for block matrices corresponding to $n = 1, 2, 3$ total excitations for a hybridization model with $L = 1, 2, 3, 4$ polarizations.

these generalized eigenvalues grow according to the sequence of binomial coefficients:

$$C(L-2,0) = 0, \quad C(L-1,1) = L-1, \quad C(L,2), \quad C(L+1,3), \ldots \tag{7.26}$$

Allowing us to write down the closed-form parition function of 7.19 in its entirety:

$$\begin{aligned} Z = \prod_{\mathbf{k}} \Bigg[1 + \sum_{n=1}^{\infty} \Bigg[& C(L+n-2,n) e^{-n\beta\hbar\omega(\mathbf{k})} \\ & + \sum_{q=0}^{n-1} C(L+q-2,q) \left(e^{-\beta\hbar\omega^{(n)}_{n-q,+}(\mathbf{k})} + e^{-\beta\hbar\omega^{(n)}_{n-q,-}(\mathbf{k})} \right) \Bigg] \Bigg], \end{aligned} \tag{7.27}$$

$$\begin{aligned} = \prod_{\mathbf{k}} \Bigg[1 + \sum_{n=1}^{\infty} e^{-n\beta\hbar\omega(\mathbf{k})} \Bigg[& C(L+n-2,n) \\ & + 2e^{-\beta\hbar\frac{(\omega_c - \omega(\mathbf{k}))}{2}} \sum_{q=0}^{n-1} C(L+q-2,q) \cosh\left(\beta\hbar \sqrt{\left(\tfrac{\omega_c - \omega(\mathbf{k})}{2}\right)^2 + (n-q)L\tilde{f}^2} \right) \Bigg] \Bigg], \end{aligned} \tag{7.28}$$

Clearly, the thermal state occupation predicted by the partition function will not reproduce the usual Bose-Einstein statistics, because each eigenvalue describes a set of hybrid states, resembling

combinations of pure phonon Fock states and spin-phonon hybrid excitations that are no longer purely bosonic, a point that is elaborated on in the succeeding section. In fact if one tries to simply assume each hybridized band individually obeys Bose-Einstein statistics, this leads to an overcounting of the total heat capacity of the system, in particular, producing a Dulong-Petit limit $C(T \to \infty) = N(L+1)k_B$ at odds with the expected $NLk_B = 3Nk_B$. Thus in order to correctly account for the state occupation of these hybrid modes and derive any related thermodynamic quantities it is fully necessary to work in terms of this hybridized partition function. It is a simple task to verify that in the decoupled limit $\tilde{f} \to 0$, where $\omega_{q,\pm}^{(n)} \to n\omega$ and $(n-1)\omega+\omega_c$, this expression of the partition function reduces to the correct decoupled partition function:

$$Z_{f\to 0} = \prod_{\mathbf{k}} (1 + e^{-\beta\hbar\omega_c}) \left(1 - e^{-\beta\hbar\omega}\right)^{-L} = (1 + e^{-\beta\hbar\omega_c})^N \left(\frac{1}{1 - e^{-\beta\hbar\omega}}\right)^{NL}, \tag{7.29}$$

for the product of N 2-level systems and NL indept. phonon modes. This reproduces a total heat capacity that is the sum of a Debye-like phonon contribution and, at finite field, a 2-level Schottky contribution.

7.5 Computing hybridized phonon thermal conductivity

Recall the Kubo-Green, fluctuation-dissipation, formula 3.46 for the thermal conductivity:

$$\kappa = \frac{\beta^2 k_B}{V} \int_0^\infty dt \ \sum_{\mathbf{k}} \left[\langle (v_{\mathbf{k}} \mathcal{H}_{\mathbf{k}} e^{-t/2\tau_{\mathbf{k}}})^2 \rangle - \langle v_{\mathbf{k}} \mathcal{H}_{\mathbf{k}} e^{-t/2\tau_{\mathbf{k}}} \rangle^2 \right], \tag{7.30}$$

To elucidate how this formula is applied for the hybridized spectrum, we first examine the form of the decoupled case ($\tilde{f} \to 0$). with a Debye-like acoustic spectrum $\omega = v_s k$. Whereby our generalized eigenvalues of the ME Hamiltonian become $\omega_\pm = n\omega$, $(n-1)\omega + \omega_c$. We treat the excitations at ω_c as a flat band with zero dispersion and zero group velocity, hence they will contribute nothing to itinerant heat transport, this is physically consistent with the real-space picture that spin flip excitations of individual ions are not mobile. We can describe the lifetime of phonons according to $\tau_P(\mathbf{k}, T)$ and although they do not contribute to itinerant transport we can also assign a lifetime $\tau_S(T)$ to the magnetic excitations. Thus we may compute the total thermal conductivity according

to:

$$\langle (v_{\mathbf{k}}\mathcal{H}_{\mathbf{k}}e^{-t/2\tau_{\mathbf{k}}})^2\rangle = \frac{\hbar^2}{Z_{\mathbf{k}}}\sum_{n=1}^{\infty}\Bigg[C(L-2+n,n)(v_s n\omega)^2 e^{-t/\tau_P}e^{-n\beta\hbar\omega} + \sum_{q=0}^{n-1}C(L+q-2,q)\Bigg[(X_1)^2e^{-n\beta\hbar\omega}+(X_2)^2e^{-\beta\hbar((n-1)*\omega+\omega_c)}.\Bigg]\Bigg], \tag{7.31}$$

$$\langle v_{\mathbf{k}}\mathcal{H}_{\mathbf{k}}e^{-t/2\tau_{\mathbf{k}}}\rangle = \frac{\hbar}{Z_{\mathbf{k}}}\sum_{n=1}^{\infty}\Bigg[C(L-2+n,n)(v_s n\omega)e^{-t/2\tau_P}e^{-n\beta\hbar\omega} + \sum_{q=0}^{n-1}C(L+q-2,q)\Bigg[X_1e^{-n\beta\hbar\omega}+X_2e^{-\beta\hbar((n-1)*\omega+\omega_c)}.\Bigg]\Bigg], \tag{7.32}$$

where we have defined the quantities:

$$\begin{aligned} X_1 &\equiv v_s n\omega e^{-t/2\tau_P}, \\ &= v_s(n-1)\omega e^{-t/2\tau_P} + v_s\omega e^{-t/2\tau_P}, \end{aligned} \tag{7.33}$$

$$X_2 \equiv v_s(n-1)\omega e^{-t/2\tau_P} + (0)\omega_c e^{-t/2\tau_S}. \tag{7.34}$$

These forms are written suggestively to illustrate their common component $v_s(n-1)e^{-t/2\tau_P}$, which will be unchanged by a finite ME coupling and precisely where the cancellations due to zero group velocity occurs for the ω_c as explicitly indicated by a factor of (0). Note that this is *not* the same as the limit $\omega_c \to 0$, in fact we must keep the ω_c terms in the exponential attached to X_2 so that the magnetic terms of $Z_{\mathbf{k}}$ cancel and the expression reduces properly. in the $\tilde{f} = 0$ case, these summations can be explicitly evaluated, and total thermal conductivity is precisely the expected thermal conductivity of the dispersive phonon part alone:

$$\kappa = \frac{Lk_B}{V}\sum_{\mathbf{k}} v_s^2\ \tau_P \left(\frac{\beta\hbar\omega}{2}\right)^2 \operatorname{csch}^2\left(\frac{\beta\hbar\omega}{2}\right). \tag{7.35}$$

The case of a finite ME coupling ($\tilde{f} > 0$) is most easily understood graphically, examining the spectrum of hybridized excitations implied by the dressed states of $\mathcal{H}_{JC}$. Each dressed state with eigenvalue $\omega^n_{q,\pm}(k)$ describes a Fock state of $(n-1)$ total ordinary phonons at frequency ω with usual dispersion $v_g = d\omega/dk$, v_s in the above decoupled example, and a single nontrivial spin-phonon excitation, which can no longer be considered purely bosonic in nature. In our notation for the

eigenvalues, this nontrivial spin-phonon excitation has an energy $\omega^{(1)}_{q,\pm} = \omega^{(n)}_{q,\pm} - (n-1)\omega$ and a nontrivial dispersion $v_g = d\omega^{(1)}_{q,\pm}/dk$. Hybridization leads to an avoided crossing in the $\pm$ bands, where the formerly flat ω_c band intersect $\omega(k)$. Such a spectrum and its non-trivial group velocity is illustrated in Fig. 7.4.

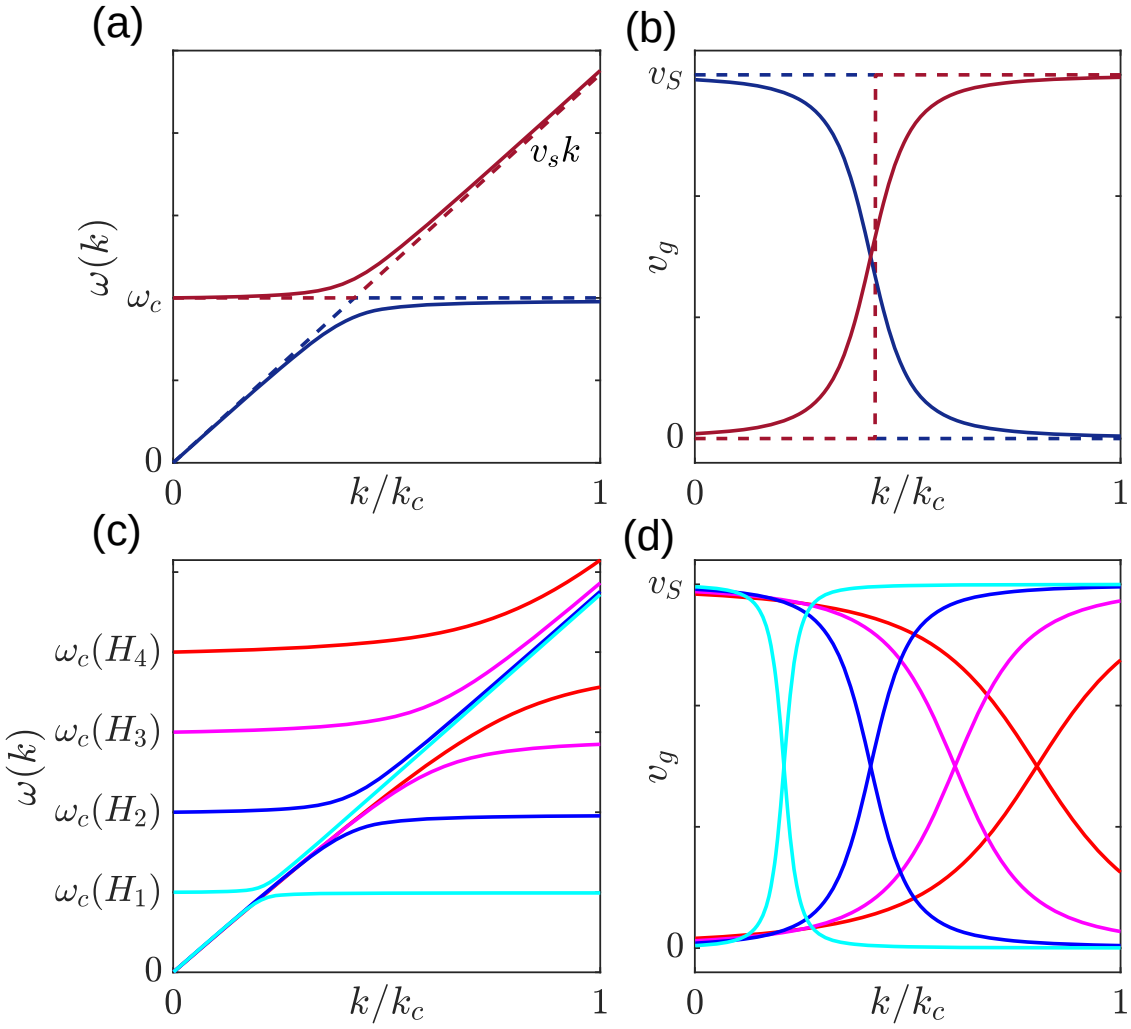

Figure 7.4: In panels (a) and (b) respectively, the dotted lines display the unperturbed spectrum of an acoustic branch $\omega = v_s k$ and spin-flip excitation branch ω_c plotted as $\omega_-(k) = \min\{\omega_c, \omega(k)\}$, $\omega_+(k) = \max\{\omega_c, \omega(k)\}$ and the corresponding group velocities of these modes. The solid lines are the spectrum of the hybridized excitation $\omega^{(1)}_{q,\pm}(k)$ and their corresponding phase velocities $d\omega^{(1)}_{q,\pm}/dk$. Panels (c) and (d) depict the field evolution of the hybridized spectrum as the field and corresponding ω_c is varied incrementally: $H_1 < H_2 < H_3 < H_4$. The field evolution of the products $\omega_+ v^2_{g,+}$, $\omega_- v^2_{g,-}$ is primarily responsible for the nontrivial field dependence of the overall thermal conductivity.

Thus, we may generalize equations 7.31 & 7.32 to compute the thermal conductivity of the hybridized spectrum:

$$\langle (v_{\mathbf{k}}\mathcal{H}_{\mathbf{k}}e^{-t/2\tau_{\mathbf{k}}})^2\rangle = \frac{\hbar^2}{Z_{\mathbf{k}}}\sum_{n=1}^{\infty}\left[C(L-2+n,n)\left(\frac{d\omega}{dk}n\omega\right)^2 e^{-t/\tau_P}e^{-n\beta\hbar\omega} + \sum_{q=0}^{n-1}C(L+q-2,q)\left[(X_+)^2 e^{-n\beta\hbar\omega^{(n)}_{n-q,+}(k)} + (X_-)^2 e^{-\beta\hbar\omega^{(n)}_{n-q,-}(k)}.\right]\right], \quad (7.36)$$

$$\langle v_{\mathbf{k}}\mathcal{H}_{\mathbf{k}}e^{-t/2\tau_{\mathbf{k}}}\rangle = \frac{\hbar}{Z_{\mathbf{k}}}\sum_{n=1}^{\infty}\left[C(L-2+n,n)\left(\frac{d\omega}{dk}n\omega\right) e^{-t/2\tau_P}e^{-n\beta\hbar\omega} + \sum_{q=0}^{n-1}C(L+q-2,q)\left[X_+ e^{-n\beta\hbar\omega^{(n)}_{n-q,+}(k)} + X_- e^{-\beta\hbar\omega^{(n)}_{n-q,-}(k)}.\right]\right], \quad (7.37)$$

where:

$$X_+ \equiv \frac{d\omega}{dk}(n-1)\omega e^{-t/2\tau_P} + \frac{d\omega^{(1)}_{n-q,+}}{dk}\omega^{(1)}_{n-q,+}e^{-t/2\tau_+}, \quad (7.38)$$

$$X_- \equiv \frac{d\omega}{dk}(n-1)\omega e^{-t/2\tau_P} + \frac{d\omega^{(1)}_{n-q,-}}{dk}\omega^{(1)}_{n-q,-}e^{-t/2\tau_-}. \quad (7.39)$$

In these expressions $\tau_P(\mathbf{k},T)$ is the mean phonon lifetime of zero-field, itinerant phonons, and $\tau_\pm(\mathbf{k},T)$ is the mean lifetime of corresponding hybrid excitations. It seems reasonable to approximate $\tau_\pm$ with a functional form similar to the Debye-Callaway like terms, given that the actual energy transport is occurring via lattice vibrations, but further theoretical work is required to fully explore the implications for scattering in this hybridized excitation regime.

7.5.1 Heat capacity and speed of sound

This crystal structure has $p = 4$ atoms per primitive cell, thus there are 12 total phonon branches/polarization to account for, 3 acoustic modes and $3p-3 = 9$ optical modes. In order to obtain a quantitative, and analytically tractable, description of the zero-field heat capacity and the phonon spectrum of $CsYbSe_2$, in the absence of any ab-initio modeling of the spectrum or independent measurements, we make a few simplifying assumptions. We assume that the thermodynamic

behavior of all low lying excitations can be effectively captured by a single effective acoustic branch, which is formally equivalent to approximating $\omega_{\mathrm{LA}} = \omega_{\mathrm{TA}_2} = \omega_{\mathrm{TA}_1}$ as a single dispersion ω_{A}. And likewise we assume that all 9 optical branches can be approximated by a single ω_{O}.

We adopt the simplest possible generic model of this spectrum assuming a Debye-like k-linear acoustic branch $\omega_{\mathrm{A}} = v_s k$, characterized by a single parameter, v_s, the speed of sound, and approximating the nearly flat optical branches by a single mean energy $\omega_{\mathrm{O}} =$ constant. These 2 parameters provide a minimal effective description of the true phonon spectrum at all temperatures which we can use to fit the experimentally measured heat capacity, numerically integrating over k using the prescription outlined in section 3.2. This summation accounts for both the low-T Debye-like contribution of the acoustic modes and the high-T Einstein-like contribution of the nearly flat optical branches:

$$C_v = 3Nk_B \int_0^{k_c} \frac{k^2\ dk}{k_c^3}\ \frac{(\beta\hbar)^2}{4} \left[3\omega_{k,\mathrm{A}}^2 \mathrm{csch}^2\left(\frac{\beta\hbar\omega_{k,\mathrm{A}}}{2}\right) + (3p-3)\omega_{k,\mathrm{O}}^2 \mathrm{csch}^2\left(\frac{\beta\hbar\omega_{k,\mathrm{O}}}{2}\right)\right], \quad (7.40)$$

In order to estimate the heat capacity we fit the data of a nonmagnetic isostructural analog $CsLaSe_2$. The Schottky-like contribution of the Yb^{3+} levels of $CsYbSe_2$ is difficult to precisely resolve, and its expected size is on the order of the noise in the $C(T)$ data. It is apparent that the $CsYbSe_2$ data series sits at a higher value of $C(T)$ than the $CsLaSe_2$ series at moderate and high temperatures, but an unambiguous separation of magnetic and lattice contributions is not possible. For this reason, we believe that $CsLaSe_2$ provides a higher fidelity estimate of the pure phonon heat capacity at high and intermediate temperatures.

Such a $C(T)$ curve formulated in terms of Eqns. 7.40 can be fit in terms of 2 parameters v_s/a, which is proportional to the Debye temperature T_D, and the parameter ω_{O}, the mean energy of the optical branch. This fit is illustrated alongside the measured heat capacities of $CsYbSe_2$ and $CsLaSe_2$ in Fig. 7.5. This fit provides a reliable estimate of the ZF speed of sound for our thermal transport analysis.

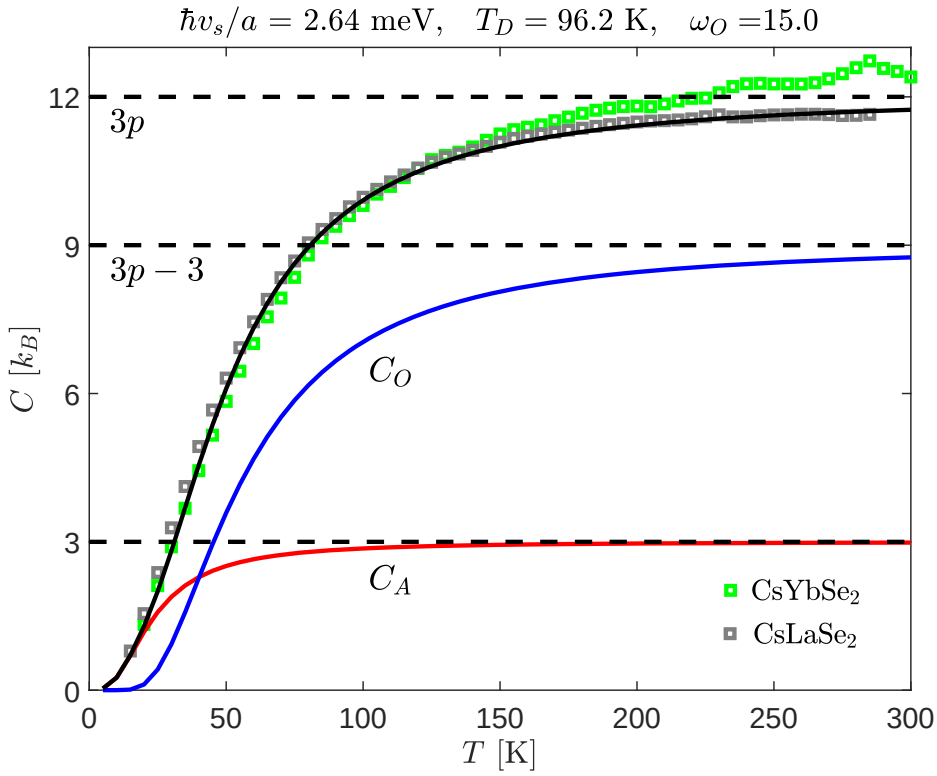

Figure 7.5: Data are fit according to Eqn. 7.40 with $\omega_{\mathrm{A}} = v_s k$ and $\omega_{\mathrm{O}} = \text{const}$. $CsLaSe_2$ is the closest available non-magnetic isostructural analog of $CsYbSe_2$. The difference between these heat capacities is especially apparent below $T = 10$ K, where the heat capacity of $CsYbSe_2$ has a very pronounced magnetic contribution [123], and at $T > 100$ K it has a distinct multilevel Schottky contribution from excited CEF states not present for $CsLaSe_2$

7.5.2 Phonon scattering lifetime

In order to employ equations 7.36-7.39, we require a basic description of the phonon lifetime $\tau_P(\mathbf{k})$. This is usually accomplished by fitting $\kappa(T)$ to a Debye-Callaway type model [44], as described in section 3.3.1. However, a model for the Thermal conductivity of acoustic phonons which accounts for boundary scattering, point-defect scattering, and Normal/Umklapp 3-phonon processes alone cannot accurately model a thermal conductivity with more than a single peak, and such a limited model is incapable of capturing the unusual shape of the zero field $\kappa(T)$ at intermediate to high temperatures, as pictured in Fig. 7.1, without significant ad-hoc modifcations to the T-dependence of the Normal and Umkalpp terms. For this reason, we restrict our fit of

the thermal conductivity to low temperatures (T <20 K), where ubiquitous boundary scattering and point defect scattering terms of the Debye-Callaway relaxation time will dominate over more complicated phonon scattering processes:

$$\tau_P^{-1}(\omega) = \tau_b^{-1} + \tau_{pd}^{-1} = \frac{v_s}{\ell_0} + A\frac{\omega^4}{v_s^3}. \tag{7.41}$$

Note that in the zero field case $\omega_c \to 0$ and equivalently in the decoupled case $\tilde{\eta} \to 0$, the thermal conductivity computed simplifies to the expression 7.35, which is exactly equivalent to the usual Debye-Callaway form:

$$\kappa(T) = \frac{k_B}{2\pi^2 v_s}\left(\frac{k_B T}{\hbar}\right)^3 \int_0^{T/T_D} \frac{x^4 e^x}{(e^x-1)^2}\ \frac{1}{\tau_b^{-1}+\tau_{pd}^{-1}}\ dx. \tag{7.42}$$

We use the parameter $v_s \approx 2070$ m/s, as independently determined from the heat capacity, and the low-T fit of $\kappa(T)$ according to the Debye-Callaway relaxation time approximation is thereby found by varying the 2 free parameters, the phonon mean-free path/intrinsic disorder length scale ℓ_0, and the point defect scattering paramater, A, which has units of volume×frequency. We find that the data is fit by $\ell_0 \approx 3.5 \times 10^{-7}$ m, which corresponds to the length of $\sim 10^3$ unit cells, and $A \approx 2.9 \times 10^{-19}$ m^3/s. In order to model the field-dependence of the thermal conductivity using equations 7.36-7.39 we must have a concrete description of $\tau_\pm$. Therefore, to account for the scattering of hybridized spin-phonon excitations, we adopt the simple assumption that these excitation scatter identically to normal phonons, subject to the same boundary and scattering point defect terms of Eqn. 7.41 for the ordinary phonon lifetime, modified to account for the effect hybridization has on the propagation velocity and density of states. Under this naive assumption, the relation time can be generalized in the following way to describe the hybrid excitations:

$$\tau_\pm^{-1}(\omega(k)) = \ell_0^{-1} v_{g,\pm} + A\frac{k^2}{v_{g,\pm}}\left(\omega^{(1)}_{n-q,+}\right)^2, \tag{7.43}$$

where $v_{g,\pm} = d\omega^{(1)}_{n-q,+}/dk$ is the group velocity of the corresponding hybrid excitation in Eqns. 7.38,7.39.

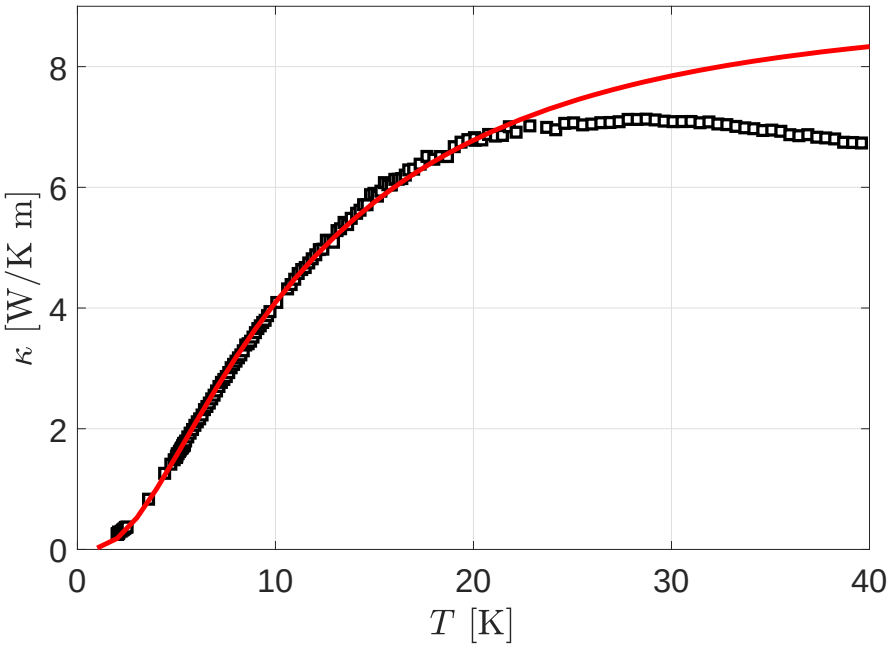

Figure 7.6: A fit of the zero-field thermal conductivity at $T < 20$ K, using the minimal phonon scattering lifetime given by Eqn. 7.41.

7.5.3 Simulated $\kappa(\mathbf{H}||ab)$ at finite T

With our characterization of the CEF spectrum $\omega_{0,\pm}$ as determined in Chapter 6 we estimate $\omega_c(H) = \gamma_c H$ where $\gamma_c = 0.203$ meV/T and use the values of v_s, ℓ_0, & A determined in the previous section to calculate the field dependence of the thermal conductivity predicted by this model. As discussed in section 7.3.3, the $\tilde{f}$ used to compute the eigenvalues $\omega^{(n)}_{n-q,+}$ have an explicit functional dependence on k that goes as $\sim \tilde{\eta} k \sqrt{\omega(k)}$. Additionally, as shown in sec 7.4, each eigenvalue depends on the quadrature sum of all possible f_λ, and therefore also the quadrature sum of all $\tilde{\eta}_\lambda$ for each polarization, as determined by the coefficients of terms in the full magnetoelastic interaction Hamiltonian, see Eqns. 7.16-7.18. As a consequence, the overall strength of the interaction is effectively described by a single parameter $\tilde{\eta} = \sqrt{|\tilde{\eta}_1|^2 + |\tilde{\eta}_2|^2 + |\tilde{\eta}_3|^2}$, and the model does distinguish variations in these individual parameters. For values of $\tilde{\eta}$ ranging from ranging from $\sim$ 2.0 - 5.0 we are able to reproduce nearly all the qualitative features of the low temperature data, see Fig. 7.2, up to 20 K. It exhibits minima locations $H_c(T)$, which move outward as a function temperature,

and are approximately consistent with those experimentally observed. Furthermore, this model is almost accurate in quantifying the maximum fractional suppression of the thermal conductivity, which is approximately -15%, although the model does not quite reach this limit.

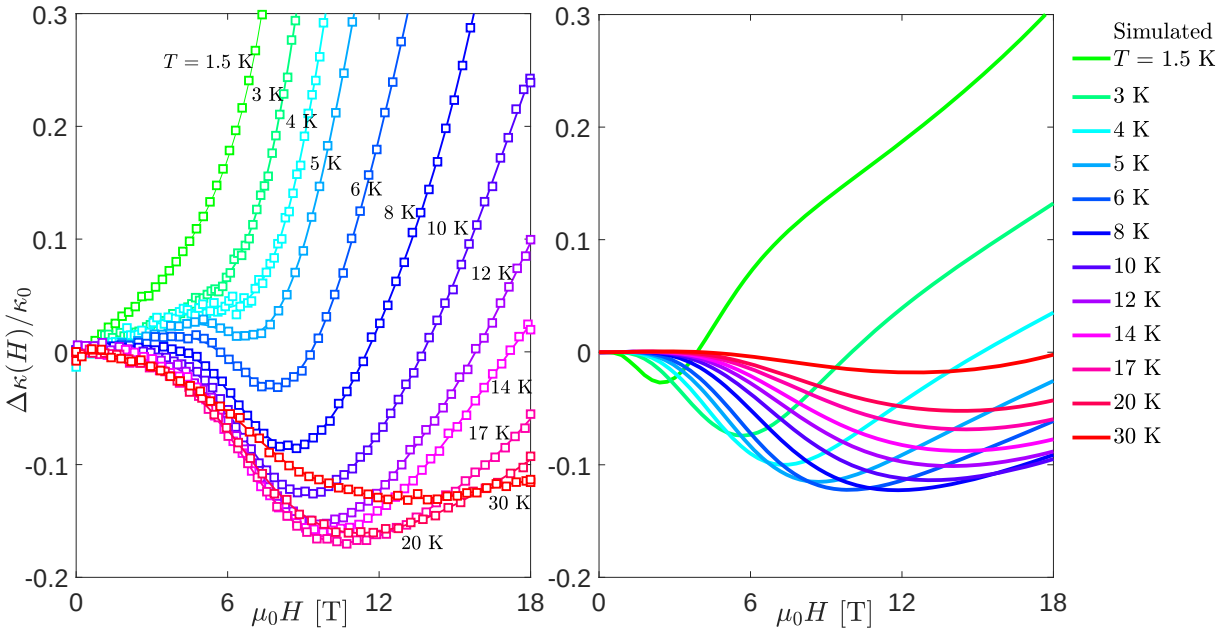

Figure 7.7: The right hand side shows the simulated thermal conductivity of $CsYbSe_2$ calculated according to Eqns. 7.36-7.39 using the explicit $\tau_P(k), \tau_\pm(k)$ of Eqn. 7.41 and 7.43 respectively, where a single value of $\tilde{\eta} = 4.0$ is assumed. The left hand side shows the real experimental data for the same temperature-series, plotted. The vertical and horizontal axes of both plots are exactly identical.

7.5.4 Interaction parameter fine-tuning and modified scattering

Given the enormous simplifying assumptions of this model, in particular those assumptions made about the hybridized mean scattering time, it is remarkable that the model is able to correctly account for some many qualitative features of the real data. By allowing $\tilde{\eta}$ to vary as a function of temperature, and introducing reasonable modifications to $\tau_\pm$ we can fine-tune this model, such that it is also quantitatively correct at all temperatures, faithfully reproducing the locations of all minima H_c, and the observed magnitudes of both the suppression at H_c and maximal enhancement at 18 T. For a sufficiently large choice of the coupling parameter $\tilde{\eta}$ we are even able to accurately

reproduce the enormous ten-fold enhancement of the $T = 1.5$ K trace.

As observed exclusively in the $\kappa(\mathbf{H}||c)$ orientation and the elevated temperature traces for the $\kappa(\mathbf{H}||ab)$ orientation the maximum suppression of $\kappa(H)$ is a factor of 2-3 times larger than the model can capture for any choice of $\omega_c(H)$ or $\tilde{\eta}$ without any modifications of the phonon or hybrid excitation scattering lifetimes $\tau_P, \tau_\pm$ respectively, this seems to suggest that the scattering lifetime must be increasing with applied field in order to account for the full magnitude of this suppression. Without more careful theoretical modeling, we can only speculate about what might be responsible for an increased quasi-particle scattering rate under an applied field, but one potential explanation relies on the sensitivity of phonon and hybrid excitation scattering alike to local spin disorder, as characterized by the bulk magnetization $M(H)$. By contrast to the case of $CrCl_3$ explored in chapter 5, the quasi-particle scattering rate of $CsYbSe_2$ seems to increase with decreasing spin disorder.

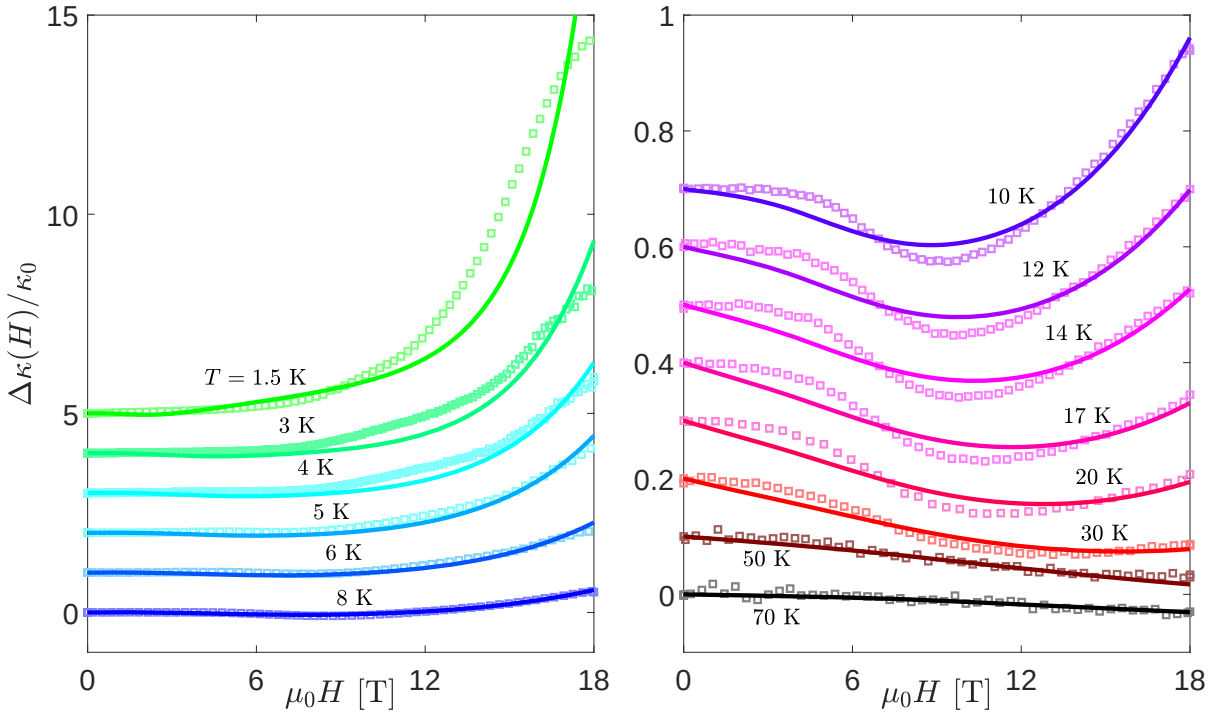

Figure 7.8: Squares are $\Delta\kappa(H)/\kappa_0$ data for $CsYbSe_2$ and lines are the spin-phonon hybridization model, where $\tilde{\eta}$ is allowed to vary as a function of temperature, and the scattering lifetimes $\tau_P^{-1}, \tau_\pm^{-1}$ have been modified with the inclusion of an additional H-linear scattering rate $\tau_H^{-1} = cH$. Curves have been offset for clarity. The exact parameters used for $\tilde{\eta}$ and c are plotted in Fig. 7.9

As observed at very low temperatures [119], a finite field applied in-plane contributes to the formation of an up-up-down (uud) spin state that produces a distinct 1/3 plateau in the low$-T$ magnetization. Due to frustration and thermal fluctuations, a long-range uud state cannot be stabilized at higher temperatures, but the formation of uud domains and spin clusters is likely, which may possibly contribute to an abundance of domain walls on short length scales. In such a scenario the increased domain wall formation associated with the gradual polarization of the spin lattice may be responsible for the enhanced quasi-particle scenario, but such a hypothesis remains highly speculative nonetheless. Whatever the actual physical mechanism, we can empirically account for the observed decrease in the mean quasi-particle lifetime at finite field by introducing an additional explicitly field-dependent scattering rate τ_H^{-1} to $\tau_P^{-1}, \tau_\pm^{-1}$ in Eqns. 7.41,7.43.

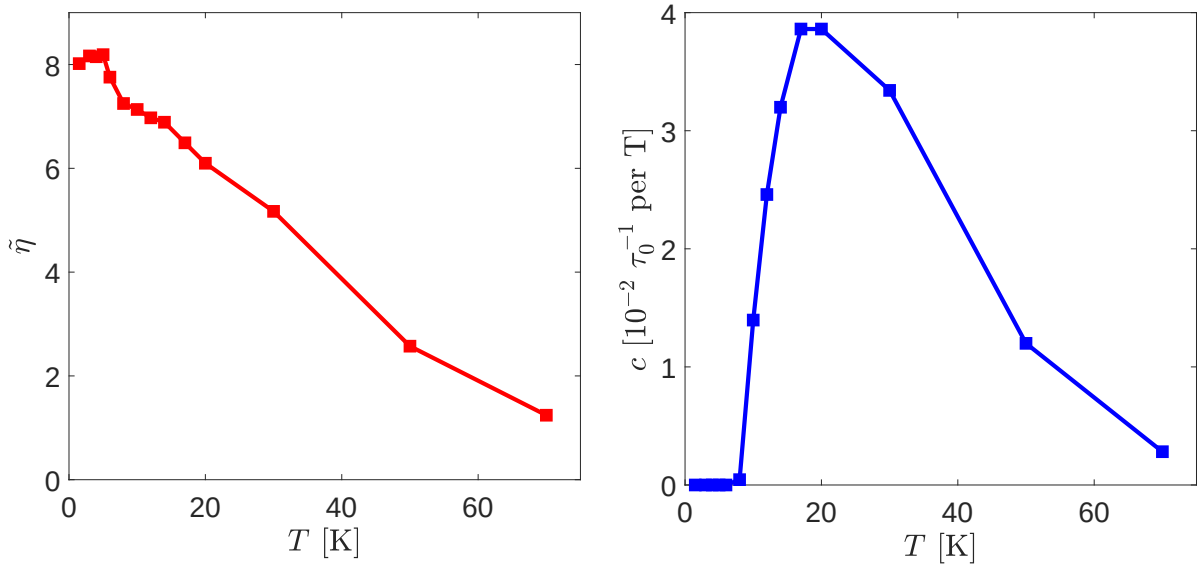

Figure 7.9: The left hand side shows the dimensionless $\tilde{\eta}$ which produce best-fits of the $\Delta\kappa(H)/\kappa_0$ at each fixed temperature. These $\tilde{\eta}$ follow an approximately linear relationship, decreasing as a function of temperature. The right hand side shows the empirical parameter c at each temperature which produces the best possible agreement of the model with actual data, given in units of τ_0^{-1} per T, which controls the size of a field-dependent correction τ_H^{-1} to the quasi=particle scattering rate.

If such a scattering rate τ_H^{-1} is indeed somehow directly correlated with magnetic disorder, at lowest order it will depend on either the magnetization $M(H)$ or the degree of spin polarization,

$[1 - M(H)/M_S]$, relative to a saturation moment M_S. Thus if we treat τ_H as a correction to the constant, boundary-scattering term $\tau_0^{-1} \equiv \ell_0^{-1} v_s$ it should generically grow H-linearly at leading order, at least for fields where $M(H)$ is not close to the saturation moment, thus $\tau_H^{-1} = cH$ is a reasonable first-order assumption. The specific dimensionless $\tilde{\eta}$, and c, given in units of τ_0^{-1} per T, which produce the best fits of our measured data are plotted in Fig. 7.9. The optimal value of $\tilde{\eta}$ seems to follow a linearly decreasing relationship with temperature, suggesting that the magnetoelastic coupling weakens as a function of temperature, almost entirely disappearing by $\sim$ 80 K. This appears to be consistent with the complete disappearance of any appreciable field dependence of $\kappa(T)$ at sufficiently elevated temperatures. By contrast, the best selection of $c(T)$ appears to vary non-monotonically, peaked around $T \sim 20$ K, this is unsurprising given that the total thermal conductivity itself, see Fig. 7.1, peaks near this temperature as well. At very low temperatures, even if c is allowed to take on negative values, no advantage in fitting the data is gained by the inclusion of finite c. This seems to suggest that the increase in the quasi-particle scattering rate τ_H^{-1} may be related to multi-phonon scattering processes, such such as Normal and Umklapp processes that only become relevant at elevated temperatures. Further theoretical work is certainly needed to explain how such terms generalize in the case of spin-phonon hybrid excitations.

7.6 Summary & Outlook

In summary, we have proposed a highly generic model of spin-phonon coupling, whereby spin-flip excitation and phonons interact and hybridize via strain-modulation of the magnetic g-tensor under applied field. From zero-field heat capacity, and low temperature thermal transport data, we were able to independently deduce the speed of sound and a minimal set of parameters that determine low-temperature phonon scattering properties. In order to explicitly model the H-dependence of the thermal conductivity of $CsYbSe_2$ we employ a straight-forward generalization of the mean phonon scattering rate. On its own, this highly-simplified minimal model is able to produce almost all of the important qualitative features of the $\kappa(\mathbf{H}||ab)$ data, namely the non-monotonic H-dependence which results in pronounced minima H_c that shift outward as

temperature increases. The model also potentially accounts for the observed massive enhancement of the thermal conductivity at low temperatures. By fine-tuning the coupling parameter $\tilde{\eta}$ and introducing additional explicit H-dependence into the quasi-particle scattering rate we can somewhat improve the success of this model in reproducing the quantitative features of the measured data. Further theoretical work is certainly required to improve the quantitative agreement of this model, but its success provides strong evidence for the presence of this g-tensor strain-modulation mechanism of spin-phonon coupling, and the associated hybridization of phonons and spin-flip excitations. We expect that this type of model is actually fairly generic and may be widely useful in explaining the thermal transport data of many other magnetic systems.

Chapter 8

Conclusion

8.1 Summary

The work presented in this thesis has developed two universal models for magentoelastic interaction in insulating magnets. The first such model, applied in our transport study of $CrCl_3$, empirically quantifies how spin disorder can modifying phonon scattering, and provides insight into how the field dependence of a phonon-dominated bulk thermal conductivity is directly influenced by magnetization in multiple behavioral regimes of a conventional antiferromagnet. In contrast to many extensions of the Debye-Callaway model, that depend on microscopic parameters which are often difficult to independently justify or quantify, this analysis is not-system specific or dependent on a particular microscopic model, and as such, is widely applicable to a wide array of insulating systems.

The second such model, used to describe features of the non-monotonically varying, field-dependent thermal conductivity in $CsYbSe_2$ describes a mechanism for magneto-elastic interaction and potential hybridization between spin excitation and acoustic phonons via a strain modulation of the magnetic g-tensor in a finite field. This culminates in a Janyes Cummings type toy model for spin-phonon interaction, whose exact solution provides a prescription for calculating the thermal properties of hybridized excitation with mixed statistical properties. Ultimately, this analysis is also enormously successful in describing all the peculiar features of the $CsYbSe_2$ data. While spin-phonon hybridization has been explored in several contexts, [154, 122], including its effect on thermal transport [50, 52], our work represents one of those most complete implementations of field-

dependent modeling in a transport study. The strain mechanism of g-tensor modulation central to this model is quite generic, and certain to appear in other contexts. Based on many distinct similarities to other observed thermal conductivity data in materials such as $RuCl_3$ [12, 14] and our own preliminary data for $K_2V_3O_8$ [24], we suspect that there are numerous other insulating systems, where such an analysis can be successfully leveraged to explain the field evolution of transport coefficients.

In studying insulating magnetic systems, we have also greatly expanded the usefulness of cantilever-based magnetometry techniques. Our analysis of field-dependent resonant torsion magnetometry data for $CsYbSe_2$ at various temperatures was successfully used to extract crystal electric field parameters in a manner completely orthogonal to conventional inelastic neutron scattering probes. Given the unique sensitivity of resonant torsion magnetometry to anisotropy and the field-dependent character of the CEF spectrum, we can strongly constrain CEF paramters, combating traditional problems of degeneracy and under-determined fitting associated with inelastic neutron scattering probes of CEF spectra. This work is broadly applicable to virtually any system featuring rare-earth, $4f$ magnetic ions, including examples of pyrochlore [38] and triangular lattices [118, 119, 112] which have recently gained intense interest for their potential to realize QSL spin states.

8.2 Outlook

Naturally, further work needs to be done to test the models that we have developed for magnetoelastic coupling. In the case of the hybridization model describing the thermal conductivity of $CsYbSe_2$ there is also a significant amount of theoretical work that remains to be done to clarify the functional dependence of scattering terms for hybridized excitations, and to verify the basic properties of this model for more generic phonon spectra. Other materials in the family of related rare-earth, delafossite compounds ARX_2, where A = Na, K, Rb, Cs, R = any of the 4f rare earth Lanthanides, and X = O, S, Se, many of which have already been synthesized, offer countless systems for direct comparison. The many options for elemental substitution in these nearly

isostructural compounds provides an amazing capability to fine tune microscopic interactions. For example, substituting the $J_{\text{eff}} = 7/2$ Yb^{3+} with either a $J_{\text{eff}} = 5/2$ Ce^{3+} or a $J_{\text{eff}} = 15/2$ Er^{3+} allows one to either greatly reduce, or greatly increase the complexity of crystal field interactions.

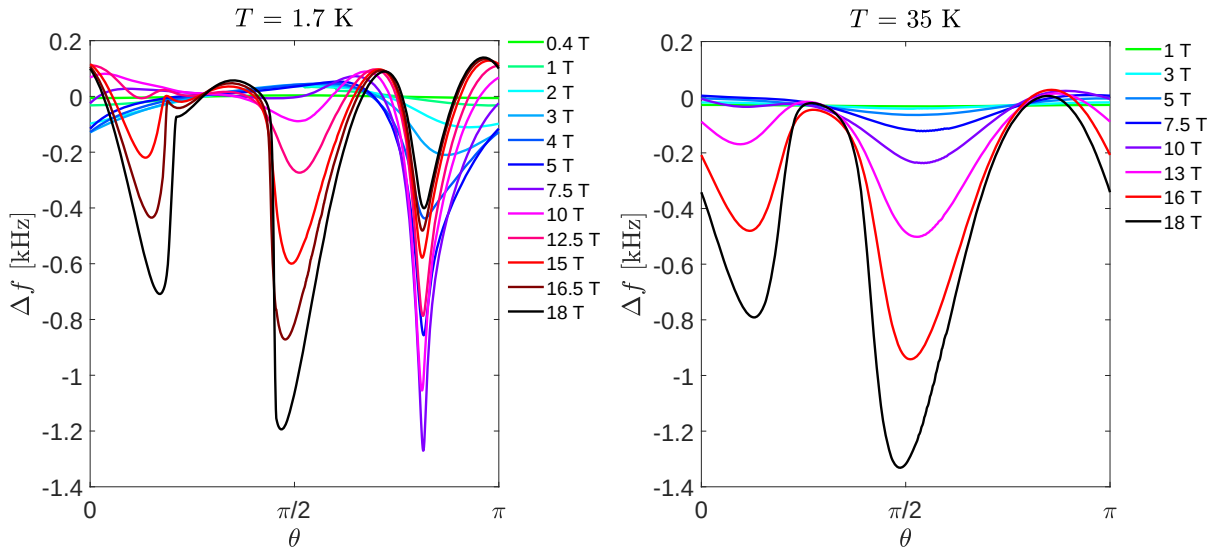

Figure 8.1: Measured magnetoropic frequency shifts $\Delta f(\theta)$ for the $J_{\text{eff.}} = 15/2$ triangular lattice delafossite system $CsErSe_2$, at various fixed fields up to 18 T at 2 temperatures, $T = 1.7$ K, 30 K. This data exhibits a very robust negative mean curvatur observed at all temperatures.

There are also many outstanding questions that remain for the technique of resonant torsion magnetometry. As discussed in chapter 4, we have observed, along with several collaborators [26], a very large negative mean curvature in the preliminary magnetotropic data of a select few frustrated, strongly interacting spin systems, namely the Kitaev candidate materials $RuCl_3$ and Na_2IrO_3, and as pictured in Fig. 8.1 triangular lattice delafossite $CsErSe_2$. This negative mean curvature is not currently predicted by our theoretical descriptions of these materials, and appears to be too large to be attributed any of several mundane systematic effects for the cantilever measurement. While it is attractive, and certainly plausible to try to explain this phenomena in terms of non-analytic properties of the respective magnetic free energies of these materials, a more mundane explanation may still exist that depends on non-linear vibration physics of the cantilever itself. In either case, significant theoretical work remains. The resolution to this question of what is behind the enormous negative mean curvature will likely require more than another PhD thesis's

work of dynamical modeling, finite element simulations, and carefully-controlled experimentation. Answering this question is absolutely crucial to the continued success and applicability of this experimental technique.

Bibliography

[1] Atsufumi Hirohata, Keisuke Yamada, Yoshinobu Nakatani, Lucian Prejbeanu, Bernard Diény, Philipp Pirro, and Burkard Hillebrands. Review on spintronics: Principles and device applications. Journal of Magnetism and Magnetic Materials, 509(January), 2020.

[2] Ville Lahtinen and Jiannis K. Pachos. A Short Introduction to Topological Quantum Computation. SciPost Phys., 3:021, 2017.

[3] R. Coldea, D. A. Tennant, A. M. Tsvelik, and Z. Tylczynski. Experimental Realization of a 2D Fractional Quantum Spin Liquid. Phys. Rev. Lett., 86:1335, 2001.

[4] Yao-Dong Li and Gang Chen. Symmetry enriched U(1) topological orders for dipole-octupole doublets on a pyrochlore lattice. Phys. Rev. B, 95:041106(R), Jan 2017.

[5] G. Chen and M. Hermele. Magnetic orders and topological phases from f-d exchange in pyrochlore iridates. Phys. Rev. B, 86:235129, 2012.

[6] Yi-Ping Huang, Gang Chen, and Michael Hermele. Quantum Spin Ices and Topological Phases from Dipolar-Octupolar Doublets on the Pyrochlore Lattice. Phys. Rev. Lett., 112:167203, Apr 2014.

[7] S. S. Pershoguba, S. Banerjee, J. C. Lashley, J. Park, H. Ågren, G. Aeppli, and A. V. Balatsky. Dirac Magnons in Honeycomb Ferromagnets. Phys. Rev. X, 8:011010, 2018.

[8] A. Kitaev. Anyons in an exactly solved model and beyond. Ann. Phys., 321:2, 2006.

[9] Lucile Savary and Leon Balents. Quantum spin liquids: a review. Rep. Prog. Phys., 80(1):016502, nov 2016.

[10] Y. Ando, J. Takeya, D. L. Sisson, S. G. Doettinger, I. Tanaka, R. S. Feigelson, and A. Kapitulnik. Thermal conductivity of the spin-Peierls compound $CuGeO_3$. Phys. Rev. B, 58:R2913, 1998.

[11] A. V. Sologubenko, K. Giannó, H. R. Ott, U. Ammerahl, and A. Revcolevschi. Thermal Conductivity of the Hole-Doped Spin Ladder System $Sr_{14-x}Ca_xCu_{24}O_{41}$. Phys. Rev. Lett., 84:2714, 2000.

[12] C. Hess, C. Baumann, U. Ammerahl, B. Büchner, F. Heidrich-Meisner, W. Brenig, and A. Revcolevschi. Magnon Heat Transport in $(Sr,Ca,La)_{14}Cu_{24}O_{41}$. Phys. Rev. B, 64:184305, 2001.

[13] M. Hofmann, T. Lorenz, G. S. Uhrig, H. Kierspel, O. Zabara, A. Freimuth, H. Kageyama, and Y. Ueda. Strong damping of phononic heat current by magnetic excitations in $SrCu_2(BO_3)_2$. Phys. Rev. Lett., 87:047202, 2001.

[14] I. A. Leahy, C. A. Pocs, P. E. Siegfried, D. Graf, S.-H. Do, K.-Y. Choi, B. Normand, and M. Lee. Anomalous Thermal Conductivity and Magnetic Torque Response in the Honeycomb Magnet α-$RuCl_3$. Phys. Rev. Lett., 118:187203, 2017.

[15] Charles Kittel. Introduction to Solid State Physics. John Wiley & Sons, Inc., New York, 6th edition, 1986.

[16] N.W. Ashcroft and N.D. Mermin. Solid State Physics. Saunders College, Philadelphia, 1976.

[17] S. Blundell. Magnetism in Condensed Matter. Oxford University Press, Oxford, 2001.

[18] Michael A. McGuire, Genevieve Clark, Santosh KC, W. Michael Chance, Gerald E. Jellison, Valentino R. Cooper, Xiaodong Xu, and Brian C. Sales. Magnetic behavior and spin-lattice coupling in cleavable van der waals layered $crcl_3$ crystals. Phys. Rev. Materials, 1:014001, 2017.

[19] R. O. Pohl and B. Stritzker. Phonon scattering at crystal surfaces. Phys. Rev. B, 25:3608–3614, 1982.

[20] Lebing Chen, Jae-Ho Chung, Bin Gao, Tong Chen, Matthew B. Stone, Alexander I. Kolesnikov, Qingzhen Huang, and Pengcheng Dai. Topological spin excitations in honeycomb ferromagnet CrI_3. Physical Review X, 8(4):41028, 2018.

[21] C. Strohm, G. L.J.A. Rikken, and P. Wyder. Phenomenological evidence for the phonon hall effect. Physical Review Letters, 95(15):1–4, 2005.

[22] K. Sugii, M. Shimozawa, D. Watanabe, Y. Suzuki, M. Halim, M. Kimata, Y. Matsumoto, S. Nakatsuji, and M. Yamashita. Thermal Hall Effect in a Phonon-Glass Ba3CuSb2 O9. Physical Review Letters, 118(14):1–5, 2017.

[23] Y. Kasahara, T. Ohnishi, Y. Mizukami, O. Tanaka, Sixiao Ma, K. Sugii, N. Kurita, H. Tanaka, J. Nasu, Y. Motome, T. Shibauchi, and Y. Matsuda. Majorana quantization and half-integer thermal quantum Hall effect in a Kitaev spin liquid. Nature, 559(7713):227–231, 2018.

[24] B. C. Sales, M. D. Lumsden, S. E. Nagler, D. Mandrus, and R. Jin. Magnetic Field Enhancement of Heat Transport in the 2D Heisenberg Antiferromagnet $K_2V_3O_8$. Phys. Rev. Lett., 88:095901, 2002.

[25] K. A. Modic, Maja D. Bachmann, B. J. Ramshaw, F. Arnold, K. R. Shirer, Amelia Estry, J. B. Betts, Nirmal J. Ghimire, E. D. Bauer, Marcus Schmidt, Michael Baenitz, E. Svanidze, Ross D. McDonald, Arkady Shekhter, and Philip J. W. Moll. Resonant torsion magnetometry in anisotropic quantum materials. Nat. Commun., 9:3975, 2018.

[26] K. A. Modic, Ross D. McDonald, J. P. C. Ruff, Maja D. Bachmann, You Lai, Johanna C. Palmstrom, David Graf, Mun K. Chan, F. F. Balakirev, J. B. Betts, G. S. Boebinger, Marcus Schmidt, Michael J. Lawler, D. A. Sokolov, Philip J. W. Moll, B. J. Ramshaw, and Arkady Shekhter. Scale-invariant magnetic anisotropy in $RuCl_3$ at high magnetic fields. Nat. Phys., 17:240, 2020.

[27] Erik Koch. Exchange Mechanisms, volume 2. 2012.

[28] Daisuke Yamamoto, Giacomo Marmorini, Masahiro Tabata, Kazuki Sakakura, and Ippei Danshita. Magnetism driven by the interplay of fluctuations and frustration in the easy-axis triangular XXZ model with transverse fields. Phys. Rev. B, 100:140410(R), 2019.

[29] Jeffrey G. Rau and Michel J.P. Gingras. Frustrated Quantum Rare-Earth Pyrochlores. Annu. Rev. Condens. Matter Phys., 10(1):357, 2019.

[30] M. Hirschberger, R. Chisnell, Y. S. Lee, and N. P. Ong. Thermal Hall effect of spin excitations in a kagome magnet. Phys. Rev. Lett., 115:106603, 2015.

[31] A. Banerjee, C. A. Bridges, J. Q. Yan, A. A. Aczel, L. Li, M. B. Stone, G. E. Granroth, M. D. Lumsden, Y. Yiu, J. Knolle, S. Bhattacharjee, D. L. Kovrizhin, R. Moessner, D. A. Tennant, D. G. Mandrus, and S. E. Nagler. Proximate Kitaev quantum spin liquid behaviour in a honeycomb magnet. Nature Mater., 15:733, 2016.

[32] Y. Li, P. Gegenwart, and A. A. Tsirlin. Spin liquids in geometrically perfect triangular antiferromagnets. J. Phys. Condens. Matter, 32:224004, 2020.

[33] Toru Moriya. Anisotropic superexchange interaction and weak ferromagnetism. Phys. Rev., 120:91–98, Oct 1960.

[34] Leo P Kadanoff. More is the Same ; Phase Transitions and Mean Field Theories. 177:777–797, 2009.

[35] Ignacio Gallo and Pierluigi Contucci. Bipartite mean field spin systems. existence and solution. arXiv: Statistical Mechanics, 2007.

[36] M. T. Hutchings. Point-Charge Calculations of Energy Levels of Magnetic Ions in Crystalline Electric Fields. Solid State Physics - Advances in Research and Applications, 16(C):227–273, 1964.

[37] Gang Cao. Towards electrical-current control of quantum states in spin–orbit-coupled matter. Journal of Physics: Condensed Matter, 32(42):423001, jul 2020.

[38] Bin Gao, Tong Chen, David W. Tam, Chien-Lung Huang, Kalyan Sasmal, Devashibhai T. Adroja, Feng Ye, Huibo Cao, Gabriele Sala, Matthew B. Stone, Christopher Baines, Joel A. T. Verezhak, Haoyu Hu, Jae-Ho Chung, Xianghan Xu, Sang-Wook Cheong, Manivannan Nallaiyan, Stefano Spagna, M. Brian Maple, Andriy H. Nevidomskyy, Emilia Morosan, Gang Chen, and Pengcheng Dai. Experimental signatures of a three-dimensional quantum spin liquid in effective spin-1/2 $Ce_2Zr_2O_7$ pyrochlore. Nat. Phys., 15:1052, 2018.

[39] Yuesheng Li, Devashibhai Adroja, Robert I. Bewley, David Voneshen, Alexander A. Tsirlin, Philipp Gegenwart, and Qingming Zhang. Crystalline Electric-Field Randomness in the Triangular Lattice Spin-Liquid $YbMgGaO_4$. Phys. Rev. Lett., 118:107202, Mar 2017.

[40] B. J. Kim, Hosub Jin, S. J. Moon, J.-Y. Kim, B.-G. Park, C. S. Leem, Jaejun Yu, T. W. Noh, C. Kim, S.-J. Oh, J.-H. Park, V. Durairaj, G. Cao, and E. Rotenberg. Novel $j = 1/2$ mott state induced by relativistic spin-orbit coupling in sr_2iro_4. Phys. Rev. Lett., 101:076402, Aug 2008.

[41] Karl W. Böer and Udo W. Pohl. Elasticity and Phonons, pages 111–150. Springer International Publishing, Cham, 2018.

[42] Woldemar Voigt. Lehrbuch der kristallphysik (mit ausschluss der kristalloptik). 1910.

[43] A. Marcolongo.

[44] J. Callaway. Model for Lattice Thermal Conductivity at Low Temperatures. Phys. Rev., 113:1046, 1959.

[45] A. A. Maznev and O. B. Wright. Demystifying umklapp vs normal scattering in lattice thermal conductivity. American Journal of Physics, 82(11):1062–1066, 2014.

[46] Yongsheng Zhang. First-principles Debye–Callaway approach to lattice thermal conductivity. Journal of Materiomics, 2(3):237–247, 2016.

[47] Zheng Zhang, Xiaoli Ma, Jianshu Li, Guohua Wang, D. T. Adroja, T. P. Perring, Weiwei Liu, Feng Jin, Jianting Ji, Yimeng Wang, Yoshitomo Kamiya, Xiaoqun Wang, Jie Ma, and Qingming Zhang. Crystalline electric field excitations in the quantum spin liquid candidate $NaYbSe_2$. Phys. Rev. B, 103:035144, Jan 2021.

[48] R Kubo. The fluctuation-dissipation theorem. Reports on Progress in Physics, 29(1):255–284, jan 1966.

[49] B Dongre, T Wang, and G K H Madsen. Comparison of the Green-Kubo and homogeneous non-equilibrium molecular dynamics methods for calculating thermal conductivity. pages 1–11.

[50] W Lovesey. Theory of the magrion and phonon interaction. 5(June), 1972.

[51] Michiyasu Mori, Alexander Spencer-Smith, Oleg P. Sushkov, and Sadamichi Maekawa. Origin of the phonon hall effect in rare-earth garnets. Physical Review Letters, 113(26):1–7, 2014.

[52] Yu Kagan and L A Maksimov. Anomalous Hall Effect for the Phonon Heat Conductivity in Paramagnetic Dielectrics. 145902(April):1–4, 2008.

[53] S. A. Owerre. Topological transitions of magnons in three-dimensional strained chiral antiferromagnets and thermal Hall effect of magnons in honeycomb ferromagnet CrI_3. pages 1–12, 2018.

[54] Theoretische Physik, Goethe-universität Frankfurt, and Frankfurt Main. Sawtooth Torque in Anisotropic j eff = 1 = 2 Magnets : Application to α -RuCl 3. 197202(September 2018):1–6, 2019.

[55] J. M. Ziman. Electrons and Phonons. Oxford University Press, Oxford, 1960.

[56] R. Jin, Y. Onose, Y. Tokura, D. Mandrus, P. Dai, and B. C. Sales. In-Plane Thermal Conductivity of Nd_2CuO_4: Evidence for Magnon Heat Transport. Phys. Rev. Lett., 91:146601, 2003.

[57] S. Y. Li, L. Taillefer, C. H. Wang, and X. H. Chen. Ballistic Magnon Transport and Phonon Scattering in the Antiferromagnet Nd_2CuO_4. Phys. Rev. Lett., 95:156603, 2005.

[58] J. C. Wu, J. D. Song, Z. Y. Zhao, J. Shi, H. S. Xu, J. Y. Zhao, X. G. Liu, X. Zhao, and X. F. Sun. Thermal conductivity of the diamond-chain compound $Cu_3(CO_3)_2(OH)_2$. J. Phys.: Condens. Matter, 28:056002, 2016.

[59] J. M. Fletcher, W. E. Gardner, A. C. Fox, and G. Topping. X-Ray, infrared, and magnetic studies of α- and β-ruthenium trichloride. J. Chem. Soc. A, page 1038, 1967.

[60] K. W. Plumb, J. P. Clancy, L. J. Sandilands, V. Vijay Shankar, Y. F. Hu, K. S. Burch, H.-Y. Kee, and Y.-J. Kim. α-$RuCl_3$: A spin-orbit assisted Mott insulator on a honeycomb lattice. Phys. Rev. B, 90:041112(R), 2014.

[61] J. A. Sears, M. Songvilay, K. W. Plumb, J. P. Clancy, Y. Qiu, Y. Zhao, D. Parshall, and Y.-J. Kim. Magnetic order in α-$RuCl_3$: A honeycomb-lattice quantum magnet with strong spin-orbit coupling. Phys. Rev. B, 91:144420, 2015.

[62] R. D. Johnson, S. C. Williams, A. A. Haghighirad, J. Singleton, V. Zapf, P. Manuel, I. I. Mazin, Y. Li, H. O. Jeschke, R. Valentí, and R. Coldea. Monoclinic crystal structure of α-$RuCl_3$ and the zigzag antiferromagnetic ground state. Phys. Rev. B, 92:235119, 2015.

[63] H. B. Cao, A. Banerjee, J.-Q. Yan, C. A. Bridges, M. D. Lumsden, D. G. Mandrus, D. A. Tennant, B. C. Chakoumakos, and S. E. Nagler. Low-temperature crystal and magnetic structure of α-$RuCl_3$. Phys. Rev. B, 93:134423, 2016.

[64] J. Zheng, K. Ran, T. Li, J. Wang, P.-S. Wang, B. Liu, Z.-X. Liu, B. Normand, J. Wen, and W. Yu. Gapless Spin Excitations in the Field-Induced Quantum Spin Liquid Phase of α-$RuCl_3$. Phys. Rev. Lett., 119:227208, 2017.

[65] A. N. Ponomaryov, E. Schulze, J. Wosnitza, P. Lampen-Kelley, A. Banerjee, J. Q. Yan, C. A. Bridges, D. G. Mandrus, S. E. Nagler, A. K. Kolezhuk, and S. A. Zvyagin. Unconventional spin dynamics in the honeycomb-lattice material α-$RuCl_3$: high-field ESR studies. Phys. Rev. B, 96:241107(R), 2017.

[66] A. Banerjee, J. Q. Yan, J. Knolle, C. A. Bridges, M. B. Stone, M. D. Lumsden, D. G. Mandrus, D. A. Tennant, R. Moessner, and S. E. Nagler. Neutron scattering in the proximate quantum spin liquid α-$RuCl_3$. Science, 356:1055, 2017.

[67] A. Banerjee, P. Lampen-Kelley, J. Knolle, C. Balz, A. A. Aczel, B. Winn, Y. Liu, D. Pajerowski, J.-Q. Yan, C. A. Bridges, A. T. Savici, B. C. Chakoumakos, M. D. Lumsden, D. A. Tennant, R. Moessner, D. G. Mandrus, and S. E. Nagler. Excitations in the field-induced quantum spin liquid state of α-$RuCl_3$. npj Quantum Materials, 3:8, 2018.

[68] R. Hentrich, A. U. B. Wolter, X. Zotos, W. Brenig, D. Nowak, A. Isaeva, T. Doert, A. Banerjee, P. Lampen-Kelley, D. G. Mandrus, S. E. Nagler, J. Sears, Y.-J. Kim, B. Büchner, and C. Hess. Large field-induced gap of Kitaev-Heisenberg paramagnons in α-$RuCl_3$. Phys. Rev. Lett., 120:117204, 2018.

[69] M. A. McGuire, H. Dixit, V. R. Cooper, and B. C. Sales. Coupling of Crystal Structure and Magnetism in the Layered, Ferromagnetic Insulator CrI_3. Chem. Mater., 27:612, 2015.

[70] B. Huang, G. Clark, E. Navarro-Moratalla, D. R. Klein, R. Cheng, K. L. Seyler, Z. Ding, E. Schmidgall, M. A. McGuire, D. H. Cobden, Y. Wang, X. Di, P. Jarillo-Herrero, and

X. Xu. Layer-dependent ferromagnetism in a van der Waals crystal down to the monolayer limit. Nature, 546:270, 2017.

[71] W. N. Hansen and M. Griffel. Heat Capacities of CrF_3 and $CrCl_3$ from 15 to 300°K. J. Chem. Phys., 28:902, 1958.

[72] J. W. Cable, M. K. Wilkinson, and E. O. Wollan. Neutron diffraction investigation of antiferromagnetism in $CrCl_3$. J. Phys. Chem. Solids, 19:29, 1961.

[73] H. Bizette, C. Terrier, and A. Adam. Aimantations principales du chlorure chromique. C. R. Acad. Sci., 252:1571, 1961.

[74] A. Narath and H. L. Davis. Spin-Wave Analysis of the Sublattice Magnetization Behavior of Antiferromagnetic and Ferromagnetic $CrCl_3$. Phys. Rev., 137:A163, 1965.

[75] B. Kuhlow. Magnetic Ordering in $CrCl_3$ at the Phase Transition. Phys. Stat. Sol., 72:161, 1982.

[76] M. N. Baibich, J. M. Broto, A. Fert, F. Nguyen Van Dau, F. Petroff, P. Etienne, G. Creuzet, A. Friederich, and J. Chazelas. Giant magnetoresistance of (001)fe/(001)cr magnetic superlattices. Phys. Rev. Lett., 61:2472–2475, 1988.

[77] R. Bergman. Thermal conduction in solids. Oxford University Press, Oxford, 1979.

[78] A. V. Sologubenko, K. Giannò, H. R. Ott, A. Vietkine, and A. Revcolevschi. Heat transport by lattice and spin excitations in the spin-chain compounds $SrCuO_2$ and Sr_2CuO_3. Phys. Rev. B, 64:054412, 2001.

[79] A. Glamazda, P. Lemmens, S.-H. Do, Y. S. Kwon, and K.-Y. Choi. Relation between Kitaev magnetism and structure in α-$RuCl_3$. Phys. Rev. B, 95:174429, 2017.

[80] B. Morosin and A. Narath. X–Ray Diffraction and Nuclear Quadrupole Resonance Studies of Chromium Trichloride. J. Chem. Phys., 40:1958, 1964.

[81] S.-H. Do, S.-Y. Park, J. Yoshitake, J. Nasu, Y. Motome, Y. S. Kwon, D. T. Adroja, D. J. Voneshen, K. Kim, T.-H. Jang, J.-H. Park, K.-Y. Choi, and S. Ji. Majorana fermions in the Kitaev quantum spin system α-$RuCl_3$. Nature Phys., 13:1079, 2017.

[82] B. Y. Pan, T. Y. Guan, X. C. Hong, S. Y. Zhou, X. Qiu, H. Zhang, and S. Y. Li. Specific heat and thermal conductivity of ferromagnetic magnons in Yttrium Iron Garnet. Europhys. Lett., 103:37005, 2013.

[83] D. R. Klein, D. MacNeill, Q. Song, D. T. Larson, S. Fang, M. Xu, R. A. Ribeiro, P. C. Canfield, E. Kaxiras, R. Comin, and P. Jarillo-Herrero. Enhancement of interlayer exchange in an ultrathin 2D magnet. Nature Phys., 15:in press; arXiv:1903.00002, 2019.

[84] J. Wang, B. Normand, and Z.-X. Liu. One Proximate Kitaev Spin Liquid in the K-J-Γ Model on the Honeycomb Lattice. to appear in Phys. Rev. Lett. (arXiv:1903.10026), 2019.

[85] Z.-X. Liu and B. Normand. Dirac and Chiral Quantum Spin Liquids on the Honeycomb Lattice in a Magnetic Field. Phys. Rev. Lett., 120:187201, 2018.

[86] M. Ye, G. B. Halasz, L. Savary, and L. Balents. Quantization of the Thermal Hall Conductivity at Small Hall Angles. Phys. Rev. Lett., 121:147201, 2018.

[87] Y. Vinkler-Aviv and A. Rosch. Approximately Quantized Thermal Hall Effect of Chiral Liquids Coupled to Phonons. Phys. Rev. X, 8:031032, 2018.

[88] Y. Kasahara, T. Ohnishi, Y. Mizukami, O. Tanaka, S. Ma, K. Sugii, N. Kurita, H. Tanaka, J. Nasu, Y. Motome, T. Shibauchi, and Y. Matsuda. Majorana quantization and half-integer thermal quantum Hall effect in a Kitaev spin liquid. Nature, 559:227, 2018.

[89] X. Cai, T. Song, N. P. Wilson, G. Clark, M. He, X. Zhang, T. Taniguchi, K. Watanabe, W. Yao, D. Xiao, M. A. McGuire, D. H. Cobden, and X. Xu. Atomically Thin $CrCl_3$: An in-Plane Layered Antiferromagnetic Insulator. Nano Lett., 19:3993, 2019.

[90] H. H. Kim, B. Yang, S. Li, S. Jiang, C. Jin, Z. Tao, G. Nichols, F. Sfigakis, S. Zhong, C. Li, S. Tian, D. G. Cory, G.-X. Miao, J. Shan, K. F. Mak, H. Lei, K. Sun, L. Zhao, and A. W. Tsen. Evolution of interlayer and intralayer magnetism in three atomically thin chromium trihalides. Proc. Natl. Acad. Sci. U.S.A., 116:11131, 2019.

[91] J. S. Helton, K. Matan, M. P. Shores, E. A. Nytko, B. M. Bartlett, Y. Yoshida, Y. Takano, A. Suslov, Y. Qiu, J.-H. Chung, D. G. Nocera, and Y. S. Lee. Spin Dynamics of the Spin-1/2 Kagome Lattice Antiferromagnet $ZnCu_3(OH)_6Cl_2$. Phys. Rev. Lett., 98:107204, Mar 2007.

[92] Jason S. Gardner, Michel J. P. Gingras, and John E. Greedan. Magnetic pyrochlore oxides. Rev. Mod. Phys., 82:53, Jan 2010.

[93] Y. Shimizu, K. Miyagawa, K. Kanoda, M. Maesato, and G. Saito. Spin Liquid State in an Organic Mott Insulator with a Triangular Lattice. Phys. Rev. Lett., 91:107001, Sep 2003.

[94] Satoshi Yamashita, Takashi Yamamoto, Yasuhiro Nakazawa, Masafumi Tamura, and Reizo Kato. Gapless spin liquid of an organic triangular compound evidenced by thermodynamic measurements. Nat. Commun., 2:275, 2011.

[95] T. Itou, A. Oyamada, S. Maegawa, M. Tamura, and R. Kato. Quantum spin liquid in the spin-1/2 triangular antiferromagnet $EtMe_3Sb[Pd(dmit)_2]_2$. Phys. Rev. B, 77:104413, Mar 2008.

[96] T. Itou, A. Oyamada, S. Maegawa, and R. Kato. Instability of a quantum spin liquid in an organic triangular-lattice antiferromagnet. Nat. Phys., 6:673, 2010.

[97] Kazuyuki Matsuhira, Makoto Wakeshima, Yukio Hinatsu, and Seishi Takagi. Metal–Insulator Transitions in Pyrochlore Oxides $Ln_2Ir_2O_7$. J. Phys. Soc. Jpn., 80:094701, 2011.

[98] G. Jackeli and G. Khaliullin. Mott Insulators in the Strong Spin-Orbit Coupling Limit: From Heisenberg to a Quantum Compass and Kitaev Models. Phys. Rev. Lett., 102:017205, Jan 2009.

[99] S. K. Choi, R. Coldea, A. N. Kolmogorov, T. Lancaster, I. I. Mazin, S. J. Blundell, P. G. Radaelli, Yogesh Singh, P. Gegenwart, K. R. Choi, S.-W. Cheong, P. J. Baker, C. Stock, and J. Taylor. Spin Waves and Revised Crystal Structure of Honeycomb Iridate Na_2IrO_3. Phys. Rev. Lett., 108:127204, Mar 2012.

[100] Yogesh Singh, S. Manni, J. Reuther, T. Berlijn, R. Thomale, W. Ku, S. Trebst, and P. Gegenwart. Relevance of the Heisenberg-Kitaev Model for the Honeycomb Lattice Iridates A_2IrO_3. Phys. Rev. Lett., 108:127203, Mar 2012.

[101] K. W. Plumb, J. P. Clancy, L. J. Sandilands, V. Vijay Shankar, Y. F. Hu, K. S. Burch, Hae-Young Kee, and Young-June Kim. $\alpha - RuCl_3$: A spin-orbit assisted Mott insulator on a honeycomb lattice. Phys. Rev. B, 90:041112(R), Jul 2014.

[102] Sae Hwan Chun, Jong-Woo Kim, Jungho Kim, H. Zheng, Constantinos C. Stoumpos, C. D. Malliakas, J. F. Mitchell, Kavita Mehlawat, Yogesh Singh, Y. Choi, T. Gog, A. Al-Zein, M. Sala, M. Krisch, J. Chaloupka, G. Jackeli, G. Khaliullin, and B. J. Kim. Direct evidence for dominant bond-directional interactions in a honeycomb lattice iridate Na_2IrO_3. Nat. Phys., 11(3):462, 2015.

[103] C. Mauws, A. M. Hallas, G. Sala, A. A. Aczel, P. M. Sarte, J. Gaudet, D. Ziat, J. A. Quilliam, J. A. Lussier, M. Bieringer, H. D. Zhou, A. Wildes, M. B. Stone, D. Abernathy, G. M. Luke, B. D. Gaulin, and C. R. Wiebe. Dipolar-octupolar Ising antiferromagnetism in $Sm_2Ti_2O_7$: A moment fragmentation candidate. Phys. Rev. B, 98:100401(R), Sep 2018.

[104] A. Scheie, V. O. Garlea, L. D. Sanjeewa, J. Xing, and A. S. Sefat. Crystal-field Hamiltonian and anisotropy in $KErSe_2$ and $CsErSe_2$. Phys. Rev. B, 101:144432, Apr 2020.

[105] A. Scheie. PyCrystalField: Software for Calculation, Analysis, and Fitting of Crystal Electric Field Hamiltonians. J. Appl. Cryst., 54:356, 2021.

[106] Romain Sibille, Elsa Lhotel, Vladimir Pomjakushin, Chris Baines, Tom Fennell, and Michel Kenzelmann. Candidate Quantum Spin Liquid in the Ce^{3+} Pyrochlore Stannate $Ce_2Sn_2O_7$. Phys. Rev. Lett., 115:097202, Aug 2015.

[107] Mitchell M. Bordelon, Eric Kenney, Chunxiao Liu, Tom Hogan, Lorenzo Posthuma, Marzieh Kavand, Yuanqi Lyu, Mark Sherwin, N. P. Butch, Craig Brown, M. J. Graf, Leon Balents, and Stephen D. Wilson. Field-tunable quantum disordered ground state in the triangular-lattice antiferromagnet $NaYbO_2$. Nat. Phys., 15:1058, 2019.

[108] Peng-Ling Dai, Gaoning Zhang, Yaofeng Xie, Chunruo Duan, Yonghao Gao, Zihao Zhu, Erxi Feng, Zhen Tao, Chien-Lung Huang, Huibo Cao, Andrey Podlesnyak, Garrett E. Granroth, Michelle S. Everett, Joerg C. Neuefeind, David Voneshen, Shun Wang, Guotai Tan, Emilia Morosan, Xia Wang, Hai-Qing Lin, Lei Shu, Gang Chen, Yanfeng Guo, Xingye Lu, and Pengcheng Dai. Spinon Fermi Surface Spin Liquid in a Triangular Lattice Antiferromagnet $NaYbSe_2$. Phys. Rev. X, 11:021044, May 2021.

[109] M. Baenitz, Ph. Schlender, J. Sichelschmidt, Y. A. Onykiienko, Z. Zangeneh, K. M. Ranjith, R. Sarkar, L. Hozoi, H. C. Walker, J.-C. Orain, H. Yasuoka, J. van den Brink, H. H. Klauss, D. S. Inosov, and Th. Doert. $NaYbS_2$: A planar spin-$\frac{1}{2}$ triangular-lattice magnet and putative spin liquid. Phys. Rev. B, 98:220409(R), Dec 2018.

[110] K. M. Ranjith, D. Dmytriieva, S. Khim, J. Sichelschmidt, S. Luther, D. Ehlers, H. Yasuoka, J. Wosnitza, A. A. Tsirlin, H. Kühne, and M. Baenitz. Field-induced instability of the quantum spin liquid ground state in the $J_{\text{eff}} = \frac{1}{2}$ triangular-lattice compound $NaYbO_2$. Phys. Rev. B, 99:180401(R), May 2019.

[111] K. M. Ranjith, S. Luther, T. Reimann, B. Schmidt, Ph. Schlender, J. Sichelschmidt, H. Yasuoka, A. M. Strydom, Y. Skourski, J. Wosnitza, H. Kühne, Th. Doert, and M. Baenitz. Anisotropic field-induced ordering in the triangular-lattice quantum spin liquid $NaYbSe_2$. Phys. Rev. B, 100:224417, Dec 2019.

[112] R. Sarkar, Ph. Schlender, V. Grinenko, E. Haeussler, Peter J. Baker, Th. Doert, and H.-H. Klauss. Quantum spin liquid ground state in the disorder free triangular lattice $NaYbS_2$. Phys. Rev. B, 100:241116(R), Dec 2019.

[113] Mitchell M. Bordelon, Chunxiao Liu, Lorenzo Posthuma, P. M. Sarte, N. P. Butch, Daniel M. Pajerowski, Arnab Banerjee, Leon Balents, and Stephen D. Wilson. Spin excitations in the frustrated triangular lattice antiferromagnet $NaYbO_2$. Phys. Rev. B, 101:224427, Jun 2020.

[114] Y. Li, G. Chen, W. Tong, L. Pi, J. Liu, Z. Yang, X. Wang, and Q. Zhang. Rare-Earth Triangular Lattice Spin Liquid: A Single-Crystal Study of $YbMgGaO_4$. Phys. Rev. Lett., 115:167203, 2015.

[115] Y. Shen, Y.-D. Li, H. Wo, Y. Li, S. Shen, B. Pan, Q. Wang, H. C. Walker, P. Steffens, M. Boehm, Y. Hao, D. L. Quintero-Castro, L. W. Harriger, M. D. Frontzek, L. Hao, S. Meng, Q. Zhang, G. Chen, and J. Zhao. Evidence for a spinon Fermi surface in a triangular-lattice quantum-spin-liquid candidate. Nature, 540:559, 2016.

[116] Joseph A. M. Paddison, Marcus Daum, Zhiling Dun, Georg Ehlers, Yaohua Liu, Matthew B. Stone, Haidong Zhou, and Martin Mourigal. Continuous excitations of the triangular-lattice quantum spin liquid $YbMgGaO_4$. Nat. Phys., 13:117, 2017.

[117] Y. Shen, Y.-D. Li, H. C. Walker, P. Steffens, M. Boehm, X. Zhang, S. Shen, H. Wo, G. Chen, and J. Zhao. Fractionalized Excitations in the Partially Magnetized Spin Liquid Candidate $YbMgGaO_4$. Nat. Commun., 9:4138, 2018.

[118] Zhenyue Zhu, P. A. Maksimov, Steven R. White, and A. L. Chernyshev. Disorder-Induced Mimicry of a Spin Liquid in $YbMgGaO_4$. Phys. Rev. Lett., 119:157201, Oct 2017.

[119] T. Xie, J. Xing, S. E. Nikitin, S. Nishimoto, M. Brando, P. Khanenko, J. Sichelschmidt, L. D. Sanjeewa, A. S. Sefat, and A. Podlesnyak. Field-Induced Spin Excitations in the Spin-1/2 Triangular-Lattice Antiferromagnet $CsYbSe_2$. arXiv:2106.12451, 2021.

[120] J. Banda, B. K. Rai, H. Rosner, E. Morosan, C. Geibel, and M. Brando. Crystalline electric field of Ce in trigonal symmetry: $CeIr_3Ge_7$ as a model case. Phys. Rev. B, 98:195120, Nov 2018.

[121] B.-Q. Liu, P. Čermák, C. Franz, C. Pfleiderer, and A. Schneidewind. Lattice dynamics and coupled quadrupole-phonon excitations in $CeAuAl_3$. Phys. Rev. B, 98:174306, Nov 2018.

[122] Petr Čermák, Astrid Schneidewind, Benqiong Liu, Michael Marek Koza, Christian Franz, Rudolf Schönmann, Oleg Sobolev, and Christian Pfleiderer. Magnetoelastic hybrid excitations in $CeAuAl_3$. Proc. Natl. Acad. Sci., 116(14):6695, 2019.

[123] Jie Xing, Liurukara D. Sanjeewa, Jungsoo Kim, G. R. Stewart, Andrey Podlesnyak, and Athena S. Sefat. Field-induced magnetic transition and spin fluctuations in the quantum spin-liquid candidate $CsYbSe_2$. Phys. Rev. B, 100:220407(R), Dec 2019.

[124] Jie Xing, Liurukara D. Sanjeewa, Jungsoo Kim, G. R. Stewart, Mao-Hua Du, Fernando A. Reboredo, Radu Custelcean, and Athena S. Sefat. Crystal Synthesis and Frustrated Magnetism in Triangular Lattice $CsRESe_2$ (RE = La–Lu): Quantum Spin Liquid Candidates $CsCeSe_2$ and $CsYbSe_2$. ACS Mater. Lett., 2(1):71, 2020.

[125] Daisuke Yamamoto, Giacomo Marmorini, and Ippei Danshita. Quantum Phase Diagram of the Triangular-Lattice XXZ Model in a Magnetic Field. Phys. Rev. Lett., 112:127203, Mar 2014.

[126] P. A. Maksimov, Zhenyue Zhu, Steven R. White, and A. L. Chernyshev. Anisotropic-Exchange Magnets on a Triangular Lattice: Spin Waves, Accidental Degeneracies, and Dual Spin Liquids. Phys. Rev. X, 9:021017, Apr 2019.

[127] J. Gaudet, E. M. Smith, J. Dudemaine, J. Beare, C. R. C. Buhariwalla, N. P. Butch, M. B. Stone, A. I. Kolesnikov, Guangyong Xu, D. R. Yahne, K. A. Ross, C. A. Marjerrison, J. D. Garrett, G. M. Luke, A. D. Bianchi, and B. D. Gaulin. Quantum Spin Ice Dynamics in the Dipole-Octupole Pyrochlore Magnet $Ce_2Zr_2O_7$. Phys. Rev. Lett., 122:187201, May 2019.

[128] M. Doerr, M. Rotter, and A. Lindbaum. Magnetostriction in rare-earth based antiferromagnets. Adv. Phys., 54(1):1, 2005.

[129] This can be understood by examining the eigenvalues of the threefold rotation operator, $e^{i\frac{2\pi J_z}{3}}$.

[130] P. W. Anderson. Resonating valence bonds: A new kind of insulator? Mat. Res. Bull., 8:153, 1973.

[131] O. Starykh. Unusual ordered phases of highly frustrated magnets: a review. Rep. Prog. Phys., 78:052502, 2015.

[132] R. Coldea, D. A. Tennant, K. Habicht, P. Smeibidl, C. Wolters, and Z. Tylczynski. Direct Measurement of the Spin Hamiltonian and Observation of Condensation of Magnons in the 2D Frustrated Quantum Magnet Cs_2CuCl_4. Phys. Rev. Lett., 88:137203, 2002.

[133] R. Coldea, D. A. Tennant, and Z. Tylczynski. Extended scattering continua characteristic of spin fractionalization in the two-dimensional frustrated quantum magnet Cs_2CuCl_4 observed by neutron scattering. Phys. Rev. B, 68:134424, 2003.

[134] K. Foyevtsova, I. Opahle, Y.-Z. Zhang, H. O. Jeschke, and R. Valentí. Determination of effective microscopic models for the frustrated antiferromagnets Cs_2CuCl_4 and Cs_2CuBr_4 by density functional methods. Phys. Rev. B, 83:125126, 2011.

[135] S. A. Zvyagin, D. Kamenskyi, M. Ozerov, J. Wosnitza, M. Ikeda, T. Fujita, M. Hagiwara, A. I. Smirnov, T. A. Soldatov, A.Ya. Shapiro, J. Krzystek, R. Hu, H. Ryu, C. Petrovic, and M. E. Zhitomirsky. Direct Determination of Exchange Parameters in Cs_2CuBr_4 and Cs_2CuCl_4: High-Field Electron-Spin-Resonance Studies. Phys. Rev. Lett., 112:077206, 2014.

[136] R. Chen, H. Ju, H.-C. Jiang, O. A. Starykh, and L. Balents. Ground states of spin-1/2 triangular antiferromagnets in a magnetic field. Phys. Rev. B, 87:165123, 2013.

[137] M. Lee, J. Hwang, E. S. Choi, J. Ma, C. R. Dela Cruz, M. Zhu, X. Ke, Z. L. Dun, and H. D. Zhou. Series of phase transitions and multiferroicity in the quasi-two-dimensional spin-1/2 triangular-lattice antiferromagnet $Ba_3CoNb_2O_9$. Phys. Rev. B, 89:104420, 2014.

[138] K. Yokota, N. Kurita, and H. Tanaka. Magnetic phase diagram of the $S = 1/2$ triangular-lattice Heisenberg antiferromagnet $Ba_3CoNb_2O_9$. Phys. Rev. B, 90:014403, 2014.

[139] Y. Shirata, H. Tanaka, A. Matsuo, and K. Kindo. Experimental Realization of a Spin-1/2 Triangular-Lattice. Phys. Rev. Lett., 108:057205, 2012.

[140] J. Ma, Y. Kamiya, T. Hong, H. B. Cao, G. Ehlers, W. Tian, C. D. Batista, Z. L. Dun, H. D. Zhou, and M. Matsuda. Static and Dynamical Properties of the Spin-1/2 Equilateral Triangular-Lattice Antiferromagnet $Ba_3CoSb_2O_9$. Phys. Rev. Lett., 116:087201, 2016.

[141] S. Ito, N. Kurita, H. Tanaka, S. Ohira-Kawamura, K. Nakajima, S. Itoh, K. Kuwahara, and K. Kakurai. Structure of the magnetic excitations in the spin-1/2 triangular-lattice Heisenberg antiferromagnet $Ba_3CoSb_2O_9$. Nat. Commun., 8:235, 2017.

[142] Y. Cui, J. Dai, P. Zhou, P. S. Wang, T. R. Li, W. H. Song, J. C. Wang, L. Ma, Z. Zhang, S. Y. Li, G. M. Luke, B. Normand, T. Xiang, and W. Yu. Mermin-Wagner physics, (H, T) phase diagram, and candidate quantum spin-liquid phase in the spin-1/2 triangular-lattice antiferromagnet $Ba_8CoNb_6O_{24}$. Phys. Rev. Mater., 2:044403, 2018.

[143] Z. Zhu, P. A. Maksimov, S. R. White, and A. L. Chernyshev. Topography of Spin Liquids on a Triangular Lattice. Phys. Rev. Lett., 120:207203, 2018.

[144] R. Kaneko, S. Morita, and M. Imada. Gapless spin-liquid phase in an extended spin 1/2 triangular Heisenberg model. J. Phys. Soc. Jpn., 83:093707, 2014.

[145] Z. Zhu and S. R. White. Spin-liquid phase of the S = 1/2 J1–J2 Heisenberg model on the triangular lattice. Phys. Rev. B, 92:041105(R), 2015.

[146] Y. Iqbal, W.-J. Hu, R. Thomale, D. Poilblanc, and F. Becca. Spin liquid nature in the Heisenberg J_1-J_2 triangular antiferromagnet. Phys. Rev. B, 93:144411, 2016.

[147] W.-J. Hu, S.-S. Gong, W. Zhu, and D. N. Sheng. Competing spin-liquid states in the spin-1/2 Heisenberg model on the triangular lattice. Phys. Rev. B, 92:140403(R), 2015.

[148] S. Hu, W. Zhu, S. Eggert, and Y.-C. He. Dirac Spin Liquid on the Spin-1/2 Triangular Heisenberg Antiferromagnet. Phys. Rev. Lett., 123:207203, 2019.

[149] E. A. Ghioldi, M. G. Gonzalez, S.-S. Zhang, Y. Kamiya, L. O. Manuel, A. E. Trumper, and C. D. Batista. Dynamical structure factor of the triangular antiferromagnet: Schwinger boson theory beyond mean field. Phys. Rev. B, 98:184403, 2018.

[150] F. Ferrari and F. Becca. Dynamical structure factor of the J_1-J_2 Heisenberg model on the triangular lattice: magnons, spinons, and gauge fields. Phys. Rev. X, 9:031026, 2019.

[151] L. Chen, D.-W. Qu, H. Li, B.-B. Chen, S.-S. Gong, J. von Delft, A. Weichselbaum, and W. Li. Two-temperature scales in the triangular-lattice Heisenberg antiferromagnet. Phys. Rev. B, 99:140404(R), 2019.

[152] P. Czarnik, J. Dziarmaga, and P. Corboz. Evolution of an infinite projected entangled pair state: an efficient algorithm. Phys. Rev. B, 99:035115, 2019.

[153] C. Gerry and P. Knight. Introductory Quantum Optics. Cambridge University Press, 2004.

[154] P Thalmeier. Theory of the bound state between phonons and a cef excitation in ceal2. Journal of Physics C: Solid State Physics, 17:4153, 11 2000.